Coherence and nonlinearity in mechanical and josephson superconducting devices

Yanai, Shun

DOI
10.4233/uuid:e107c39b-e0ed-4318-9780-207bae9df24d

Publication date
2018

Document Version
Final published version

Citation (APA)
Yanai, S. (2018). *Coherence and nonlinearity in mechanical and josephson superconducting devices*. [Dissertation (TU Delft), Delft University of Technology]. https://doi.org/10.4233/uuid:e107c39b-e0ed-4318-9780-207bae9df24d

COHERENCE AND NONLINEARITY IN MECHANICAL AND JOSEPHSON SUPERCONDUCTING DEVICES

COHERENCE AND NONLINEARITY IN MECHANICAL AND JOSEPHSON SUPERCONDUCTING DEVICES

Dissertation

for the purpose of obtaining the degree of doctor
at Delft University of Technology
by the authority of the Rector Magnificus prof. dr. ir. T.H.J.J. van der Hagen,
chair of the Board for Doctorates
to be defended publicly on
Wednesday 28 November 2018 at 15:00 o'clock

by

Shun YANAI

Master of Science in Frontier Science, University of Tsukuba, Japan
born in Fujimi, Japan

This dissertation has been approved by the promotors.

Composition of the doctoral committee:

Rector Magnificus	chairperson
Prof. dr. G. A. Steele	Delft University of Technology, promotor
Prof. dr. ir. H. S. J. van der Zant	Delft University of Technology, promotor

Independent members:

Prof. dr. ir. P. G. Steeneken	Delft University of Technology
Prof. dr. M. Poggio	University of Basel, Switzerland
Prof. dr. E. Verhagen	AMOLF
Dr. G. S. Paraoanu	Aalto University, Finland
Dr. R. A. Norte	Delft University of Technology
Prof. dr. A. F. Otto	Delft University of Technology, reserve member

Keywords: mechanical oscillators, parametric excitation, Josephson junctions, SQUIDs, TLSs, cavity optomechanics, nanotechnology

Printed by: Gildeprint, Enschede

Front & Back: SEM picture of Josephson device embedded in a superconducting cavity taken in the cleanroom

ISBN 978.90.8593.376.2

An electronic version of this dissertation is available at
http://repository.tudelft.nl/.

CONTENTS

1

INTRODUCTION

1

1.1. NANOSCIENCE/NANOTECHNOLOGY

Science at dimensions below 100 nm Nanoscience deals with objects at least one of the dimensions of which are ~100 nm or less. The objects studied in this thesis can be categorized as nanoscale objects. Figure 1.1 (a) is a dimensional chart of things and is helpful for understanding how small the nanoscale (~ 100 nm or less) is. A size of 100 nm is 1/1000 of the diameter of a typical human hair. A single blood cell has a typical size of 5 μm. Figure 1.1 (b) shows a carbon nanotube hanging on a trench whose typical diameter is 5 nm. By using cleanroom equipment, we can fabricate nanoscale devices. The aim of this chapter is to give a brief introduction of nanoscience including a short history of nanoscience in order to provide enough background information for later chapters. There are generally two approaches to making nanoscale devices. One is the bottom up approach. This approach tries to build functional constituents made of atoms or molecules with nanotechnological processes. Single crystal nanowire is a prominent example of the bottom up approach. Nanowire is synthesised using the saturation of a molten metal on top of a single crystal substrate inside a tube furnace. This gives rise to the growth of a single crystal to form a nanowire[1]. The other approach is the top–down process. This approach is a subtractive process, by reducing the size of an object by slicing its bulk material to reach a size below 100 nm using cleanroom equipment.

For over thirty years, nanoscience has been a vehicle of affluence in society. We benefit from the tremendous amount of technologies of nanoscience in our life. One leading contribution is silicon transistors. The performance of a computer relies greatly on the size of its transistors. It depends on how fast the transistors can be turned on and off, which has to do with how quickly the electrons can flow in the semiconductor. An increase in the number of transistors boosts the performance of a computer. The number of transistors per square inch has doubled every year since its invention, something which is called Moore's law[2], illustrated in Figure 1.2. Silicon transistors are used in every electrical component that can be imagined. In the 70 s, the size of the gate of a transistor of the first microprocessor was 10 μm. After 40 years, the size was reduced to 15 nm.

Quantum phenomena at the nanoscale that are impossible at a larger scale In nanoscale devices, the non-classical nature of things becomes apparent, something which would not appear in larger scale objects. The Josephson junction is one example. A Josephson junction consists of two superconducting electrodes that lie on top of each other, having an insulating layer in between. At temperatures below the transition temperature of the supercondcuting metal, the electrons condense into Cooper pairs, and they tunnel through the insulating barrier without a voltage drop. This unique phenomenon appears only if the insulating layer is thin enough. Josephson junctions are used for a flux-tunable resonator in Chapter 6 and 7. A basic description of the Josephson junction is given in the background and theory chapter.

(a)

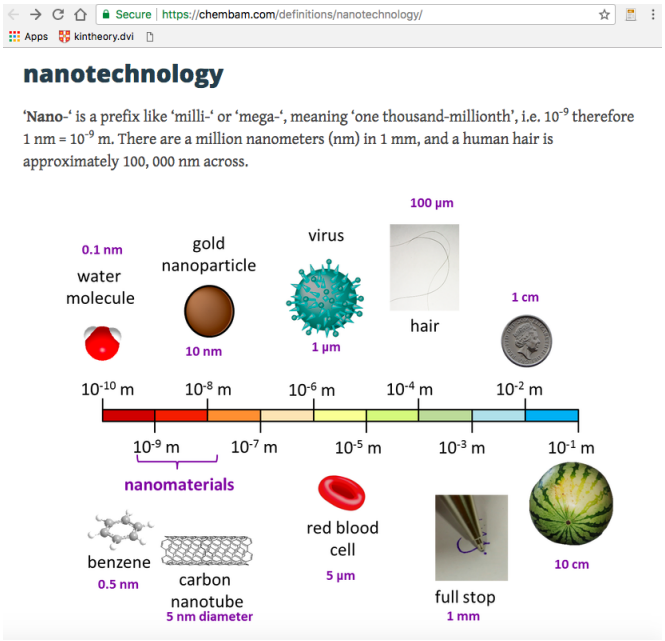

(b)

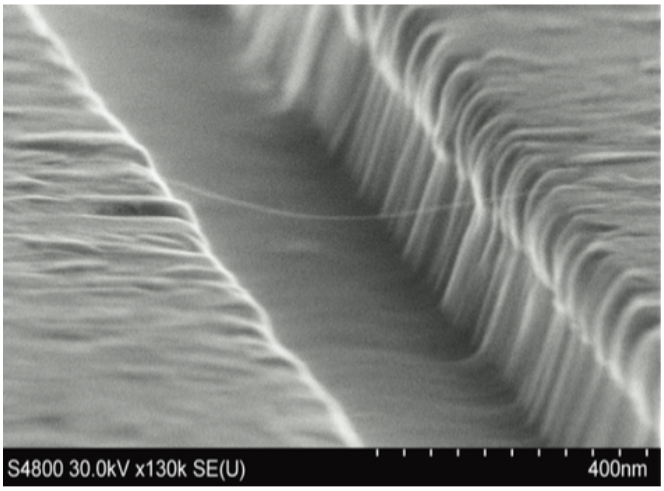

Figure 1.1: (a) The general sizes of things. (b) Scanning electron microscope image of single carbon nanotube. The picture is adapted from [3]. The typical diameter of a carbon nanotube is 5 nm.

1

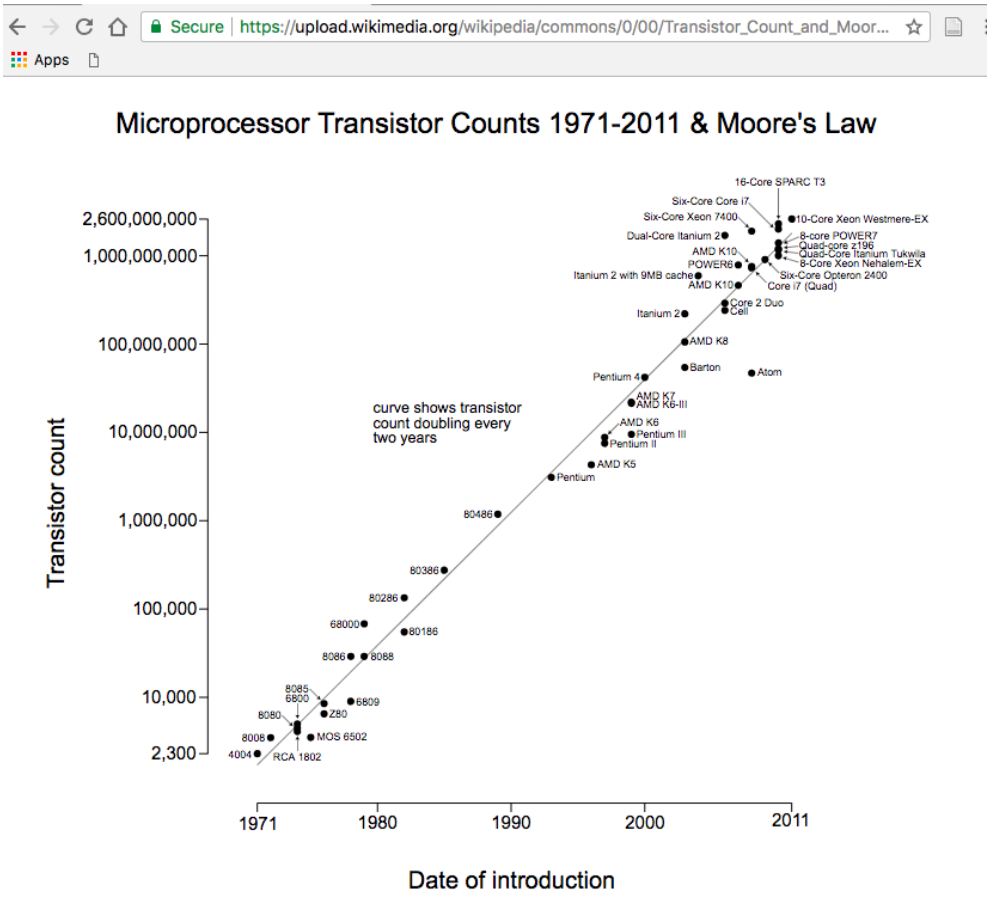

Figure 1.2: Number of transistors in computers vs years of production.

1.2. PROBING QUANTUM SYSTEMS WITH SUPERCONDUCTING MICROWAVE RESONATORS

Microwave cavities as a tool to probe quantum mechanical objects A superconducting microwave resonator is a versatile microwave element. It can probe the quantum nature of any coupled objects. A superconducting microwave resonator is essentially an LC resonant circuit which can be fabricated inside a cleanroom. The low microwave loss in a superconducting resonator makes it suitable for detecting small signals. A small perturbation of the electromangetic field due to the object of interest causes a frequency modulation through the changing capacitance or inductance. The readout of quantum systems with microwave resonators, first implemented for superconducting qubits, is called dispersive readout. The initial motivation for this readout scheme was to eliminate backaction noise due to quasiparticle generation in a resistor [4]. This system is a microwave analogue of cavity quantum electrodynamics (CQED)[5], and is actively investigated as a building block for quantum computers. One advantage of superconducting qubits is their ability to manipulate quantum states quickly. Superconducting resonators are also used to readout other media as well. For instance, the electron spin of a nitrogen vacancy center in a diamond[6] is being quite actively investigated for storage purposes. Although such a system does not have a controllability similar to that seen in a circuit QED system, its long coherence is an attractive property.

Probing mechanical objects with superconducting microwave resonators A mechanical object is also interesting to probe with superconducting resonators. This configuration implements a microwave version of optomechanics[7]. Figure 1.3 shows two pictures of mechanical resonators coupled to a superconducting resonator. A small mechanical motion of a nanowire or drum modulates the cavity frequency via radiation pressure when the microwave cavity is driven near the cavity frequency. This principle is referred to as cavity optomechanics. The field has been evolving quite rapidly for just slightly over a decade as a method for the sensitive detection of mechanical motion with unprecedented accuracy, as well as for experiments for probing the quantum mechanical nature of macroscopically large mechanical objects.

The two pictures of Figure 1.3 are common realizations for optomechanical systems in the microwave regime. Regal et al. [8] demonstrated radiation pressure cooling of Al-based nanowires (Figure 1.3 (a)) coupled to a microwave superconducting cavity. Subsequent experiments improved the optomechanical coupling by changing to mechanical drums, as shown in Figure 1.3 (b), which leads to achieving a strong coupling regime[9], and demonstrated ground state cooling[10]. These milestones allowed novel experiments not possible in the classical regime, such as quantum noise squeezing [11][12].

In this thesis, we study microwave optomechanics to understand dissipation mechanisms, both mechanical dissipation and microwave dissipation. We also explore new types of optomechanical implementations, including new hybrid electromechani-

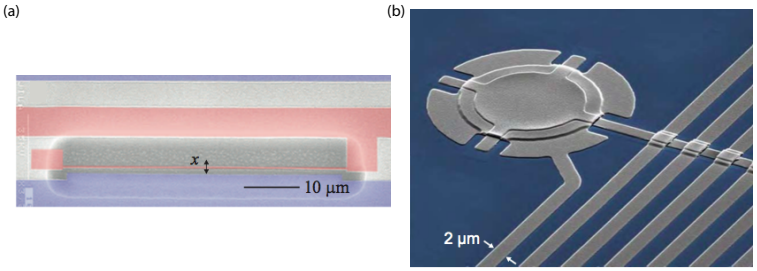

Figure 1.3: (a) False-colour scanning electron microscope image of a mechanical nanowire (pink) [8]. (b) False-colour scanning electron microscope image of an Al drum [9].

cal/microwave and optomechanical devices and new cavity designs for implementing flux-mediated optomechanics.

1.3. THESIS OUTLINE

Chapter 2 provides briefly the background and theory related to the other chapters. It consists of four main sections: cavity optomechanics, electrostatic driving, the SQUID cavity, and nonlinear dissipation.
Chapter 3 treats fabrication. This chapter contains detailed explanations of the fabrication procedures, including the fabrication of microwave cavities, Josephson junctions, flux-tunable Josephson junction based microwave resonators, and silicon nitride mechanical resonators.
The next three chapters are experimental chapters. **Chapter 4**, treats the mechanical loss in the superconducting metal mechanical drums. We study nonlinear loss in mechanically compliant superconducting molybdenum rhenium (MoRe) drums in a cavity optomechanical setup. Quality factors and the frequency shift of our mechanical drum as a function of the temperature show a trend similar to two level systems (TLSs) observed in superconducting microwave resonators. Further, the mechanical quality increases as a function of power in both the linear and nonlinear regime, which is suggestive evidence that our mechanical resonators are nonresonantly coupled to TLS defects.
Chapter 5 talks about the parametric excitation of mechanical nanowires in a cavity optomechanical setup. A MoRe covered silicon nitride mechanical nanowire is dissipatively coupled to a coplanar waveguide (CPW) microwave resonator. This configuration allows electrostatically actuating the mechanical oscillator. With electrostatic excitation at twice the natural frequency of the nanowire, the mechanical mode can be parametrically excited. When a microwave signal is sent to the CPW resonator near the cavity frequency, the parametically excited mechanical signal is up-converted to a microwave frequency, resulting in a parametric excitation (amplification/squeezing) of a microwave signal.

Chapter 6 is about the microwave loss in superconducting flux-tunable resonators. We compare the microwave losses in two different fabrication techniques, and found that the electron beam resist used for lift off leads to losses in microwave resonators. A comparison is made between MoRe lumped elements with Al/AlOx/Al dc SQUID and an Al/AlOx/Al SQUID cavity fabricated in one single step. Optimizing the conditions of the surface of the metal deposition is a key element for achieving highly coherent Josephson junction based resonant circuits.
Chapter 7 discusses higher order dissipation in Josephson junction resonators. We model the cavity response of a side coupled Josephson junction resonator $S21$ with Duffing coefficient β and a nonlinear damping term γ_{nl}. We observed the frequency shift and the amplitude of the cavity response as a function of power, which deviates from the expected trends. By numerically simulating the cavity response with known β, we determined the nonlinear damping rate γ_{nl} and the input power.

1

REFERENCES

[1] P. J. Pauzauskie and P. Yang, *Nanowire photonics,* Materials Today **9**, 36 (2006).

[2] G. Moore, *Cramming More Components Onto Integrated Circuits,* Proceedings of the IEEE **86**, 82 (1998).

[3] B. H. Schneider, *Suspended carbon nanotubes coupled to superconducting circuits*, Ph.D. thesis, TU Delft (2014).

[4] M. Metcalfe, *A new microwave resonator readout scheme for superconducting qubits*, Ph.D. thesis, Yale University (2008).

[5] A. Wallraff, D. I. Schuster, A. Blais, L. Frunzio, R.-S. Huang, J. Majer, S. Kumar, S. M. Girvin, and R. J. Schoelkopf, *Strong coupling of a single photon to a superconducting qubit using circuit quantum electrodynamics,* Nature **431**, 162 (2004).

[6] C. Grezes, B. Julsgaard, Y. Kubo, W. L. Ma, M. Stern, A. Bienfait, K. Nakamura, J. Isoya, S. Onoda, T. Ohshima, V. Jacques, D. Vion, D. Esteve, R. B. Liu, K. Mølmer, and P. Bertet, *Storage and retrieval of microwave fields at the single-photon level in a spin ensemble,* Physical Review A **92**, 020301 (2015).

[7] M. Aspelmeyer, T. J. Kippenberg, and F. Marquardt, *Cavity Optomechanics,* Reviews of Modern Physics **86**, 1391 (2014), arXiv: 1303.0733.

[8] C. A. Regal, J. D. Teufel, and K. W. Lehnert, *Measuring nanomechanical motion with a microwave cavity interferometer,* Nature Physics **4**, 555 (2008).

[9] J. D. Teufel, D. Li, M. S. Allman, K. Cicak, A. J. Sirois, J. D. Whittaker, and R. W. Simmonds, *Circuit cavity electromechanics in the strong-coupling regime,* Nature **471**, 204 (2011).

[10] J. D. Teufel, T. Donner, D. Li, J. W. Harlow, M. S. Allman, K. Cicak, A. J. Sirois, J. D. Whittaker, K. W. Lehnert, and R. W. Simmonds, *Sideband cooling of micromechanical motion to the quantum ground state,* Nature **475**, 359 (2011).

[11] J.-M. Pirkkalainen, E. Damskägg, M. Brandt, F. Massel, and M. A. Sillanpää, *Squeezing of quantum noise of motion in a micromechanical resonator,* Physical Review Letters **115** (2015), 10.1103/PhysRevLett.115.243601, arXiv: 1507.04209.

[12] F. Lecocq, J. B. Clark, R. W. Simmonds, J. Aumentado, and J. D. Teufel, *Quantum nondemolition measurement of a nonclassical state of a massive object,* Physical Review X **5** (2015), 10.1103/PhysRevX.5.041037, arXiv: 1509.01629.

2

BACKGROUND AND THEORY

2.1. OPTOMECHANICS

2.1.1. INTRODUCTION

Cavity optomechanics: The interaction of a mechanical object with an electromagnetic field via radiation pressure. This rapidly growing field of physics has attracted interest as a tool for probing the quantum mechanical nature of macroscopically large objects, as well as for technological applications to quantum information processing. The interaction of a photon and a phonon in cavity optomechanics can be pictured in a Fabry–Perot cavity with one movable mirror connected to a wall via a spring. The general Hamiltonian can be expressed as follows[1].

$$H = \hbar\omega_{cav} a^\dagger a + \hbar\omega_m b^\dagger b + \hbar g_0 a^\dagger a (b^\dagger + b) \tag{2.1}$$

The right-hand side of this equation has three terms. The cavity and the mechanical element can be approximated as two harmonic oscillators, where a and b are the annihilation operators of the photon and the mechanical phonon, respectively. The third term is the interaction term, where $g_0 = \frac{d\omega_{cav}}{dx} x_{zpf}$ is a single photon coupling. The strength of the single photon coupling is the frequency pull due to the zero point motion of the mechanical element. In most experiments done to date, the value of g_0 is small. To compensate for this weak optomechanical coupling, the procedure typically taken is to increase the input laser power, which enhances the effective optomechanical coupling in exchange for giving up the quadratic nature of the optomechanical interaction.

For systems whose vacuum coupling is relatively small compared with the decay rates of the cavity/mechanical elements, a linearization can be applied. This is an approximation which disregards the interaction due to the constant drive field. The

procedure is implemented by splitting the cavity field operator into two contributions, where a is the average amplitude of the light field, and a small quantum fluctuation term δa, with $a = \alpha + \delta a$. Substituting a into the interaction term of Equation 2.1, there are three different terms, and the terms proportional to $|\alpha|^2$ and $\delta a^\dagger \delta a$ are omitted. The resulting interaction Hamiltonian can be expressed as follows.

$$H_{int} = \hbar g(\delta a^\dagger b + \delta a b^\dagger) \tag{2.2}$$

Here, $g = g_0\sqrt{n_{cav}}$ is the optomechanical coupling strength. It is clear that the optomechanical coupling is enhanced by increasing the amplitude of the driving field of the cavity. Operation under linearization benefits from the enhancement of the optomechanical coupling, g, but the downside of this coupling is that the resulting state is always Gaussian.

2.1.2. THE STRONG COUPLING REGIME

Stronger optomechanical interaction serves for a full quantum control. The control and manipulation of mechanical objects in a quantum coherent fashion must satisfy two criteria: there must be a near zero averaged thermal occupation and the system should be in the strong-coupling regime. The resonance frequencies of the mechanical elements vary from several hundreds of KHz to GHz. Thermal occupation in a mechanical oscillator whose resonance frequency is below the GHz range is well above unity. Under certain conditions, this thermal phonon occupation can be removed with a technique of resolved sideband cooling. The other criterion is that the system be in the strong coupling regime. In the strong coupling regime, the interaction between the mechanical element and the cavity is larger than the decay rates of the mechanics and cavity, which enables a coherent energy exchange within the system. Experimental realisations of the strong coupling regime have been achieved [2][3][4], along with ground state cooling[5]. When driving the optomechanical system at a frequency ω_d, it is possible to linearize the Hamiltonian[1]. In this case, the system is equivalent to two linearly coupled modes, similar to two harmonic oscillators coupled by a spring. What results is then two hybridized modes with correponding frequencies:

$$\omega_\pm^2 = \frac{1}{2}[\Delta^2 + \omega_m^2 \pm \sqrt{(\Delta^2 - \omega_m^2)^2 + 4g^2\Delta\omega_m}] \tag{2.3}$$

where $\Delta = \omega_d - \omega_{cav}$ is the detuning between the driving field at ω_d and the cavity frequency ω_{cav}, and ω_m is the mechanical frequency. For the case where the coupling is not zero, two eigenmodes create anticrossing $\omega_+ - \omega_- \sim g$. In the case of a damped system, g needs to satisfy the condition $g > \kappa_{cav}, \gamma_m$ to observe normal-mode splitting, which is an unambiguous signature of the strong coupling regime. Analogous effects have been observed in cavity/circuit QED systems[6][7], called vacuum Rabi oscillation, where the excited atom(s) exchange a photon with a cavity through spontaneous emission and reabsorption of a photon from the electromagnetic mode emission of the cavity.

2.1.3. COOPERATIVITY

For quantum ground state cooling, an optomechanical system can be cooled down to the quantum ground state without reaching the strong coupling regime. The useful figure of merit to look at is cooperativity. Cooperativity is defined as $C = \frac{4g^2}{\kappa\gamma_m}$, which connects the optomechanical coupling constant g, the cavity decay rate κ, and the mechanical decay rate γ_m. Physically, the number indicates how efficiently the photon/phonon is transferred from the cavity to the mechancal oscillator, and vice versa.

2.1.4. QUADRATIC COUPLING

Coupling the electromagnetic field as the square of the displacement enables novel experiments. Cavity optomechanics uses dispersive coupling with radiation pressure, in which the cavity resonant mode is coupled to the motion of a mechanical element. Current experiments to date have employed a linear coupling to first order. However, a non-linear coupling where the cavity is coupled to the square of the position of the oscillator is another attractive method in the field. The unique nature of this coupling enables it to be used as a tool to detect the energy of a mechanical mode[8]. Quadratic coupling has been experimentally demonstrated in [9, 10]. This measurement is called a quantum non-demolition measurement (QND). This technique uses the fact that the measurement of the square of the position commutes with the Hamiltonian of the system. Other novel physics can be studied with quadratic coupling, including cooling and squeezing[11]

2.2. ELECTROSTATIC DRIVING

2.2.1. ELECTROSTATIC DRIVING

The electrostatic actuation of a mechanical oscillator uses the electrostatic force between two electrodes. Applying a voltage between the electrodes results in a force that can be expressed as in the equation below.

$$F = \frac{1}{2}\frac{\partial C}{\partial x}V^2 = \frac{1}{2}\frac{\partial C}{\partial x}(V_{dc}+V_{ac})^2 = \frac{1}{2}\frac{\partial C}{\partial x}(V_{dc}^2+2V_{dc}V_{ac}+V_{ac}^2) \tag{2.4}$$

This equation expresses the distinct contributions of the force acting on a mechanical oscillator. The first term in the right-hand side of the equation, which is proportional to V_{dc}^2, represents the dc static force on the mechanical oscillator. A dc voltage can be applied via a gate electrode located near a mechanical element. It induces the opposite charge on the mechanical resonator element attracted to the gate electrode. This static force competes against the spring force, $k_0 x$. Thus, the effective spring constant k is reduced. This effect is approximately quadratically dependent on the applied dc voltage. This leads to a reduction of the mechanical resonance frequency, called capacitive softening.

$$k_{tot} = k_0 - \frac{1}{2}\frac{\partial^2 C}{\partial^2 x}V^2 \tag{2.5}$$

The second term in the right hand side of Equation 2.4 is an ac driving force, F_{ac}.

$$F_{ac} = \frac{\partial C}{\partial x}(V_{dc}V_{ac}) \tag{2.6}$$

For the actuation of the mechanical oscillators in our experiments, this force was produced by applying a combination of a dc voltage from bias and a small ac voltage, V_{ac}. The position of the mechanical oscillator was optimized for applying the maximum V_{ac}. The third term, V_{ac}^2, is small compared with F_{ac}, and generally ignored.

2.2.2. PARAMETRIC DRIVING

Unlike the previous section, here the discussion is focused on a case of actuation of a resonant mode whose actuation frequency differs from the natural frequency, called parametric excitation. Especially when the driving frequency is twice the natural frequency, the drive (pump) tone transfers energy to two normal modes of the system, the signal and the idler. One example is a child on a swing. The motion of the swing gradually increases as the child gives a kick, which essentially changes the effective length of the swing, at the highest point of curvature of the motion. Parametric oscillation is an open oscillating system where an external force (the child's kick) acts on the system and modulates one of the parameters of the system periodically at a certain frequency. An equivalent phenomenon can be observed in an LRC circuit with a movable capacitor[12], where the distance of the capacitor is modulated externally.

Here we look at the behaviour of a resonant mode where one of the parameters is modulated at twice the natural frequency. We consider a mechanical system which

oscillates at its resonance frequency ω_0. Then an external force is applied at twice the natural frequency of the resonator. We shall start with the one dimensional motion of a simple harmonic oscillator. A thorough derivation can be found in [13].

$$\frac{d^2x}{dt^2} + \omega^2(t)x = 0 \tag{2.7}$$

Now we consider the case where ω is modulated at twice the natural frequency with a small detuning.

$$\omega = \omega_0(1 + \alpha\cos(\gamma t)) \tag{2.8}$$

Here,

$$\gamma = 2\omega_0 + \epsilon. \tag{2.9}$$

Plugging Equation 2.8 into 2.7, and omitting the second degree term in α leads to $\alpha \ll 1$.

$$\frac{d^2x}{dt^2} + \omega_0^2[1 + 2\alpha\cos(\gamma t)]x = 0 \tag{2.10}$$

We expect a solution of Equation 2.10 in the form of

$$x(t) = a(t)\cos\left(\omega_0 + \frac{\epsilon}{2}\right)t + b(t)\sin\left(\omega_0 + \frac{\epsilon}{2}\right)t \tag{2.11}$$

where $a(t)$ and $b(t)$ are time dependent, but much slower than the sinusoidal parts. For slow changes in time, $\sim \frac{da}{a} \ll \alpha$, the second derivative of $a(t)$ and $b(t)$ with respect to time is small enough, and these terms are omitted.

Substituting this into Equation 2.10, Equation 2.10 yields

$$\begin{aligned}(-2\dot{a(t)} - b(t)\epsilon - \frac{1}{2}\omega_0 b(t)\alpha)\omega_0\sin\left(\omega_0 + \frac{\epsilon}{2}\right)t + \\ (2\dot{b(t)} - a(t)\epsilon + \frac{1}{2}\omega_0 a(t)\alpha)\omega_0\cos\left(\omega_0 + \frac{\epsilon}{2}\right)t = 0.\end{aligned} \tag{2.12}$$

To satisfy the equation above, the two coefficients in front of the two sinusoidal terms have to be zeros. We expect the signal to increase as a function of time, $a(t) \sim ae^{st}$, $b(t) \sim be^{st}$. The equation can be further developed to

$$sa + \frac{b}{2}\epsilon + \frac{1}{4}\omega_0 b\alpha = 0 \tag{2.13}$$

$$\frac{a}{2}\epsilon - \frac{1}{4}\omega_0 a\alpha - sb = 0. \tag{2.14}$$

We now write this system of equations in matrix form.

$$\begin{pmatrix} s & \frac{1}{2}\epsilon + \frac{1}{4}\alpha\omega_0 \\ \frac{1}{2}\epsilon - \frac{1}{4}\alpha\omega_0 & -s \end{pmatrix}\begin{pmatrix} a \\ b \end{pmatrix} = \begin{pmatrix} 0 \end{pmatrix} \tag{2.15}$$

s must satisfy the characteristic equation, which gives $s = \frac{1}{2}\sqrt{(\frac{\omega_0\alpha}{2})^2 - \epsilon^2}$. It can be seen that parametric amplification reaches a maximum for zero detuning, and reduces its magnitude as the detuning increases. The amplification diminishes when detuning, ϵ, reaching $\pm\frac{1}{2}\alpha\omega_0$.

$$-\frac{1}{2}\alpha\omega_0 < \epsilon < \frac{1}{2}\alpha\omega_0 \tag{2.16}$$

2.2.3. PARAMETRIC AMPLIFICATION AND SQUEEZING

There are two types of parametric amplification: the **three-wave amplifier** and the **four-wave amplifier**. The parametric resonance discussed in the previous section and the parametric amplification/squeezing of nanowire discussed in the other chapter uses the three-wave mixing mode. The difference between three-wave mixing and four-wave mixing is explained with examples of Josephson parametric amplifiers, which hopefully makes a smooth transition to the subsequent section.

Three-wave amplifiers have the form $\omega_d = \omega_{sig} + \omega_{idl}$, which is also called three-photon mixing. This mode of operation consists of the interaction of three waves: the pump, the signal, and the idler. Another example besides the mechanical amplification of a nanowire discussed in the other chapter is the flux driven Josephson parametric amplifier[14], where the resonance frequency of a $\lambda/4$ resonator which is terminated with a dc SQUID is modulated at twice the resonance frequency via inductance. What these two systems have in common is that they both operate at points using either magnetic flux or bias voltage in order to break a symmetry, which gives rise to modulation of a parameter. The amplification can be done in the linear regime where there is no shift in the resonance frequency due to the pump. In case there is a degenerate mode of amplification where $\omega_{sig} = \omega_{idl}$, the signal can be amplified noiselessly. This can be seen in Figure 2.1 (a), where the pump signal is applied through the device via a different port whose frequency is detuned far away from the fundamental or other higher harmonics, so that a separation of the signal from the pump could be done quite easily. Also, this reduces the possibility of leakage of the pump signal to the signal mode.

Another type of parametric amplifier is the **four-wave amplifier**, also known as four-photon mixing, where $\omega_d + \omega_d = \omega_{sig} + \omega_{idler}$[15][16][17]. This mode of operation is named after the interaction, which consists of four waves: the signal, the pump, the amplified signal, and the idler. Four-wave mixing in a Josephson parametric amplifier uses the Kerr non-linearity of Josephson inductance. As the circuit is driven near the bifurcation point, where the amplitude of the Duffing oscillator still has a single-valued solution, the resonance frequency is modulated at twice the pump frequency, $\omega_s = \omega_{idl} = \omega_d$. A four-wave mixing Josephson parametric amplifier uses the non-linear term of the Josephson junction to modulate the resonance frequency of the Josephson junction based LC circuit, which requires no flux pump.

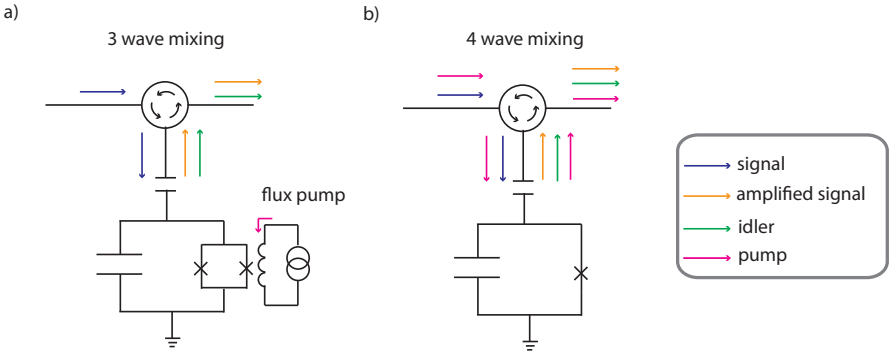

Figure 2.1: Circuit representation of a three-wave mixing amplifier (a) and a four-wave mixing amplifier (b). The three-wave mixing amplifies the signal (blue) with an external pump via a flux line at twice the natural frequency $\omega_{pump} = 2\omega_0$ (pink).

2.3. THE SQUID CAVITY

2.3.1. THE JOSEPHSON JUNCTION

In the field of superconducting circuits, Josephson junctions play important roles: as a non-linear, non-dissipative circuit element for superconducting qubits[6], SQUIDs for detecting magnetic nano-particles [15][18], and quantum limited JPA[16]. Although there is a wide variety of novel Josephson junctions being investigated, only Al/AlOx/Al SIS junctions are used in this project. Therefore, here we focus on the theory of SIS Josephson junctions. An SIS Josephson junction consists of two superconducting electrodes with an insulating layer in between them, as shown in Figure 2.2. The wave function on each superconducting electrode overlap on the insulating barrier, which allows tunneling Cooper pairs from one electrode to the other. This behaviour can be expressed in the equations below.

$$I = I_0 \sin(\delta) \tag{2.17}$$

$$d(\delta)/dt = 2eV/\hbar \tag{2.18}$$

Here, I_0 is the critical current of the junction and δ is the gauge invariant phase between the two superconducting electrode. The critical current is the maximum current to maintain superconductivity. Equation 2.17 shows that the phase difference is the element which drives the Cooper pairs across the Josephson junction. Cooper pairs can tunnel through a junction without breaking the pairs. I_0 is the critical current of the junction, whose value depends on the thickness of the insulating layer, the area, and the resistance of the junction, as will be discussed later in this section. When the junction is biased with a voltage larger than the critical voltage, Vc, the resistance

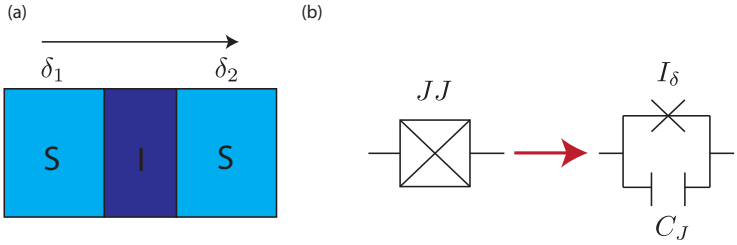

Figure 2.2: (a) SIS junction consisting of two superconducting electrodes with an insulating layer in the middle. Cooper pairs tunnel through the insulating barrier as a supercurrent which is proportional to the phase difference between the two electrodes, $\delta_1 - \delta_2$; the voltage difference does not play a role in driving the Cooper pairs. In our case, the Josephson junctions are made of Aluminium superconductor and an Aluminium Oxide insulating layer. The left-hand side of the figure (b) shows a circuit representation of a Josephson junction. A Josephson junction can be considered as a lumped element lc resonant circuit with a non-linear inductance and parasitic capacitance due to the two superconducting electrodes. The resonance frequency between the Josephson inductance and the parasitic capacitance is referred to as the plasma frequency. However, the plasma frequency of a Josephson junction typically lies way above our measurement bandwidth. For microwave measurements, Josephson junctions are usually shunted by a capacitance or diluted with a geometric inductance to bring down the plasma frequencies.

has a non-zero value, but the current has an oscillation frequency of $\omega = 2eV/\hbar$[19]. This is referred to as the Josephson effect. The temperature dependence of the critical current can be expressed by the Ambegaokar–Barratoff relation [20].

$$I_c R_n = (\pi\Delta/2e)\tanh(\Delta/2k_B T) \tag{2.19}$$

Here, R_n, Δ, and T are the resistance of a Josephson junction at room temperature, the superconducting gap, and the temperature, respectively. When $T \sim 0$, the critical current can be derived as $I_c = \pi\Delta/2e$. For Aluminium Josephson junctions, the typical transition temperature is around 1.2 K with a superconducting gap around $18e^{-5}$ eV.

2.3.2. THE DC SQUID AS A SOURCE OF INDUCTANCE

For this project, our aim is to use a Josephson junction as a source of inductance for the detection of the motion of a mechanical resonator embedded in the SQUID loop[21]. To quantify the Josephson inductance of a single Josephson junction, the derivative of Equation 2.17. is taken and substituted into $\frac{\partial\delta}{\partial t}$ of Equation 2.18.

$$\frac{dI_J}{dt} = I_0 \cos\delta \frac{2\pi}{\Phi_0} V. \tag{2.20}$$

From Equation 2.20, the inductance of a single Josephson junction can be found using the relation $V = L\frac{dI}{dt}$.

$$L_J = \frac{\Phi_0}{2\pi I_0 \cos\delta} \tag{2.21}$$

From this equation, we can see that the Josephson inductance is a non-linear inductance whose value is inversely proportional to the critical current of the Josephson junction, and it diverges as δ approaches $\pi/2$. Φ_0, I_0, and δ are the flux quantum, the critical current of the Josephson junction, and the phase difference of the Josephson junction, respectively.

A Superconducting Quantum Intereference Device (SQUID) is made by embedding two Josephson junctions in a superconducting loop. The critical current of a dc SQUID decreases on applying a magnetic field. When the geometric inductance of the SQUID is much smaller than the Josephson inductance of the SQUID, the critical current can be expressed as

$$I(\Phi) = 2I_0 \cos|(\frac{\pi\Phi}{\Phi_0})| \tag{2.22}$$

where Φ is the strength of the magnetic field applied through the SQUID loop, which is quantised by $\Phi_0 = h/2e = 2.07e^{-15}Tm^2$. From Equation 2.22, dc SQUID can be considered as a single junction whose critical current depends on the magnetic field. The Josephson inductance for a dc SQUID is found by substituting Equation 2.22 into 2.21.

$$L_J = \frac{\Phi_0}{2\pi I_0 \cos|\frac{\pi\Phi}{\Phi_0}|} \tag{2.23}$$

A Josephson inductance using a single junction or a dc SQUID acts as a non-linear and non-dissipative element, as is clear from the result of the dc Josephson effect. The parasitic capacitance between the two superconducting electrodes is typically small. The junction itself acts as a resonant circuit with a parasitic capacitance whose resonance frequency, called the plasma frequency, is still outside of the measurement bandwidth, and typically lies around several tens to 100 of GHz.

2.3.3. SQUID CAVITIES

The term SQUID cavity refers to a Josephson junction resonator where a Josephson inductance contributes as a part of a resonance system. Our circuits consist of a dc SQUID galvanically shorted to a microwave coplanar wavelength resonator or lumped element resonator. These types of resonant circuits are quite common, such as superconducting qubits[22], Josephson bifurcationi amplifiers[23] [24] [25], adjustable couplers with SQUIDs[26][27], etc. These resonance circuits are quite versatile. They can be operated in linear or non-linear fashion, depending on the application.

Here we analytically investigate the behavior of a SQUID cavity under resonant drive. The circuit we consider is a Josephson inductance shunted by a capacitance to form a resonant circuit. The circuit model we consider is shown in Figure 2.3 (a). The Josephson junction is shunted by a capacitance whose resonant frequency is $1/\sqrt{L_J C}$. For the resonant drive, a microwave signal is applied externally via a transmission line. Figure 2.3 (b) is the Norton equivalent circuit of Figure 2.3 (a). Using

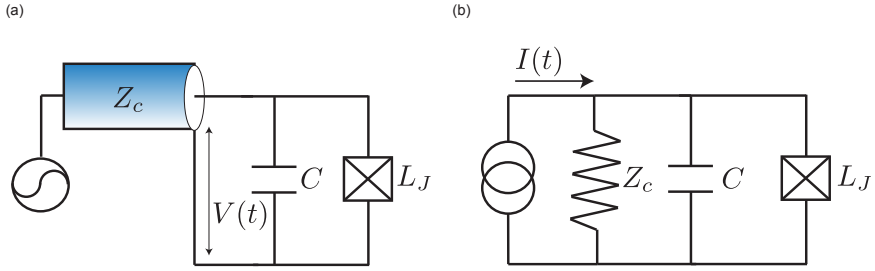

Figure 2.3: (a) Josephson junction resonator where a single junction is shunted by a capacitance. The resonant circuit is galvanically shorted to a transmission line. (b) Norton equivalent circuit of (a). The microwave generator is replaced by an ideal current source parallel with the impedance of the transmission line, Z_c.

Kirchoff's law, the driving current can be equated with the currents going through the three circuit components, JJ, C, and Z_c.

$$C\varphi_0\frac{d^2\delta}{dt^2}+\frac{\varphi_0}{Z_C}\frac{d\delta}{dt}+I_0\sin(\delta(t))=I(t) \tag{2.24}$$

For simplicity, the geometric inductance, L_J, and the parasitic capacitance of the Josephson junction, C_J, are omitted. The current $I(t)$ on the right hand side of the equation above is a driving term, and the circuit resonates at the driven frequency, ω_d, like a forced oscillation. δ is the gauge invariant phase over the SQUID. Under resonant drive on the circuit, the right hand side of the equation above can be expressed as follows.

$$C\varphi_0\frac{d^2\delta}{dt^2}+\frac{\varphi_0}{Z_C}\frac{d\delta}{dt}+I_0\sin(\delta(t))=I_{drive}\cos(\omega_d t) \tag{2.25}$$

or

$$\frac{d^2\delta}{dt^2}+2\gamma\frac{d\delta}{dt}+\omega_0^2\sin(\delta(t))=\omega_0^2\frac{I_{drive}}{I_0}\cos(\omega_d t) \tag{2.26}$$

where $\gamma=1/2CZ_c$ and $\omega_0=\sqrt{I_0/C\varphi_0}$. Bifurcation conditions have been analysed in [28][29]:

$$\omega_c=\omega_0-\sqrt{3}\gamma \tag{2.27}$$

and

$$F_c^2=\frac{256\gamma^3\omega_0^3}{9\sqrt{3}|\beta|}. \tag{2.28}$$

Here, ω_c denotes the critical detuning and F_c the critical driving force. By substituting the driving force term of Equation 2.26 into Equation 2.28 with the amplitude of the

Duffing coefficient $\beta = -\frac{\omega_0^2}{6}$, one obtains the driving current required for reaching the onset of bifurcation,

$$I_{drive-c}^2 = \frac{512\gamma^3}{3\sqrt{3}\omega_0^3} I_0^2 \tag{2.29}$$

where $I_{dtive-c}$ is the critical drive current of the system.

2.3.4. FLUX MODULATION DUE TO A SMALL SIGNAL

A SQUID can be used for detecting small signals which modulate a magnetic field via the SQUID loop. Here we consider the case where a small signal is applied to the resonant mode along with a strong pump tone. This could be a mechanical signal, magnetic molecules, or a qubit, as described in [29][28]. Here, we start from Equation 2.25, which is a simple Duffing equation driven at ω_d. Now substitute $\delta_d + \delta_s$ into the equation, where δ_d is a solution of the Duffing equation (2.25), and δ_s is a small perturbation corresponding to the signal of interest, where $\delta_s << \delta_d$.

$$\frac{d^2\delta_d}{dt^2} + \frac{d^2\delta_s}{dt^2} + 2\gamma(\frac{d\delta_d}{dt} + \frac{d\delta_s}{dt}) + \omega_0^2[\delta_d + \delta_s - \frac{(\delta_d+\delta_s)^3}{6}] - \omega_0^2\frac{I_p}{I_0}\cos(\omega_d t) = \frac{I_{in}(t)}{C\varphi_0 Z_c} \tag{2.30}$$

Keeping only terms depending on the small signal, the equation above can be expressed as follows.

$$\frac{d^2\delta_s}{dt^2} + 2\gamma\frac{d\delta_s}{dt} + \omega_0^2\delta_s(1 - \frac{1}{4}\delta_a^2 - \frac{1}{4}\delta_a^2\cos(2\omega_d t + 2\phi)) = \frac{I_{in}(t)}{C\varphi_0 Z_c} \tag{2.31}$$

where δ_a is the amplitude of zeroth order solution of δ_d.

In the presence of a small signal, the third term in the left hand side of the equation shows that the resonance frequency is modulated at twice the driving frequency. This modulation effectively acts as a four-wave mixing parametric amplifier.

2.3.5. APPLICATIONS OF SQUID CAVITIES

SQUIDs are good magnetometors. For over 50 years, dc SQUIDs have been used as one of most sensitive magnetometers for measuring a small magnetic field. By exploiting the concept of a periodic magnetic flux over a single junction, the parallel Josephson junction geometry (dc SQUID) can be used for detecting a magnetic field where the field inside the superconducting loop is quantised with $\Phi_0 = h/2e = 2.07e^{-15}$ Tm^2. Usually, dc SQUIDs are operated in the non-superconducting regime, where both Junctions are resistively shunted by biasing a dc current which is larger than the critical current of the junctions, $I_{bias} > I_0$. The flux change due to an object gives rise to a field dependent voltage change across the SQUID. The downside of this measurement is the contribution of dissipation due to heating at the shunting resistor, which makes it not ideal for the operation of a magnetometer with unprecedented flux noise sensitivity. There is another type of SQUID, called the rf SQUID. The

rf SQUID has the geometry of a single Josephson junction in a large superconducting loop, which typically has a resonance frequency of 20 ~ 30 MHz. Since it is shorted by dc, the circuit is probed with rf current, hence it is called an rf SQUID. The standard technique for an rf SQUID measurement is to couple some resonant circuit to the rf SQUID via a mutual inductance. The dissipation of the resonant circuit is detected, which depends on the dc flux through the rf SQUID loop. Therefore, the voltage change on the capacitive element of the resonant circuit can be measured. With a large geometric inductance and circulating current in the SQUID, the effective flux through the loop can be multivalued for a certain region, which results in hysteresis as well as dissipation in the resonant circuit coupled inductively[20].

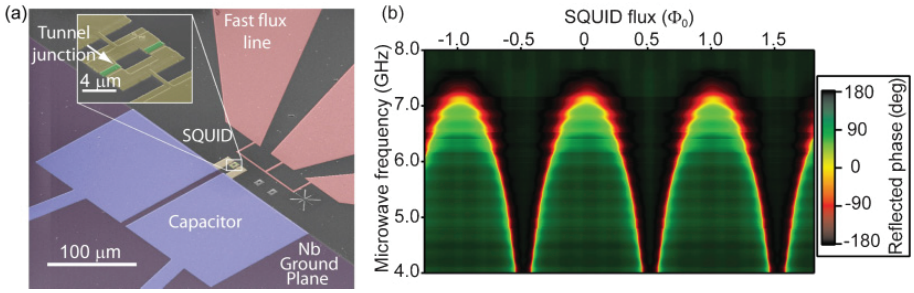

Figure 2.4: SQUID cavities used for parametric amplification. Figures are adapted from [15].

In Hatridge et al.[15] a novel type of dc SQUID operation for magnetic sensing, where the dc SQUID is in a superconducting state during the operation. The system consists of a dc SQUID which is shunted with a parallel plate capacitor. Unlike the conventional resistive readout, the supercurrent passing through the junctions has sinusoidal dependence on the externally applied magnetic field due to the quantised flux, Φ_0. Also, all the circuit elements are in a superconducting state, so there will be only a negligible noise contribution from the circuit elements. The inductance originating from the SQUID is inversely proportional to the supercurrent of the dc SQUID as discussed in the previous section. The circuit works as a flux tunable resonator driven slightly below the bifurcation point (paraamp regime). Low frequency spins are detected similarly to the way they are in cavity optomechanics. A magnetic signal is inductively coupled to the resonant circuit via the dc SQUID. With resonant drive of the cavity, the magnetic signal modulates the cavity field, and the signal is detected by monitoring its phase. This scheme is called dispersive magnetometry.

Dispersive magnetometry can be operated in two different regimes. One is the linear regime, which upconverts a magnetic signal with a transduction factor. The other regime is the paraamp regime. As the circuit is driven near the bifurcation point, the Lorentzian shape of the mode is skewed as a function of the input power. In phase space, the slope of the phase response as a function of frequency becomes steep in a narrow region, which enhances the flux sensitivity. By monitoring its phase, a magnetic signal can be amplified. The height of the sidebands is proportional to the input flux signal and the transduction factor $\frac{\partial V}{\partial \Phi}$, as well as the quality factor of the resonator. In the presence of the sidebands coming from the magnetic signal at the stage of upconversion to a microwave signal, the up-converted signals can be used as a phase sensitive amplifier.

2.3.6. GOAL: OPTOMECHANICS WITH FLUX TUNABLE SQUID CAVITIES

The interaction of macroscopically large objects with a radiation field mode has attracted a great deal of interest, not only due to its being a new field of physics, but also since recent progress has shed light on the quantum mechanical effects in macroscopic objects. Ground state cooling is one example, and has been a starting point for non-classical experiments. The resolved sideband cooling of a mechanical object has successfully implemented dumping a thermal phonon out of the mechanical element to the cavity field to be cooled down to the quantum ground state[5, 30], which must satisfy $C/n_{thermal} \gg 1$. Technically, a mechanical oscillator can be cooled down to the ground state without reaching the strong coupling regime. However, for the purpose of control and manipulation, optomechanical coupling needs to be in the strong coupling regime so that the coherent interaction between the mechanical element and the cavity can become the leading term of the interaction. In the strong coupling regime, the two modes show normal mode splitting due to a hybridazation of the two coupled modes.

However, not much research has focused on the strong coupling itself. Almost all experiments in the field exploit an enhancement of the coupling by introducing a large input power for a high frequency drive tone, and benefit from the increase in the optomechanical coupling $\propto \sqrt{n_{drive}}$. The cavity shift is proportional to the displacement x, which is clear from linearisation. But, the standard optomechanical interaction at single photon level is quadratic in the field operator, which indicates a non-linear process for the case where the cavity pull due to the zero-point motion of the mechanical oscillator is comparable or larger than the cavity decay rate, which is called the single photon strong coupling. Theoretical proposals suggest exploiting the quadratic term in the interaction Hamiltonian, creating, e.g. non-classical states, photon blockade, QND, etc. [31].

One of the goals of out project is to the enhance vacuum coupling strength g_0 with a new approach using flux-tunable cavities, and ultimately the single photon strong coupling regime. In the microwave regime, the embodiment of optomechanical systems with a capacitive coupling is common, and their motion creates a modulation in the capacitor with a superconducting electrode. However, in current state of the art experiments, g_0 is limited to several hundred Hz in the microwave field due to the gap between the superconducting electrodes, the resonance frequency of mechanical resonator, and the linewidth of the cavity. In our approach, we couple a doubly clamped nanobeam to a Josephson junction based flux tunable LC circuit where a dc SQUID is shunted by a capacitance. A doubly clamped mechanical oscillator is embedded inside the SQUID loop, so that the motion of the nanobeam under an external magnetic field is coupled to the cavity via flux. The low frequency mechanical resonance is up-converted to create red and blue sidebands, or, signal and idler. g_0 can be expressed as follows.

$$g_0 = \frac{\partial \omega}{\partial x} = \frac{1}{I_c}\frac{dI_c}{d\Phi}\frac{d\Phi}{dx}\omega_{cav}x_{zpf} \tag{2.32}$$

The second term in the equation is the slope of the critical current as a function of the external flux through the SQUID loop. Therefore, the coupling approaches a maximum as it reaches the highest slope. There are also other operating points where the slope is a minimum, e.g. $\Phi = 0$ and $\Phi = \Phi_0/2$. The first contributing term is quadratic in the field. The third term on the right hand side of the equation is the flux modulation due to the motion of a mechanical beam. Thus the term linearly increases with the magnetic field, $\propto B$.

2.4. NON-LINEAR DISSIPATION

Power dependent loss in microwave resonators due to TLS is commonly observed[32–34]. However, in resonant circuits with Josephson junctions, there is another dissipation channel where the microwave loss increases as a function of the input power. Non-linear dissipation is a higher order process of dissipation in which two photons inside the system are absorbed concurrently. The process annihilates two photons of the system, and creates one photon in the thermal bath of the channel. This process is known as two-photon absorption loss[35]. Here, we approach analytically the behavior of the Duffing equation with a non-linear dissipation term.

2.4.1. ANALYTICAL CALCULATION WITH NON-LINEAR DISSIPATION TERM

Here we start with the standard Duffing equation, closely following [36]

$$\ddot{x} + 2\gamma\dot{x} + x + \alpha x^3 = \phi\cos(\Omega t) \tag{2.33}$$

where γ is the damping ratio, α is the Kerr coefficient, and ϕ is the normalized force. I assume $\alpha < 0$ such that the frequency pull due to the Kerr non-linearity is negative, which is in agreement with the behavior of Josephson junction based resonant circuits. We introduce an additional dissipation channel corresponding to two-photon loss,γ_{nl}, which is proportional to x^2.

$$\ddot{x} + 2(\gamma + \gamma_{nl}x^2)\dot{x} + x + \alpha x^3 = \phi\cos(\Omega t) \tag{2.34}$$

We will make a few assumptions: the driving frequency is close to the natural frequency, and the resonant system oscillates at the natural frequency $\omega \sim \omega_0$. By moving into the rotating frame of Ω,

$$u = x\cos\Omega t - \frac{1}{\Omega}y\sin\Omega t \tag{2.35}$$

$$v = -x\sin\Omega t - \frac{1}{\Omega}y\cos\Omega t \tag{2.36}$$

where $y = \dot{x}$. Differentiating Equations 2.35 and 2.36 with respect to time gives

$$\dot{u} = \frac{1}{\Omega}[-x\Omega^2 - \ddot{x}]\sin\Omega t \tag{2.37}$$

$$\dot{v} = \frac{1}{\Omega}[-x\Omega^2 - \ddot{x}]\cos\Omega t. \tag{2.38}$$

By substituting $\ddot{x}$ of Equation 2.38 into the equations above, we obtain

$$\dot{u} = \frac{1}{\Omega}[\rho x + \alpha x^3 + 2(\gamma + \gamma_{nl}x^2)y - \phi\cos(\Omega t)]\sin\omega t \tag{2.39}$$

$$\dot{v} = \frac{1}{\Omega}[\rho x + \alpha x^3 + 2(\gamma + \gamma_{nl}x^2)y - \phi\cos(\Omega t)]\cos\omega t. \tag{2.40}$$

Next, the rotating wave approximation will be applied. This procedure is equivalent to taking the average of the equations over $\dot{u}$ and $\dot{v}$ for the period of $2\pi/\omega$. After averaging, most oscillating terms vanish. The surviving terms are

$$f < \sin^2\omega t >=< \cos^2\omega t >= \frac{1}{2} \tag{2.41}$$

$$< \sin^4\omega t >=< \cos^4\omega t >= \frac{3}{8} \tag{2.42}$$

$$< \sin^2\omega t\cos^2\omega t >= \frac{1}{8} \tag{2.43}$$

After averaging, $\dot{u}$ and $\dot{v}$ have the forms of,

$$\dot{u} = (\frac{-1}{2\Omega})[\rho v + \frac{3\alpha}{4}(u^2+v^2)v + \gamma\Omega u + \frac{\gamma_{nl}\Omega}{4}(u^2+v^2)u] \tag{2.44}$$

$$\dot{v} = (\frac{1}{2\Omega})[\rho u + \frac{3\alpha}{4}(u^2+v^2)u - \gamma\Omega v - \frac{\gamma_{nl}\Omega}{4}(u^2+v^2)v - \phi] \tag{2.45}$$

where $\rho = 1 - \Omega^2$. The expressions above can be simplified in polar coordinate by setting $u = r\cos\theta$ and $v = r\sin\theta$. Searching for a stable solution, we get

$$0 = \rho\sin\theta + \frac{3\alpha}{4}r^2\sin\theta + 2\gamma\Omega\cos\theta + \frac{\gamma_{nl}}{4}\Omega r^2\cos\theta \tag{2.46}$$

$$\frac{\phi}{r} = \rho\cos\theta + \frac{3\alpha}{4}r^2\cos\theta - 2\gamma\Omega\sin\theta - \frac{\gamma_{nl}}{4}\Omega r^2\sin\theta \tag{2.47}$$

These equations can be simplified further by multiplying Equation 2.46 with $\sin\theta$ and Equation 2.47 with $\cos\theta$, and adding them together. Similarly, by multiplying Equation 2.46 with $\cos\theta$ and Equation 2.47 with $\sin\theta$, then subtracting one from another, we get

$$\frac{\phi}{r}\cos\theta = \rho + \frac{3\alpha}{4}r^2 \tag{2.48}$$

$$-\frac{\phi}{r}\sin\theta = 2\gamma\Omega + \frac{\gamma_{nl}}{4}r^2 \tag{2.49}$$

$\$\sin\theta$ and $\cos\theta$ can be eliminated by taking the squares of Equations 2.48 and 2.49 and adding them together, which leads to a bicubic equation for r,

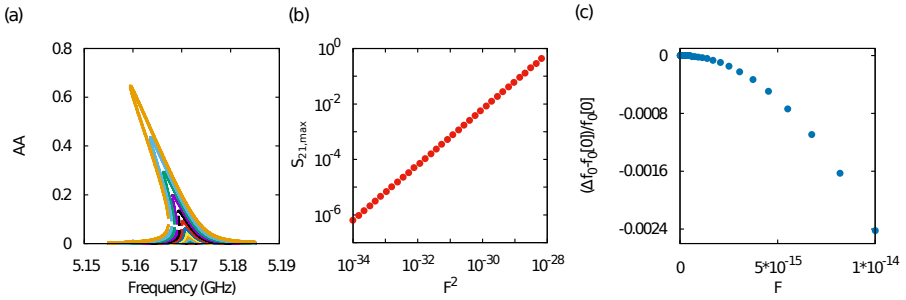

Figure 2.5: (a)Non-linear Duffing response of Equation 2.50 with zero non-linear dissipation, $\gamma_{nl} = 0$,$\alpha = 1.0e-2$, $\omega_0 = 5.172$ GHz and $\alpha = 1.0e-2$. (b) Maximum amplitude of Duffing response vs squared driving force F. (c) Resonance frequency shift from the response of the lowest power which is normalized by the resonance frequency of the lowest power.

$$16\phi^2 = (9\alpha^2 + \gamma_{nl}\Omega^2)r^6 + (24\rho\alpha + 16\gamma\gamma_{nl}\Omega^2)r^4 + (\rho^2 + \sigma^2)r^2 \tag{2.50}$$

where $\sigma = 2\gamma\Omega$. For zero non-linear loss, $\gamma_{nl} = 0$, Equation 2.50 matches with equation (4.1) of [36]. The frequency shift should have a purely quadratic relation to the driving force [37], where $\Delta\omega \propto kF^2$.

2.4.2. DUFFING RESPONSE SIMULATION

Duffing response without non-linear dissipation. Here we numerically simulate the Duffing response from the equation in the previous section. Equation 2.50 is a bicubic equation for r^2 which can be solved numerically. The non-linear dissipation term γ_{nl} is set to be zero. The solutions of the equation are either three real roots which are positive, or one real root with two complex roots. Figure 2.5(a) shows a Duffing response with zero non-linear dissipation as a function of power. The frequency response is pulled to a lower frequency due to setting α to be negative. The parameters of the plot are set close to the experimental values. Figure 2.5(b) is a plot of the amplitude of the Duffing response as a function of the square of the force. For zero-non-linear damping, the amplitude of the response increases linearly with power. Figure 2.5(c) shows that the frequency pull due to Kerr non-linearity is quadratic in the force. Python code to plot Figure 2.5 (a) can be found in the Appendix.

Duffing response with non-linear dissipation. Now we introduce a non-zero non-linear inductance γ_{nl} into Equation 2.50, and see how γ_{nl} plays a role in the amplitudes of the Duffing response and the frequency pull. Figure 2.6 (a) is the Duffing response after introducing a non-zero non-linear dissipation term. The same parameters except γ_{nl} are used as in the case of zero non-linear dissipation. It can be seen that by introducing γ_{nl}, a larger driving power is required to reach the bifurcation point. In Figure 2.6(b), the amplitude of the Duffing response is suppressed and deviates from the linear trend at high power. In Figure 2.6(c), the normalized frequency

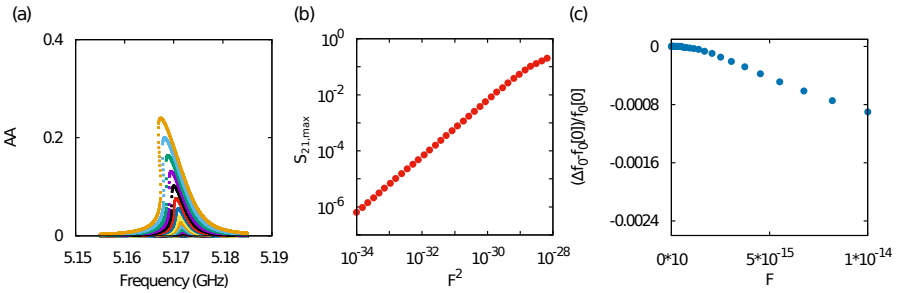

Figure 2.6: (a) Non-linear Duffing response of Equation 2.51 with non-zero non-linear dissipation. $\gamma_{nl} = 1.0e-3$, and the other parameters are kept the same. (b) Amplitude of the Duffing response deviates from the linear trend at higher driving power. (c) Normalized frequency shift also no longer behaves quadratically.

shift is shown as a function of the driving force. It is also clear that the shift deviates from the quadratic trend seen in Figure 2.5(c).

REFERENCES

[1] M. Aspelmeyer, T. J. Kippenberg, and F. Marquardt, *Cavity Optomechanics,* Reviews of Modern Physics **86**, 1391 (2014), arXiv: 1303.0733.

[2] S. Gröblacher, K. Hammerer, M. R. Vanner, and M. Aspelmeyer, *Observation of strong coupling between a micromechanical resonator and an optical cavity field,* Nature **460**, 724 (2009).

[3] J. D. Teufel, D. Li, M. S. Allman, K. Cicak, A. J. Sirois, J. D. Whittaker, and R. W. Simmonds, *Circuit cavity electromechanics in the strong-coupling regime,* Nature **471**, 204 (2011).

[4] K. Schneider and P. Seidler, *Strong optomechanical coupling in a slotted photonic crystal nanobeam cavity with an ultrahigh quality factor-to-mode volume ratio,* Optics Express **24**, 13850 (2016).

[5] J. D. Teufel, T. Donner, D. Li, J. W. Harlow, M. S. Allman, K. Cicak, A. J. Sirois, J. D. Whittaker, K. W. Lehnert, and R. W. Simmonds, *Sideband cooling of micromechanical motion to the quantum ground state,* Nature **475**, 359 (2011).

[6] A. Wallraff, D. I. Schuster, A. Blais, L. Frunzio, R.-S. Huang, J. Majer, S. Kumar, S. M. Girvin, and R. J. Schoelkopf, *Strong coupling of a single photon to a superconducting qubit using circuit quantum electrodynamics,* Nature **431**, 162 (2004).

[7] A. Fedorov, A. K. Feofanov, P. Macha, P. Forn-Díaz, C. J. P. M. Harmans, and J. E. Mooij, *Strong Coupling of a Quantum Oscillator to a Flux Qubit at Its Symmetry Point,* Physical Review Letters **105**, 060503 (2010).

[8] J. D. Thompson, B. M. Zwickl, A. M. Jayich, F. Marquardt, S. M. Girvin, and J. G. E. Harris, *Strong dispersive coupling of a high finesse cavity to a micromechanical membrane,* Nature **452**, 72 (2008), arXiv: 0707.1724.

[9] J. C. Sankey, C. Yang, B. M. Zwickl, A. M. Jayich, and J. G. E. Harris, *Strong and Tunable Nonlinear Optomechanical Coupling in a Low-Loss System,* Nature Physics **6**, 707 (2010), arXiv: 1002.4158.

[10] T. P. Purdy, D. W. C. Brooks, T. Botter, N. Brahms, Z.-Y. Ma, and D. M. Stamper-Kurn, *Tunable Cavity Optomechanics with Ultracold Atoms,* Physical Review Letters **105** (2010), 10.1103/PhysRevLett.105.133602, arXiv: 1005.4085.

[11] A. Nunnenkamp, K. Borkje, J. G. E. Harris, and S. M. Girvin, *Cooling and squeezing via quadratic optomechanical coupling,* Physical Review A **82** (2010), 10.1103/PhysRevA.82.021806, arXiv: 1004.2510.

[12] E. D. Reed, *The Variable-Capacitance, Parametric Amplifier (Übersicht über parametrische Verstärker mit gesteuerten Kapazitäten),* in *Systeme mit Nichtlinearen oder Gesteuerten Elementen / Systems with Non-Linear or Controllable Elements*, Nachrichtentechnische Fachberichte, edited by D.-I. J. Wosnik (Vieweg+Teubner Verlag, 1960) pp. 27–37, dOI: 10.1007/978-3-663-04359-1_5.

[13] *Vol 1 - Landau, Lifshitz - Mechanics (3rd Edition) (197p),* .

[14] T. Yamamoto, K. Inomata, M. Watanabe, K. Matsuba, T. Miyazaki, W. D. Oliver, Y. Nakamura, and J. S. Tsai, *Flux-driven Josephson parametric amplifier,* arXiv:0808.1386 [cond-mat] (2008), arXiv: 0808.1386.

[15] M. Hatridge, R. Vijay, D. H. Slichter, J. Clarke, and I. Siddiqi, *Dispersive magnetometry with a quantum limited SQUID parametric amplifier,* Physical Review B **83**, 134501 (2011).

[16] M. A. Castellanos-Beltran, K. D. Irwin, G. C. Hilton, L. R. Vale, and K. W. Lehnert, *Amplification and squeezing of quantum noise with a tunable Josephson metamaterial,* Nature Physics **4**, 929 (2008), arXiv: 0806.0659.

[17] R. Vijay, D. H. Slichter, and I. Siddiqi, *Observation of Quantum Jumps in a Superconducting Artificial Atom,* Physical Review Letters **106**, 110502 (2011).

[18] L. Hao, D. Cox, P. See, J. Gallop, and O. Kazakova, *Magnetic nanoparticle detection using nano-SQUID sensors,* **43**, 474004.

[19] C. Kittel, *Introduction to Solid State Physics.*

[20] M. Tinkham, *Introduction to Superconductivity: Second Edition* (Dover Publications, 2004) google-Books-ID: k6AO9nRYbioC.

[21] S. Etaki, F. Konschelle, Y. M. Blanter, H. Yamaguchi, and H. S. J. v. d. Zant, *Self-sustained oscillations of a torsional SQUID resonator induced by Lorentz-force back-action,* Nature Communications **4**, 1803 (2013).

[22] J. Clarke and F. K. Wilhelm, *Superconducting quantum bits,* Nature **453**, 1031 (2008).

[23] I. Siddiqi, R. Vijay, F. Pierre, C. M. Wilson, L. Frunzio, M. Metcalfe, C. Rigetti, and M. H. Devoret, *The Josephson Bifurcation Amplifier for Quantum Measurements,* arXiv:cond-mat/0507248 (2005), arXiv: cond-mat/0507248.

[24] V. Schmitt, X. Zhou, K. Juliusson, A. Blais, P. Bertet, D. Vion, and D. Esteve, *Multiplexed Readout of Transmon Qubits with Josephson Bifurcation Amplifiers,* Physical Review A **90** (2014), 10.1103/PhysRevA.90.062333, arXiv: 1409.5647.

[25] K. Kakuyanagi, H. Nakano, S. Kagei, R. Koibuchi, S. Saito, A. Lupascu, and K. Semba, *Readout strength dependence of state projection in superconducting qubit,* arXiv:1004.0182 [cond-mat] (2010), arXiv: 1004.0182.

[26] Y. Yin, Y. Chen, D. Sank, P. J. J. O'Malley, T. C. White, R. Barends, J. Kelly, E. Lucero, M. Mariantoni, A. Megrant, C. Neill, A. Vainsencher, J. Wenner, A. N. Korotkov, A. N. Cleland, and J. M. Martinis, *Catch and Release of Microwave Photon States,* Physical Review Letters **110**, 107001 (2013).

[27] *Storage and on-demand release of microwaves using superconducting resonators with tunable coupling,* Applied Physics Letters **104**, 232604 (2014).

[28] C. Beltran, *Development of a Josephson Parametric Amplifier for the Preparation and Detection of Nonclassical States of Microwave Fields*, Ph.D. thesis.

[29] R. Vijayaraghavan, *Josephson Bifurcation Amplifier: Amplifying quantum signals using a dynamical bifurcation*, Ph.D. thesis.

[30] J. Chan, T. P. M. Alegre, A. H. Safavi-Naeini, J. T. Hill, A. Krause, S. Gröblacher, M. Aspelmeyer, and O. Painter, *Laser cooling of a nanomechanical oscillator into its quantum ground state,* Nature **478**, 89 (2011).

[31] A. Nunnenkamp, K. Borkje, and S. M. Girvin, *Cooling in the single-photon strong-coupling regime of cavity optomechanics,* Physical Review A **85** (2012), 10.1103/PhysRevA.85.051803, arXiv: 1202.3263.

[32] D. P. Pappas, M. R. Vissers, D. S. Wisbey, J. S. Kline, and J. Gao, *Two Level System Loss in Superconducting Microwave Resonators,* IEEE Transactions on Applied Superconductivity **21**, 871 (2011).

[33] M. S. Khalil, M. J. A. Stoutimore, S. Gladchenko, A. M. Holder, C. B. Musgrave, A. C. Kozen, G. Rubloff, Y. Q. Liu, R. G. Gordon, J. H. Yum, S. K. Banerjee, C. J. Lobb, and K. D. Osborn, *Evidence for hydrogen two-level systems in atomic layer deposition oxides,* (2013), 10.1063/1.4826253.

[34] A. Bruno, G. de Lange, S. Asaad, K. L. van der Enden, N. K. Langford, and L. DiCarlo, *Reducing intrinsic loss in superconducting resonators by surface treatment and deep etching of silicon substrates,* Applied Physics Letters **106**, 182601 (2015), arXiv: 1502.04082.

[35] B. Yurke and E. Buks, *Performance of Cavity-Parametric Amplifiers, Employing Kerr Nonlinearites, in the Presence of Two-Photon Loss,* Journal of Lightwave Technology **24**, 5054 (2006).

[36] P. J. Holmes and D. A. Rand, *The bifurcations of duffing's equation: An application of catastrophe theory,* Journal of Sound and Vibration **44**, 237 (1976).

[37] L. L. D. and E. M. Lifshitz, *Mechanics.*

3

FABRICATION AND MEASUREMENT SETUP

In this chapter, the fabrication procedures used for the project are discussed, including the fabrication of the superconducting resonators, the Josephson junctions, the Josephson junction based flux tunable resonators, and the SiN nanowires. The aim of this chapter is to give not only the recipes for the fabrication, but also describe the challenges and techniques to circumvent the problems we encountered.

3.1. MoRe superconducting resonators

Low loss superconducting microwave resonators play very important roles in quantum nanoscience, including superconducting detectors[1][2], circuit quantum electrodynamic experiments[3],[4], electron spins in nitrogen vacancy centers[5], and cavity optomechanical systems[6]. For this project, cavity optomechanical system which is interest of research which mechanical elements are parametrically coupled to microwave cavities, and we use microwave resonators as tools to study their mechanical motion. Highly coherent microwave cavity is desirable for aiming larger coupling.

For high quality superconducting thin film, our choice of superconducting metal is molybdenum rhenium (MoRe) 60:40. This alloy has a relatively high transition temperature, ranging from 8 to 13 K, with an RRR of about 1, which indicates that the alloy is a highly disordered superconductor. The maximum transition temperature is achieved when the alloy ratio is 60 : 40. MoRe is a relatively noble metal that is resistant against corrosion and oxdization. Although the alloy tends to be oxidized to form Mo_xO_y on the surface when the sample is kept in an ambient condition so as to be observed in XPS measurements[7], they are pretty stable as long as the sample is stored inside a dessicator. The other advantage of MoRe is that it is a very good material to make superconducting contacts with carbon nanotubes[8] and graphene[9]. Its microwave characteristics have already been investigated and it has a high unloaded quality factor reaching 0.7 million on a sapphire substrate[10]. Here, the intrinsic silicon has been used throughout the project becaus we need to release the nanowire by etching a substrate, which can exhibit internal Q_s of up to 100,000 [6]

MoRe microwave superconducting resonators are fabricated with sputtering for deposition, and electron beam lithography and etching for patterning. A high resistivity intrinsic Silicon (100) substrate is first cleaned to remove organic material left on the surface as well as particles. The substrate is cleaned with RCA1 and piranha solutions. RCA1 solution is a mixture of 5 parts of H_2O, 1 part of hydrogen peroxide(H_2O_2), and 1 part of ammonium hydroxide (NH_4OH). The substrate is soaked in the solution at 70°C for 10 min, followed by a piranha solution at 90°C for 10 min, which is a mixture of 3 parts Sulphuric acid (H_2SO_4) and 1 part of Hydrogen Peroxide (H_2O_2). Then the sample is rinsed thoroughly with two different beakers of deionized water. The piranha solution is a strong oxidizer, so that the surface becomes hydrophilic. Subsequently, the native oxide layer on top of the silicon substrate is removed with buffered hydrofluoric acid (BHF). The contributions of the TLS losses in metal–vacuum and substrate–metal interfaces is not negligible [11]. BHF cleaning aims to make a clean metal–substrate interface by removing OH groups from the substrate surface to minimize the energy loss due to TLS. The sample is soaked in a BHF solution for 2~3 minutes, followed by rinsing with deionized water and a nitrogen blow dry. The substrate is terminated with hydrogen, and has a hydrophobic surface after native oxide etching. Soon after the BHF wet etch, the sample is quickly placed inside the load-lock chamber of the MoRe sputtering machine, and 60 nm of MoRe is deposited by rf

sputter at 100 W in an Ar atmosphere.

Microwave resonators are patterned by electron-beam lithography using a tri-layer resist stack. The resist layer consists of S1813, 9 nm of tungsten, and 200 nm of PMMA 950 A4. Since we used a PMMA positive resist top layer, the exposure areas are where the metals are supposed to be gone after etching, such as gaps between the transmission line and ground planes. The exposure dose ranges typically around 1150 $\sim$ 1250 μC/cm^2. After exposure, the sample is developed in a solution of MIBK:IPA 1:3 for 70 s followed by a quick rinse with IPA and a nitrogen blow dry, which develops only the PMMA exposed areas, leaving the tungsten layer, as can be seen in Figure 3.1 (b). Now the tungsten, S1813, and MoRe for the exposed areas are etched using reactive ion etching (RIE). The tungsten layer ($\sim$ 9 nm) is etched with a mixture of SF_6 and He at 45 W for 30 s with flow rates of 12.5 sccm and 10 sccm respectively at 10 μbar, which is long enough for etching 9 nm of tungsten. Subsequently, the S1813 layer is etched with an oxygen plasma at 50 W for about 30 minutes at a flow rate of 20 sccm at 3.6 μbar. Finally, the MoRe layer is etched with a SF_6/He mixture. The parameters for this etching are the same as for the tungsten layer, which can be found in the Appendix. The resist mask is removed in a solution of resist stripper, PRS 3000, at 80°C with a stirring magnet for 30 minutes. The process of patterning MoRe resonators is shown in Figure 3.1.

Two different kinds of resonators were designed, fabricated and tested. One is the coplanar wave guide (CPW) resonator. The center conductor of a CPW resonator has a width of 10 μ m with a gap of 6 μm from the ground plane. These resonators are designed to have a characteristic impedance of Z = 50 Ω with a resonance frequency near 7 to 8 GHz. However, due to the kinetic inductance of MoRe, typically the cavity resonances are found to have lower frequencies and high characteristic impedance, $\sim$ 71Ω. The kinetic inductance contribution of this 60 nm sputtered film will be estimated in a later section. An optical microscopic image is shown in Figure 3.2 (a). The other kind of resonator is a lumped element resonator, as shown in Figure 3.2 (b). In simulation, the resonator is designed to have a resonance frequency around 7 GHz. Due to kinetic inductance, the resonance frequency is found to be around 5.4 GHz in measurements. The lumped element resonators were also tested as a reference resonator for the ones with the dc SQUIDs. The characteristic impedance of the resonator is estimated to be 91 Ω. As can be seen, both resonators are side coupled to the transmission line, which enables frequency multiplexing to test several resonators in one sample.

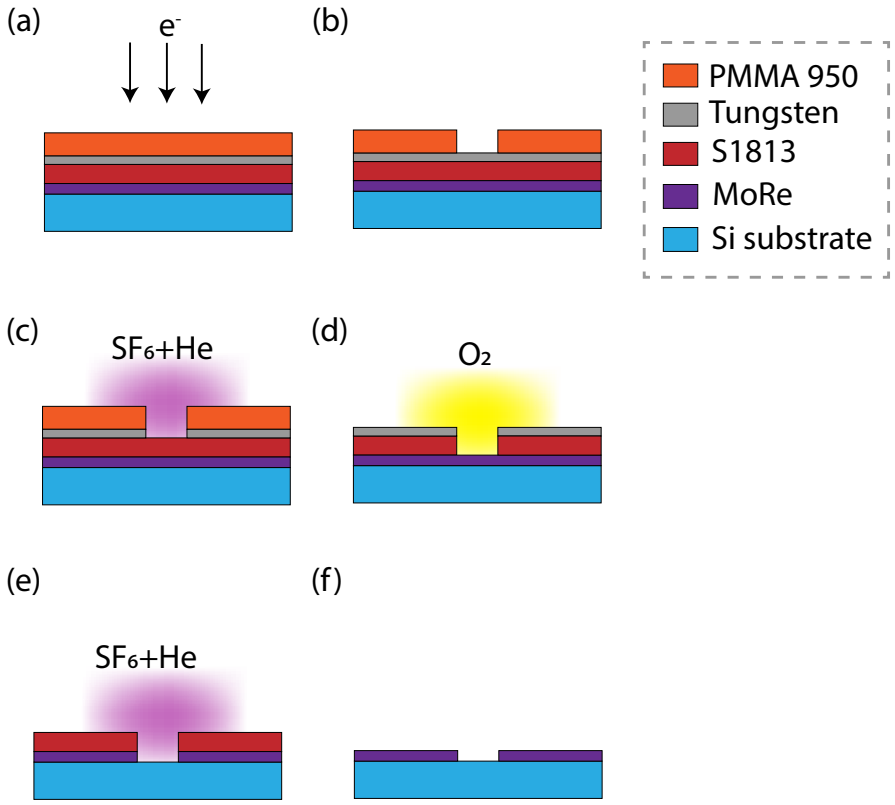

Figure 3.1: **Fabrication steps of MoRe resonators for patterning with reactive ion etching (RIE)**. (a) Microwave resonator patterns are exposed on a tri-layer resist spun on a high resistivity silicon wafer. The resist layer consists of PMMA 950, tungsten, and S1813. For a typical exposure, the dose lies around 1200 μC/cm^2 to expose the PMMA 950 with a certain thickness. (b) After exposure, the sample is developed inside a mixture of MIBK:IPA 1:3 for 70 s. Only the top PMMA layer is developed, and the surface of the exposed area is 9 nm of sputtered tungsten. (c) Tungsten is etched with SF_6 and He for 30 s, which is long enough to etch 9 nm of tungsten, and short enough to keep the patterns on the PMMA layer not etched with SF_6. S1813 is etched with oxygen, where PMMA and tungsten act as etch masks. It usually takes slightly less than 30 minutes to etch 1.5 μm of S1813. The S1813 layer is anisotropic by setting the pressure inside the chamber as low as possible. (e) Now MoRe is etched with SF_6 and He, for which the S1813 acts as a resist mask. Finally the resist stack is removed with resist stripper PRS 3000.

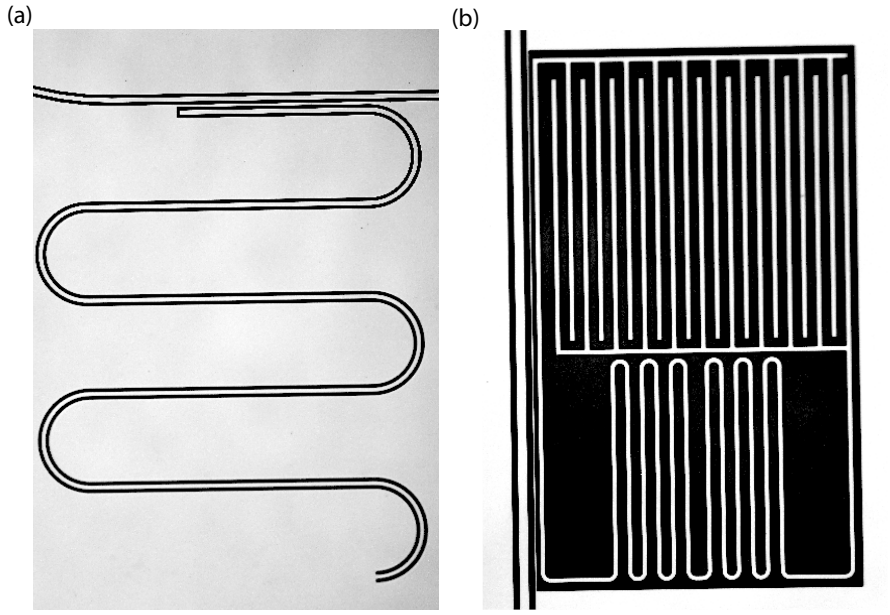

Figure 3.2: **Optical microscopic image of MoRe superconducting resonators** (a) CPW resonator (b) lumped element resonator

3.2. JOSEPHSON JUNCTIONS

The Josephson junction is a non-linear and non-dissipative element, where two superconductors are isolated with an insulator. Microscopically, Cooper pairs tunnel through the insulating barrier without a voltage drop, but with a phase difference across the junction. The most commonly used fabrication process is diffusion-limited oxidization of aluminium, which forms a uniform amorphous AlOx insulating layer[12]. Efforts are being made to fabricate junctions capable of operating at higher temperatures and higher magnetic fields, with different kinds of junctions [8, 13, 14]. However, it is still difficult to consistently make a high quality Josephson junction with the new processes as good as the AlOx made by diffusion-limited oxdization. Throughout the project, diffusion-limited oxidization has been used for the junction fabrication.

The process of fabricating Josephson junctions uses the Niemeyer–Dolan technique, commonly known as the Dolan bridge technique. Figure 3.3 shows the flow of the fabrication process. This technique uses a bi-layer resist stack, and creates a suspended resist bridge by exposing two neighbouring areas using electron beam lithography (EBL). Therefore a soft resist layer was chosen for the bottom resist layer. Figure 3.3 (a) shows the exposure of two neighbouring areas after the exposure sample is developed. Figure 3.3 (b) depicts a suspended resist bridge. By evaporating aluminium from a particular angle, aluminium is projected on a location displaced from the expected position by the vertical evaporation, as shown in Figure 3.3 (c). The fabrication of Josephson junctions requires forming an insulating layer in the middle of the two aluminium evaporations. This can be done by diffusion-limited oxidization of aluminium. After the first angle evaporation, typically the sample is moved to a load lock chamber or an evaporation chamber which is separated from another main chamber without breaking the vacuum. Inside the chamber where the sample is now placed, oxygen is introduced. By exposing oxygen on the surface of the first aluminium layer, the surface forms a thin layer of aluminium-oxide with a typical thickness of 1~2 nm. After the oxidization, the sample is placed back into the main evaporation chamber and the second layer of aluminium is evaporated, as shown in Figure 3.3 (e). The second aluminium is evaporated at a particular angle chosen such that the second layer of aluminium overlaps with the first layer of the aluminium. After the second angle evaporation, the sample is exposed to high pressure oxygen before being taken out of the sample for the purpose of capping the surface of aluminium with aluminium oxide. The capping process is not necessary, but advisable for high quality junctions. An unterminated surface with oxygen inside the evaporator could cause more flux noise inside superconducting qubits[15]. The surface is oxidized in air when the sample is taken out of the evaporator, which leads to higher contamination of the surface. In the final step, the resist stack is removed with lift-off in a resist stripper, as shown in Figure 3.3 (f).

In our fabrication process, a MAA/PMMA 950 bi-layer resist stack is used for a lift-off mask. A pattern of the Dolan bridge is exposed by EBL with a dose around $1150 \sim 1250 \mu C/cm^2$, which is near the critical dose of the PMMA resist. The dose is

tuned, depending on the thickness of the resist stack and design. After an exposure, the sample is developed in a solution of MIBK:IPA 1:3 for 70 s, followed by two quick dip rinses in isopropanol for 10 s in each beaker and a nitrogen blow dry. Then oxygen plasma ashing of the device before evaporation is done for the purpose of removing the organic residue of the resist on the exposed area. A sample is placed inside a special chamber and oxygen is introduced. High frequency voltage ionizes the oxygen gas in a slightly low pressure. This ashing process breaks the organic bonds of the surface by vacuum UV, and reactive oxygen species further reacts with the organics to form compounds, which are evacuated. The substrate is cleaned inside the oxygen plasma with an oxygen flow of 150 ml/min at 150 watts for 30s. We further clean the substrate in BFH for 30 s. Subsequently, the substrate is quickly loaded into an electron-beam evaporator, and the junctions are evaporated as discussed above. The first Al layer is evaporated at 11° of tilt with a thickness of 25 ~ 30 nm. Then inside the upper main chamber of the evaporator, pure oxygen is introduced till $5.0e^{-5}$ mbar, and kept for 8 minutes. The second layer is evaporated at 11° symmetrically opposite from the first angle, with a thickness of 50 nm. Finally the device is capped with oxygen at $5.0e^{-3}$ mbar for 5 minutes. After taking the sample out of the evaporator, the substrate is lifted off in a beaker of hot NMP at 80°C. During the lift off, a stirring magnet is helpful to minimize the resist walls' collapsing on top of the device. Finally the sample is rinsed in isopropanol and nitrogen blow dried.

Figure 3.4 shows an SEM picture of a Josephson junction. The darker areas around the junction and the SQUID loop can be seen. This comes from cleaning with O_2 ashing and BHF cleaning. Although post-evaporation cleaning with oxygen ashing was not done in our fabrication, it is known to be effective for minimizing junction aging, as well as removing the resist collapsed on top of the device which could possibly degrade the device's performance[16]. The left-over resist could be a source of dielectric loss and degassing or introducing water to cause diffusion in junctions[17]. In our measurements, the internal quality factors of our devices are not limited by the dielectric loss of Josephson junction, but may be useful to understand the origins of microwave dielectric losses.

Figure 3.5 (a) shows an SEM image of the bilayer resist stack after development. The sample was coated with a metal layer in order to increase the visibility in SEM and high contrast. Each Dolan bridge has a length of 2.5 μm and width of 160 nm. Figure 3.5 (b) shows an SEM image of a shadow evaporated Josephson junction. The overlap area of each junction is $2.5\mu\text{m}\times 190$ nm, and typically each junction has 200 Ω ~1 KΩ of normal state resistance. The picture was taken at a tilt of 80°. Figure 3.6 shows a few examples of an unsuccessful batch of Josephson junction fabrication. Figure 3.6 (a) shows that Dolan bridge falls off after development. This could be because either the bridge was too thin or the bridge was too high. The problem could be circumvented by increasing the thickness of the PMMA top layer, which does not change the are of the evaporated junction. Figure 3.6 (b) is after evaporation and lift off. It can be seen that there is no junction formed, due to the Dolan bridge's having broken before the

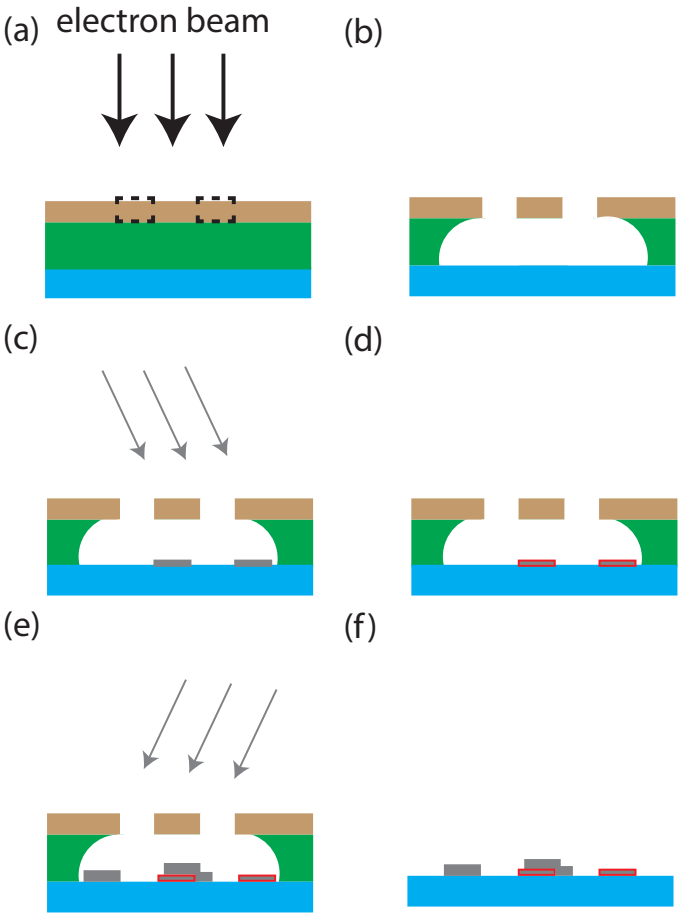

Figure 3.3: **Evaporation of a Josephson junction with Dolan bridge technique.** (a) Design of two closely neighbouring electrodes is exposed with electron beam lithography. (b) Sample is developed in a resist developer with a suspended toplayer resist bridge. (c) Evaporation of the first Al layer. The bottom layer of Al is evaporated against the resist mask where the two neighbouring electrodes are evaporated on the substrate. (d) Oxygen is introduced inside a loadlock/upper-main chamber of an evaporator for oxidization of the first layer Al surface. (e) Second layer of aluminium is evaporated at the opposite angle of the first evaporation. The second layer is typically thicker than the first evaporation thickness to cover the substrate and the surface of AlOx layer. (f) Lift off process to remove the resist mask.

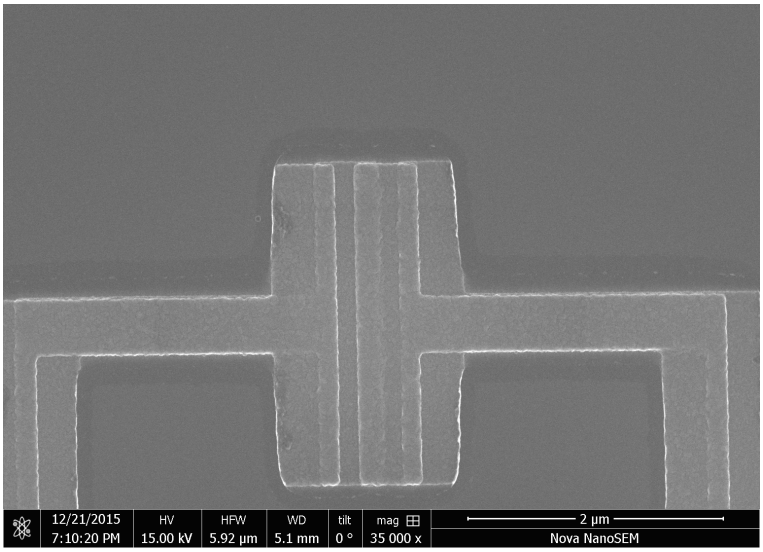

Figure 3.4: **SEM image of Josephson junction after lift off**: Darker areas can be observed around evaporated aluminium, which is most likely a signature that resist is removed with oxygen plasma cleaning prior to the evaporation..

evaporation of the junction. In Figure 3.6 (c), we can see that a dark grainy layer is on top of the junction, which is the resist layer, most likely copolymer with Al evaporated from the wall of copolymer.

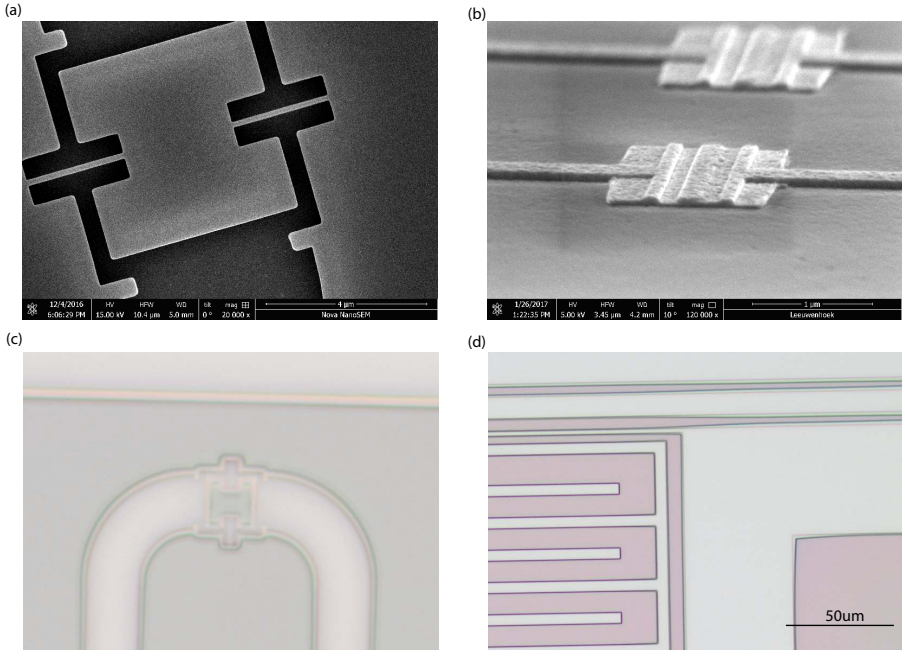

Figure 3.5: (a): SEM image of bilayer resist stack after exposure and development of Dolan bridges. The SQUID loop has a width of 1μm with area 5× 5 μm^2. Each free suspended resist bridge has a length of 2.5 μm and width of 160 nm. Prior to the inspection, 15 ~ 20 nm of tungsten was sputtered for better visibility. (b): SEM image of Josephson junctions in a SQUID geometry. The overlap of each junction is 2.5 μm × ~ 160 nm. (c) Optical image of the resist layer after development with MIBK:IPA. Undercut of MMA layer can be seen on edges of exposed area. (d) Optical microscopic image after development with MIBK:IPA. White areas are places where electron beam is exposed. It should be noted that there are large undercuts, roughly 2 μm on the edges of the large ground plane due to proximity exposure. Smaller exposure areas like the fingers of the interdigitated capacitor have smaller undercuts around 250 nm. More details are discussed in the Appendix.

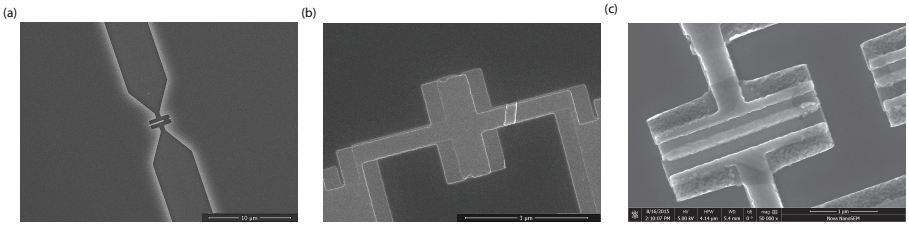

Figure 3.6: **Problems seen in fabrication with double angle evaporation**(a): SEM image of a broken Dolan bridge. Sometimes Dolan bridges appear that are not freely standing after development, which results in shorting the Josephson junctions. (b) One of an unsuccessful batch of shadow evaporated dc SQUID. The Josephson junction is shorted, most likely due to collapse of a Dolan bridge before evaporation of aluminium. The broken Dolan bridge crosses over the SQUID loop on the right hand side of the junction. (c) Resist residue from sidewalls falling on top of Josephson junctions (black veil of death[17]).

3.3. FLUX-TUNABLE JOSEPHSON RESONATORS (SQUID CAVITIES)

The combination of a microwave superconducting resonant circuit and a Josephson junction is ubiquitous in the field, such as superconducting qubits, Josephson parametric amplifiers, and non-linear readouts of superconducting qubits[18]. A Josephson junction resonator consists of one or more Josephson junctions and a microwave superconducting resonator, which acts as a non-linear resonator when the circuit is driven near the threshold power. When the circuit has a dc SQUID instead of single junction, the circuit gains flux tunability by an external magnetic field. Our interest is in using flux-tunable Josephson junction resonators to read out the motion of nanomechanical beams.

We fabricated flux-tunable superconducting resonators with two different processes. Our first attempt for making SQUID superconducting cavities was by lifting off the two circuit components, the microwave resonator and dc SQUID, at once. This process provides simple fabrication steps, requiring only one step of lift-off after the double angle evaporation. This is commonly used in the fabrication of superconducting qubits, especially in 3D realizations[19] as well as the first generation of 2D realizations of transmon qubits[3]. The fabrication procedure is basically the same as described in the previous section on Josephson junction fabrication, except the exposure area is large because the design includes a microwave resonator. We used a Copolymer/PMMA bilayer resist stack. The bottom layer, copolymer EL13, is spincoated at a rate of 2000 rpm for 60 s, and baked for 15 minutes at 175°C. The top resist layer, PMMA 950 A4, is spincoated at 3000 rpm for 60 s, and baked for 15 minutes at 175°C. A microwave resonator pattern along with a dc SQUID is written by EBL. Exposure is typically around 1200 $\mu C/cm^2$, which slightly varies depending on the thickness of the resist layer. After the exposure, the sample is developed in a solution of MIBK:IPA 1:3 for 70 s. The sample is rinsed in two beakers of IPA for 10 s each,

followed by a nitrogen blow dry. The substrate is placed inside oxygen plasma with an oxygen flow of 150 ml/min at 150 W for 30 s. This helps remove organic residue on the surface of the exposed areas. Subsequently, the substrate is etched in BHF for 30 s, followed by rinsing in water for termination and a nitrogen blow dry. As soon as the sample is dried, it is placed inside the loadlock chamber of an evaporator. Aluminium is evaporated from 11° from each side with oxidisation after the first evaporation. After the evaporation, the sample is lifted off in NMP at 80°C. While the sample is being lifted off, a stirring magnet is used, which helps remove the bilayer resist.

In this type of fabrication process, we noticed that the large dimensional difference in our design makes a difficulty for a proper exposure. In our design, the microwave launcher has the largest exposure, roughly 200 to 700μm. The smallest dimension of the structure is the freely suspended bridge of PMMA with a width of 160 nm. This is a similar size to a conventional 3D transmon. However, in 3D Transmon exposure, two capacitor pads are separated by from 80 to 100 μm, whereas our exposure has two large exposure ares sitting close together, which gives rise to the proximity effect, and results in an overdose in certain areas. The main problem we had was near the edges close to the large exposure area, such as the ground planes or microwave launchers. The effective dose on the edges near the large exposure areas is not negligible, which creates a large undercut in the MMA layer, which causes the top PMMA layer to collapse by losing its support. To circumvent this problem, we split the pattern and wrote on two different beams, coarse and fine, in order to minimize the exposure time and to prevent a large accumulation of an effective dose in certain areas. With a large beam, 60~140 nm, the inner parts of the design require a large exposure area. When writing with a single beam, we encountered singificant problems with over-exposure with the copolymer resist. To address this, a fine beam was also used around the edges of the coarse patterns, which helped with overexposure problems, while keeping the writing times reasonable. For the small beam, we incorporated a proximity effect correction (PEC) which allows assigning different doses depending on the location, so as to compensate for an overdose. Figure 3.5 (d) shows one of the problems. The picture is a resist pattern before evaporation of Al/AlO_x/Al. In the transmission line, the gap to the ground planes appears to change, depending on the location. This decrease of the gap is due to a combination of two things: (1) A large undercut on the gaps originating from the accumulation of effective dose around the gaps. (2) The PMMA layer is pulled downwards by losing its support by the MMA. PEC is applied for the exposure of the picture, and the device is from one of the successful exposures.

The flux-tunable Josephson junction resonators with hybrid structure fabricated with the process described previously, where the whole circuit is fabricated in a single lift off process, suffered from low internal quality factors. We believe this was due to a combination of dielectric loss from the AlOx layer in the resonators and resist residue from the lift-off process. To solve these problems, we fabricated the microwave resonator and dc SQUID separately, by lifting-off the dc SQUID on top of a microwave

resonator to make superconducting contacts. This technique provides a cleaner substrate/metal surface everywhere except at the dc SQUID, and the microwave loss due to carbon residue from lift off can be eliminated. We refer to devices fabricated with this technique as hybrid devices. We believe the microwave loss also originates from the AlO_x layer inside the resonator of the previous paragraph: There is a large portion of the electromagnetic field of the cavity stored inside this dielectric layer, which could cause a large microwave loss. The fabrication of hybrid devices allows eliminating the AlO_x and resist residue on the microwave resonator.

For the metal of the superconducting resonators, we use MoRe. The patterning of the microwave resonators is done in the same way as discussed in a previous section. The fabrication of Josephson junction was also described in a previous section. Here, the superconducting contacts between the MoRe and the Al is made by evaporating aluminium on top of the MoRe. In order to have clean MoRe–Al interfaces, the sample is processed to remove resist residue and native oxide, which can possibly degrade the superconducting contacts, as well as the quality of the circuit. First the sample is de-scummed in oxygen plasma to remove organic compounds on the surface of the exposed areas (the MoRe electrodes and silicon substrate). Then the sample is soaked inside BHF for a short period of time to etch the native oxide on top of the MoRe and silicon prior to junction evaporation. During the de-scumming and BHF cleaning, precautions are taken not to break suspended PMMA resist bridges. Once the junctions are evaporated, the sample is lifted off with hot N-Methyl-2-pyrrolidone (NMP). Figure 3.6 shows an SEM image of a superconducting contact between the MoRe and the aluminium. The image shows that the silicon substrate is slightly overetched but nonetheless, it does appear that the MoRe electrodes made contact to the Al layer.

To understand the parameters of our devices, a simulation of the resonance frequency of a flux-tunable Josephson junction resonator was carried out using Sonnet. A hybrid device measured in experiments contains multiple resonators along with one reference linear lumped element resonator and two reference linear CPW resonators. The resonance frequency estimated from the Sonnet simulation deviated from the measured resonance due to the kinetic inductance of the MoRe. This deviation is greater than 1 GHz. The reference lumped element resonator has the same geometry but a dc SQUID. The basic design of the device and simulation can be seen in Figure 3.8 (a). In order to accurately estimate the resonance frequency of a hybrid resonator, the kinetic inductance of the reference lumped element resonator was estimated by introducing the sheet inductance of the metal into the simulation until it matched with the resonance measured in the experiment. Figure 3.8 (b) is the response of the simulation after introducing the sheet inductance that yields the same resonance frequency as the measurement. The corresponding sheet inductance is 1.525 pH/sq.

Subsequently, we estimated the resonance frequency of one of the hybrid SQUID cavities that has the same geometry as the reference lumped element resonator at

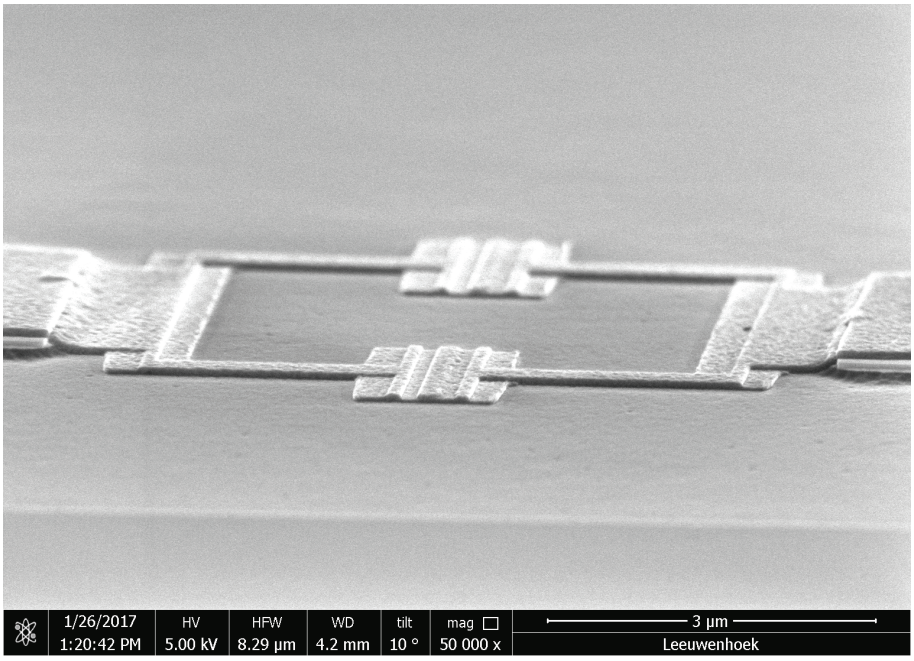

Figure 3.7: Superconducting contacts between MoRe and Al are made by evaporating Al on top of a MoRe lumped element resonator. Due to a slightly overetched silicon substrate, the Al contacts at the sidewalls of 60 nm MoRe electrodes.

integer flux quantum. This also includes the contribution of the kinetic inductance of the Josephson junctions in the dc SQUID. We introduced an ideal inductive element in the middle of the lumped element inductor in Sonnet, and increased its inductance until the response of the simulation matched the maximum frequency of the hybrid at integer flux quantum. The estimated value of the Josephson inductance is 0.35 nH, which is the Josephson inductance of the circuit. Figure 3.8 (d) is the response of the Sonnet simulation when an ideal inductor has 0.35 nH, which corresponds to the resonance at integer flux quantum in the measurement.

Figure 3.8 (e) shows a fit to the square of the frequency as a function of the ideal inductance value. The geometric inductance and capacitance are simultaneously determined from the fit, where the geometric inductance and the capacitance are estimated to be 2.9 nH and 288 fF, respectively. More details are discussed in the Appendix to Chapter 5.

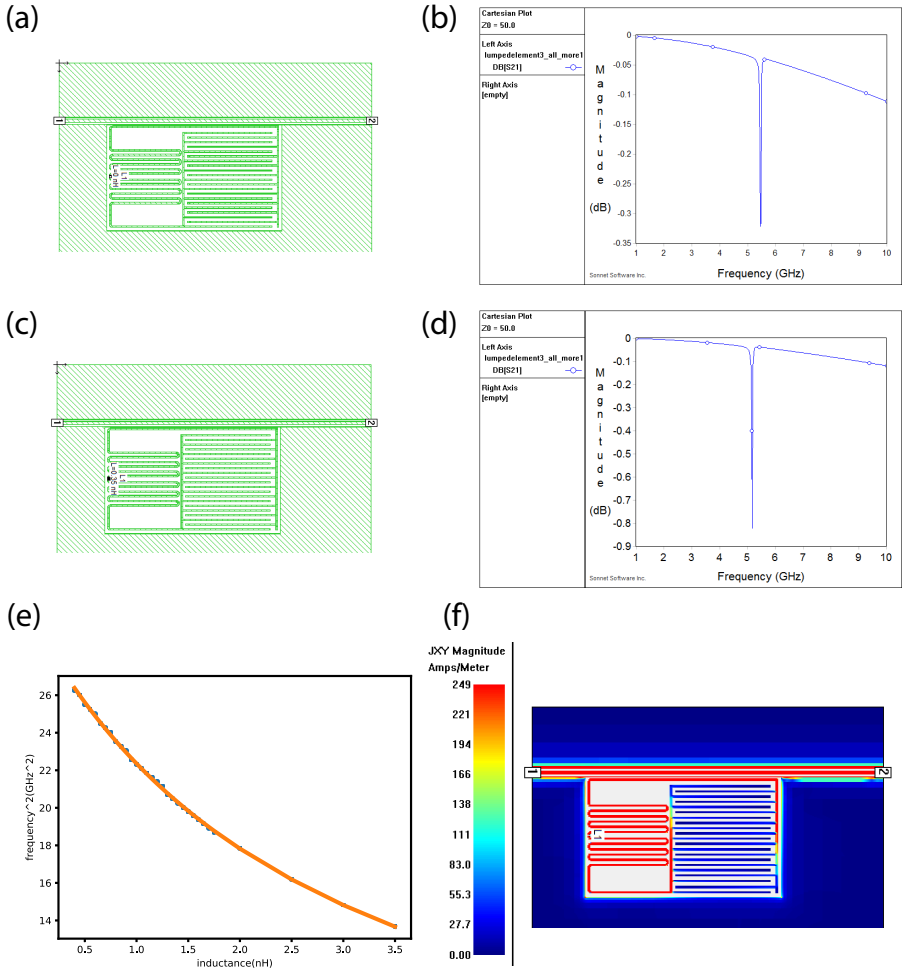

Figure 3.8: **Determining resonance frequency, kinetic inductance, Josephson inductance, and geometric inductance of a lumped element resonator** (a) Sonnet simulation design of a lumped element resonator whose dimensions are equivalent to what we measured in the experiments. Frequency mismatch between simulation and measurement was over 1 GHz due to kinetic inductance. For simulation, we changed the metal surface inductor until it matched with what we measured in the experiments. (b) Frequency response of the simulation that matches with the experimental value. Kinetic inductance of 60 nm thick MoRe is estimated as 1.525 pH/sq. (c) For the experiments, we measured several designs of flux-tunable resonators. One of them is exactly with the same design parameters, but with a dc SQUID. Here, in simulation, manually changing the ideal inductance of the circuit to match with the resonance frequency at zero flux quantum. (d) Josephson inductance, L_J is estimated as 0.35 nH. (e) Estimation of geometric inductance, L_g, and capacitance, C_g. Geometric inductance and capacitance can be estimated by introducing an ideal inductor into the circuit as a Josephson inductance. From the shift in resonance mode when the Josephson inductance is varied, the geometric inductance and capacitance can be calculated. (f) Current flow diagram of the design, which can be used to identify a resonance of the circuit.

3.4. NANOWIRE FABRICATION

In Chapter 5, we used stoichiometric high stress silicon nitride (Si_3N_4) as the mechanical element, as well as for a substrate for microwave cavity. Stoichiometric LPCVD Si_3N_4 is a material investigated in many experiments. The mechanical nature of stochiometric LPCVD Si_3N_4 is well known for high quality factors[20][21][22]. The large difference in the thermal expansion coefficients of Si_3N_4 and Si, along with a high deposition temperature, gives rise to high in-plane tensile stress. Si_3N_4 film acts as an ideal substrate for microwave circuits, as well[23, 24] for low loss tangent δ.

In order to incorporate high stress stoichiometric SiN nanowire into superconducting circuits, we cover it with superconductors such as MoRe or NbTiN. High stress stoichiometric LPCVD Si_3N_4 film has a much lower etch rate against BHF than PECVD SiN [25]. The film stress is found to be slightly over 1 GPa. The initial idea was to combine a mechanical oscillator and a microwave SQUID cavity by fabricating both elements on top of Si_3N_4 film. However, we observed a degradation of the microwave cavity when the cavity was fabricated on top of the Si_3N_4 LPCVD film. This degradation has been observed by [26] as well. We do not know the real reason for the low quality factors of the microwave cavities on top of LPCVD Si_3N_4 film. This might be due to an accumulation of charge carriers at the interface between the Si_3N_4 and Si formed when the substrate is heated up to from 600°C to 800°C, considering that the deposition temperature in ICP CVD is about 300°C, which is much lower than that for the LPCVD process, and maintains a low loss tangent[24].

Our goal is to combine a SiN nanowire and a superconducting resonator while minimising the microwave decoherence originating from the SiN–Si interface. To do this, we carefully removed the SiN layer except for only a small strip, with a combination of dry etching and BHF etching[27][28]. First, the substrate was cleaned in RCA1, RCA2, and BHF before the LPCVD stoichiometric SiN deposition. SiN was deposited with a thickness of 100 nm with a stress of over 1 GPa. The first step was the deposition of alignment markers with lift-off. Using an e-beam evaporator, first the chromium sticking layer was evaporated for 10 nm, and 50 ~ 60 nm of gold was evaporated subsequently. A Cr sticking layer was used because it is resistant to the BHF solution that the sample is eventually going to be soaked in for 50 minutes. Then the bilayer resist was lifted off in resist stripper PRS 3000 at 80°C for 30 minutes with a stirring magnet. The sample was rinsed with two beakers of IPA and blow dried with a nitrogen gun. The next step was to etch away the SiN on the Si substrate except at the positions of the nanowires. To do that, we spun coat a trilayer resist on the substrate, S1813/tungsten/ARN. The top layer resist was AR-N 7700, which is a negative resist good for sensitive exposure and well resistant to plasma etching. And 5×50 μm square patterns were written with a dose of 150 $\mu C/cm^2$. This resist requires a post bake after exposure. The sample was developed with MF 321 with H_2O termination. Here, we used trilayer resist for enough etch time of the SiN. Similar to etching the MoRe resonator, the tungsten and S1813 were etched with SF_6 + He and oxygen, respectively. Subsequently, the SiN was etched with SF_6 + He, leaving 10 ~ 20 nm of

SiN. The thickness of SiN was measured with a Woolam spectroscopic ellipsometer. After RIE, the resist stack was removed in a PRS 3000 solution followed by IPA and a nitrogen blow dry. The purpose of terminating the etching before reaching the Si is to protect the surface of the Si substrate. And the SiN is further etched with BHF for 50 minutes to etch 20 nm of SIN. At this time, the exposed areas of the SiN strips for the nanowires were also etched BHF, so that after 50 minutes of etching the thickness of the SiN nanowire foundation (base) was ~80 nm. After the BHF etching, the substrate was sputtered with MoRe using a MB-AJA sputter machine. Due to the two-inch target of MoRe used in the sputtering machine, we could not sputter isotropically, and had to sputter at two different angles to cover the side walls of the square section of SiN which is to become a section of the SQUID loop. Based on gold markers, resonator patterns were written with a trilayer resist stack S1813/tungsten/PMMA. The procedure of patterning the resonator incorporating a 80 nm SiN rectangular strip is essentially the same as the one described in the previous section. Finally, nanowire was released with dry-etching. Again, the sample was spin coated with tri-layer resist S1813/tungsten/PMMA. This time the exposure went on top of the SiN strips covered by the MoRe with two rectangular shapes, separated by a distance equal to the width of the nanowires to form a nanowire. After development with MIBK:IPA 1:3, the sample was dry etched for releasing. The etching procedure was the same as that up to the etching of the S1813. To release the nanowire from the substrate, one must etch the MoRe, SiN, and Si within the resist mask. The layer of MoRe/SiN/Si was etched in one procedure with SF_6 and He using the same parameters as before. Whether the nanowires are now released or not can be checked with an optical inspection. Finally, the resist mask was removed with oxygen plasma with RIE. Figure 3.9 is after the release of the nanowire and the removal of the S1813 with oxygen plasma. As can be seen in Figure 3.9 (b), there is some residue around the nanowire, which might be resist residue or some redeposition due to reaction with the etching gasses. Geometrically, the nanowires are not located in proximity to anything. There should be an option to remove the resist layer stack using PRS 3000 or NMP, which would probably not leave the residue seen in Figure 3.9 (b).

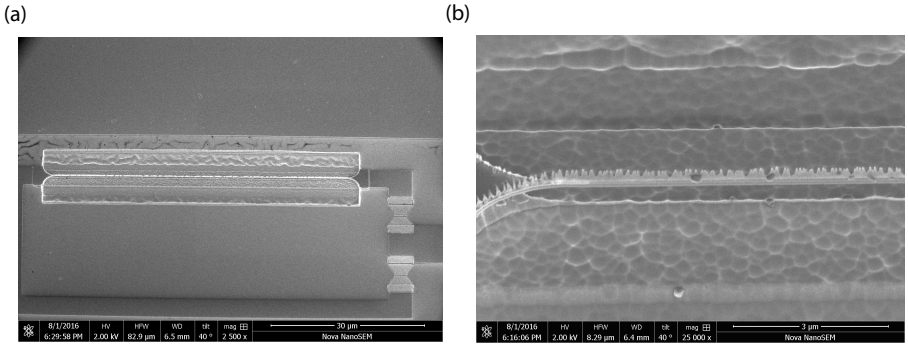

Figure 3.9: (a) After releasing the nanowire and dry etching the S1813. The image shows a SQUID loop containing a suspended nanowire and two Josephson junctions. (b) Zoomed image of nanowire. We observed flags on the edges of etch windows, which might be redeposition of polymer or some contamination inside the etcher.

3.5. MEASUREMENT SETUP

In this section, I will briefly explain our measurement setup used for the experiments to be presented in the following chapters. All the measurements were done inside a dilution refrigerator whose base temperature is below 20 mK. A basic characterisation of the microwave cavities was done by either measuring the reflection or transmission coefficient of the cavity inside an Oxford Triton dilution refrigerator.

A pulse tube cooler performs a work by transporting helium gas along with heat from the compressor to a pulse tube. The pulse tube cools by achieving a pressure difference between the two ends of the inside of the tube, which is the same as the temperature difference in the tube. The cold side of the tube is connected to a regenerator, which is typically made of a magnetic material with a large heat capacity. This acts as a reservoir of heat. The hot side of the tube is connected to a reservoir via an orifice (or impedance). When it is in compression, the heat created is removed in the heat exchanger of the regenerator (water cooled). Then the gas is transferred into the pulse tube. On expansion, the gas flow is in the opposite direction from the compression phase, and releases heat from the cold side of the pulse tube to perform the cooling.

The fridge uses a mixture of He_3 and He_4, which is a standard and the only technique to cool to below 100 mK. The technique uses the latent heat of the mixture of He isotopes, He_3 and He_4, at a concentration of 6.6 percent of He_3. Once the mixture is cooled down below 870 mK, the liquid becomes separated into two different phases: One is an He_4 rich liquid and the other is an He_3 rich liquid. The lower density He_3 liquid stacks on top of the He_4 liquid. As the temperature decreases, the He_3 rich liquid becomes pure He_3. However, the He_4 liquid allows dissolving the He_3 up to 6.6 percent. At a certain temperature, the He_3 of the He_4 rich liquid can be selectively

evaporated, and dissolve the He_3 from the top floating phase. By using the entropy difference between the two phases, cooling can be achieved. The cooling power of a dilution refrigerator is proportional to T^2, whereas it is exponentially proportional to the temperature in evaporative cooling, which is due to the finite solubility of He_4-He_3.

The devices were measured inside an Oxford Triton bottom loading type refrigerator. The system contains two measurement setups. A schematic diagram of the measurement setup is shown in Figure 3.10. Each setup contains an HEMT amplifier on the output line. For each amplifier line, there are three input lines. There are several requirments to be satisfied by the material of the RF cables. They need to have high electric conductivity and low thermal conductivity. In addition, the microwave loss should be reasonably small. To quantify these values, the Widemann–Franz law can be used. The ratio of thermal conductivity to electric conductivity is the product of a constant L_0 and the temperature T.

$$\kappa/\sigma = L_0 T \tag{3.1}$$

where the Lorentz number $L_0 = (\pi\kappa_B/e)^2/3 = 2.44e^{-8}$ WΩ/K^2 is a universal constant. This relation reflects the connection between the electrical and thermal conductivity of free electrons. To overcome this limitation, one can used superconducting cables. For superconductors, one must have $\Delta E \sim 1.76 k_B T_c$ to break Cooper pairs for the electrons to carry thermal energy. Below the superconducting state, only unpaired electrons carry heat, while electrical current can still be carried by the paired electrons with no resistance. In the setups used here below the 3K stage, NbTi cables with a Tc of around 10K are used, allowing simultaneous low insertion loss and low thermal conductance.

Thermal noise coming from higher temperature stages could reduce the sensitivity of measurements. When signals are sent from room temperature, Nyquist noise is also included because of the cables used at room temperature and cold stages inside the fridge. This thermal noise can be properly filtered with attenuators thermally anchored at each cold stage. The temperature difference between room temperature and 20 mK gives a little over 41 dB, which gives an idea of the amount of attenuation required to suppress the Nyquist noise. Currently, each input line has an attenuation of ~ 50 dB inside the fridge. We use the equation below to calculate the attenuation needed at each temperature stage inside the fridge.

$$T2_{noise} = T1_{noise} \times 10^{(-dB/10)} + T2 \tag{3.2}$$

Here, $T2_{\text{noise}}, T1_{\text{noise}}, dB$, and $T2$ are the noise temperature at the colder stage, the noise temperature at the warmer stage,the attenuation in units of dB between the two temperature stages, and temperature of the stage, respectively. In the current setup of the Triton fridge, there are in all 9 dB of attenuation for the 50 K stage plate, 6 dB above the 50 K plate, and 3 dB below the plate. The noise temperature is reduced only to 87.8 K. The noise temperature is reduced to 3.9 K at the 3 K stage with -13

dB attenuation. At the 10 mK stage, the noise temperature is reduced to 30.9 mK. For each bundle of measurement lines, one of the input lines is connected to a port of a directional coupler or a circulator on the output lines, which enables reflection measurement. The other four input lines are kept for transmission measurements or other purposes.

NbTi is used for the output line cables from the bottom of the fridge to the 3 K stage. The reason for this is its high electron conductivity and low thermal conductivity. Nb could be used for the same purpose. However, the thermal conductivity of NbTi is much lower than that of Nb. At the 3 K stage, an HEMT amplifier, $LNF\_LNC4-8A$, is connected to each output line. The gain of the amplifier is 40 dB. The cables from room temperature and 3 K stage are made of stainless steel, whose loss will not contribute much to the S/N ratio because of the large gain from the HEMT amplifiers.

Two sets of twisted pair looms are connected, both routed through two of 24 pin cinchi connectors at the MC stage. The looms are made of a high Tc superconductor that runs from the 50 K stage to the MC stage. At the 3 K stage, a dc voltage is applied to the high electron mobility transistor (HEMT) amplifiers.

Once the sample has been fabricated, it is mounted on a sample box and loaded inside the fridge. When the sample is ready, the device is glued to the copper plate of a sample box and wirebonded to a PCB, as shown in Figure 3.11 (a). The sample is tightly shielded with a copper lid, Figure 3.11 (b), and bolted to a puck of the fridge, shown in Figure 3.11 (c). The puck has 14 SMP female connectors on its top side, which can be seen in Figure 3.12 (a). The cold stage of the inside of the fridge has connectors of the opposite gender, which can be seen in Figure 3.12 (b). The system has a bottom loading system which enables inserting the puck inside the fridge without warming up the whole fridge all the way to room temperature and breaking the vacuum. Once the mixture is collected inside the tank, and the puck in a loader is pumped with an external turbo pump along with OVC, the puck can be inserted and bolted to the cold plate of the fridge, which is thermally anchored to the MC plate as shown in Figure 3.12 (b) and Figure 3.12 (c). Once the puck is tightly bolted to the cold plate, it can be released from the loader. Subsequently the OVC can be closed and precooling can be started by introducing a small mixture in the precool circuit.

To apply a dc magnetic field, a superconducting solenoid, which is shown in Figure 3.5, is used. The magnet leads between 4 K and 50 K are made from high-Tc superconductor, and the magnet itself is NbTi. The magnet wire is independent of the other dc looms, and the current is applied with a current source, Keysight B2961. A magnetic field is applied vertically with respect to the MC plate. The magnet produces a maximum field of 100 mT with a current of 1.47 A.

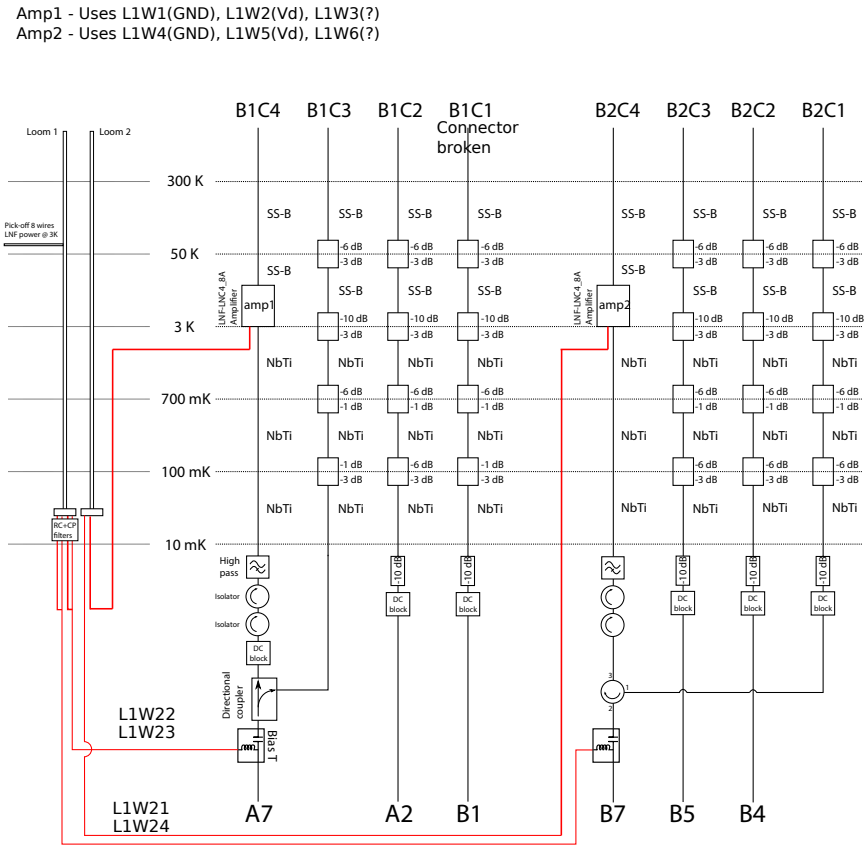

Figure 3.10: **Schematic of wiring inside Triton**: There are 8 microwave lines B1C1, B1C2, B1C3, B1C4, B2C1, B2C2, B2C3, and B2C4. B1C4 and B2C4 are amplifier lines. Each amplifier line is connected to the input lines using either a directional coupler or a circulator, which enables reflection measurements. By using other input lines with B1C4 or B2C4, transmission measurements are enabled. Also, each output line contains a bias tee for applying dc current or voltage to the samples. The dc connectors of the bias tees are connected to a superconducting loom.

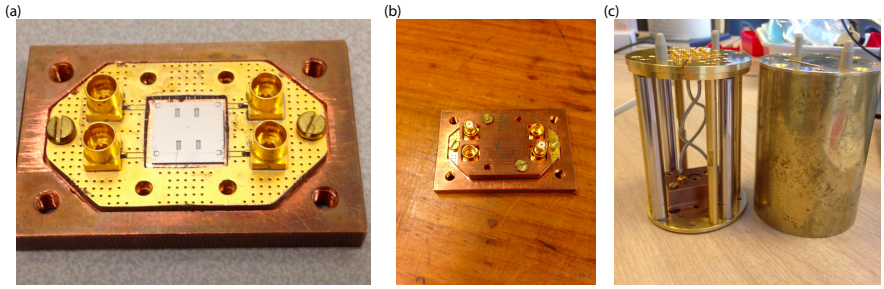

Figure 3.11: (a) Mounting a sample to sample box. (b) Sample box with lid. (c) Sample box inside pack.

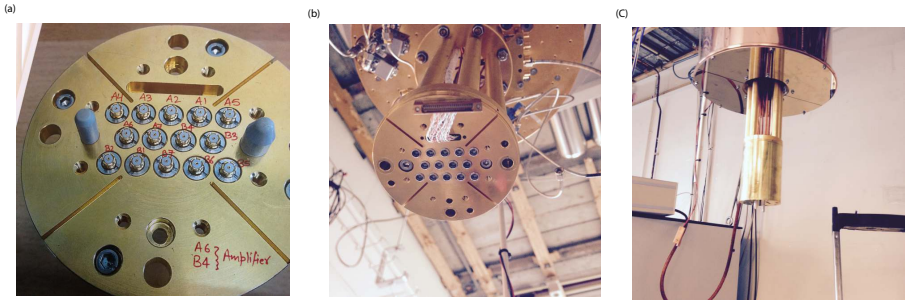

Figure 3.12: (a) Topside of a puck. (b) The bottom side of the cold plate which is thermalized to MC. When a puck is inserted, top side of the puck, female SMP connectors as shown in (a) match to the male connector of the SMP pin to make microwave contacts. The puck is tightly bolted into four screw holes (one screw hole is not shown in the picture). (c) A puck connected to the cold plate.

(a)

Figure 3.13: Magnet is thermalized to the 3 K stage. As a puck is inserted, the puck is located slightly above inside the solenoid.

REFERENCES

[1] J. Gao, M. R. Visser, M. O. Sandberg, F. C. S. da Silva, S. W. Nam, D. P. Pappas, K. D. Irwin, D. S. Wisbey, E. Langman, S. R. Meeker, B. A. Mazin, H. G. Leduc, and J. Zmuidzinas, *A titanium-nitride near-infrared kinetic inductance photon-counting detector and its anomalous electrodynamics,* Applied Physics Letters **101**, 142602 (2012), arXiv: 1208.0871.

[2] W. Guo, X. Liu, Y. Wang, Q. Wei, L. F. Wei, J. Hubmayr, J. Fowler, J. Ullom, L. Vale, M. R. Vissers, and J. Gao, *Counting Near Infrared Photons with Microwave Kinetic Inductance Detectors,* Applied Physics Letters **110**, 212601 (2017), arXiv: 1702.07993.

[3] A. Wallraff, D. I. Schuster, A. Blais, L. Frunzio, R.-S. Huang, J. Majer, S. Kumar, S. M. Girvin, and R. J. Schoelkopf, *Strong coupling of a single photon to a superconducting qubit using circuit quantum electrodynamics,* Nature **431**, 162 (2004).

[4] A. Blais, R.-S. Huang, A. Wallraff, S. M. Girvin, and R. J. Schoelkopf, *Cavity quantum electrodynamics for superconducting electrical circuits: an architecture for quantum computation,* Physical Review A **69** (2004), 10.1103/PhysRevA.69.062320, arXiv: cond-mat/0402216.

[5] D. I. Schuster, A. P. Sears, E. Ginossar, L. DiCarlo, L. Frunzio, J. J. L. Morton, H. Wu, G. A. D. Briggs, and R. J. Schoelkopf, *High cooperativity coupling of electron-*

spin ensembles to superconducting cavities, Physical Review Letters **105** (2010), 10.1103/PhysRevLett.105.140501, arXiv: 1006.0242.

[6] V. Singh, S. J. Bosman, B. H. Schneider, Y. M. Blanter, A. Castellanos-Gomez, and G. A. Steele, *Optomechanical coupling between a multilayer graphene mechanical resonator and a superconducting microwave cavity,* Nature Nanotechnology **9**, 820 (2014), arXiv: 1403.5165.

[7] V. A. Seleznev, M. A. Tarkhov, B. M. Voronov, I. I. Milostnaya, V. Y. Lyakhno, A. S. Garbuz, M. Y. Mikhailov, O. M. Zhigalina, and G. N. Gol'tsman, *Deposition and characterization of few-nanometers-thick superconducting Mo–Re films,* Superconductor Science and Technology **21**, 115006 (2008).

[8] B. H. Schneider, S. Etaki, H. S. J. van der Zant, and G. A. Steele, *Coupling carbon nanotube mechanics to a superconducting circuit,* Scientific Reports **2** (2012), 10.1038/srep00599, arXiv: 1209.1514.

[9] V. E. Calado, S. Goswami, G. Nanda, M. Diez, A. R. Akhmerov, K. Watanabe, T. Taniguchi, T. M. Klapwijk, and L. M. K. Vandersypen, *Ballistic Josephson junctions in edge-contacted graphene,* Nature Nanotechnology **10**, 761 (2015), arXiv: 1501.06817.

[10] V. Singh, B. H. Schneider, S. J. Bosman, E. P. J. Merkx, and G. A. Steele, *Molybdenum-Rhenium alloy based high-Q superconducting microwave resonators,* Applied Physics Letters **105**, 222601 (2014), arXiv: 1411.4815.

[11] J. Wenner, R. Barends, R. C. Bialczak, Y. Chen, J. Kelly, E. Lucero, M. Mariantoni, A. Megrant, P. J. J. O'Malley, D. Sank, A. Vainsencher, H. Wang, T. C. White, Y. Yin, J. Zhao, A. N. Cleland, and J. M. Martinis, *Surface loss simulations of superconducting coplanar waveguide resonators,* Applied Physics Letters **99**, 113513 (2011), arXiv: 1107.4698.

[12] M. Gurvitch, M. A. Washington, and H. A. Huggins, *High quality refractory Josephson tunnel junctions utilizing thin aluminum layers,* Applied Physics Letters **42**, 472 (1983).

[13] E. Levenson-Falk, F. Kos, R. Vijay, L. Glazman, and I. Siddiqi, *Single-Quasiparticle Trapping in Aluminum Nanobridge Josephson Junctions,* Physical Review Letters **112**, 047002 (2014).

[14] E. Pallecchi, M. Gaaß, D. A. Ryndyk, and C. Strunk, *Carbon nanotube Josephson junctions with Nb contacts,* Applied Physics Letters **93**, 072501 (2008).

[15] Y. Chu, C. Axline, C. Wang, T. Brecht, Y. Y. Gao, L. Frunzio, and R. J. Schoelkopf, *Suspending superconducting qubits by silicon micromachining,* Applied Physics Letters **109**, 112601 (2016), arXiv: 1606.02822.

[16] J. Birenbaum, *The C-shunt Flux Qubit: A New Generation of Superconducting Flux Qubit*, Ph.D. thesis, University of California, Berkeley (2014).

[17] D. H. Slichter, *Quantum Jumps and Measurement Backaction in a Superconducting Qubit*, Ph.D. thesis, University of California, Berkeley (2011).

[18] P. Bertet, F. R. Ong, M. Boissonneault, A. Bolduc, F. Mallet, A. C. Doherty, A. Blais, D. Vion, and D. Esteve, *Circuit quantum electrodynamics with a nonlinear resonator*, arXiv:1111.0501 [quant-ph] (2011), arXiv: 1111.0501.

[19] H. Paik, D. I. Schuster, L. S. Bishop, G. Kirchmair, G. Catelani, A. P. Sears, B. R. Johnson, M. J. Reagor, L. Frunzio, L. Glazman, S. M. Girvin, M. H. Devoret, and R. J. Schoelkopf, *Observation of high coherence in Josephson junction qubits measured in a three-dimensional circuit QED architecture*, Physical Review Letters **107** (2011), 10.1103/PhysRevLett.107.240501, arXiv: 1105.4652.

[20] B. M. Zwickl, W. E. Shanks, A. M. Jayich, C. Yang, A. C. B. Jayich, J. D. Thompson, and J. G. E. Harris, *High quality mechanical and optical properties of commercial silicon nitride membranes*, Applied Physics Letters **92**, 103125 (2008), arXiv: 0711.2263.

[21] J. M. Fink, M. Kalaee, A. Pitanti, R. Norte, L. Heinzle, M. Davanco, K. Srinivasan, and O. Painter, *Quantum Electromechanics on Silicon Nitride Nanomembranes*, Nature Communications **7**, 12396 (2016), arXiv: 1512.04660.

[22] M. Yuan, M. A. Cohen, and G. Steele, *Silicon nitride membrane resonators at millikelvin temperatures with quality factors exceeding 10^8*, Applied Physics Letters **107**, 263501 (2015), arXiv: 1510.07468.

[23] J. M. Martinis, K. B. Cooper, R. McDermott, M. Steffen, M. Ansmann, K. D. Osborn, K. Cicak, S. Oh, D. P. Pappas, R. W. Simmonds, and C. C. Yu, *Decoherence in Josephson Qubits from Dielectric Loss*, Physical Review Letters **95**, 210503 (2005).

[24] H. Paik and K. D. Osborn, *Reducing quantum-regime dielectric loss of silicon nitride for superconducting quantum circuits*, Applied Physics Letters **96**, 072505 (2010), arXiv: 0908.2948.

[25] K. R. Williams, K. Gupta, and M. Wasilik, *Etch rates for micromachining processing-Part II*, Journal of Microelectromechanical Systems **12**, 761 (2003).

[26] R. A. Norte, *Nanofabrication for On-Chip Optical Levitation, Atom-Trapping, and Superconducting Quantum Circuits*, Ph.D. thesis, California Institute of Technology (2015).

[27] X. Zhou, F. Hocke, A. Schliesser, A. Marx, H. Huebl, R. Gross, and T. J. Kippenberg, *Slowing, advancing and switching of microwave signals using circuit nanoelectromechanics*, Nature Physics **9**, 179 (2013).

[28] A. Iniguez Rabago, *Electrostatical and optomechanical detection of a superconductive nanowire coupled to a microwave cavity*, Master's thesis, TU Delft (2016).

4

MECHANICAL DISSIPATION IN MoRe DRUMS

We experimentally investigate dissipation in mechanical resonators made of a disordered superconducting thin film of Molybdenum-Rhenium(MoRe) alloy. Electrostatically driving the drum with a resonant AC voltage, we detect its motion using a superconducting microwave cavity. From the temperature dependence of mechanical resonance frequencies and quality factors, we find evidence for non-resonant, mechanically active two-level systems (TLSs) limiting its quality factor at low temperature. In addition, we observe a strong suppression of mechanical dissipation at large mechanical driving amplitudes, suggesting an unconventional saturation of the non-resonant TLSs. These observations shed light on the mechanism of mechanical damping in superconducting drums and routes towards understanding dissipation in such devices.

Nanoelectromechanical systems have evolved into an important platform in modern information technology. They are extensively used for applications in sensing, filtering and timing[1]. One remarkable example is cavity opto/electro-mechanics[2, 3]. The demonstrations of the quantum ground state of mechanical resonators have opened new applications of NEMS devices in quantum information technology[4, 5]. To this end, the approach of cavity optomechanics which uses the interaction between light and mechanical motion has enabled the applications of NEMS towards the near-quantum limited frequency conversion[6, 7], temporal and spectrum shaping of signals[8], and a nearly quantum limited frequency-mixer [9].

A common implementation of an optomechanical system is realized by coupling a superconducting drumhead resonator to a microwave cavity. For quantum-limited performance of such a coupled system, both the drumhead resonator and the superconducting cavity should have low dissipation rates. In recent years, superconducting metal drums[10] have emerged as a popular platform for microwave optomechanics. While such drums can exhibit very low dissipation, there is also a large spread in reported mechanical Q-factors [10–13] and not many reports studying the dissipation mechanisms in such devices.

Here, we explore mechanical dissipation mechanisms in such superconducting drum resonators as a function of temperature and driving amplitude. The variation of dissipation rate and resonant frequency with temperature suggest that mechanically active two-level systems (TLSs)[14, 15, 30] play an important role, setting the dissipation in these disordered superconductors akin to acoustic studies performed earlier on superconducting glasses [16]. By varying the acoustic excitation strength, we further observe an amplitude dependent damping rate supporting the role of TLSs, similar to the observations made in superconducting microwave resonators in response to the electromagnetic field[17, 18] with electrical TLSs, but with an unconventional saturation of the non-resonant mechanical TLSs by the mechanical drive.

The drums studied in this letter were made using films of a superconducting alloy of Molybdenum and Rhenium (MoRe 60-40). The compatibility of MoRe with HF, oxygen plasma, and an elastic modulus of ≈1 GPa makes it an attractive candidate for making hybrid electromechanical devices[19]. The electrical properties of MoRe are well studied establishing its disordered nature with a residual resistance ratio of approximately unity and a superconducting transition temperature of 9.2 K[20–23]. The electrical dissipation of such films in microwave frequency domain has been characterized in earlier studies[24], as well as recent reports in coplanar waveguides [25].

Fig. 4.1(a) shows an optical microscope image of our complete optomechanical device. It consists of a superconducting drumhead resonator and a high-impedance microwave cavity both made of MoRe. The mechanically compliant drumhead resonator is galvanically shorted to the high-impedance microwave cavity, enabling electrostatic actuation of its motion. The microwave cavity is coupled through the drumhead to the feedline, such that its response can be accessed in a reflection measurement. Fig. 4.1(b) shows a scanning electron microscope of the drumhead resonator.

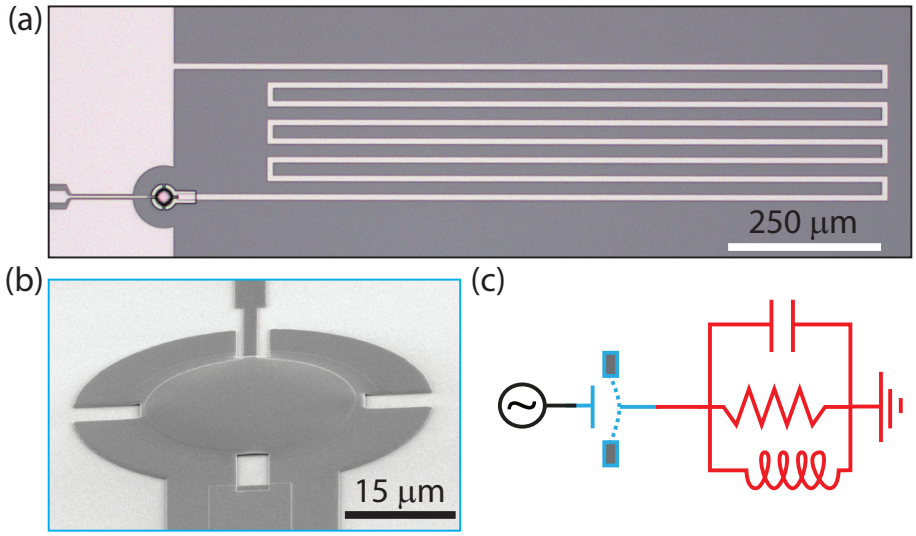

Figure 4.1: Microwave cavity readout of a superconducting drum with electrostatic driving. a) Optical microscope image of the device. A drumhead mechanical oscillator is capacitively coupled to the microwave input port of a high impedance microwave cavity on a sapphire substrate. b) Scanning electron microscope image of MoRe drumhead resonator. The drum is 30 μm in diameter and is suspended approximately 290 nm above the gate bottom electrode. c) Device schematic diagram: the mechanical drum is capacitively coupled to the microwave input port. Motion of the drum modulates both the resonance frequency ω_c and the external coupling rate κ_e of the cavity.

We apply microwave signals to the cavity via mechanically compliant capacitor. Detection of the motion of the drum occurs through its modulation of the cavity frequency, ω_c, as well as the external cavity decay rate, κ_e as schematically shown in Fig. 4.1(c).

To actuate the drumhead resonator, we apply a DC signal V_{DC} and a small RF signal V_{AC} near the mechanical resonance frequency ω_m simultaneously to the input port. Due to capacitive attraction, this signal exerts a force $C_g^{'} V_{DC} V_{AC}$ on the drumhead resonator, where $C_g^{'} = dC_g/dx$ is the derivative of the capacitance between the resonator and the feedline with respect to distance. In order to read out the mechanical motion, we drive the system with a microwave tone at the cavity resonance frequency ω_c. Due to electro-mechanical coupling, mechanical motion modulates the intra-cavity power, creating sideband signals in the reflected signal. The sideband signals are amplified and then mixed down with a local oscillator tone at the cavity resonance frequency. The signal is further amplified and sent to a spectrum analyzer. Using the mechanical resonator as the coupling capacitor to the cavity enables both direct electrostatic actuation of the motion and tuning of the mechanical resonance frequency using voltages applied to the feedline.

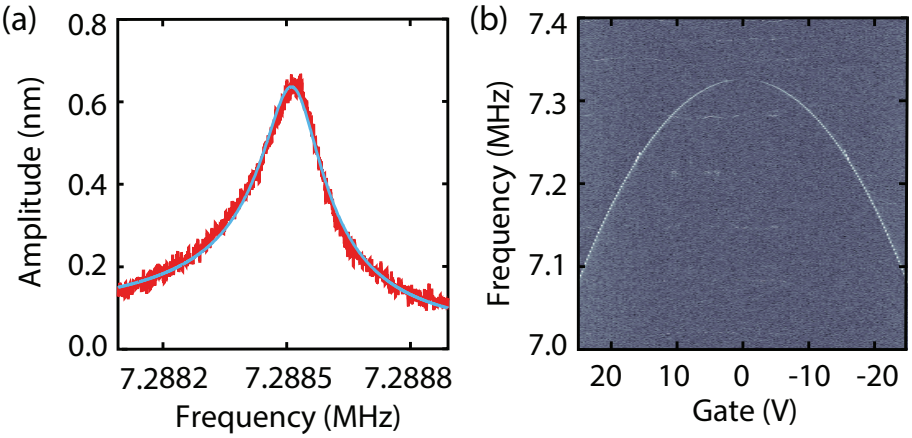

Figure 4.2: Characterization of the mechanical response of the drumhead resonator. a) Mechanical response of MoRe drumhead resonator at 10 V of applied voltage (red curve) along with the fitted curve (light blue), yielding a quality-factor of 50248 and resonant frequency of 7.2885 MHz. b) Colorscale plot of the measured response with frequency of the applied RF signal used for mechanical driving (near ω_m) and DC gate voltage. Mechanical response can be tuned over 200 kHz with ±28 V of DC gate voltage.

The fabricated samples are placed in a radiation-tight box and cooled down to 20 mK in a dilution refrigerator with sufficient attenuation at each temperature stages to thermalize the microwave signals (see Supplementary Materials for measurement chain schematic (SM)). We first begin by characterizing the microwave cavity. The microwave cavity has a resonance frequency of $\omega_c/2\pi = 6.30 \times 10^9$ s^{-1}, external coupling rate $\kappa_e/2\pi = 31.0 \times 10^6$ s^{-1}, and internal dissipation rate of $\kappa_i/2\pi = 25.8 \times 10^6$ s^{-1} (see SM for detailed measurements). The red curve in Fig. 4.2(a) shows the measured mechanical response of the resonator along with a skewed-Lorentzian fit (light-blue line). The slight asymmetry in the measured homodyne signal arises from the finite electrical isolation and is discussed in the supplementary material. From the fit, we find a mechanical resonance frequency of $\omega_m/2\pi = 7.2885 \times 10^6$ s^{-1} with a quality-factor Q_m of 50×10^3 at $V_{DC} = 10$ V. Fig. 4.2(b) shows a colorscale plot of the measured homodyne signal as a function of frequency of the RF signal used for mechanical driving and DC gate voltage applied to the feedline using a bias tee. The sharp change in color reflects the mechanical resonance frequency. As the DC voltage is tuned away from zero, the mechanical resonance frequency decreases approximately quadratically, showing the well-studied capacitive softening effect[26]. The mechanical frequency is pulled by 200 kHz for gate voltages of 20 V. The mechanical signal is no longer visible around zero gate voltage due to the vanishing electrostatic force.

In Fig 4.3, we investigate the temperature dependence of the mechanical response from 23 mK to 1.5 K. We measured the mechanical resonance frequencies and the quality-factors at different temperatures and at different applied DC voltages, $V_g = 7$, 14, and 28 V. Fig 4.3(a) shows the normalized shift in the resonance frequency for various temperature points. As the temperature is increased the resonance frequency increases logarithmically up to a cross-over temperature of ≈ 900 mK. At higher temperatures, we see a slight drop in the resonance frequency. Fig. 4.3(b) shows the quality-factor Q_m change as a function of temperature. As the temperature is increased from 23 mK, Q_m shows a sharp decrease for all gate voltages. Above the approximate cross-over temperature observed in the mechanical frequency, Q_m stops decreasing and saturates at a value around 10,000.

The logarithmic increase in the frequency shift suggests the presence of two-level systems[16, 27–30]. TLSs can have a very broad spectral distribution[31]. At temperatures $k_B T \gg \hbar\omega_m$, the resonant TLSs are expected to be saturated, and not able to contribute to mechanical dissipation. However, coupling of the mechanical motion to higher energy, off-resonant TLSs can still have a significant contribution to the frequency shift. Comparing results at three different voltages, the normalized shifts are independent of mechanical resonant frequency below the cross over temperature. Such a temperature dependence can also be interpreted in the context of a TLSs model: at high temperatures, part of the mechanical restoring force arises from the dispersive shift of the thermal population of the high frequency TLSs. Beyond the cross-over temperature, these TLSs decouple from the mechanics due to either changes of their thermal populations or the relaxation rate. As the TLSs are decoupled the mechanical spring constant reduces, giving a lower mechanical frequency. For an off-resonant dispersive interaction, the normalized frequency shift is expected to scale as $\delta f / f_0 = C_s \log(T/T_0)$, where C_s is a constant proportional to the filling factor and TLSs loss tangent[31]. For the fit shown in Fig 4.3(a), we find $C_s \approx 5.3 \times 10^{-5}$, similar to previously reported values for mechanical TLSs in disordered superconducting films[16, 32]. To compare the behavior of dissipation with the frequency shift, we plot Q_m^{-1} in the subpanel of Fig. 4.3(b). In lower temperature ranges, we observe an increase in the mechanical dissipation rate with temperature, which slows down as the temperature approaches ≈ 700 mK. As discussed above, the interaction with resonant TLSs can be neglected due the low frequency of the drum ($k_B T >> \hbar\omega_m$). Non-resonant TLSs, however, can also result in dissipation due to the lag between the dispersive shift of their energies due to the mechanical coupling and their equilibration time with the bath. The contribution of the off-resonant interaction to the damping scale as $Q_m^{-1} = C_s \frac{\Gamma(T)}{\omega_m}$ for $\omega_m > \Gamma(T)$, where Γ is the TLSs relaxation rate[31]. As shown in Fig. 4.3(b), the numerical fits to the mechanical dissipation rate suggest that TLSs relaxation rate increases linearly with the temperature.

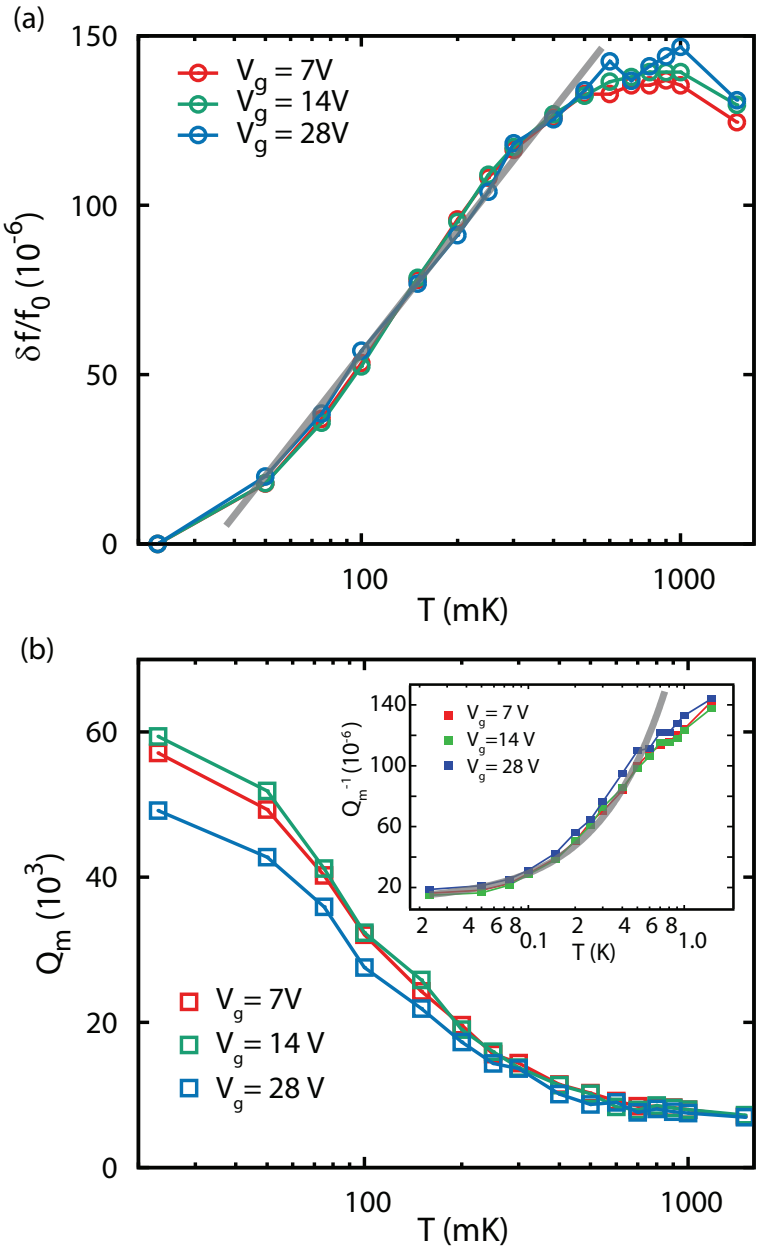

Figure 4.3: Temperature dependence of a) Normalized relative frequency shift $\delta f = (f_0(T) - f_0(23\text{ mK}))/f_0(23\text{ mK})$ and b) the mechanical quality factor. The mechanical quality-factor is determined from fitting to a Lorentzian function. Measurements are taken at three different voltages 7, 14, 28 V. The inset shows the plot of inverse quality-factor Q_m^{-1}. The gray lines are the numerical fits to the data as described in the main text.

In Fig. 4.4, we explore saturation effects of the TLSs in these drums by applying a large mechanical driving force. To increase the acoustic excitation strength, we varied the *AC* driving voltage for mechanical actuation. Fig. 4.4(a) shows mechanical responsivity (also known as mechanical susceptibility and referred to as normalized response) at different driving voltages in the limits of linear restoring force (Lorentzian mechanical response) and non-linear restoring forces (Duffing response from nonlinear spring effects). At higher amplitude drive forces, the responsivity increases, indicating the presence of a nonlinear damping term[30], but with a negative coefficient, similar to recent reports with multilayer graphene resonators [33]. Note also, however, that the net damping, including both linear and nonlinear terms, is still positive. We also note that the response observed here has the opposite sign to the nonlinear damping terms to the commonly observed in NEMS devices [30]. In the regime of linear restoring forces, we can quantify the decrease in the damping with driving force by fitting the mechanical response to extract an effective power-dependent quality factor, Fig. 4.4(b). Similar negative nonlinear damping characteristics were also observed in a similar second device (data included in the supplemental materials).Although a qualitatively similar increase in responsivity could also arise from electrostatic parametric gain, we find that the power of the AC drive voltage is at least three orders of magnitude to small to explain our observations by parametric effects.

While a decrease in the mechanical damping shown in figure 4.4 appears similar to the case of the saturation of resonant TLSs in superconducting microwave cavities, such saturation effects are not typically observed when the interaction with the TLSs is non-resonant, as the non-resonant drive is not able to excite the TLSs directly. The observation presented here of decreased damping at large mechanical excitation, also recently reported for the case of graphene resonators, suggests that a strongly non-equilibrium population of high frequency TLSs is induced by the low frequency driving forces, for example, by either strong higher-order excitation processes, or by a decoupling of the non-resonant TLSs from their bath.

In conclusion, we have studied dissipation in mechanical drumhead resonators made of a superconducting alloy of MoRe. The temperature dependence of the dissipation and resonant frequency strongly suggest the presence of mechanically active TLSs in these disordered superconducting thin film mechanical resonators. At low temperatures, the main contribution to dissipation and frequency shift stems from the dispersive interaction with TLSs, with slow relaxation rates < 7 MHz. We further explored the mechanical dissipation while varying the strength of acoustic field and observe an amplitude dependent damping, suggesting a non-equilibrium population of non-resonant TLSs induced by the mechanical drive.

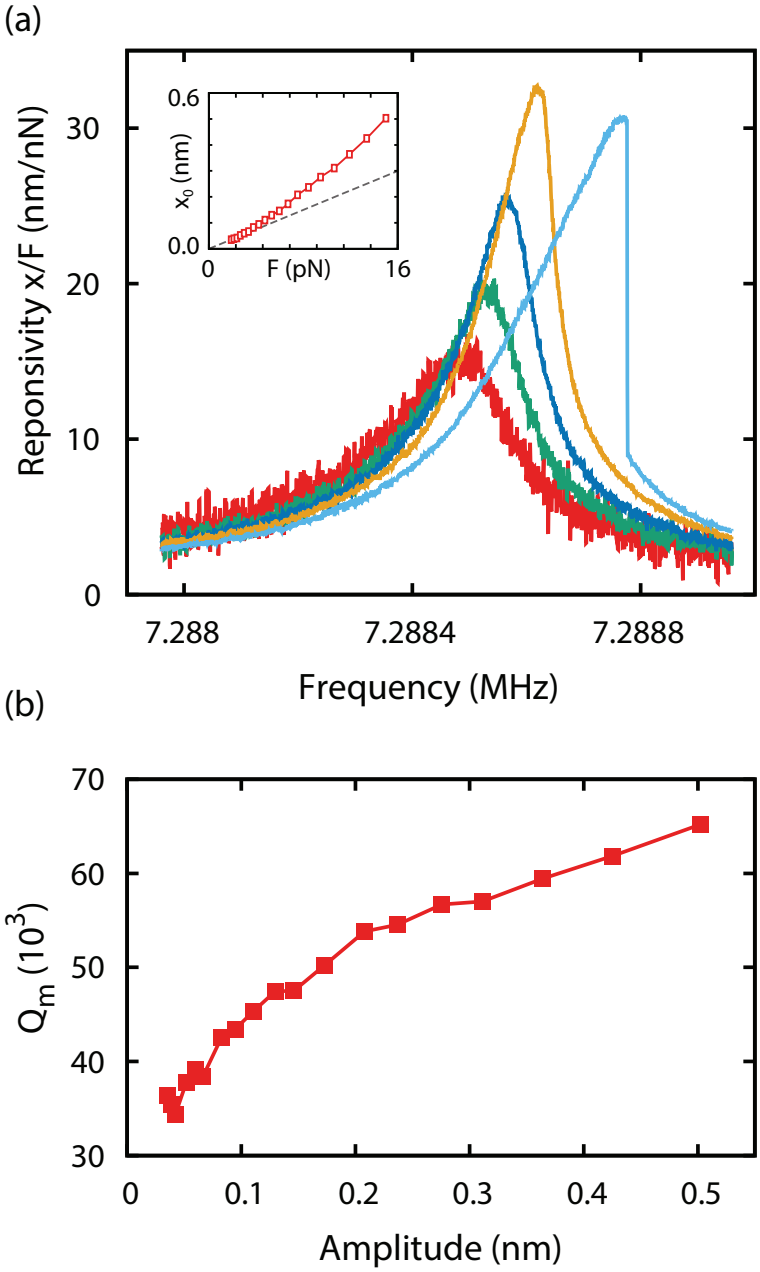

Figure 4.4: Negative nonlinear damping of a superconducting metal drum. Mechanical responsivity or normalized amplitude (x_0/F_0) of the drum for different driving forces (Red - light blue: 2.9, 5.8, 11.2, 29.3, 82.8 pN). As the driving force is increased (red-dark blue), the responsivity of the drum on resonance increases, indicating a increase in the mechanical quality-factor. As the drum is driven into the nonlinear regime (yellow), the Q_m continues to increase, and at higher powers, the Q_m in the nonlinear regime begins to drop, as can be seen by the decreased responsivity of the light blue curve. In the linear regime, Q_m is extracted by fitting the curves with a Lorentzian curve with a Fano correction. b) Mechanical quality-factor as a function of mechanical amplitudes. Actuation force is varied with different RF power on a signal generator for driving mechanics. Inset shows the plot of mechanical amplitude x_0 (red squares) for different driving forces, clearly showing a deviation from the linear fit (dotted line). A 3 dB uncertainty in power reaching at the sample results in 25% uncertainty in the estimation of mechanical amplitude.

Supplementary material See supplementary material for device fabrication steps, cavity characterization, measurement setup and estimation of the mechanical amplitude.

Acknowledgments The work was supported by the Dutch Science Foundation (NWO/FOM).

REFERENCES

[1] Ekinci, K. L. and Roukes, M. L. *Review of Scientific Instruments* **76**(6), 061101 June (2005).

[2] Aspelmeyer, M., Kippenberg, T. J., and Marquardt, F. *Reviews of Modern Physics* **86**(4), 1391–1452 December (2014).

[3] Metcalfe, M. *Applied Physics Reviews* **1**(3), 031105 September (2014).

[4] Teufel, J. D., Donner, T., Li, D., Harlow, J. W., Allman, M. S., Cicak, K., Sirois, A. J., Whittaker, J. D., Lehnert, K. W., and Simmonds, R. W. *Nature* **475**(7356), 359–363 July (2011).

[5] Chan, J., Alegre, T. P. M., Safavi-Naeini, A. H., Hill, J. T., Krause, A., Gröblacher, S., Aspelmeyer, M., and Painter, O. *Nature* **478**(7367), 89–92 October (2011).

[6] Andrews, R. W., Peterson, R. W., Purdy, T. P., Cicak, K., Simmonds, R. W., Regal, C. A., and Lehnert, K. W. *Nature Physics* **10**(4), 321–326 April (2014).

[7] Bochmann, J., Vainsencher, A., Awschalom, D. D., and Cleland, A. N. *Nature Physics* **9**(11), 712–716 November (2013).

[8] Andrews, R. W., Reed, A. P., Cicak, K., Teufel, J. D., and Lehnert, K. W. *Nature Communications* **6**, 10021 November (2015).

[9] Lecocq, F., Clark, J. B., Simmonds, R. W., Aumentado, J., and Teufel, J. D. *arXiv:1512.00078 [quant-ph]* November (2015). arXiv: 1512.00078.

[10] Teufel, J. D., Li, D., Allman, M. S., Cicak, K., Sirois, A. J., Whittaker, J. D., and Simmonds, R. W. *Nature* **471**(7337), 204–208 March (2011).

[11] Suh, J., Shaw, M. D., LeDuc, H. G., Weinstein, A. J., and Schwab, K. C. *Nano Letters* **12**(12), 6260–6265 December (2012).

[12] Wollman, E. E., Lei, C. U., Weinstein, A. J., Suh, J., Kronwald, A., Marquardt, F., Clerk, A. A., and Schwab, K. C. *Science* **349**(6251), 952–955 August (2015).

[13] Pirkkalainen, J.-M., Damskagg, E., Brandt, M., Massel, F., and Sillanpaa, M. *Physical Review Letters* **115**(24), 243601 December (2015).

[14] Anderson, P. w., Halperin, B. I., and Varma, c. M. *Philosophical Magazine* **25**(1), 1–9 January (1972).

[15] Phillips, W. A. *Reports on Progress in Physics* **50**(12), 1657 December (1987).

[16] Raychaudhuri, A. K. and Hunklinger, S. *Zeitschrift für Physik B Condensed Matter* **57**(2), 113–125 October (1984).

[17] Gao, J., Daal, M., Vayonakis, A., Kumar, S., Zmuidzinas, J., Sadoulet, B., Mazin, B. A., Day, P. K., and Leduc, H. G. *Applied Physics Letters* **92**(15), 152505 April (2008).

[18] Pappas, D. P., Vissers, M. R., Wisbey, D. S., Kline, J. S., and Gao, J. *IEEE Transactions on Applied Superconductivity* **21**(3), 871–874 June (2011).

[19] Leonhardt, T., Carlén, J.-C., Buck, M., Brinkman, C. R., Ren, W., and Stevens, C. O. In *AIP Conference Proceedings*, volume 458, 685–690. AIP Publishing, January (1999).

[20] Lerner, E., Daunt, J. G., and Maxwell, E. *Physical Review* **153**(2), 487–492 January (1967).

[21] Seleznev, V. A., Tarkhov, M. A., Voronov, B. M., Milostnaya, I. I., Lyakhno, V. Y., Garbuz, A. S., Mikhailov, M. Y., Zhigalina, O. M., and Gol'tsman, G. N. *Superconductor Science and Technology* **21**(11), 115006 November (2008).

[22] Sundar, S., Sharath Chandra, L. S., Sharma, V. K., Chattopadhyay, M. K., and Roy, S. B. *AIP Conference Proceedings* **1512**(1), 1092–1093 February (2013).

[23] Aziz, M., Hudson, D. C., and Russo, S. *Applied Physics Letters* **104**(23), 233102 June (2014).

[24] Yasaitis, J. and Rose, R. *IEEE Transactions on Magnetics* **11**(2), 434–436 March (1975).

[25] Singh, V., Schneider, B. H., Bosman, S. J., Merkx, E. P. J., and Steele, G. A. *Applied Physics Letters* **105**(22), 222601 December (2014).

[26] Kozinsky, I., Postma, H. W. C., Bargatin, I., and Roukes, M. L. *Applied Physics Letters* **88**(25), 253101 June (2006).

[27] Imboden, M. and Mohanty, P. *Physical Review B* **79**(12), 125424 March (2009).

[28] Hoehne, F., Pashkin, Y. A., Astafiev, O., Faoro, L., Ioffe, L. B., Nakamura, Y., and Tsai, J. S. *Physical Review B* **81**(18), 184112 May (2010).

[29] Venkatesan, A., Lulla, K. J., Patton, M. J., Armour, A. D., Mellor, C. J., and Owers-Bradley, J. R. *Physical Review B* **81**(7), 073410 February (2010).

[30] Imboden, M. and Mohanty, P. *Physics Reports* **534**(3), 89–146 January (2014).

[31] Esquinazi, P., editor. *Tunneling Systems in Amorphous and Crystalline Solids*. Springer Berlin Heidelberg, Berlin, Heidelberg, (1998).

[32] Esquinazi, P., Ritter, H. M., Neckel, H., Weiss, G., and Hunklinger, S. *Zeitschrift für Physik B Condensed Matter* **64**(1), 81–93 March (1986).

[33] Singh, V., Shevchuk, O., Blanter, Y. M., and Steele, G. A. *arXiv:1508.04298 [cond-mat]* August (2015). arXiv: 1508.04298.

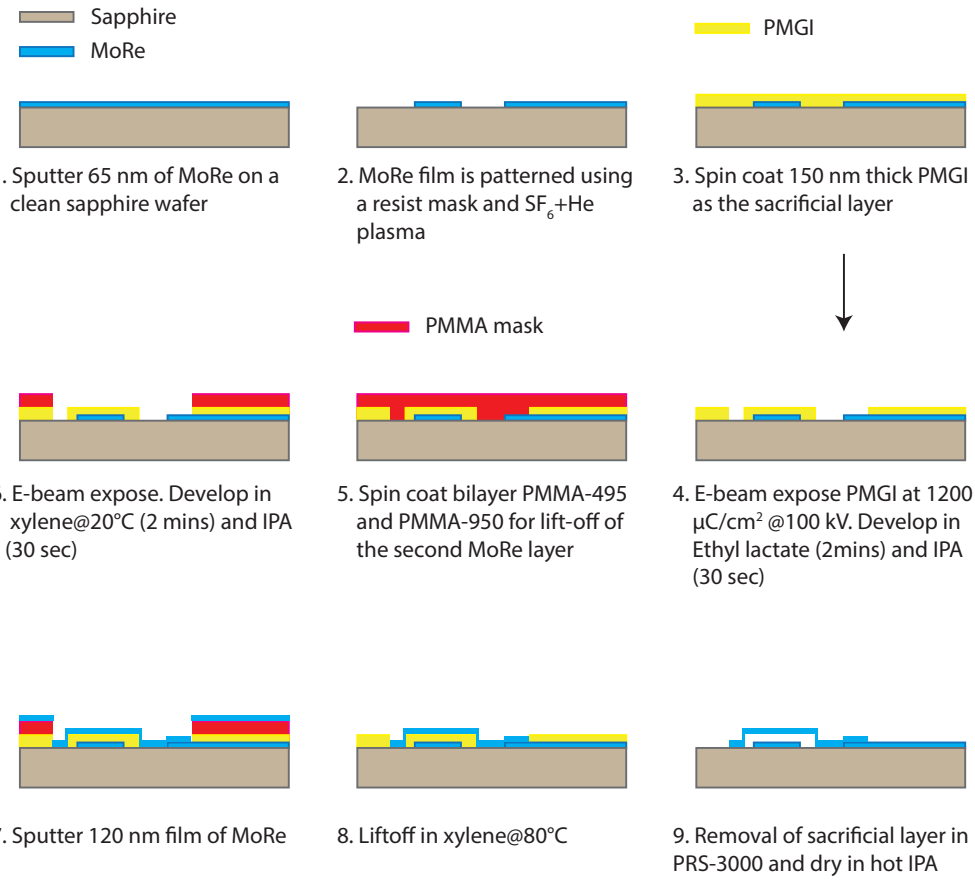

Figure 4.5: An illustration of complete fabrication process with brief outline.

4.1. SUPPLEMENTARY MATERIAL

4.1.1. FABRICATION DETAILS

The fabrication process is mainly based on using PMGI as the sacrificial layer together with its compatibility with PMMA based resist. Steps of the fabrication process are illustrated in Fig. 4.5.

4.1.2. CHARACTERIZATION OF THE CAVITY

For a single port cavity, the reflection coefficient S_{11} is given by,

$$|S_{11}|(\omega) = \left|1 - \frac{\kappa_e}{i(\omega - \omega_c) + (\kappa_i + \kappa_e)/2}\right| \tag{4.1}$$

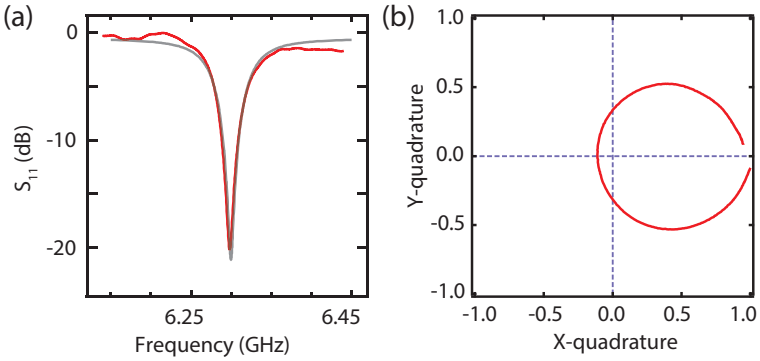

Figure 4.6: (a) Measurement of the normalized reflection coefficient S_{11} of the cavity at base temperature (red curve). The gray curve is the fit to the data yielding an internal dissipation rate $\kappa_i = 2\pi \times 25.8$ MHz $\kappa_i/2\pi = 25.8 \times 10^6$ s^{-1} and an external coupling rate $\kappa_e = 2\pi \times 31.0$ MHz$\kappa_e/2\pi = 31.0 \times 10^6$ s^{-1}. (b) Two quadratures of S_{11} plotted against each other, reflecting the over-coupled behavior of the cavity.

where κ_e is the external coupling rate, κ_i is the internal dissipation rate, and ω_c is the cavity resonance frequency. Fig. 4.6(a) shows the measurement of S_{11} at $T = 14$ mK. The gray curve in Fig. 4.6(a) is the numerically fitted curve using equation 1. To differentiate between over-coupling ($\kappa_e > \kappa_i$) and under-coupling ($\kappa_i > \kappa_e$) limits, one must measure the phase arg($S_{11}(\omega)$) of the reflection coefficient. Equivalently, one can also parametrically plot two quadratures X =Re(S_{11}) and Y =Im(S_{11}) against each other. For an overcoupled cavity the resonance circle appears to enclose the origin as shown in Fig 4.6(b).

4.1.3. HOMODYNE DETECTION SCHEME

To detect the mechanical motion, we use the superconducting microwave cavity in a homodyne detection setup. The mechanical resonator is actuated by capacitive forces by adding a radio-frequency signal V_{AC} (near the mechanical resonance frequency) and a DC voltage V_{DC} to the feedline (using a bias-tee at low temperature). Due to electrostatic force, the mechanical resonator experiences a modulating force of magnitude given by $\frac{dC_c}{dx} V_{DC} V_{AC}$, where C_c is the capacitance between the mechanical resonator and the feedline electrode.

To detect the mechanical motion, we use the cavity as an interferometer. The cavity is driven by a signal at its resonance frequency ω_c acting as the carrier signal. The motion of the mechanical resonator (at frequency ω_m) modulates this signal and produces mechanical sidebands at frequencies $\omega_c \pm \omega_m$. The sideband signal along with the carrier is amplified by a low noise amplifier and then passed through a high-pass filter (3 GHz-9 GHz) before entering the second amplifier at room temperature. The amplified signal is then mixed down to RF frequencies by using a mixer (MiniCircuits-ZMX8GH+). To avoid any phase drifts, we have used the same source to drive the

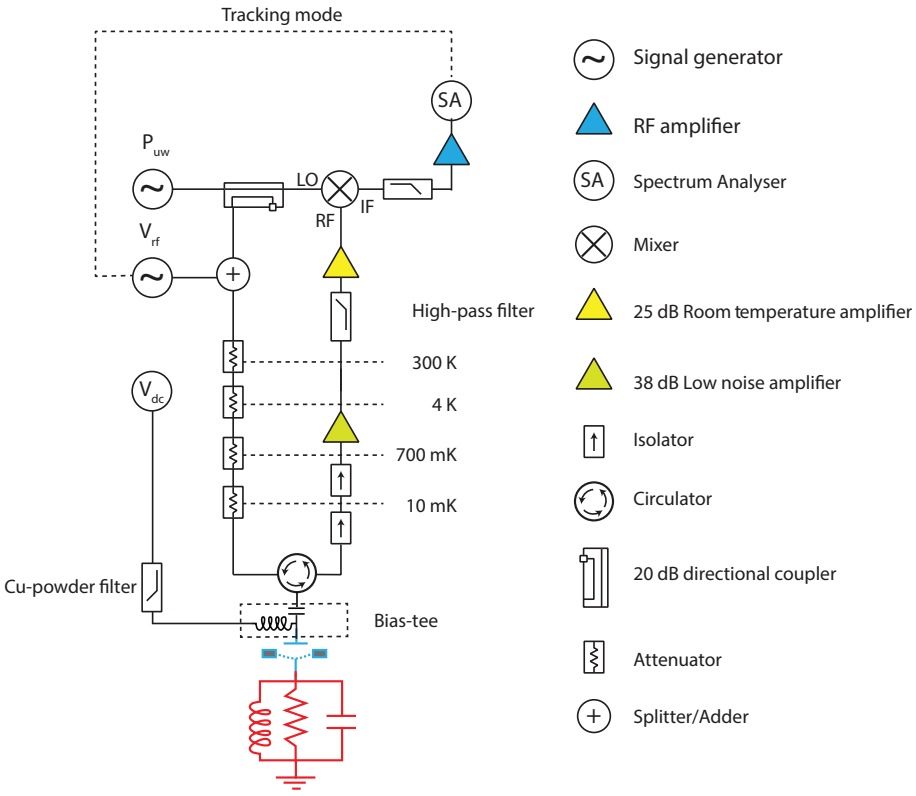

Figure 4.7: Schematic diagram of the homodyne detection setup.

local oscillator (LO) port of the mixer. The mixed-down RF signal is filtered and amplified further before entering the spectrum analyzer. The spectrum analyzer is used in tracking mode with the signal generator used to mechanically drive the resonator, thus allowing to record the response as function of actuation frequency. A complete schematic of the measurement scheme is shown in Fig. 4.7.

It should be noted that AC signals which are applied through the high frequency coaxial lines are attenuated at different temperature stages for thermalization. The DC signal however is applied through a separate low resistance DC line and added to AC signals at the mK stage, and therefore it does not get attenuated.

4.1.4. FITTING THE ASYMMETRIC RESPONSE WITH FANO-FUNCTION

Due to finite isolation of the circulator for low frequency RF signals (used for mechanical driving), part of the RF signal leaks directly into the output measurement chain, producing frequency independent constant background signal in the measurement.

This background signal interferes with the signal generated due to the mechanical motion of the resonator, giving a Fano-lineshape in the measured data. Taking this background signal into account, the measured response can be fitted to the following Fano-form, also known as skewed-Lorentzian

$$\tilde{V}_{measured} = \frac{V_0}{1 - 2iQ_m \frac{f - f_m}{f_m}} + \alpha e^{i\phi} \tag{4.2}$$

where f_m is the mechanical resonant frequency, Q_m is the mechanical quality-factor, $\alpha e^{i\phi}$ is a small background signal with amplitude α and phase ϕ.

4.1.5. MODEL FOR THE ESTIMATION OF THE MECHANICAL AMPLITUDE

The combined effect of charging the transmission line and applying an AC-voltage leads to a force on the drum given by:

$$F = \frac{1}{2}\frac{dC}{dx}V^2 = \frac{1}{2}\frac{dC}{dx}(V_{DC} + V_{AC}\cos(\omega t))^2 = \frac{1}{2}\frac{dC}{dx}(V_{DC}^2 + 2V_{DC}V_{AC}\cos(\omega t) + V_{AC}^2\cos^2(\omega t)) \tag{4.3}$$

The first term V_{DC}^2 is a constant force which will attract the drum, increasing the stress of its membrane and thus lowering its frequency quadratically. The last term V_{AC}^2 can be neglected. The second term in the above equation least to an AC force that oscillates at frequency ω with a magnitude given by F_{AC}. By assuming the capacitance of the drum to the transmission line to be that of a vacuum-gap, parallel plate capacitor, we can write:

$$F_{AC} = V_{AC}V_{DC}\frac{d}{dx}\left(\frac{\epsilon_0 A}{\bar{d} + x}\right) \tag{4.4}$$

Where ϵ_0 is the permittivity of vacuum, A is the area of the capacitive plates, $\bar{d}$ is the gap between the plates after having taken into account the constant displacement induced by the gate voltage. x is the vertical displacement from this equilibrium position and is taken as a small quantity $x \ll \bar{d}$ resulting in the expression for the AC drive:

$$F_{AC} = -V_{AC}V_{DC}\left(\frac{\epsilon_0 A}{\bar{d}^2}\right) \tag{4.5}$$

Assuming the drum behaves as a damped harmonic oscillator with an effective mass m, eigen frequency ω_m and quality factor Q_m, the amplitude of the mechanical oscillations can be related to the strength of the (resonant) drive:

$$x_0 = \frac{F_{AC}Q_m}{m\omega_m^2} \tag{4.6}$$

In this analysis the effective mass is taken to be the total mass of the drum (this choice defines the amplitude x_0 which is otherwise ambiguous due to the geometry of the drum). We calculate the amplitude of the AC-voltage from the input power at the device P_{DUT}

$$V_{AC} = \sqrt{2Z_0 P_{DUT}} \tag{4.7}$$

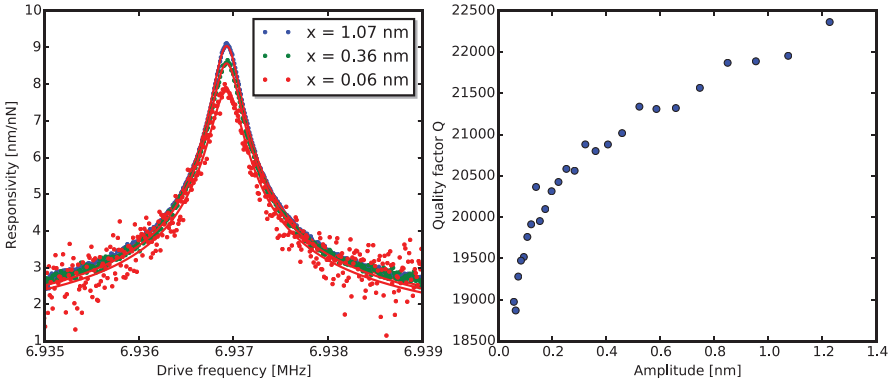

Figure 4.8: Mechanical response and mechanical quality factor as a function of power

where $Z_0 = 50\ \Omega$ is the characteristic impedance of our line. This power can be calculated from the output power of our signal generator and an estimation of the attenuation on the input measurement chain. The following steps are then taken:

- We convert the input power at our signal generator to the force acting upon the drum using S4.7 and S4.5
- We associate the peak measured power P_0 with the amplitude mechanical oscillation x_0 using S4.6
- We convert the power received off-resonance P to a mechanical amplitude $x = x_0\sqrt{P/P_0}$

Alternatively, one could also use the measured homodyne signal to work out the amplitude of the mechanical resonator under a coherent drive. For a single port cavity driven at its resonant frequency ($\Delta = 0$), amplitude of the drumhead resonator can be written as, $x_P^2 = \frac{\omega_m^2+\kappa^2/4}{(\eta G)^2}\frac{P_o}{P_i}$, where G is the cavity pull-in parameter, $\eta = \kappa_e/\kappa$ is the coupling fraction, P_o is the homodyne power (after removing gain, loss of the output chain, and conversion loss of the mixer), and P_i is the injected power outside the cavity.

4.1.6. ADDITIONAL DATA FROM SECOND DEVICE

Additional data from second device showing the nonlinear damping of the mechanical resonator is shown in Fig. 4.8.

4.1.7. ESTIMATION OF THE GAP BETWEEN THE DRUM AND THE BOTTOM ELECTRODE

The gap between the drum and the bottom electrode can be estimated from the total inductance of the high impedance resonator. The total inductance of the microstrip resonator is estimated to be 3.43 nH using finite element modeling and considering kinetic inductance of Mo-Re. Total capacitance is calculated from geometric inductance and the cavity frequency. Coupling quality factor in single port cavity is given as,

$$Q_{ext} = \frac{C_l + C_c}{\omega_c C_c^2 Z_0} \tag{4.8}$$

where C_c is coupling capacitance, ω_c is resonance frequency of the cavity, Z_0 is input impedance of transmission line, and C_l is lumped capacitance of the resonator line. From the parameters of cavity characterization, coupling capacitance is 21.5 fF. Assuming a parallel plate capacitor model, we found the mean position of the drum head resonator $\bar{d}$ to be 291 nm for the device represented in Fig. 4.4 of main text.

Alternatively, one can perform opto-mechanically induced absorbtion (OMIA) [1] leading to a measurement of the cooperativity $C = 4g^2/\kappa\Gamma$ where κ is the cavity line-width, Γ the mechanical line-width and $g = G\sqrt{n_d}\sqrt{\hbar/2m\omega_m}$ is the opto-mechanical coupling strength where the average number of photons in the cavity n_d in that particular measurement is calculated from our estimation of the input attenuation. OMIA thus provides a measure of the cavity pull-in parameter $G = d\omega_c/dx$ =8.53×10^{14} Hz/m. For a $\lambda/4$ resonator, the pull-in parameter assuming a parrallel plate capacitor is given by:

$$G = \frac{2Z_0\omega_r^2}{\pi}\frac{\epsilon A}{\bar{d}^2} \tag{4.9}$$

from this we estimate the mean position of the drum head resonator $\bar{d}$ to 481 nm for the device represented in Fig. S4 of the supplementary materials.

4.1.8. PARAMETERS FOR THE DEVICES SHOWN IN THE MAIN TEXT (DEVICE 1) AND IN SUPPLEMENTAL MATERIALS (DEVICE 2)

4.1.9. COMPARISON OF POWER DEPENDENCE OF MECHANICAL AT LOW AND HIGH TEMPERATURE

Fig. 4.9 shows the measurements of the responsivity (normalized amplitude) at 23 mK and 1.5 K. By comparing the measurements with low and high driving powers, amplitude dependent damping is clearly visible at low temperature, and is not apparent at high temperatures.

Table 4.1: Important parameters of the devices

Parameters	**Device 1**	**Device 2**
Density of MoRe	14.5 g/cm^3	14.5 g/cm^3
Diameter of drum	30 μm	30 μm
Gap between the drumhead and the feedline	291 nm	481 nm
Thickness of the mechanical resonator	125 nm	131 nm
Equivalent lumped inductance of the cavity	3.43 nH	2.37 nH
Drumhead capacitance	21.5 fF	12.6 fF
Cavity pull-in parameter $\frac{G}{2\pi}$	1.2×10^{15} Hz/m	8.53×10^{14} Hz/m
Total attenuation on low frequency drive line	65 dB	55 dB

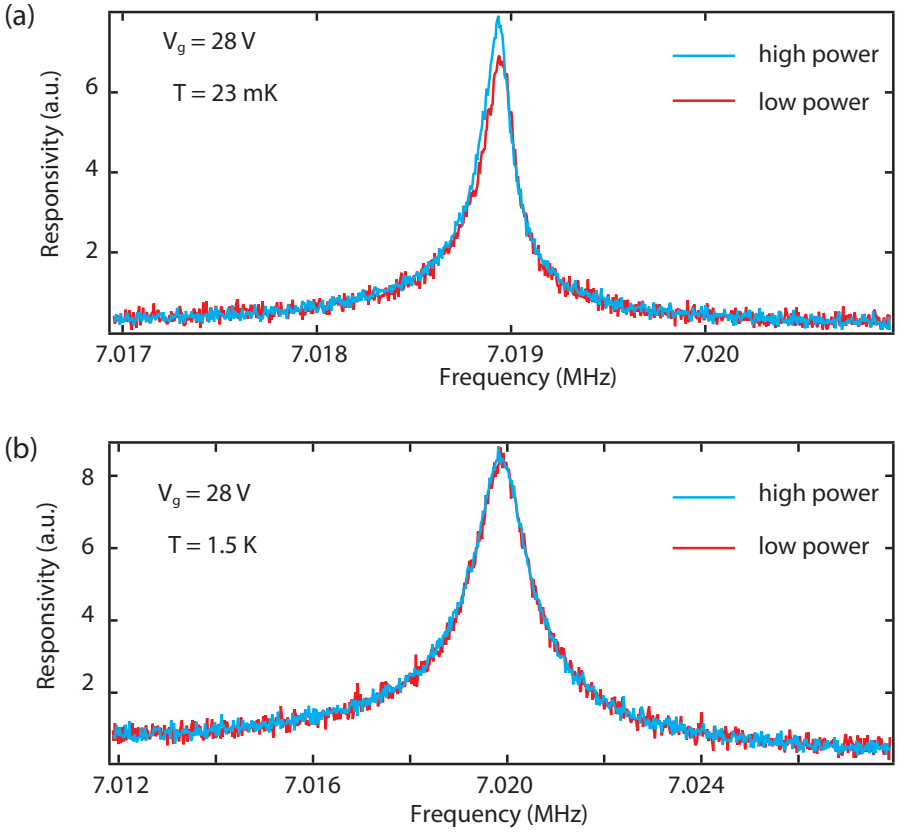

Figure 4.9: (a, b) Comparison of responsivity (normalized amplitude) at 23 mK and 1.5 K. The cyan and red curves are measurements with high and low driving powers, respectively.

4.1.10. NORMALIZED AMPLITUDE IN PRESENCE OF THE NONLINEAR DAMPING TERM:

In this section, we consider the modification to the response of a mechanical resonator by taking Duffing and nonlinear-damping terms. In presence of the Duffing αx^3 and nonlinear damping term $\eta x^2 \dot{x}$, the equation of motion under a harmonic drive can be expressed as,

$$m\ddot{x} + m\gamma_m \dot{x} + kx + \alpha x^3 + \eta x^2 \dot{x} = G_0 \cos\omega t. \tag{4.10}$$

Using a perturbative expansion approach, a closed form of the mechanical amplitude can be given by,

$$x^2 = \frac{(G_0/2k)^2}{(\frac{\omega-\omega_m}{\omega_m} - \frac{3}{8}\frac{\alpha x^2}{k})^2 + (\frac{\gamma_m}{2\omega_m} + \frac{1}{8}\frac{\eta\omega_m}{k}x^2)^2}. \tag{4.11}$$

In Fig. 4.10, we have plotted the solution to above equation for different values of parameters. Panel (a) shows the plot of normalized amplitude for $\eta = 0$. As one can see that as the driving force on the resonator is increased the maximum peak amplitude does not change and remains constant as expected since Duffing term (αx^3) only leads to the modification of the spring constant.

In the presence of the nonlinear damping term ($\eta x^2 \dot{x}$, with $\eta > 0$), however, the normalized amplitude decreases due to additional damping as driving force on the resonator is increased as shown in panel (b).

For a negative nonlinear damping term ($\eta x^2 \dot{x}$, with $\eta < 0$), we observe an opposite behavior where normalized amplitude increases as the driving force is increased as shown in panel (c)

REFERENCES

[1] Singh, V., Bosman, S. J., Schneider, B. H., Blanter, Y. M.,Castellanos-Gomez, A., and Steele, G. A *Nature Nanotechnology* **9**(10), 820-824 Agust (2014).

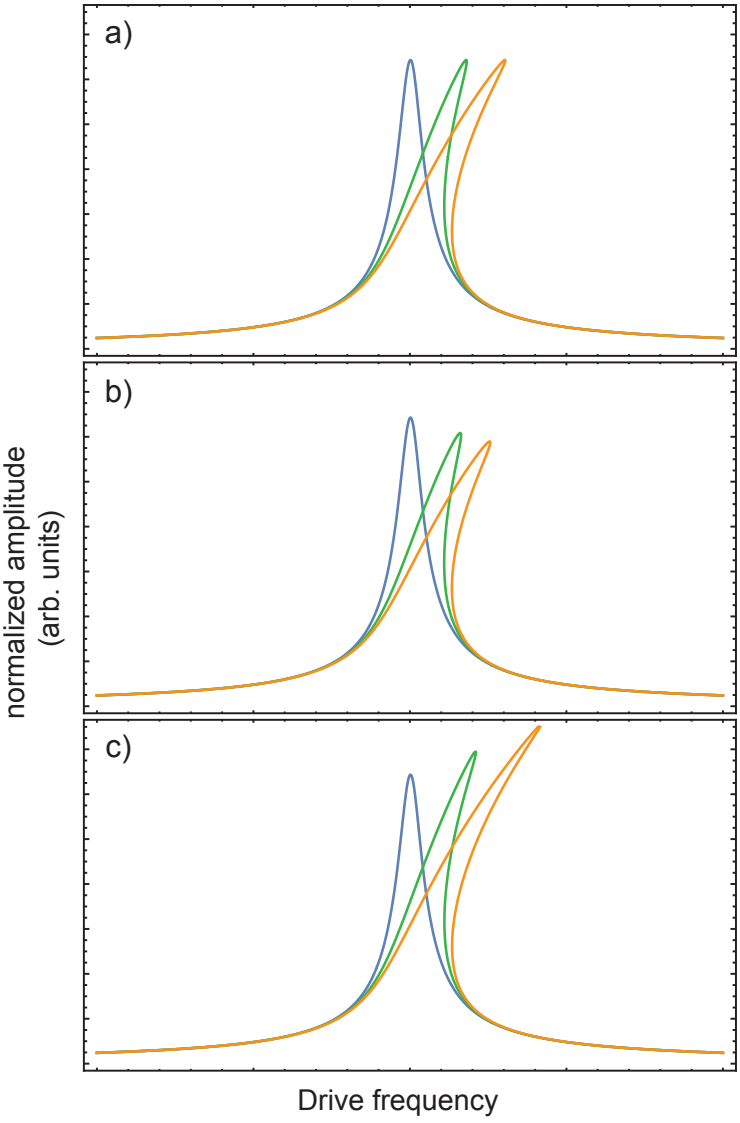

Figure 4.10: Plots of normalized amplitude for different driving forces. Panel a, b, and c show the normalized amplitude with $\eta = 0$, $\eta > 0$ and $\eta < 0$. For these plots we have taken $\alpha > 0$

5

A MICROWAVE OPTOMECHANICAL CIRCUIT WITH PARAMETRIC MECHANICAL DRIVING

Microwave optomechanical circuits have been demonstrated in the past years to be powerfool tools for both, exploring fundamental physics of macroscopic and massive quantum objects as well as being promising candidates for novel on-chip quantum limited microwave devices. In this work, we explore a microwave optomechanical device consisting of a coplanar microwave cavity coupled to a mechanical high quality factor nanobeam resonator. By design, we have direct access to the mechanical subsystem, which allows for frequency tuning, coherent driving and parametric modulation of the nanobeam resonance frequency. We experimentally explore and theoretically model phase-sensitive parametric mechanical amplitude amplification and thermomechanical noise squeezing and detect both effects by an optomechanical readout scheme. Finally, we demonstrate that the amplification of the mechanical amplitude by parametric frequency modulation can be used to build a novel type of phase-sensitive microwave amplifier. In contrast to the common microwave amplification scheme in optomechanical circuits by driving the cavity on the blue sideband, our technique allows for simultaneous cooling of the mechanical element and in principle is quantum-limited.

5.1. INTRODUCTION

Superconducting microwave circuits have been demonstrated to be extremely powerful tools for the fields of quantum information processing [1–3], circuit quantum electrodynamics [4–7], astrophysical detector technologies [8] and microwave optomechanics [9–12]. In the latter, microwave fields in superconducting microwave cavities are parametrically coupled to mechanical elements such as suspended capacitor drumheads or metallized nanobeams, enabling high-precision detection and manipulation of mechanical motion. Milestones achieved in the field include microwave sideband-cooling of mechanical oscillators to the quantum ground state [13] and others. Recently, there are increasing efforts taken towards building passive and active quantum limited microwave elements for quantum technologies based on microwave optomechanical circuits, connecting the fields of microwave optomechanics, circuit quantum electrodynamics and quantum information science. Among the most important developments into this direction are the demonstration of microwave amplification by blue sideband driving in simple optomechanical circuits [14], and the realization of directional microwave amplifiers [15] as well as microwave circulators [16] in more complex multimode systems.

Here, we present a superconducting microwave optomechanical device which per design allows for direct static and low frequency manipulation of the mechanical subsystem. This approach allows for the investigation of a class of phenomena not observable in the most common approaches for optomechanical circuits, where a manipulation of the mechanical element is only possible via the radiation pressure force of the cavity fields. By modulating the mechanical resonance frequency, we generate parametric amplitude amplification and thermomechanical noise squeezing of the mechanical motion, both detected by means of optomechanical sideband generation.

Finally, we demonstrate how a parametric modulation of the mechanical resonance frequency can be used to generate phase-sensitive amplification of a microwave probe tone, which is about three orders of magnitude larger in frequency than the parametric pump tone itself. Our results constitute an experimentally unexplored approach for building an integrated and quantum-limited, phase-sensitive microwave amplifier, which recently has been investigated theoretically [17].

5.2. RESULTS

5.2.1. THE DEVICE

We use a superconducting coplanar waveguide (CPW) quarter-wavelength ($\lambda/4$) resonator as cavity, cf. Fig. 5.1. The cavity is patterned from a $\sim 60\,\mathrm{nm}$ thick film of 60/40 molybdenum-rhenium alloy (MoRe, superconducting transition temperature $T_c \sim 9\,\mathrm{K}$ [11]) on a $10 \times 10\,\mathrm{mm}^2$ and $500\,\mu\mathrm{m}$ thick high-resistivity silicon substrate. For driving and readout, the cavity is capacitively side-coupled to a transmission feedline by means of a coupling capacitance $C_c = 16\,\mathrm{fF}$. The cavity has a fundamental

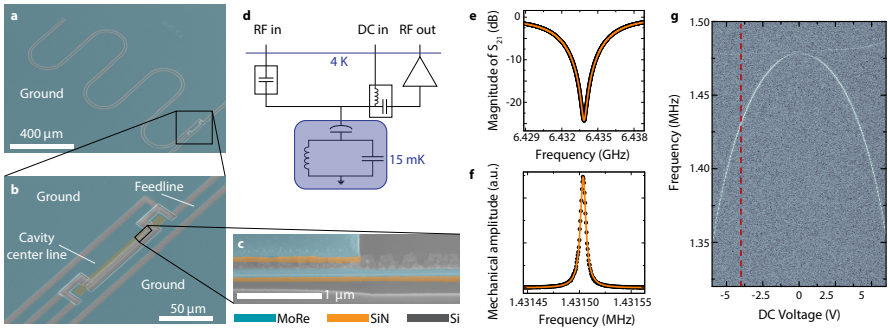

Figure 5.1: **Superconducting circuit nano-electromechanical system with DC and low-frequency access to the mechanical nanobeam.** **a**, False-color scanning electron microscopy image of a superconducting quarter-wavelength cavity (here for $\omega_c = 2\pi \cdot 7.5\,\mathrm{GHz}$), capacitively side-coupled to a coplanar waveguide feedline. The molybdenum-rhenium (MoRe) metallization is shown in blue and the silicon (Si) substrate in gray. **b**, Zoom into the coupling capacitance region, where the mechanical nanobeam as part of the coupling capacitance is visible. The dimensions of the beam, which consists of MoRe on top of high-stress silicon-nitride (Si_3N_4), are $100\,\mu\mathrm{m} \times 150\,\mathrm{nm} \times 143\,\mathrm{nm}$. **c**, A magnified view of the suspended nanobeam. **d**, Simplified circuit and measurement scheme, showing a lumped element circuit representation of the device as well as the microwave input and output lines (including a DC block and high electron mobility transistor amplifier shown as triangle) and the DC input line connected to the microwave lines via a bias-tee. A more detailed version of the set-up is given in the Supplementary Information. **e**, Cavity resonance data (black) and fit curve (orange). From the fit, we extract the cavity resonance frequency $\omega_c = 2\pi \cdot 6.434\,\mathrm{GHz}$ and the internal and external linewidths $\kappa_i = 2\pi \cdot 370\,\mathrm{kHz}$ and $\kappa_e = 2\pi \cdot 5.7\,\mathrm{MHz}$, respectively. **f**, Resonance curve of the mechanical oscillator read-out via the superconducting cavity. Data are shown as black dots, a Lorentzian fit as orange line. From the fit we extract the mechanical resonance frequency $\Omega_m = 2\pi \cdot 1.4325\,\mathrm{MHz}$ and a quality factor $Q_m = 190000$. **g**, Optomechanically detected excitation spectrum of the nanobeam vs applied DC voltage. The bright line resembling an inverted parabola represents the resonance of the in-plane mode, which was used everywhere throughout this paper. The red dashed line at $V_{\mathrm{dc}} = -4\,\mathrm{V}$ indicates the voltage operation point we chose to use.

mode resonance frequency $\omega_c = 2\pi \cdot 6.434\,\mathrm{GHz}$ and internal and external linewidths $\kappa_i = 2\pi \cdot 370\,\mathrm{kHz}$ and $\kappa_e = 2\pi \cdot 5.7\,\mathrm{MHz}$, respectively. The transmission spectrum of the cavity around its resonance frequency is shown in Fig. 5.1**e**.

The superconducting cavity is parametrically coupled to a MoRe-coated high-stress Si_3N_4 nanobeam, which is electrically integrated into the transmission feedline. The nanobeam has a width $w = 150\,\mathrm{nm}$, a total thickness $t = 143\,\mathrm{nm}$ (of which $\sim 83\,\mathrm{nm}$ are Si_3N_4 and 60 nm are MoRe) and a length $r = 100\,\mu\mathrm{m}$. It is separated from the center conductor of the cavity by a $\sim 200\,\mathrm{nm}$ wide gap, cf. Fig. 5.1**c**. More design and fabrication details are described in the Supplementary Material.

The mechanical nanobeam oscillator of our device has a resonance frequency of its fundamental in-plane mode of $\Omega_{m0} = 2\pi \cdot 1.475\,\mathrm{MHz}$. The resonance frequency can be significantly tuned by applying a DC voltage V_{dc} between center conductor and ground of the coplanar waveguide feedline, adding an electrostatic spring con-

stant to the intrinsic spring. The measured functional dependence of the resonance frequency on DC voltage is shown in Fig. 5.1**g**. Throughout this whole article, we bias the mechanical resonator with $V_{\mathrm{dc}} = -4\,\mathrm{V}$, leading to a resonance frequency $\Omega_m = 2\pi \cdot 1.4325\,\mathrm{MHz}$ and a linewidth $\Gamma_m \approx 2\pi \cdot 7.5\,\mathrm{Hz}$. A resonance curve of the mechanical oscillator at $V_{\mathrm{dc}} = -4\,\mathrm{V}$ is shown in Fig. 5.1**f**.

The device is operated in a dilution refrigerator with a base temperature of $T_b = 15\,\mathrm{mK}$, which leaves the thermal excitations of the cavity insignificant, as $\hbar\omega_c/k_B \sim 310\,\mathrm{mK}$, where $\hbar = 1.055 \cdot 10^{-34}\,\mathrm{Js}$ is the reduced Planck constant and $k_B = 1.381 \cdot 10^{-23}\,\mathrm{J/K}$ is the Boltzmann constant. Assuming the mode temperature of the nanobeam being the fridge base temperature, we expect an average occupation of the mechanical mode with $n_m = k_{\mathrm{B}} T_m/\hbar\Omega_m \sim 220$ thermal phonons. We estimate, however, that the real mechanical mode temperature is approximately one order of magnitude higher than the base temperature, i.e., $T_m \sim 150\,\mathrm{mK}$, which corresponds to an average mode occupation with ~ 2200 phonons.

5.2.2. PARAMETRIC MECHANICAL AMPLITUDE AMPLIFICATION

When the resonance frequency Ω_m of a harmonic oscillator is modulated with twice the resonance frequency $\Omega_p = 2\Omega_m$, then a small starting amplitude of the oscillator motion can be increased or reduced, depending on the relative phase between the oscillator motion and the frequency modulation [19]. To modulate the resonance frequency of a mechanical oscillator, one of the relevant system parameters like the oscillator mass m or the restoring spring force constant k can be modulated. Here, we follow the latter approach and modulate the effective spring constant of the nanobeam by applying a combination of a static voltage V_{dc} and an oscillating voltage $V_{2\Omega} \cdot \sin 2\Omega t$ with roughly twice the mechanical resonance frequency $\Omega \sim \Omega_m$. The static voltage adds an electrostatic spring contribution k_{dc} to the intrinsic spring constant k_m and the oscillating part modulates the total spring constant with $\sim 2\Omega_m$. In addition, we slightly excite the mechanical oscillator by adding a near-resonant oscillating voltage $V_0 \cos(\Omega t + \phi_p)$ and characterize its steady-state displacement amplitude depending on the parametric modulation amplitude $V_{2\Omega}$ and on the relative phase difference between resonant drive and parametric modulation ϕ_p. The mechanical amplitude is detected by monitoring the optomechanically generated sidebands to a microwave drive tone sent into the cavity, which is constant in amplitude and frequency with $\omega \sim \omega_c$, cf. Fig. 5.2**a**.

As discussed in detail in the Supplementary Material, we operate the nanobeam in a regime of voltages where it can be modelled by the equation of motion

$$\ddot{x} + \Gamma_m \dot{x} + \frac{1}{m}\left[k_0 + k_p \sin 2\Omega t\right] x = \frac{F_0}{m}\cos\left(\Omega t + \phi_p\right) \tag{5.1}$$

where m is the effective nanowire mass, x is the effective nanowire displacement, $k_0 = k_m + k_{\mathrm{dc}}$, $k_p \propto V_{\mathrm{dc}} V_{2\Omega}$ and $F_0 \propto V_{\mathrm{dc}} V_0$. From an approximate solution of this equation of motion, the parametric amplitude gain $G_p = |x|_{\mathrm{on}}/|x|_{\mathrm{off}}$ can be derived to be given by (for details see Supplementary Material)

$$G_p = \left[\frac{\cos^2(\phi_p + \varphi)}{\left(1 + \frac{V_{2\Omega}}{V_t}\right)^2} + \frac{\sin^2(\phi_p + \varphi)}{\left(1 - \frac{V_{2\Omega}}{V_t}\right)^2} \right]^{1/2} . \tag{5.2}$$

The detuning dependent threshold voltage V_t for parametric instability in this relation is given by

$$V_t = V_{t0}\sqrt{1 + \frac{4\Delta_m^2}{\Gamma_m^2}} \tag{5.3}$$

with the threshold voltage on resonance V_{t0} and the detuning from mechanical resonance $\Delta_m = \Omega - \Omega_m$. The phase $\varphi = -\arctan(2\Delta_m/\Gamma_m)$ considers the detuning dependent phase difference between the near-resonant driving force and the mechanical motion.

Figure 5.2 summarizes our results on the phase and detuning dependent parametric frequency modulation. When we excite the mechanical resonator exactly on resonance, apply a parametric modulation with twice the resonance frequency and sweep the phase ϕ_p, we find an oscillatory behaviour between amplitude amplification and de-amplification with a periodicity of $\Delta\phi_p = \pi$, cf. Fig. 5.2 **b**. To explore the dependence of the amplification on the parametric modulation amplitude $V_{2\Omega}$, we repeat this experiment for different voltages $V_{2\Omega}$ and extract maximum and minimum gain by fitting the data with Eq. (5.2) for $V_t = V_{t0}$ and $\varphi = 0$. The extracted values follow closely the theoretical curves up to a voltage $V_{2\Omega} \approx 0.9V_{t0}$, above which we are limited by resonance frequency fluctuations of the mechanical resonator. The maximum gain we achieve by this is about $\sim 22\,\mathrm{dB}$.

In order to characterize the device response also for drive frequencies detuned from resonance, we repeat the above measurements for different detunings and extract the maximum and minimum gain for each of these data sets. Hereby, we always keep the parametric drive frequency twice the excitation frequency and not twice the resonance frequency. The maximum and minimum values of gain we find for $V_{2\Omega} \approx 0.75V_{t0}$ are shown in Fig. 5.2 **d** and are in good agreement with theoretical curves shown as lines. We note, that the dependence of maximum and minimum gain of detuning is not Lorentzian lineshaped, as the threshold voltage is detuning dependent itself and the deviations between experimental data and theoretical lines mainly occurs due to slow and small resonance frequency drifts of the nanobeam. Moreover, the phase between near-resonant excitation drive and parametric modulation for maximum/minimum gain does not have a constant value, it follows an arctan-function as is discussed in more detail in the Supplementary Material.

In summary, we have achieved an excellent experimental control and theoretical modelling regarding the parametric amplification of the coherently driven nanobeam in both parameters, the relative phase between the drives and the detuning from mechanical resonance.

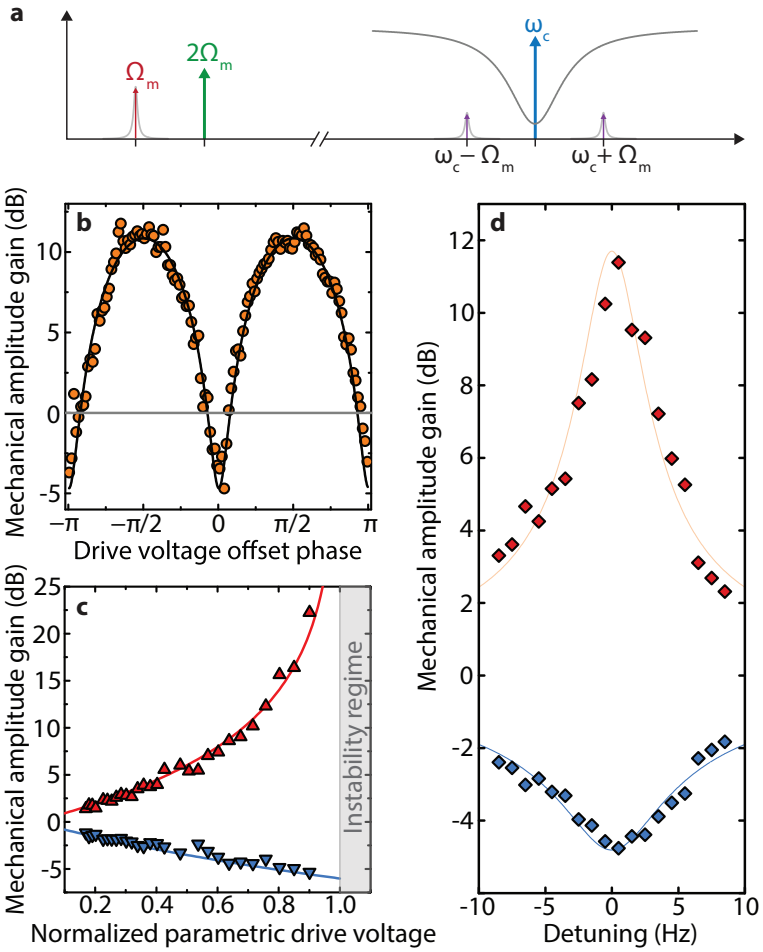

Figure 5.2: **Optomechanical detection of parametric, phase-sensitive mechanical amplitude amplification by means of modulating the electrostatic spring constant.** **a**, Experimental scheme. The mechanical oscillator is coherently driven by a combination of DC and alternating voltage with frequency $\Omega \sim \Omega_m$, while the electrostatic spring constant is modulated with twice this frequency $2\Omega \sim 2\Omega_m$. Via the optomechanical coupling, the mechanical oscillations generate sidebands to a microwave pump tone sent to the cavity with frequency $\omega = \omega_c$, which are used for detection of the mechanical amplitude. **b**, Mechanical amplitude gain vs offset phase ϕ_p between resonant drive and parametric modulation. When the phase is swept, the mechanical amplitude is oscillating between amplification or de-amplification with a periodicity of π. Circles show data and the line shows a fit with the theoretical expression Eq. (5.2). **c**, Maximum and minimum gain on resonance vs parametric modulation strength. The maximum ($\phi_p = \pi/2$) and minimum ($\phi_p = 0$) gain values on resonance follow the theoretical curves (lines) up to a maximum gain of ~ 22dB. For stronger parametric modulation amplitudes close to the instability threshold (indicated as vertical line), the gain in our experiments is limited by resonance frequency fluctuations of the mechanical resonator. **d**, Maximum and minimum gain vs detuning from resonance. For a driving frequency slightly detuned from resonance, the maximum gain gets reduced compared to the resonant case. Points are extracted from phase-sweep curve fits. Lines show the corresponding theoretical curves and the shaded area contains all gain values achievable by changing ϕ_p.

5.2.3. THERMOMECHANICAL NOISE SQUEEZING

As the nanobeam in our device is far away from being in the quantum ground state but occupied by $\sim 10^3$ thermal phonons, its displacement is subject to thermal fluctuations, which in a narrow bandwidth can be described by

$$x_{\mathrm{th}}(t) = X(t)\cos\Omega_m t + Y(t)\sin\Omega_m t. \tag{5.4}$$

Here, $X(t)$ and $Y(t)$ are random variable quadrature amplitudes, which vary slowly compared to Ω_m^{-1}. Similarly to the coherently driven mechanical amplitude detection discussed above, this thermal motion or thermomechanical noise can be measured by optomechanical sideband generation in the output field of a microwave signal sent into the superconducting cavity, cf. Fig. 5.3**a**.

We measure the thermomechanical noise quadratures $X(t)$ and $Y(t)$ with and without parametric pump. An exemplary result for the case without parametric pump is shown in Fig. 5.3**b**. As we have demonstrated above by amplification and de-amplification of a coherent excitation, one of the quadrature amplitudes, here $Y(t)$, is getting amplified while the other, here $X(t)$, is simultaneously reduced, when the mechanical resonance frequency is parametrically modulated with $2\Omega_m$. This puts the mechanical nanobeam into a squeezed thermal state. From the time traces of the quadratures, we reconstruct by a Fourier transformation the power spectral density of the noise as well as the quadrature amplitude noise histograms, shown in Figs. 5.3**c** and **d**, respectively. With parametric pumping, the total power spectral density is larger than without, as the additional energy pumped into the amplified quadrature $Y(t)$ is larger than the energy reduction in $X(t)$ and at the same time the total linewidth decreases for the same reason. In the histograms, Fig. 5.3**d**, the squeezing of the thermal noise is clearly visible as a deformation from a circular, two-dimensional (2D) Gaussian distribution in the case without parametric pump to a cigar-like shaped overall probability distribution, when the parametric modulation is applied. To determine the squeezing factor we achieve by this, we integrate the 2D-histrograms along the Y-quadrature and extract the variance $(\Delta X)^2$ from a Gaussian fit to the resulting data, cf. Fig. 5.3**e**. For the parametric modulation amplitudes used here, we find the squeezing factor

$$\sigma = [(\Delta X_{\mathrm{on}})^2 - \sigma_{\mathrm{amp}}^2]/[(\Delta X_{\mathrm{off}})^2 - \sigma_{\mathrm{amp}}^2] = 0.48 \tag{5.5}$$

, which is close to the maximally achievable value of $\sigma_{\mathrm{opt}} = 0.5$. More details about the measurement scheme and data processing can be found in the Supplementary Material.

5.2.4. PARAMETRIC MICROWAVE AMPLIFICATION

Finally, we use the above demonstrated control over the mechanical amplitude gain by parametric modulation to amplify a small microwave field injected into the cavity. In a cavity optomechanical system, the mechanical oscillator can not only be

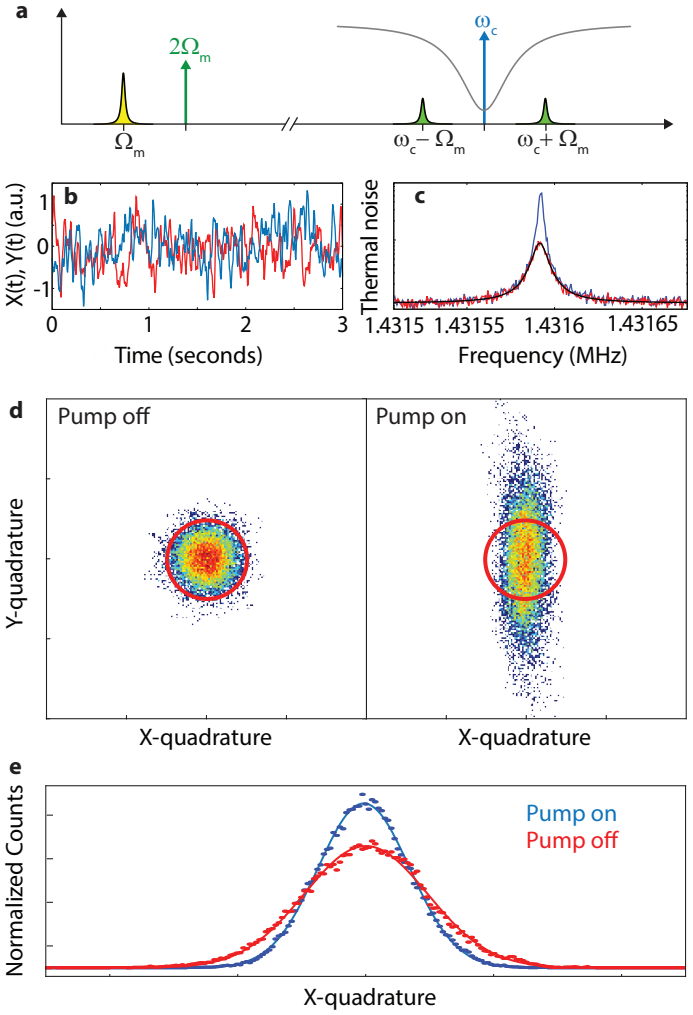

Figure 5.3: **Squeezing of the thermomechanical noise in a nanomechanical oscillator a**, Experimental scheme. The resonance frequency of the mechanical nanobeam is modulated with twice its resonance frequency $\Omega = 2\Omega_m$. A drive resonant with the cavity is modulated by the thermomechanical position noise of the nanobeam, which generates sidebands at $\omega_c - \Omega_m$ and $\omega_c + \Omega_m$. The sidebands are used for the detection of the two mechanical noise quadratures $X(t)$ and $Y(t)$. **b**, Exemplary mechanical amplitude quadratures $X(t)$ and $Y(t)$ versus time t without a parametric drive applied. **c**, Thermal noise spectral power density calculated from the quadratures measurement without parametric driving (red line) and with parametric driving (blue line). The black line shows a Lorentzian fit to the noise without parametric excitation. **d** Quadrature amplitude probability distributions for the unsqueezed (left panel) and the squeezed (right panel) thermomechanical noise of the nanobeam, respectively. The circles represent a guide to the eye. **e** Histograms showing the relative probability measuring an X-quadrature noise amplitude value, where data corresponding to the mechanical noise without parametric modulation is shown in red and data corresponding to the mechanical noise under parametric modulation is shown in blue. Lines are Gaussian fits to the data points and we determine the maximum squeezing factor in our device to be $\sigma = 0.48$, cf. Supplemetary Information. The parametric drive voltage in all panels is about $V_{2\Omega} = 10\,\mathrm{dBm}$.

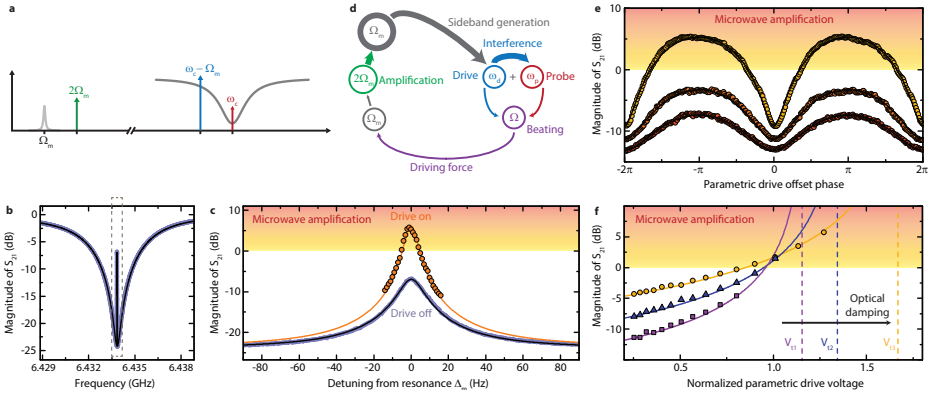

Figure 5.4: **Phase-sensitive and tunable amplification of microwaves by parametrically pumping a nanomechanical oscillator in an optomechanical system. a** Experimental scheme. The cavity is coherently driven by a strong drive tone on the red sideband $\omega_d = \omega_c - \Omega_m$. In addition a small probe tone is swept through the cavity resonance with $\omega_p = \omega_d + \Omega \sim \omega_c$ where $\Omega \sim \Omega_m$. At the same time, the resonance frequency of the mechanical oscillator is parametrically modulated with 2Ω. **b** Optomechanically induced transparency (OMIT) without parametric modulation $P_{2\Omega} = 0$. By the presence of the red-sideband drive tone, an amplitude beating generated by interference with the probe tone drives the mechanical nanobeam around its resonance frequency, which in turn modulates the drive tone and generates sidebands, which by interference open a narrow transparency window in the absorption dip of the cavity. Data is shown in blue and black line is a fit, and the dashed box indicates the zoom-in region shown in **c**. **c** Zoom into the OMIT transparency window. In addition to the data without parametric modulation, we show the highest achieved transmission with the parametric drive switched on as orange circles. Close to the mechanical resonance we observe gain of the microwave input probe signal up to ~ 7dB. The orange line shows a theoretical fit. The schematic shown in **d** visualizes the amplification mechanism. By the beating of the two cavity tones, energy from the cavity field is converted into mechanical motion. This mechanical motion is amplified by means of parametric modulation and the hereby increased energy is upconverted back to the probe tone frequency by sideband generation of the red-sideband tone. **e** The microwave gain is phase-sensitive, i.e., it depends on the relative phase between the parametric modulation and the amplitude beating in the cavity. The three datasets (black lines are fits) show the gain for different detunings from $\omega_p - \omega_d = \Omega_m$ (0Hz, 7Hz and 12Hz). **f** Probe tone gain vs parametric drive voltage for three different red sideband drive powers. The parametric drive voltage is normalized to its value obtained in Fig. 2 using a resonant drive for amplitude detection. Lines are theoretical calculations based on independently extracted system parameters. The parametric instability threshold, indicated by dashed vertical lines, is shifted to higher values with increasing red-sideband drive power due to optical damping.

coherently driven by a directly applied resonant force, but also by amplitude modulations of the intracavity field. Such a near-resonant amplitude modulation can be generated by sending two microwave tones with a frequency difference close to the mechanical resonance into the cavity. Here, we apply a strong microwave drive tone on the red sideband of the cavity, i.e., at $\omega_d = \omega_c - \Omega_m$, and add a small probe signal around the cavity resonance frequency at $\omega_p \sim \omega_c$. This experimental scheme generates a phenomenon called optomechanically induced transparency (OMIT), where by interference a narrow transparency window opens up in the center of the cavity absorption dip. The width of the transparency window is given by the sum of intrinsic mechanical linewidth Γ_m and the additional linewidth due to the red sideband drive-induced optical damping Γ_o. The effect of OMIT effect can be understood as follows. The amplitude beating between the two microwave tones coherently drives the nanobeam by an oscillating radiation pressure force, which transfers energy from the cavity field to the nanobeam. The resulting mechanical motion with frequency $\Omega = \omega_p - \omega_d$ modulates the cavity resonance frequency and hereby generates sidebands to the intracavity drive tone at $\omega_d \pm \Omega$, with a well-defined phase relation to the probe tone. The sideband generated at $\omega_d + \Omega$ interferes with the probe signal and generates OMIT, cf. Fig. 5.4 **a** (for vanishing parametric modulation) and **b**. In **b** the transparency window can be seen in the center of the cavity transmission spectrum as extremely narrow spectral line and a zoom into this region, shown in **c** reveals the Lorentzian lineshape with a width $\Gamma_{\text{eff}} \approx 2\pi \cdot 12\,\text{Hz}$.

When we perform the OMIT protocol with a parametric modulation applied to the nanobeam, the mechanical oscillations get modified according to the previously shown results, i.e., dependent on the relative phase between the cavity field-induced mechanical oscillation and the parametric modulation, the mechanical amplitude gets amplified or de-amplified. By choosing the optimal phase for each detuning $\Delta_m = \Omega - \Omega_m$, the transparency window amplitude can be increased above 1, i.e., we amplify the microwave probe tone by parametrically pumping the mechanical resonator, which is three orders of magnitude smaller in frequency than the probe signal, cf. Fig. 5.4**c**. However, through the amplified mechanical motion, there in turn occurs an amplified sideband-generation of the drive tone, such that the sideband amplitude at the probe frequency can be enhanced above 1. A schematic of the amplification mechanism is shown in Fig. 5.4**d** The observed microwave amplification is, similar to the bare mechanical amplitude gain, phase-sensitive and modulates between amplification and de-amplification, with a phase periodicity of 2π. This phase-sensitivity of the microwave gain is shown in Fig. 5.4**e** for three different detunings from the mechanical resonance $\omega_p - \omega_c = \Omega_m$, $\omega_p - \omega_c \approx \Omega_m + \Gamma_{\text{eff}}/2$, and $\omega_p - \omega_c \approx \Omega_m + \Gamma_{\text{eff}}$. Note, that the phase periodicity here is equivalent to the case of the mechanical amplitude amplification, but due to our theopretical analysis of the system (see SI) the phase is given for the parametric drive instead of the resonant force here, which doubles its value.

Similar to the mechanical amplitude amplification, the microwave gain depends

on the parametric drive voltage, which has a threshold value above which the parametric instability regime begins. When we plot the maximally achievable transmission $|S_{21}|$ exactly on the mechanical resonance vs the parametric excitation voltage, we find a monotonously increasing behaviour as shown in Fig. 5.4**f** for three different red-sideband drive powers (shown are powers corresponding to cooperativities $C_1 \sim 0.18$, $C_2 \sim 0.32$ and $C_3 \sim 0.56$). From fits to the data, shown as lines, we can extract the instability threshold voltages, indicated as dashed vertical lines. Due to the additional damping induced by the red sideband drive, this threshold voltage gets shifted towards higher values with increasing cooperativity and mechanical linewidth, respectively. At the same time, the net microwave gain increases with increasing sideband drive power, as the baseline (the peak height of the transparency window) gets upshifted as well and because the gain in this experiment was limited by the mechanical nonlinearity, which gets less significant for a higher total mechanical linewidth.

5.3. CONCLUSION

In this work, we have fabricated and investigated a microwave optomechanical system based on superconducting structures, which allowed us to experimentally investigate optomechanical phenomena induced by a parametric modulation of the mechanical resonance frequency. By means of an optomechanical readout scheme of a high quality factor mechanical nanobeam oscillator, we have demonstrated full control over the phase-sensitive mechanical amplitude amplification and de-amplification and thermomechanical noise-squeezing. Finally, we have shown that this parametric control over the mechanical oscillator allows for the generation of an optomechanically induced, phase-sensitive microwave amplification in a regime, where the mechanical oscillator can be simultaneously sideband-cooled, which is fundamentally different from most other optomechanical amplification schemes. In an optimized device, it should be possible to cool the mechanical oscillator into its quantum ground state to perform quantum a limited amplification scheme, a highly promising perspective for applications in different fields of superconducting quantum electronics.

5.4. APPENDIX 1: DEVICE FABRICATION

The device fabrication started with the deposition of a 100 nm thick layer of high-stress Si_3N_4 on top of a two inch silicon wafer by means of low pressure chemical vapour deposition (LPCVD). Afterwards, 60 nm thick gold markers on a 10 nm chromium adhesion layer were patterned onto the wafer using electron beam lithography (EBL), electron beam evaporation of the metals and lift-off. Then, the wafer was diced into individual $10 \times 10\,\mathrm{mm}^2$ chips, which were used for the subsequent fabrication steps.

By using a three-layer mask (consisting of S1813, tungsten and ARN-7700-18), EBL and several reactive ion etching (RIE) steps with O_2 and a SF_6/He gas mixture, the Si_3N_4 was thinned down everywhere to ~ 10 nm on the chip surface except for rectangular patches ($124 \times 9\,\mu$m large) around the future locations of the nanobeams. After resist stripping in PRS3000, the remaining ~ 10 nm of Si_3N_4 were removed in a buffered oxide etching (BOE) step, which also thinned down the Si_3N_4 in the rectangular patch areas to ~ 83 nm. This two-step removal of Si_3N_4 by dry and wet etching was performed in order to avoid over-etching with RIE into the silicon substrate.

Immediately afterwards, a ~ 60 nm thick layer of superconducting molybdenum-rhenium alloy (MoRe, 60/40) was sputtered onto the chip. By means of another three-layer mask (S1813, W, PMMA 950K A6), EBL, O_2 and SF_6/He RIE, the microwave structures were patterned into the MoRe layer. The remaining resist was stripped off in PRS3000.

Finally, the nanobeam patterning and release was performed. Similarly to before, the pattern definition was done using a three-layer mask (S1813, W, PMMA 950K A6), EBL and RIE. After the MoRe-Si_3N_4 bilayer was completely etched by the SF_6/He gas mixture, the etching was continued for several minutes. As we had chosen the RIE parameters to achieve slight lateral etching, the silicon underneath the narrow nanobeam was etched away by this measure and the beam was released from the substrate. After the nanobeam release, the remaining resist was stripped using an O_2 plasma.

A simplified schematic of the fabrication is shown in Fig. 5.1, omitting the patterning of the electron beam markers.

5.5. APPENDIX 2: MEASUREMENT SETUP

Figure 5.2 shows a schematic of the measurement setup configurations, which we used for the experiments reported in this paper. All experiments were carried out in a dilution refrigerator with the sample at a temperature $T = 15\,\mathrm{mK}$, cf. Fig. 5.2**a**. The sample was mounted into a radiation tight copper housing and connected to two coaxial high-frequency lines. By means of two bias-tees, the center conductors of the coaxial cables were also connected to DC wires and a DC voltage source, which allowed for DC access to the sample. The input line was heavily attenuated to equilibrate the thermal radiation on the line to the refrigerator base temperature. To isolate the sample from the noise of the cryogenic amplifier on the output line, we used two

isolators in series on the milliKelvin plate.

Outside of the refrigerator, we used different configurations of microwave signal sources and high-frequency electronics for the three experiments presented here. All three are shown in Figs.5.2**b**,**c** ,and **d**, where the setup for the mechanical parametric amplification experiment is shown in **b**, the setup for the thermomechanical noise squeezing is shown in **c** and the configuration for the parametric microwave amplification in **d**. For all experiments, the microwave sources and vector network analyzers (VNA) as well as the lock-in amplifier used a single reference clock of one of the devices.

Figure5.2**e** provides a symbol legend for **a** to **d**.

5.6. APPENDIX 3: CAVITY CHARACTERIZATION

5.6.1. THE CAVITY MODEL

The cavity used in this experiment is a quarter-wavelength ($\lambda/4$) transmission line cavity, capacitively side-coupled to a microwave feedline via a coupling capacitor C_c at the open end and shorted to ground at the other end. Cavity and feedline have both the characteristic impedance Z_0 and the cavity has length l and resonance frequency ω_c. From an input impedance viewpoint, such a transmission line cavity can be modeled around its fundamental mode resonance by a lumped element RLC circuit with the equivalent capacitor, inductor and resistor

$$C = \frac{C'l}{2}, \quad L = \frac{8}{\pi^2}L'l, \quad R = Z_0\alpha l \tag{5.1}$$

respectively. Here, C' and L' denote capacitance and inductance of the transmission line per unit length and α is the line attenuation constant.

For a capacitively coupled parallel RLC circuit, the ideal S_{21} response function is in high-Q approximation given by

$$S_{21} = 1 - \frac{\kappa_e}{\kappa_i + \kappa_e + 2i\Delta} \tag{5.2}$$

with the internal and external decay rates

$$\kappa_i = \frac{1}{R(C+C_c)}, \quad \kappa_e = \frac{\omega_c^2 C_c^2 Z_0}{2(C+C_c)} \tag{5.3}$$

and the detuning from the resonance frequency

$$\Delta = \omega - \omega_c, \quad \omega_c = \frac{1}{\sqrt{L(C+C_c)}}. \tag{5.4}$$

5.6.2. EXTRACTING CAVITY PARAMETERS FROM DATA

In any real experiment with microwave cables and microwave elements such as attenuators, circulators and amplifiers, the measured resonance line is not described

by Eq. (5.2) anymore. To model the measured complex scattering parameter S_{21}, we use

$$S_{21} = (\alpha_0 + \alpha_1\omega)\left(1 - \frac{\kappa_e e^{i\theta}}{\kappa_i + \kappa_e + 2i\Delta}\right) e^{i(\beta_1\omega+\beta_0)} \tag{5.5}$$

where we consider a modification of the background signal and phase by using the frequency dependent complex scaling factor

$$(\alpha_0 + \alpha_1\omega) \cdot e^{i(\beta_1\omega+\beta_0)} \tag{5.6}$$

and also include an additional rotation of the complex resonance circle around its anchor point by the phase factor $e^{i\theta}$.

Figure 5.3 shows an experimentally determined resonance curve in both, magnitude (**a**) and the complex plane (**b**), in direct comparison with the fit we obtained using Eq. 5.5. Both curves are normalized by $\alpha_0 + \alpha_1\omega_c$, i.e., by the background value at the fitted resonance frequency. From the fit, we extract the cavity parameters $\kappa_i = 2\pi \cdot 370\,\text{kHz}$, $\kappa_e = 2\pi \cdot 5.7\,\text{MHz}$, and $\omega_c = 2\pi \cdot 6.4339\,\text{GHz}$. Thus, the cavity is highly overcoupled with a coupling efficiency $\eta = \kappa_e/(\kappa_i + \kappa_e) = 0.94$.

5.6.3. CAVITY PARAMETERS VS SIDEBAND DRIVE POWER

In the parts of the experiments, where we investigate optomechanically induced transparency and demonstrate microwave amplification, we add a high-power microwave tone on one of the cavity sidebands. This strong tone slightly modifies the cavity linewidths and the cavity resonance frequency depending on its power. In Fig. 5.4, we plot the resonance frequency (**a**) as well as external (**b**) and internal (**c**) cavity linewidths as extracted from fitting the corresponding curves with Eq. (5.5). The frequency of the sideband drive was set to $\omega \approx \omega_c \pm \Omega_m$ and kept fixed for all powers and the probe tone power was much smaller than the sideband drive. Thus, due to the slight dependence of the cavity resonance frequency on the drive power it is not exactly on the red/blue sideband for all powers. The deviation from the low-power resonance frequency, however, is given by maximally $0.007(\kappa_i + \kappa_e)$, i.e., less than one percent of the linewidth, and thus we consider it as negligible.

The photon numbers in the cavity are calculated by using

$$n = \frac{2P_{\text{in}}}{\hbar\omega_d}\frac{\kappa_e}{\kappa^2 + 4\Omega_m^2}, \tag{5.7}$$

where P_{in} is the input power on the chip feedline, ω_d is the drive frequency and we assume a detuning of the drive tone from the cavity resonance by one mechanical frequency $\Delta = -\Omega_m$.

5.6.4. COUPLING CAPACITANCE AND CHARACTERISTIC IMPEDANCE

With the formula for the external decay rate for a capacitively side-coupled RLC circuit

$$\kappa_e = \frac{\pi\omega_c C_c^2}{8\sqrt{C(C+C_c)^3}} \tag{5.8}$$

the calculated capacitance per unit length $C' = 187\,\text{pF/m}$ for our coplanar waveguide geometry (center conductor width $S = 10\,\mu\text{m}$, gap width $W = 6\,\mu\text{m}$, substrate permittivity $\epsilon_r = 11.6$) and the cavity length $l = 3450\,\mu\text{m}$, we can determine the coupling capacitance as $C_c = 15.9\,\text{fF}$. In the expression for κ_e, we have used that the resonance impedance of the equivalent RLC circuit $Z_r = \sqrt{L/C} = \frac{4}{\pi}Z_0$ is related to the feedline impedance Z_0 for our geometry.

With the value for the coupling capacitance, we calculate the equivalent inductance $L = 1.8\,\text{nH}$, the inductance per unit length $L' = 645\,\text{nH/m}$, which is considerably larger than the calculated geometric inductance per unit length $L'_g = 375\,\text{nH/m}$ due to kinetic contributions, and finally the characteristic impedance of feedline and cavity as $Z_0 = 65.6\,\Omega$.

5.6.5. ESTIMATED POWER CALIBRATION

From the mechanical parametric amplification, we got as theory value for the threshold voltage $V_t = 330\,\mu\text{V}$. One specific output power of the 2Ω-drive source was $+10\,\text{dBm}$, which corresponded to $0.8V_t = 264\,\mu\text{V}$. Assuming a $65\,\Omega$ line, we get as power on the chip $P = 536\,\text{pW}$ or $-63\,\text{dBm}$. Thus, from this we get a total input attenuation of $-73\,\text{dB}$. Attributing $-6\,\text{dB}$ to losses in the splitter, the in-fridge attenuation is about $-67\,\text{dBm}$. The bias-tee has an attenuation of $-7\,\text{dB}$ at $2.8\,\text{MHz}$ and the circulator (not shown in diagram) of $\sim -4\,\text{dB}$ (bias-tee and circulator measured at RT). The nominal attenuation on the input line was $-48\,\text{dB}$. In total this leaves us with $-8\,\text{dB}$ unexplained attenuation, but this is not unlikely to be carried by the cables, connectors, DC blocks, impedance mismatch to the chip etc.

From the measurements of OMIT/OMIA, we find a background value of the transmission on resonance of $\sim 2.75\cdot 10^{-2}$, which corresponds to $-31.2\,\text{dB}$. Taking into account that on the output line we have a total amplifier gain of $+67\,\text{dB}$, the total attenuation on input and output line for the high frequencies is about $-98\,\text{dB}$. On the input line, we had an attenuator of $-20\,\text{dB}$ directly at the output port and two splitters with

in total −10 dB loss. In addition we have approximately −5 dB of RT cable losses and −48 dB attenuation in the fridge. Bias-tee and circulator add another −1 dB, which gives −84 dB of total input attenuation.

On the output line, we have another −1 dB from circulator and bias-tee and −5 dBm from RT cabling. Thus, again, −8 dB seem to be missing. The power calibration can thus be made consistent by assuming ∼ 8 dB additional losses on the input lines, though in reality they might be frequency dependent. The input power on the chip is hence 92 dB smaller than the output power of the VNA.

5.7. APPENDIX 4: THEORY OF OPTOMECHANICAL MOTION DETECTION

When a microwave signal is sent into the cavity on resonance, the ideal response is given by

$$V(t) = V_\omega \left(\frac{\kappa_i}{\kappa_i + \kappa_e} \right) e^{i\omega t}. \tag{5.9}$$

If on the other hand the resonance frequency is modulated by mechanical motion, i.e., $\omega_c = \omega_c - Gx(t)$ with the cavity pull $G = -\frac{\partial \omega_c}{\partial x}$ and under the assumption that $x(t)$ is a real-valued function, we get

$$V(t) = V_\omega \left(\frac{\kappa_i + 2iGx(t)}{\kappa_i + \kappa_e + 2iGx(t)} \right) e^{i\omega t} \tag{5.10}$$

$$\approx V_\omega \left(\frac{\kappa_i}{\kappa_i + \kappa_e} + 2iG \frac{\kappa_e}{(\kappa_i + \kappa_e)^2} x(t) \right) e^{i\omega t}. \tag{5.11}$$

where the approximation in the last step was done for $G^2 x^2 \ll (\kappa_i + \kappa_e)^2$, i.e., the motion induced frequency shift is much smaller than the cavity linewidth.

Now assuming that the mechanical position is given by

$$x(t) = x_0 \cos \Omega t = \frac{x_0}{2} \left(e^{i\Omega t} + e^{-i\Omega t} \right) \tag{5.12}$$

we get for the response voltage

$$V(t) = V_\omega \frac{\kappa_i}{\kappa} e^{i\omega t} + i V_\omega G x_0 \frac{\kappa_e}{\kappa^2} \left(e^{i(\omega+\Omega)t} + e^{i(\omega-\Omega)t} \right). \tag{5.13}$$

To calculate the effect of mixing this response with a signal oscillating with ω, as we do in the experiment, we take the real part first given by

$$V_r(t) = V_\omega \frac{\kappa_i}{\kappa} \cos \omega t - V_\omega G x_0 \frac{\kappa_e}{\kappa^2} \left[\sin(\omega + \Omega) t + \sin(\omega - \Omega) t \right] \tag{5.14}$$

and multiply this with a mixing local oscillator $\cos(\omega t + \gamma)$ containing an arbitrary phase offset γ. The result is given by

$$V_f(t) = \frac{V_\omega}{2}\frac{\kappa_i}{\kappa}\cos\gamma - \frac{V_\omega}{2}\frac{\kappa_e}{\kappa^2}Gx_0\cos\Omega t\sin\gamma + ... \tag{5.15}$$

where we omitted frequency components oscillating with 2ω or $2\omega \pm \Omega$. Thus, if the mixer phase γ is different from zero or π, this technique will generate a signal with the frequency of the mechanical motion and the amplitude of this signal is proportional to the mechanical displacement amplitude. This way we detected both the mechanical amplitude amplification as well as the thermal noise squeezing in this work.

5.8. APPENDIX 5: NANOWIRE CHARACTERIZATION

5.8.1. NANOWIRE TUNING WITH A DC VOLTAGE

In this paper, we describe the nanowire as a point-like mechanical harmonic oscillator, cf. Sec. 5.10. When a DC voltage is applied to the center conductor of the transmission feedline, cf. Figs. 5.2**a** and 5.1**d**, a static force is exerted to the nanowire and the equation of motion is given by

$$m\ddot{x} + m\Gamma_m\dot{x} + k_m x = \frac{1}{2}V_{\rm dc}^2\frac{\partial C_{\rm nw}}{\partial x}, \tag{5.16}$$

were x is the nanowire position, k_m is the intrinsic spring constant, m is the effective mass and Γ_m is the intrinsic damping or mechanical linewidth. The force will lead to a new nanowire equilibrium position x_0 which is defined by

$$k_m x_0 = \frac{1}{2}V_{\rm dc}^2\frac{\partial C_{\rm nw}}{\partial x}\bigg|_{x_0}. \tag{5.17}$$

A Taylor approximation of the electrostatic force around the new equilibrium position x_0 gives

$$F_{\rm el} = \frac{1}{2}V_{\rm dc}^2\left[\frac{\partial C_{\rm nw}}{\partial x}\bigg|_{x_0} + \frac{\partial^2 C_{\rm nw}}{\partial x^2}\bigg|_{x_0}(x-x_0)...\right]. \tag{5.18}$$

Absorbing the new equilibrium position in a redefinition of the position coordinate x allows to write the full equation of motion as

$$m\ddot{x} + m\Gamma_m\dot{x} + [k_m + k_{\rm dc}]\,x = F(t) \tag{5.19}$$

where

$$k_{\rm dc} = -\frac{1}{2}V_{\rm dc}^2\frac{\partial^2 C_{\rm nw}}{\partial x^2}\bigg|_{x_0} \tag{5.20}$$

is the electrostatic spring constant and $F(t)$ is a possible additional external driving force. In general, the equilibrium position and the second derivative of the capacitance will depend on the applied DC voltage themselves.

From the equation of motion it follows that the mechanical resonance frequency is given by

$$\Omega_m = \sqrt{\frac{k_m + k_{\mathrm{dc}}}{m}} \tag{5.21}$$

$$= \Omega_{m0}\sqrt{1 - \frac{k_{\mathrm{dc}}}{k_m}} \tag{5.22}$$

where $\Omega_{m0} = \sqrt{k_m/m}$ is the intrinsic mechanical resonance frequency.

To characterize the mechanical oscillator, we drive it with an additional near-resonant harmonic voltage as described in Secs. 5.2.2 and 5.10 and record the resonance peak for different DC voltages. Taking into account that the effective mass of the fundamental mode of a doubly clamped nanobeam is given by $m = 0.735 m_0$ with its real mass m_0, we can extract the effective spring constant from the zero voltage resonance frequency. With the dimensions of the beam, its full mass is calculated by using the densities $\rho_{\mathrm{SiN}} = 3.2\,\mathrm{g/cm^3}$ and $\rho_{\mathrm{MoRe}} = 14.5\,\mathrm{g/cm^3}$ to be $m_0 = 17\,\mathrm{pg}$, which gives $m = 12.5\,\mathrm{pg}$.

From the resonance frequency $\Omega_{m0} = 2\pi \cdot 1.478\,\mathrm{MHz}$, we can thus extract the intrinsic spring constant $k_m = 1\,\mathrm{N/m}$. In addition, we can calculate the electrical spring constant k_{dc} from here. The measured resonance frequency vs DC voltage in the negative voltage range is plotted in Fig. 5.5**a** and a fit with Eq. (eqn:Tuning) assuming $k_{\mathrm{dc}} \propto V_{\mathrm{dc}}^2$ describes the behaviour very accurately in the shown voltage range.

With Eq. (5.22) we can also calculate the elctrostatic spring constant

$$k_{\mathrm{dc}} = k_m\left(1 - \frac{\Omega_m^2}{\Omega_{m0}^2}\right) \tag{5.23}$$

from our data and $k_m = 1\,\mathrm{N/m}$. The result is plotted together in Fig. 5.5**b** with a line obtained from the fit in **a**.

5.9. APPENDIX 6: OPTOMECHANICAL DEVICE CHARACTERIZATION

5.9.1. OPTOMECHANICAL COUPLING RATE g_0

To calculate the optomechanical single-photon coupling

$$g_0 = -\frac{\partial \omega_c}{\partial x} x_{\mathrm{zpf}} \tag{5.24}$$

we need the mechanical zero-point fluctuations, which we get from the resonance frequency and the effective nanowire mass as

$$x_{\mathrm{zpf}} = \sqrt{\frac{\hbar}{2m\Omega_m}} = 21\,\mathrm{fm}. \tag{5.25}$$

To get the cavity pull parameter, we estimate from simulations that the mechanical capacitance is approximately half of the total capacitance, i.e. $C_m = 8\,\mathrm{fF}$ and then calculate

$$\frac{\partial\omega_c}{\partial C_m} = -\frac{\omega_c^3}{2}L = -2\pi\cdot 9.5\cdot 10^{21}\,\mathrm{Hz/m}. \tag{5.26}$$

The final quantity we need is

$$\frac{\partial C_m}{\partial x} = 10^{-8}\,\mathrm{F/m} \tag{5.27}$$

which we estimate again from simulations.

Putting all together we get

$$g_0 = 2\pi\cdot 2\mathrm{Hz}. \tag{5.28}$$

5.9.2. OPTOMECHANICAL COUPLING RATIO

Resonance frequency and external coupling rate of our cavity are given by

$$\omega_c = \frac{1}{\sqrt{L(C+C_c)}} \tag{5.29}$$

$$\kappa_e = \frac{Z_0 C_c^2}{2L(C+C_c)^2} \tag{5.30}$$

with the characteristic feedline impedance Z_0. Assuming that the cavity is highly overcoupled $\kappa_e + \kappa_i \approx \kappa_e$ as in our device, the ratio of dissipative optomechanical coupling rate g_κ to dispersive optomechanical coupling rate g_ω is given by

$$\frac{g_\kappa}{g_\omega} = 2Z_0\omega_c\frac{CC_c}{C+C_c} \approx 0.08, \tag{5.31}$$

which is small enough to neglect the dissipative optomechanical coupling contribution to first order throughout the paper. Thus, we will restrict our theoretical calculations and device modeling to purely dispersive coupling.

5.9.3. THEORY OF OPTOMECHANICALLY INDUCED TRANSPARENCY AND ABSORPTION WITHOUT THE RESOLVED SIDEBAND LIMIT

We model the system without the parametric driving by means of the classical, coupled equations of motion for the mechanical displacement x and the intracavity field amplitude α

$$\ddot{x} = -\Omega_m^2 x - \Gamma_m \dot{x} + \frac{1}{m}(F_r + F_e) \tag{5.32}$$

$$\dot{\alpha} = \left[i(\Delta + Gx) - \frac{\kappa}{2} \right] \alpha + \sqrt{\frac{\kappa_e}{2}} S_{\text{in}} \tag{5.33}$$

where external forces to the mechanical oscillator are expressed by F_e in the first equation and the radiation pressure force due to the intracavity field is given by

$$F_r = \hbar G |\alpha|^2. \tag{5.34}$$

Further parameters in the equations are the cavity pull parameter $G = -\partial\omega_c/\partial x$, the detuning between a cavity drive and the cavity resonance frequency $\Delta = \omega_d - \omega_c$ and the total cavity linewidth $\kappa = \kappa_i + \kappa_e$. In the second equation, the field amplitude α is normalized such that $|\alpha|^2$ corresponds to the photon number in the cavity and the input field S_{in} is normalized such that $|S_{\text{in}}|^2$ corresponds to the photon number flux of the input field.

5

Under the assumption that it is sufficient to consider only small deviations from the steady state solutions $\bar{x}, \bar{\alpha}$ of the full equations, i.e., $x = \bar{x} + \delta x, \alpha = \bar{\alpha} + \delta\alpha$, these two equations can be linearized as

$$\delta\ddot{x} = -\Omega_m^2 \delta x - \Gamma_m \delta\dot{x} + \frac{\hbar G\bar{\alpha}}{m}\left(\delta\alpha + \delta\alpha^*\right) \tag{5.35}$$

$$\delta\dot{\alpha} = \left[i\bar{\Delta} - \frac{\kappa}{2} \right] \delta\alpha + iG\bar{\alpha}\delta x + \sqrt{\frac{\kappa_e}{2}} S_p. \tag{5.36}$$

where we omitted a possible external driving force F_e. Here, $\bar{\Delta} = \omega_d - \omega_c + G\bar{x}$ is the detuning from the modified resonance frequency, when the mechanical oscillator is pushed by radiation pressure to its new equilibrium position $\bar{x}$, and $\sqrt{\kappa_e/2}S_p$ with $S_p = S_0 e^{-i\Omega t}$ ($\Omega = \omega - \omega_d$) accounts for small additional drive fields or field fluctuations.

We solve these equations with the Ansatz

$$\delta\alpha = a_- e^{-i\Omega t} + a_+ e^{+i\Omega t} \tag{5.37}$$

$$\delta\alpha^* = a_-^* e^{+i\Omega t} + a_+^* e^{-i\Omega t} \tag{5.38}$$

$$\delta x = x_1 e^{-i\Omega t} + x_1^* e^{+i\Omega t} \tag{5.39}$$

and get as solution in high-Q_m approximation the modified mechanical response function

$$\chi_m^{\text{eff}} = \frac{1}{2m\Omega_m} \frac{1}{\Omega_m - \Omega - i\frac{\Gamma_m}{2} + \Sigma'(\Omega_m)} \tag{5.40}$$

where

$$\Sigma'(\Omega_m) = -ig^2\left[\chi_c(\Omega_m) - \chi_c^*(-\Omega_m)\right]. \tag{5.41}$$

Here,

$$\chi_c = \frac{1}{\frac{\kappa}{2} - i(\bar{\Delta} + \Omega)} \tag{5.42}$$

with $\bar{\Delta} = \omega_d - \omega_c + G\bar{x}$ represents essentially the (modified) cavity response lineshape, for which we use from here on just Δ as the difference is negligibly small in our experiment.

Expression (5.41) can be split into an imaginary and a real part $\Sigma' = \delta\Omega_m - i\Gamma_o/2$, of which the real part corresponds to a modification of the mechanical resonance frequency (optical spring)

$$\delta\Omega_m = g^2\left[\frac{\Delta + \Omega_m}{\frac{\kappa^2}{4} + (\Delta + \Omega_m)^2} + \frac{\Delta - \Omega_m}{\frac{\kappa^2}{4} + (\Delta - \Omega_m)^2}\right] \tag{5.43}$$

and the imaginary part

$$\Gamma_o = g^2\kappa\left[\frac{1}{\frac{\kappa^2}{4} + (\Delta + \Omega_m)^2} - \frac{1}{\frac{\kappa^2}{4} + (\Delta - \Omega_m)^2}\right] \tag{5.44}$$

represents an additional damping term (optical damping).

For the cavity amplitude, we find the solution

$$a_- = \chi_c\left[1 + 2im\Omega_m g^2 \chi_c \chi_m^{\text{eff}}\right]\sqrt{\frac{\kappa_e}{2}}S_0 \tag{5.45}$$

which with $S_{21} = 1 - \sqrt{\frac{\kappa_e}{2}}\frac{a_-}{S_0}$ can be directly translated into the full cavity response function in presence of a harmonic drive

$$S_{21} = 1 - \frac{\kappa_e}{2}\chi_c\left[1 + 2im\Omega_m g^2 \chi_c \chi_m^{\text{eff}}\right]. \tag{5.46}$$

DRIVE ON THE RED SIDEBAND

When the constant frequency drive is set to the red cavity sideband, i.e., $\Delta = -\Omega_m$, and the probe tone is swept only very close to the cavity resonance, i.e., $\Omega = \Omega_m + \Delta_m$ with $\Delta_m \ll \kappa$, the effective cavity susceptibility is given by

$$\chi_c = \frac{2}{\kappa} \tag{5.47}$$

and the effective mechanical susceptibility can be approximated as

$$\chi_m^{\text{eff}} = -\frac{1}{m\Omega_m}\frac{1}{2\Delta_m - i\Gamma_{\text{eff}}} \tag{5.48}$$

with

$$\Gamma_{\text{eff}} = \Gamma_m + \Gamma_o = \Gamma_m \left(1 + C \frac{16 \frac{\Omega_m^2}{\kappa^2}}{1 + 16 \frac{\Omega_m^2}{\kappa^2}} \right) \tag{5.49}$$

where $C = 4g^2/\kappa\Gamma_m$ is the cooperativity.

The scattering parameter is then given by

$$S_{21} = 1 - \frac{\kappa_e}{\kappa} \left[1 - 4i \frac{g^2}{\kappa} \frac{1}{2\Delta_m - i\Gamma_{\text{eff}}} \right] \tag{5.50}$$

$$= \frac{\kappa_i}{\kappa} + i \frac{\kappa_e}{\kappa} \frac{C\Gamma_m}{2\Delta_m - i\Gamma_{\text{eff}}}. \tag{5.51}$$

The transmitted power is then described by a Lorentzian

$$|S_{21}|^2 = S_c + \frac{C\Gamma_m}{4\Delta_m^2 + \Gamma_{\text{eff}}^2} S_{\text{om}} \tag{5.52}$$

with the background value

$$S_c = \frac{\kappa_i^2}{\kappa^2} \tag{5.53}$$

and the optomechanical amplitude

$$S_{\text{om}} = 2 \frac{\kappa_i \kappa_e}{\kappa^2} \Gamma_{\text{eff}} + \frac{\kappa_e^2}{\kappa^2} C\Gamma_m. \tag{5.54}$$

DRIVE ON THE BLUE SIDEBAND

With $\Delta = +\Omega_m$ and $\Omega \approx -\Omega_m + \Delta_m$ we get

$$\chi_m^{\text{eff}} = \frac{1}{m\Omega_m} \frac{1}{2\Delta_m + i\Gamma'_{\text{eff}}} \tag{5.55}$$

where

$$\Gamma'_{\text{eff}} = \Gamma_m - \Gamma_o = \Gamma_m \left(1 - C \frac{16 \frac{\Omega_m^2}{\kappa^2}}{1 + 16 \frac{\Omega_m^2}{\kappa^2}} \right) \tag{5.56}$$

As transmission paramater we thus get

$$S_{21} = 1 - \frac{\kappa_e}{\kappa} \left[1 + 4i \frac{g^2}{\kappa} \frac{1}{2\Delta_m + i\Gamma'_{\text{eff}}} \right] \tag{5.57}$$

$$= \frac{\kappa_i}{\kappa} - i \frac{\kappa_e}{\kappa} \frac{C\Gamma_m}{2\Delta_m + i\Gamma'_{\text{eff}}} \tag{5.58}$$

and for the transmitted power

$$|S_{21}|^2 = S_c + \frac{C\Gamma_m}{4\Delta_m^2 + \Gamma_{\text{eff}}'^2} S'_{\text{om}} \tag{5.59}$$

with

$$S'_{\text{om}} = -2\frac{\kappa_i \kappa_e}{\kappa^2}\Gamma_{\text{eff}} + \frac{\kappa_e^2}{\kappa^2} C\Gamma_m \tag{5.60}$$

5.9.4. OMIT, OMIA AND COOPERATIVITY WITH THE DEVICE

In the experiment, we drive the cavity with a drive tone on one of the sidebands, i.e. at $\omega = \omega_c \pm \Omega_m$ and variable power. Then, we sweep a weak probe tone around the cavity resonance and measure the resulting optomechanically induced transparency or absorption. Figure 5.6 shows the resulting transparency and absorption windows for different drive powers, i.e., for different drive photon numbers inside the cavity. In (a), the optomechanically induced transparency window for a drive on the red sideband $\omega = \omega_c - \Omega_m$ is shown and in (b) the corresponding data for a drive on the blue sideband $\omega = \omega_c + \Omega_m$. The different curves correspond to different drive powers (steps of 2 dBm) or intracavity photon numbers, respectively.

From the amplitude of the Lorentzians, we can extract the cooperativity and the total coupling rate g. The extracted values for the highest power data are given in Fig. 5.6. In combination with an estimate of the intracavity photon number, we get also

5.9.5. ESTIMATION FOR THE SINGLE-PHOTON COUPLING RATE g_0

From the extracted multi-photon coupling g and the estimated intracavity photon number, we can calculate also a value for the single-photon coupling strength g_0 and get

$$g_0 = 2\pi \cdot \text{Hz}. \tag{5.61}$$

5.10. APPENDIX 7: THEORY OF PARAMETRIC MECHANICAL AMPLITUDE AMPLIFICATION

We model the nanowire as mechanical harmonic oscillator with the effective equation of motion of a point-like particle having the position coordinate x

$$m\ddot{x} + m\Gamma_m \dot{x} + k_m x = F(t). \tag{5.62}$$

Here, m is the effective mass of the nanowire, Γ_m is its damping rate, k_m is the mechanical spring constant and $F(t)$ is a time dependent external driving force. When a time-dependent voltage $V(t)$ is applied to the center conductor of the microwave feedline, the nanowire experiences a corresponding electrical force

$$F_{\mathrm{el}} = \frac{1}{2}\frac{\partial C_{\mathrm{nw}}}{\partial x} V^2 \tag{5.63}$$

where C_{nw} is the capacitance between the nanowire and the center conductor of the cavity (DC ground). In our experiment, the total voltage applied to the center conductor (without the microwave tone) is given by

$$V(t) = V_{\mathrm{dc}} + V_0 \cos\left(\Omega t + \phi_p\right) + V_{2\Omega} \sin 2\Omega t \tag{5.64}$$

which corresponds to a total force of

$$\begin{aligned} F_{\mathrm{el}}(t) \quad &= \tfrac{1}{2}\tfrac{\partial C_{\mathrm{nw}}}{\partial x} \quad \Big[V_{\mathrm{dc}}^2 + V_0^2 \cos^2(\Omega t + \phi_p) + V_{2\Omega}^2 \sin^2 2\Omega t && (5.65)\\ &\quad + 2V_{\mathrm{dc}} V_0 \cos(\Omega t + \phi_p) + 2V_{\mathrm{dc}} V_{2\Omega} \sin 2\Omega t && (5.66)\\ &\quad + V_0 V_{2\Omega} \cos(\Omega t + \phi_p) \sin 2\Omega t \Big] && (5.67) \end{aligned}$$

Here, V_{dc} is a static voltage, V_0 is the voltage peak amplitude of a harmonic drive close to resonance with frequency Ω and $V_{2\Omega}$ is the corresponding amplitude of the parametric drive voltage with twice the frequency of the near-resonant drive. We consider a phase shift between the near-resonant and the parametric drive by the phase ϕ_p in the near-resonant term.

In the experiment, we have used $V_{\mathrm{dc}} = -4\,\mathrm{V}$, $V_{2\Omega} \leq 100\,\mu\mathrm{V}$ and $V_0 \approx 100\,\mathrm{nV}$. Keeping only the leading terms under these conditions, we get

$$F_{\mathrm{el}} \approx \frac{1}{2}\frac{\partial C_{\mathrm{nw}}}{\partial x}\left[V_{\mathrm{dc}}^2 + 2V_{\mathrm{dc}} V_0 \cos(\Omega t + \phi_p) + 2V_{\mathrm{dc}} V_{2\Omega} \sin 2\Omega t\right]. \tag{5.68}$$

A Taylor approximation to first order in x around the equilibrium position x_0 gives

$$F_{\mathrm{el}} \approx \frac{1}{2}\left[V_{\mathrm{dc}}^2 + 2V_{\mathrm{dc}} V_0 \cos(\Omega t + \phi_p) + 2V_{\mathrm{dc}} V_{2\Omega} \sin 2\Omega t\right]\left[\frac{\partial C_{\mathrm{nw}}}{\partial x}\Big|_{x_0} + \frac{\partial^2 C_{\mathrm{nw}}}{\partial x^2}\Big|_{x_0} \cdot (x - x_0) + \ldots\right] \tag{5.69}$$

The first order terms proportional to $x - x_0$ can now be regarded as an electrostatic spring force with the spring constant

$$k_{\mathrm{el}}(t) = \underbrace{-\frac{1}{2}\frac{\partial^2 C_{\mathrm{nw}}}{\partial x^2}\Big|_{x_0} V_{\mathrm{dc}}^2}_{=k_{\mathrm{dc}}} \underbrace{-\frac{\partial^2 C_{\mathrm{nw}}}{\partial x^2}\Big|_{x_0} V_{\mathrm{dc}} V_{2\Omega}}_{=k_p} \sin 2\Omega t \tag{5.70}$$

where we have omitted the $\cos(\Omega t + \phi_p)$ term due to its smallness and the reduced effect of resonant parametric modulations compared to a 2Ω-term []. Similarly, we can omit the 2Ω-term in the remaining driving force and after absorbing the remaining static force into a redefinition of the equilibrium position $x_0 = 0$ we finally get

$$m\ddot{x} + \Gamma_m \dot{x} + \left[k_0 + k_p \sin 2\Omega t\right] x = F_0 \cos(\Omega t + \phi_p) \tag{5.71}$$

with

$$k_0 = k_m + k_{\mathrm{dc}}, \quad F_0 = V_{\mathrm{dc}} V_0 \frac{\partial C_{\mathrm{nw}}}{\partial x}\Big|_{x_0}. \tag{5.72}$$

This is the well-known equation of motion for a parametrically modulated harmonic oscillator [].

With the transformations

$$\Omega_1 = \Omega_m \left[\left(1 - \frac{1}{4Q_m^2}\right)^{1/2} + \frac{i}{2Q_m}\right], \tag{5.73}$$

$$A = \dot{x} + i\Omega_1^* x \tag{5.74}$$

$$A^* = \dot{x} - i\Omega_1 x \tag{5.75}$$

we rewrite the equation of motion as

$$\dot{A} = i\Omega_1 A + i\frac{k_p \sin 2\Omega t}{m} \frac{A - A^*}{\Omega_1^* + \Omega_1} + \frac{F_0}{m}\cos(\Omega t + \phi_p). \tag{5.76}$$

With the ansatz

$$A = A_0 e^{i\Omega t}, \tag{5.77}$$

and the high-Q_m approximations

$$\Omega_1^* + \Omega_1 \approx 2\Omega_m, \tag{5.78}$$

$$\Omega_1 - \Omega \approx i\frac{\Omega_m}{2Q_m} - \Delta_m \tag{5.79}$$

where $\Delta_m = \Omega - \Omega_m$, we find in rotating wave approximation

$$\frac{\Omega_m}{2Q_m} A_0 + i\Delta_m A_0 + \frac{k_p}{4m\Omega_m} A_0^* - \frac{F_0}{2m} e^{i\phi_p} = 0. \tag{5.80}$$

We can solve this equation for the real and the imaginary part of A_0. Setting $x(t) = x_1 \cos\Omega t + x_2 \sin\Omega t$ and using $x_1 = \mathrm{Im}(A_0)/\Omega_m$, $x_2 = \mathrm{Re}(A_0)/\Omega_m$ we get

$$x_1 = F_0 \frac{Q_m}{k_0} \left[\frac{\left(1 + \frac{Q_m k_p}{2k_0}\right) \sin\phi_p - \frac{2Q_m \Delta_m}{\Omega_m} \cos\phi_p}{1 - \frac{Q_m^2 k_p^2}{4k_0^2} + \frac{4Q_m^2 \Delta_m^2}{\Omega_m^2}} \right] \tag{5.81}$$

$$x_2 = F_0 \frac{Q_m}{k_0} \left[\frac{\left(1 - \frac{Q_m k_p}{2k_0}\right) \cos\phi_p + \frac{2Q_m \Delta_m}{\Omega_m} \sin\phi_p}{1 - \frac{Q_m^2 k_p^2}{4k_0^2} + \frac{4Q_m^2 \Delta_m^2}{\Omega_m^2}} \right]. \tag{5.82}$$

From this we can calculate the mechanical amplitude as $|x| = \sqrt{x_1^2 + x_2^2}$ and get

$$|x|_{\text{on}} = |x|_{\text{off}} \left[\frac{\cos^2(\phi_p + \varphi)}{\left(1 + \frac{V_{2\Omega}}{V_t}\right)^2} + \frac{\sin^2(\phi_p + \varphi)}{\left(1 - \frac{V_{2\Omega}}{V_t}\right)^2} \right]^{1/2} \tag{5.83}$$

5

where the amplitude without parametric drive is given by the usual expression

$$|x|_{\text{off}} = F_0 \frac{Q_m}{k_0} \frac{1}{\sqrt{1 + \frac{4Q_m^2 \Delta_m^2}{\Omega_m^2}}} \tag{5.84}$$

describing the square root of a Lorentzian line around the resonance frequency.

Equation (5.83) is a generalization of the expression given in Ref. [19] for non-zero detunings from the resonance frequency. The threshold voltage for parametric instability V_t' in Eq. (5.83) describes the square root of an inverted Lorentzian

$$V_t = V_{t0} \sqrt{1 + \frac{4Q_m^2 \Delta_m^2}{\Omega_m^2}}, \tag{5.85}$$

increasing with detuning from the resonant value

$$V_{t0} = \frac{2k_0}{Q_m V_{\text{dc}} \frac{\partial^2 C_{\text{nw}}}{\partial x^2}}, \tag{5.86}$$

and the additional phase φ appearing originates from the usual phase shift between the driving force and the mechanical response in absence of a parametric modulation. It is given by

$$\varphi = -\arctan\left(\frac{2Q_m \Delta_m}{\Omega_m}\right) \tag{5.87}$$

and appears, because for the phase sensitivity of the parametric modulation the phase difference between motion and 2Ω-drive is relevant and not the phase difference between the driving force and the modulation.

Finally, we can give the expression for the mechanical gain as

$$G = \frac{|x|_{\text{on}}}{|x|_{\text{off}}} = \left[\frac{\cos^2(\phi_p + \varphi)}{\left(1 + \frac{V_{2\Omega}}{V_t}\right)^2} + \frac{\sin^2(\phi_p + \varphi)}{\left(1 - \frac{V_{2\Omega}}{V_t}\right)^2} \right]^{1/2} \tag{5.88}$$

with the maximum and minimum values

$$G_{\max} = \frac{1}{1 - \frac{V_{2\Omega}}{V_t}}, \quad G_{\min} = \frac{1}{1 + \frac{V_{2\Omega}}{V_t}} \tag{5.89}$$

for

$$\phi_p^{\max} = \frac{\pi}{2} - \varphi, \quad \phi_p^{\min} = -\varphi, \tag{5.90}$$

respectively.

Figure 5.7 shows the parametric mechanical gain as a function of parametric phase ϕ_p and detuning from the mechanical resonance frequency $\Delta_m = \Omega - \Omega_m$, calculated using Eq. 5.88. The three different subplots show the gain for three different ratios of parametric drive voltage to threshold voltage $V_{2\Omega}/V_t$. As expected from the equations, we find a π-periodicity of the gain and the maximum and minimum values follow an arctangent as a function of detuning from the resonance frequency. We also see that with increasing parametric drive voltage and gain, respectively, the gradient of the gain with detuning also increases, demonstrating that frequency instabilities of the mechanical oscillator will lead to strong fluctuations of the gain as well in the high gain regime.

5.11. APPENDIX 8: PARAMETRIC MECHANICAL AMPLITUDE AMPLIFICATION - ANALYSIS AND ADDITIONAL DATA

To measure the mechanical amplitude amplification, we had to sweep the phase between the drive tone and the parametric pump. Instead of actually sweeping the phase, we decided to add a small detuning on the order of ~ 0.1 Hz to one of the tones, i.e., we measured a time trace of the transmission signal at Ω while parametrically modulating the mechanical resonance frequency with $(2\Omega + \delta)t = 2\Omega t + \delta t$. Then, the parametric phase is given by $\phi_p = \delta t + \gamma$ with an arbitrary offset term γ. We fitted the resulting power curves with

$$f(t) = \alpha_1 \left[\frac{\cos^2(\alpha_2 t + \alpha_3)}{(1 + \alpha_4)^2} + \frac{\sin^2 \alpha_2 t + \alpha_3}{(1 - \alpha_4)^2} \right] \tag{5.91}$$

from where we get

$$G_{\min} = \frac{1}{1 + \alpha_4}, \quad G_{\max} = \frac{1}{1 - \alpha_4}. \tag{5.92}$$

Repeating this procedure for different detuning allows to determine the maximum and minimum gain dependent on Δ_m. Finally, we fit the detuning dependent maximum and minimum gain points with the corresponding theoretical expression

$$f(\Delta_m) = \frac{\beta_1}{\left(\sqrt{1+\beta_2(\Delta_m-\beta_3)^2} \pm \beta_4\right)^2} \tag{5.93}$$

where $\pm$ is chosen for minimum and maximum gain, respectively. By this method, we can determine the maximum gain on resonance with higher fidelity than just setting the excitation frequency to the resonance frequency. This is due to small mechanical resonance frequency drifts and fluctuations of unknown origin in the device. Ultimately and for very high parametric excitation close to the threshold voltage, these frequency shifts also limit the observable gain, as it becomes more and more sensitive to frequency fluctuations.

5

5.12. APPENDIX 9: THEORY OF PARAMETRIC MICROWAVE AMPLIFICATION

We include the parametric driving equivalently to the case of mechanical parametric amplification into the optomechanical equations of motion and get

$$\delta\ddot{x} = -\left[\Omega_m^2 + \Omega_p^2\cos(2\Omega t+\phi_t)\right]\delta x - \Gamma_m\delta\dot{x} + \frac{\hbar G\bar{\alpha}}{m}\left(\delta\alpha+\delta\alpha^*\right) \tag{5.94}$$

$$\delta\dot{\alpha} = \left[i\bar{\Delta} - \frac{\kappa}{2}\right]\delta\alpha + iG\bar{\alpha}\delta x + \sqrt{\frac{\kappa_e}{2}}S_p. \tag{5.95}$$

where $\Omega_p^2 = k_p/m$ and ϕ_t considers an additional possible phase shift. We solve these equations again with the Ansatz

$$\delta\alpha = a_- e^{-i\Omega t} + a_+ e^{+i\Omega t} \tag{5.96}$$

$$\delta\alpha^* = a_-^* e^{+i\Omega t} + a_+ e^{-i\Omega t} \tag{5.97}$$

$$\delta x = x_1 e^{-i\Omega t} + x_1^* e^{+i\Omega t} \tag{5.98}$$

and the identity

$$\cos(2\Omega t+\phi_t) = \frac{1}{2}\left[e^{+i2\Omega t}e^{+i\phi_t} + e^{-i2\Omega t}e^{-i\phi_t}\right]. \tag{5.99}$$

Using rotating wave approximation and a lot of algebra yields the solution

$$x_1 = \hbar G\bar{\alpha}\chi_m^{\text{eff}}\left[\frac{\chi_c - \left(\chi_m^{\text{eff}}\right)^* \chi_c^* \frac{m\Omega_p^2}{2} e^{-i\phi_t}}{1 - \left|\chi_m^{\text{eff}}\right|^2 \frac{m^2\Omega_p^4}{4}}\right]\sqrt{\frac{\kappa_e}{2}}S_0 \tag{5.100}$$

$$a_- = \chi_c\left[1 + i2m\Omega_m g^2 \chi_m^{\text{eff}} \frac{\chi_c - \left(\chi_m^{\text{eff}}\right)^* \chi_c^* \frac{m\Omega_p^2}{2} e^{-i\phi_t}}{1 - \left|\chi_m^{\text{eff}}\right|^2 \frac{m^2\Omega_p^4}{4}}\right]\sqrt{\frac{\kappa_e}{2}}S_0. \tag{5.101}$$

This is a big and complicated expression, but it can significantly simplified for drives on one of the sidebands, i.e., for $\omega_d = \omega_c \pm \Omega_m$ and a probe very close to the cavity resonance $\omega_p \sim \omega_c$.

DRIVE ON THE RED SIDEBAND

When the cavity drive is set to the red sideband $\omega_d = \omega_c - \Omega_m$ and the probe tone is sweeping only very close to the cavity resonance frequency $\omega_p = \omega_c + \Delta_m$ with $\Delta_m \ll \kappa$, we can significantly simplify the equations. The cavity susceptibility becomes $\chi_c = \chi_c^* = 2/\kappa$ and the effective mechanical susceptibility becomes

$$\chi_m^{\text{eff}} = -\frac{1}{m\Omega_m}\frac{1}{2\Delta_m - i\Gamma_{\text{eff}}}. \tag{5.102}$$

After introducing $\chi_m^{\text{eff}} = |\chi_m^{\text{eff}}|e^{i\varphi_m}$ and the parameter

$$B = \frac{\Omega_p^2}{2\Omega_m}\frac{1}{\sqrt{\Gamma_{\text{eff}}^2 + 4\Delta_m^2}} = |\chi_m^{\text{eff}}|\frac{m\Omega_p^2}{2} \tag{5.103}$$

we can rewrite the intracavity amplitude as

$$a_- = \frac{2}{\kappa}\left[1 - i\frac{C\Gamma_m}{2\Delta_m - i\Gamma_{\text{eff}}}\frac{1 - Be^{-i(\phi_t+\varphi_m)}}{1 - B^2}\right]\sqrt{\frac{\kappa_e}{2}}S_0 \tag{5.104}$$

and the transmission as

$$S_{21} = \frac{\kappa_i}{\kappa} + i\frac{\kappa_e}{\kappa}\frac{C\Gamma_m}{2\Delta_m - i\Gamma_{\text{eff}}}\frac{1 - Be^{-i(\phi_t+\varphi_m)}}{1 - B^2}. \tag{5.105}$$

For the minimum and maximum transmitted power exactly on resonance we get

$$|S_{21}|^2 = \frac{\kappa_i^2}{\kappa^2} + \frac{C_p\Gamma_m}{\Gamma_{\text{eff}}^2}\left[2\frac{\kappa_i\kappa_e}{\kappa^2}\Gamma_{\text{eff}} + \frac{\kappa_e^2}{\kappa^2}C_p\Gamma_m\right] \tag{5.106}$$

,i.e., the same equation as without parametric drive, but with a parametrically enhanced/reduced cooperativity

$$C_p = \frac{C}{1 \pm B_0} \tag{5.107}$$

with $B_0 = \Omega_p^2/2\Omega_m\Gamma_m$ The net microwave power gain in this regime is given by $G_{\mathrm{mw}} = |S_{21}|^2_{\mathrm{max}} - 1$.

DRIVE ON THE BLUE SIDEBAND

On the blue sideband, we get $\chi_m^{\mathrm{eff}} = -|\chi_m^{\mathrm{eff}}|e^{-i\phi_m}$ and thus

$$a_- = \frac{2}{\kappa}\left[1 + i\frac{C\Gamma_m}{2\Delta_m + i\Gamma'_{\mathrm{eff}}}\frac{1 + Be^{-i(\phi_t-\varphi_m)}}{1-B^2}\right]\sqrt{\frac{\kappa_e}{2}}S_0 \tag{5.108}$$

for the intracavity field. The transmission parameter becomes

$$S_{21} = \frac{\kappa_i}{\kappa} - i\frac{\kappa_e}{\kappa}\frac{C\Gamma_m}{2\Delta_m + i\Gamma'_{\mathrm{eff}}}\frac{1 + Be^{-i(\phi_t-\varphi_m)}}{1-B^2} \tag{5.109}$$

Due to the nature of the interference when driving on the blue sideband (going from the OMIA regime to the OMIT regime with increasing cooperativity), it is not straightforward here to give a general expression for the minimum and maximum transmitted power.

REFERENCES

[1] A. Wallraff, D. I. Schuster, A. Blais, L. Frunzio, R.-S. Huang, J. Majer, S. Kumar, S. M. Girvin, and R. J. Schoelkopf, Nature **431**, 162 (2004).

[2] L. DiCarlo, J. M. Chow, J. M. Gambetta, Lev S. Bishop, B. R. Johnson, D. I. Schuster, J. Majer, A. Blais, L. Frunzio, S. M. Girvin, and R. J. Schoelkopf, Nature **460**, 240 (2009).

[3] R. Barends, A. Shabani, L. Lamata, J. Kelly, A. Mezzacapo, U. Las Heras, R. Babbush, A. G. Fowler, B. Campbell, Yu Chen, Z. Chen, B. Chiaro, A. Dunsworth, E. Jeffrey, E. Lucero, A. Megrant, J. Y. Mutus, M. Neeley, C. Neill, P. J. J. O'Malley, C. Quintana, P. Roushan, D. Sank, A. Vainsencher, J. Wenner, T. C. White, E. Solano, H. Neven, and J. M. Martinis, Nature **534**, 222 (2016).

[4] D. I. Schuster, A. A. Houck, J. A. Schreier, A. Wallraff, J. M. Gambetta, A. Blais, L. Frunzio, J. Majer, B. Johnson, M. H. Devoret, S. M. Girvin, and R. J. Schoelkopf, Nature **445**, 515 (2007).

[5] M. Hofheinz, E. M. Weig, M. Ansmann, R. C. Bialczak, E. Lucero, M. Neeley, A. D. O'Connell, H. Wang, J. M. Martinis, and A. N. Cleland, Nature **454**, 310 (2008).

[6] S. J. Bosman, M. F. Gely, V. Singh, A. Bruno, D. Bothner, and G. A. Steele, npj Quantum Information **3**, 46 (2017).

[7] N. K. Langford, R. Sagastizabal, M. Kounalakis, C. Dickel, A. Bruno, F. Luthi, D. J. Thoen, A. Endo, and L. DiCarlo, Nature Communications **8**, 1715 (2017).

[8] P. K. Day, H. G. LeDuc, B. A. Mazin, A. Vayonakis, and J. Zmuidzinas, Nature **425**, 817 (2003).

[9] C. A. Regal, J. D. Teufel, and K. W. Lehnert, Nature Physics **4**, 555 (2008).

[10] J. Suh, A. J. Weinstein, C. U. Lei, E. E. Wollman, S. K. Steinke, P. Meystre, A. A. Clerk, and K. C. Schwab, Science **344**, 6189 (2014).

[11] V. Singh, S. J. Bosman, B. G. Schneider, Y. M. Blanter, A. Castellanos-Gomez, and G. A. Steele, Nature Nanotechnology **9**, 820 (2014).

[12] M. Aspelmeyer, T. J. Kippenberg, and F. Marquardt, Rev. Mod. Phys. **86**, 1391 (2014).

[13] J. D. Teufel, T. Donner, D. Li, J. W. Harlow, M. S. Allman, K. Cicak, A. J. Sirois, J. D. Whittaker, K. W. Lehnert, and R. W. Simmonds, Nature **475**, 359 (2011).

[14] F. Massel, T. T. Heikkilä, J.-M. Pirkkalainen, S. U. Cho, H. Saloniemi, P. J. Hakonen, and M. A. Sillanpää, Nature **480**, 351 (2011).

[15] D. Malz, L. D. Tóth, N. R. Bernier, A. F. Feofanov, T. J. Kippenberg, and A. Nunnenkamp, Phys. Rev. Lett. **120**, 023601 (2018).

[16] S. Barzanjeh, M. Wulf, M. Peruzzo, M. Kalaee, P. B. Dieterle, O. Painter, and J. M. Fink, Nature Communications **8**, 953 (2017).

[17] B. A. Levitan, A. Metelmann, and A. A. Clerk, New J. Phys. **18**, 093014 (2016).

[18] V. Singh, B. H. Schneider, S. J. Bosman, E. P. J. Merkx, and G. A. Steele, Appl. Phys. Lett. **105**, 222601 (2014).

[19] D. Rugar and P. Grütter, Phys. Rev. Lett. **67**, 699 (1991).

[20] S. Weis, R. Rivière, S. Deléglise, E. Gavartin, O. Arcizet, A. Schliesser, and T. J. Kippenberg, Science **330**, 1520 (2010).

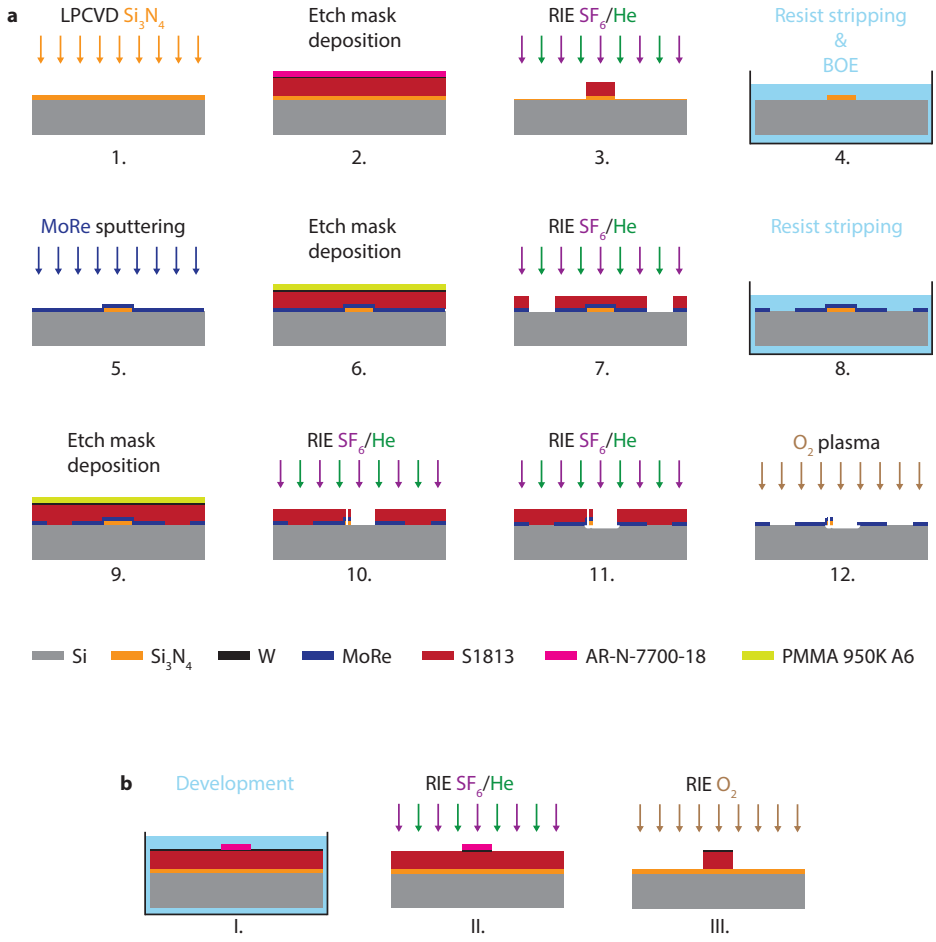

Figure 5.1: **Schematic device fabrication.** **a** 1.-4. show the deposition and patterning of the Si_3N_4 patches, 5.-8. show the deposition and patterning of the superconducting microwave structures and 9.-12. show the nanobeam patterning and release. **b** Steps between 2. and 3. of a. Equivalent steps are performed between 6. and 7. and between 9. and 10. of a. Dimensions are not to scale. A description of the individual steps is given in the text.

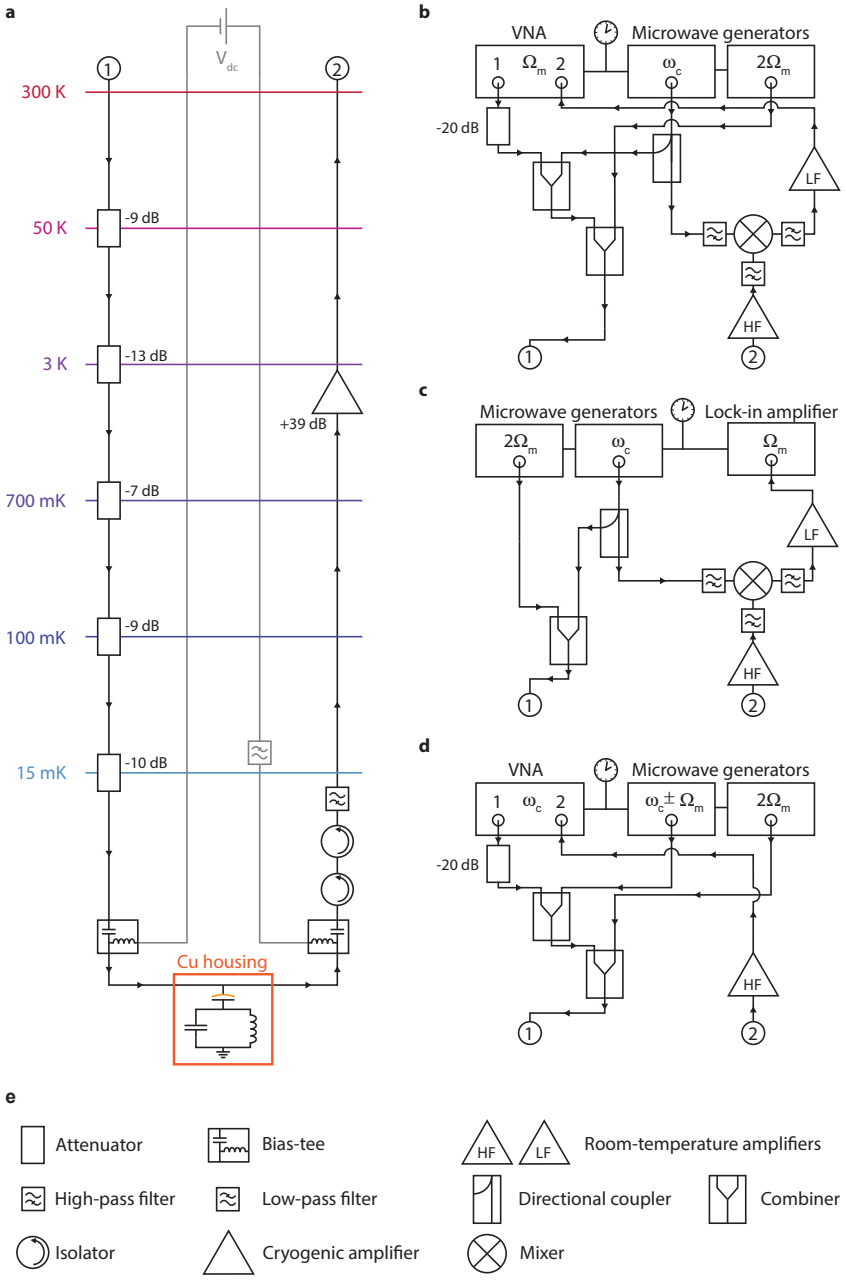

Figure 5.2: **Schematic of the measurement setup.** Details are given in the text.

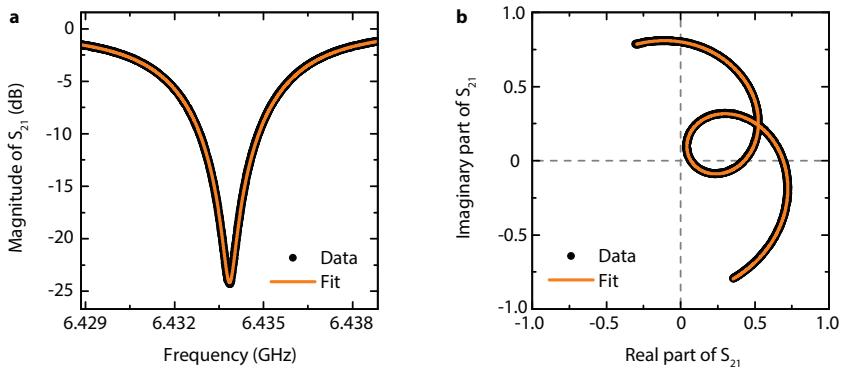

Figure 5.3: **Fitting the resonance line and extraction of the relevant parameters**

5

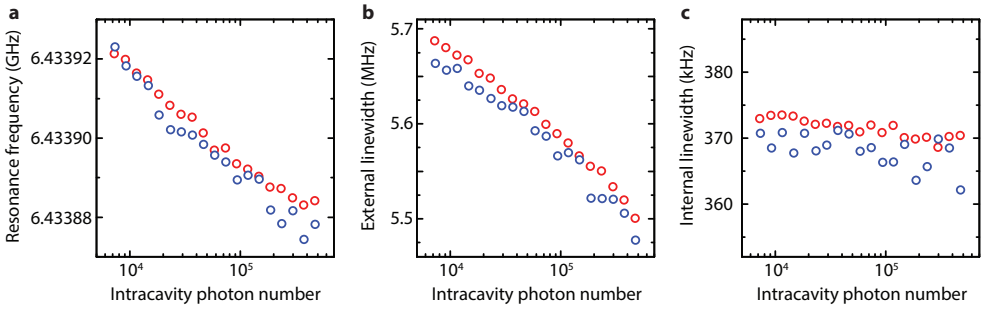

Figure 5.4: **Cavity parameters in presence of a sideband drive vs intracavity photon number.** Red data points correspond to a drive at $\omega \sim \omega_c - \Omega_m$, blue data points to a drive at $\omega \sim \omega_c + \Omega_m$.

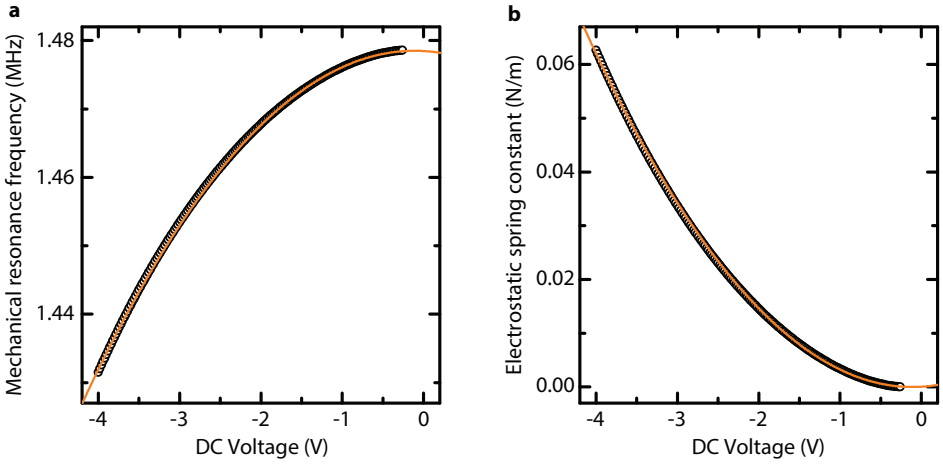

Figure 5.5: **Mechanical resonance frequency tuning and electrostatic spring constant.** In **a** the measured resonance frequency is plotted vs applied DC voltage on the feedline (black circles). The orange line is a fit using Eq. (5.22) with $k_{\mathrm{dc}} \propto V_{\mathrm{dc}}^2$. In **b** the electrostatic spring constant calculated from the fit in **a** is shown as orange line. The experimental data (black circles) are calculated using Eq. (5.70) At the operation point of this paper $V_{\mathrm{dc}} = -4\,\mathrm{V}$, we obtain $k_{\mathrm{dc}} = 0.063\,\mathrm{N/m}$.

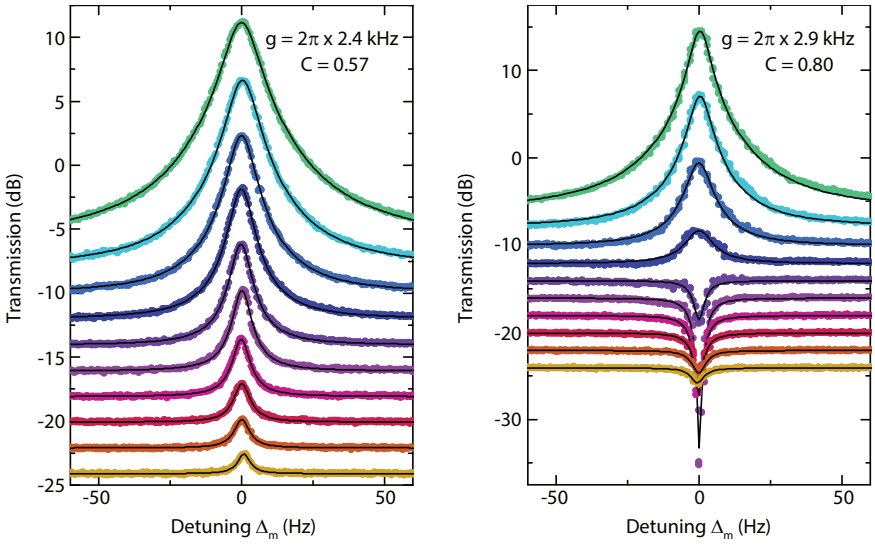

Figure 5.6: **Optomechanically induced transparency and absorption.** For this experiment we drive the cavity with a strong drive tone on either the red sideband $\omega = \omega_c - \Omega_m$ (**a**) or on the blue sideband $\omega = \omega_c + \Omega_m$ (b). Then we sweep a weak probe signal around $\Delta_m = \omega - \omega_c$. In **a**, a Lorentzian shaped peak corresponding to exciting the mechanical resonator appears and grows with increasing sideband drive power in both, height and width. In **b**, the cavity response for a drive on the blue sideband is shown. For the lower powers, optomechanically induced absorption appears, i.e., a narrow absorption dip in the cavity minimum. For higher powers, this dip turns into a transparency peak as well. The lowest line in both (baseline at $-24\,\mathrm{dBm}$), **a** and **b**, corresponds to the lowest drive power and subsequent lines are manually upshifted by $2\,\mathrm{dB}$ each for better visibility. For both plots, the difference in drive power between subsequent lines is $2\,\mathrm{dBm}$, where the largest power corresponds to an intracavity drive photon number of $\sim 3 \cdot 10^5$ for the red sideband and $\sim 3 \cdot 10^5$ for the blue sideband drive.

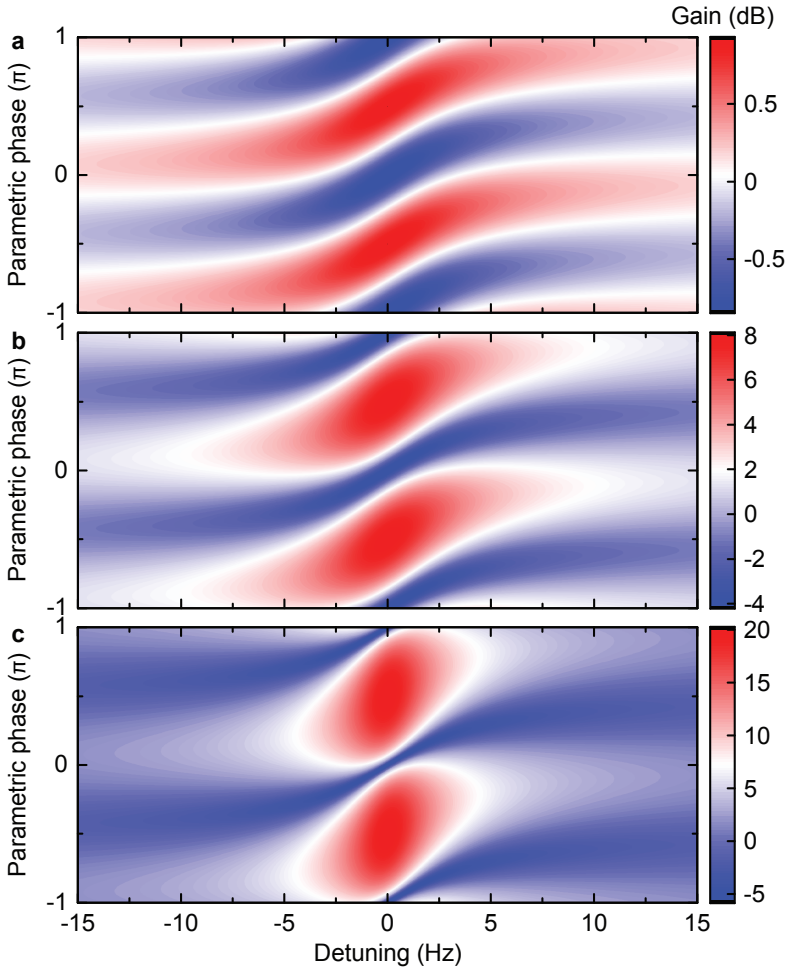

Figure 5.7: **Calculated mechanical parametric gain.** Plots showing the mechanical parametric gain vs parametric phase ϕ_p and vs detuning from the mechanical resonance frequency Ω_m for three different parametric modulation amplitudes. **a** $V_{2\Omega}/V_t = 0.1$, **b** $V_{2\Omega}/V_t = 0.6$, **c** $V_{2\Omega}/V_t = 0.9$. The gain shows a π-periodicity and maxima/minima values follow an arctangent function with detuning. The calculation parameters were chosen close to the experimental device with $\Omega_m = 2\pi \cdot 1.4\,\text{MHz}$ and $Q_m = 195000$.

6

HYBRID SQUID CAVITIES FOR IMPROVED COHERENCE COMPARED TO ALL-ALUMINIUM, SINGLE STEP DEVICES

Here, we study coherence in flux-tunable Josephson junction resonators made with two different fabrication processes. We compare the same design of lumped element resonators made with two different techniques. In one process, we fabricate hybrid devices, etching a MoRe layer, and subsequently, an aluminium dc SQUID is evaporated using the Dolan bridge technique. In the other process, we fabricate devices with a single Al lift off process for both the SQUID and the cavity using the Dolan bridge technique. We then study the coherence of the two types of SQUID cavities by measuring the quality factor of their resonances as a function of flux and photon number. After comparing the coherence in these flux tunable resonators, we conclude that the hybrid fabrication method yields much higher internal quality factors.

6.1. INTRODUCTION

High coherence in superconducting resonant circuits is a highly desired property for any superconducting microwave component in the field of low temperature microwave circuits. The reduction of microwave losses benefits many applications, including high kinetic inductance detectors[1–3], superconducting qubits[4, 5], Josephson parametric amplifiers[6–8], and superconducting hybrid systems [9–11]. Recent research shows that the reduction of the participation ratio of the dielectric lossy layer with respect to the mode volume improves the coherence of superconducting qubits in 3D realization[5]. It is also proven that this knowledge can be applied to two dimensional circuits, providing a higher scalability beneficial for quantum information processing[12].

In this chapter, we compare the coherence of flux-tunable resonators fabricated with two different processes. The devices tested are lumped element resonators coupled to a microwave transmission line, along with the second device, which is a coplanar waveguide resonator terminated by a dc SQUID. In one of the fabrication processes, we made samples with a combination of reactive ion etching of MoRe lumped element resonators and lift-off of dc SQUIDs. The other procedure is a single lift-off process with a double angle evaporation of Al/AlOx/Al. In this study, we find that the single lift-off process resulted in internal quality factors two orders of magnitude lower than those yielded by the process with a reactive ion etching of resonators and lift-off of only the dc SQUIDs.

The system that we study is a lumped element resonator side coupled to a transmission line, and is illustrated schematically in Fig. 6.1 (a). In the resonator, a dc SQUID is embedded inside the inductive part of the resonator, which can be seen Fig. 6.1 (b). The dc SQUID provides a Josephson inductance that oscillates as a function of the externally applied flux with a periodicity of $\Phi_0 = \frac{e}{2\hbar}$. The total inductance of the resonator is given by $L_g + L_J(\Phi)$, where L_g and $L_J(\Phi)$ are the geometric and Josephson inductance, respectively.

Here we start by deriving an analytical expression for the Josephson inductance. Due to the large designed $L_J = 300$ pH, we have neglected the geometric inductance of the SQUID loop $L_g^{SQ} \sim 10$ pH in the following analysis. (A detailed analysis of such circuits can be found in [13]). We consider a symmetric dc SQUID where the two Josephson junctions have the same critical current, I_1, I_2, where $I_n = I_{c0}\sin\gamma_n$, with $n = 1,2$, where n indicates the two Josephson junctions of the SQUID. The total current is given by $I = I_1 + I_2$, and circulating current by $J = (I_1 - I_2)/2$. These two equation can be expressed in the following forms:

$$I = 2I_{c0}\cos\phi\sin\gamma \tag{6.1}$$

$$J = I_{c0}\sin\phi\sin\gamma \tag{6.2}$$

where $\phi = \pi\frac{\Phi}{\Phi_0}$ is the flux frustration and $\gamma = \frac{1}{2}(\gamma_1 + \gamma_2)$ is the phase difference across the SQUID, $\theta_2 - \theta_1$, shown in the right side of Fig. 6.1 (a). An important consequence of

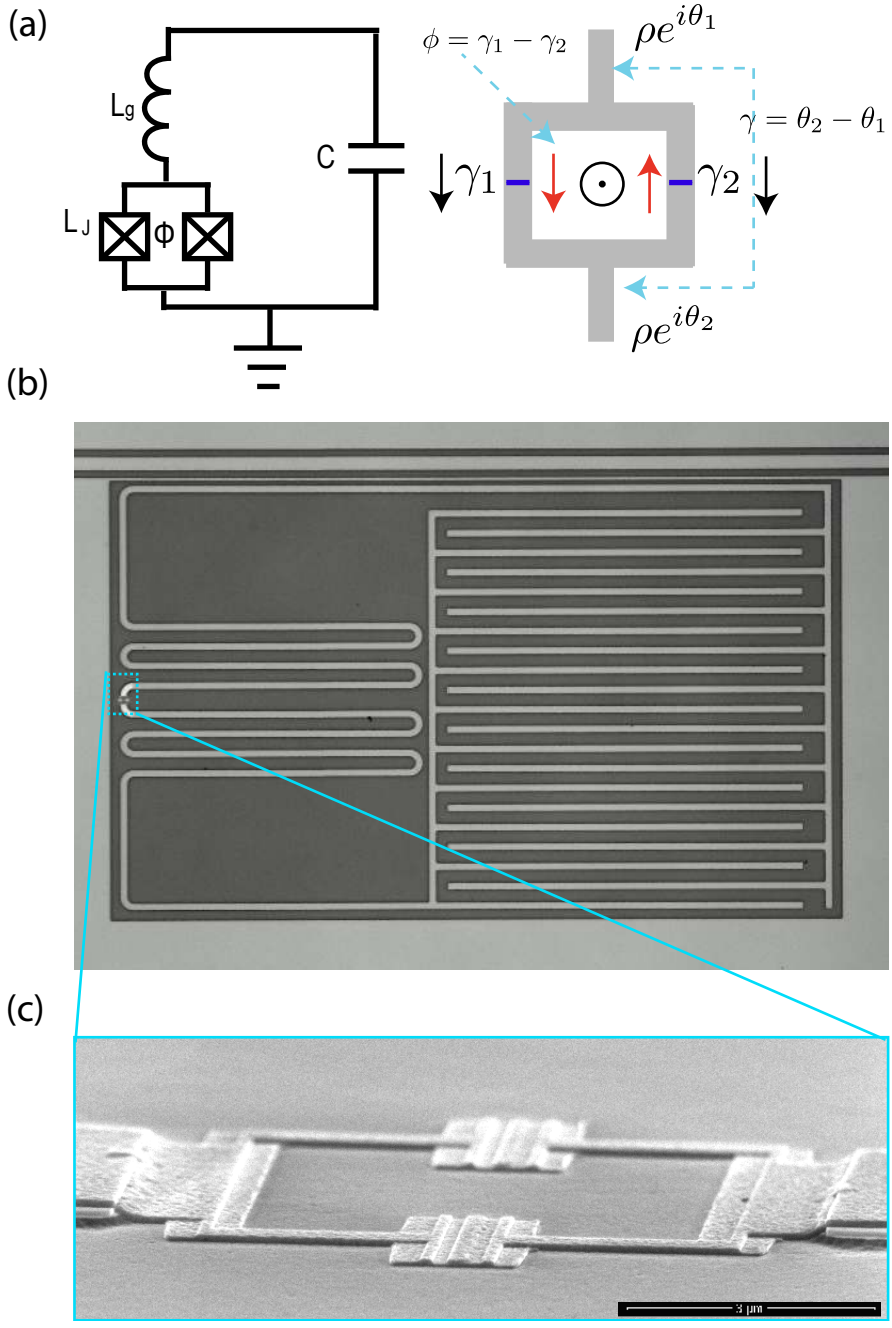

Figure 6.1: (a) Left figure shows a schematic circuit representation of a flux-tunable Josephson junction resonator. Right figure shows a schematic diagram of a dc SQUID. γ_1 and $\gamma 2$ are the superconducting phase of each junction indicated by black arrows. Red arrows indicate a circulating current. γ is the superconducting phase difference over the SQUID, and ϕ is the magnetic flux through the SQUID loop, which consists of the difference between the phases of each junction. (b) Optical microscopic image of the device. The device is side coupled to the transmission line. In the cyan inset (dotted), the dc SQUID is galvanically coupled to the lumped element inductor. (c) Scanning electron microscopic image of dc SQUID.

these expressions is the appearance of an inductance L_J associated with the Josephson junction in the form

$$V = L_J(\phi)\frac{dI}{dt} \tag{6.3}$$

From the Josephson relation, we can obtain

$$L_J = \varphi_0 \frac{d\gamma/dt}{dI/dt} \tag{6.4}$$

where $\varphi_0 = \frac{\Phi_0}{2\pi}$ is the reduced flux quantum.

In the following, we will neglect $d\phi/dt$. This is justified due to the small geometric inductance of the SQUID loop (see Appendix 5.). With $d\phi/dt$=0, we have the following for dI/dt from Eq. 6.1.

$$\frac{dI}{dt} = I_c \cos\phi \cos\gamma \frac{d\gamma}{dt}, \tag{6.5}$$

Here, I_c is the critical current of the SQUID. Using Eq. 6.4, the Josephson inductance is given by

$$L_J = \varphi_0 \frac{1}{I_c \cos\phi \cos\gamma}. \tag{6.6}$$

For small excitation powers, $\cos\gamma \sim 1 - \frac{\gamma^2}{2}$, using $1/(1-\gamma^2/2) \sim 1+\gamma^2/2$, which gives

$$L_J = \varphi_0 \frac{1}{I_c \cos\phi}(1 + \frac{\gamma^2}{2}). \tag{6.7}$$

Now we consider only the linear term in Eq. 6.7, which will be valid only when the SQUID cavities are driven at sufficiently low excitation powers, and where the junctions are still under a linear operation regime:

$$L_J = \varphi_0(\frac{1}{I_c \cos\phi}). \tag{6.8}$$

When operating in a linear regime (where $I << I_c$), only the first term in Eq. 6.7 plays a role as a Josephson inductance, and the total inductance of the cavity can be expressed as follows.

$$L_{tot} = L_g + \frac{\varphi_0}{I_c \cos|\frac{\pi\Phi}{\Phi_0}|} \tag{6.9}$$

Here, the first term on the right hand side of the equation is the geometric inductance of the resonator, the second term is the contribution of the Josephson junctions, and Φ is the applied flux through the SQUID loop. Furthermore, from the expression of the resonance frequency of a flux tunable resonator $\omega(\Phi) = 1/\sqrt{L_l(\Phi)C_l}$, one can also express this as

$$\omega(\Phi) = \frac{\omega_0}{\sqrt{1 + \Gamma/\cos(\frac{\Phi}{\Phi_0})}} \tag{6.10}$$

where $\Gamma = \frac{L_J}{L_J + Lg}$ is the SQUID inductance participation ratio and ω_0 is the frequency of the cavity in the limit, $L_J \to 0$.

6.2. EXPERIMENTAL METHODS

We have tested two different fabrication procedures for flux tunable resonators. One type of resonator consists of a lumped element resonator made of 60 nm thick molybdenum rhenium (MoRe) which is deposited by rf sputtering and etched with reactive ion etching (RIE). Subsequently, the dc SQUID with Al/AlOx/Al is shadow evaporated with the Dolan bridge technique.

The substrate, high resistivity ($\rho \sim 10000\Omega cm$) silicon (100) wafer, is first cleaned in an RCA 1 solution at 70°C for 10 minutes, followed by piranha cleaning at 90°for 10 minutes. The purpose of this cleaning is to remove particles and any organic chemicals on the surface of the substrate. Subsequently, the substrate is cleaned in a BHF solution to remove native oxide and terminate the surface with hydrogen, which has a hydrophobic surface.

MoRe superconducting metal is then deposited with rf sputtering with the thickness of 60 nm immediately after the BHF wet etching. An S1813/Tungsten/PMMA tri-layer resist stack is then spin coated on the surface of the substrate and afterwards the microwave circuits are patterned with electron beam lithography (EBL) and reactive ion etching (RIE). Finally, the substrate is developed in a solution ofMIBK: IPA 1:3, followed by IPA in order to stop the developing process. The surface of the exposed areas is tungsten. In the RIE, tungsten, S1813, and MoRe are etched sequentially with SF_6/He, oxygen, and SF_6/He, respectively. After etching, the resist mask is removed in hot PRS 3000 resist stripper.

Next, the substrate is spin coated with a bi-layer MMA / PMMA 950 resist stack, and patterns for the Dolan bridges are exposed. The substrate is developed in a mixture of MIBK: IPA 1:3 and IPA to stop the development. Right before the evaporation of the junctions, the substrate is de-scummed in the oxygen plasma at 150 W for 30 s and then cleaned in BHF for 30 s. With this procedure we can remove all contaminants and native oxide on the surface of the MoRe and therefore obtain a much better MoRe–Al interface. Immediately after the BHF cleaning, the substrate is loaded in an electron beam evaporator, and Al is evaporated from 11°from each side over the Dolan bridges with an oxidization step in the middle. The substrate is then lifted off with a hot NMP solution until the resist stack comes off completely.

Fig. 6.2 (b)) is an optical microscopic image of the device. Fig. 6.2 (c) shows a high angle electron microscope image of the SQUID. The SQUID loop is designed to be $5 \times 5\ \mu m^2$, but due to angle evaporation, the side is slightly less than 5 μm. Each sample has multiple lumped element (LE) flux-tunable resonators, which are side coupled in order to measure more than one resonator at once. On each chip, we also include CPW and LE resonators without SQUIDs as reference devices. The other type of resonator was fabricated with a single step lift-off of the Al/AlO_x/Al, including the microwave resonators and ground planes. In [14], a comparison of 2D CPW linear resonator from both procedures is presented. Here we compare the microwave coherence of flux tunable resonators whose inductance is modulated with a dc SQUID.

The fabrication procedure of the flux-tunable resonator of this type is the same

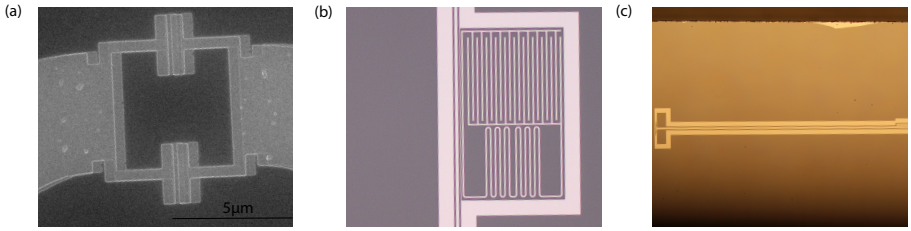

Figure 6.2: (a) SEM image of the device fabricated with single lift-off. (b) Optical microscope image of the device. The picture does not contain a SQUID, but the measured device contains a dc SQUID the same as shown in (a). (c) CPW resonator terminated by a dc SQUID fabricated the same way as the device shown in Fig. 6.2 (b).

as the second half of the previous fabrication technique. The single lift-off procedure uses the same resist stack MMA/PMMA 950. The microwave resonator patterns including the Dolan bridges are exposed with EBL. The substrate is developed in a solution of MIBK: IPA 1:3 and IPA. The substrate is de-scummed in oxygen plasma at 150 W for 30 s and cleaned in BHF for 30 s prior to shadow evaporation and the substrate is then lifted off in hot NMP. Fig. 6.2 (b) shows an image of a lumped element resonator fabricated with this technique. The structure of the resonator is the same, but due to the limited time of exposure, the ground plane is limited to 50 μm. We also tested a SQUID cavity made from a CPW shorted by a SQUID, as shown in Fig. 6.2 (c). This device is configured in a reflection geometry.

All devices were mounted in a light-tight copper sample box and thermally anchored to the mixing chamber plate of a dilution refrigerator where the base temperature is below 20 mK. The microwave signal was attenuated at each stage inside the dilution refrigerator to provide thermalization of the microwave photons, and the signal was applied through a 50 Ω transmission line. The transmission or reflection spectrum was measured using a vector network analyser (VNA). The magnetic field was externally applied through the SQUID loop with a superconducting solenoid mounted on the mixing chamber of the dilution refrigerator. No magnetic shielding was used during these measurements.

6.3. BASIC CHARACTERIZATION

In our measurements, the transmission spectrum S_{21} of the flux-tunable lumped element resonators was analysed. Fig. 6.3 shows the basic characterization of the hybrid resonators. Fig. 6.3 (a) shows a colour scale plot of $|S_{21}|$ as a function of the flux and the flux dependence of resonance frequencies, f_0, of the devices. The y axis is the drive frequency f. Each SQUID cavity on the chip was designed with a different geometric inductance, and therefore, at integer flux quantum it resonates at a different maximum frequency. The difference in resonance frequencies allows identifying each of the SQUID cavities in the multiple measurements.

There are in all 5 resonant modes (Fig. 6.3 (a)), where only 3 of them depend on the external magnetic field. These have their integer flux quantum peaks around 5.2 GHz, 5.75 GHz, and 6.47 GHz (outside the measurement window). Note that the external magnetic fields corresponding to integer flux quantum for the three resonators are different, probably due to the flux induced in the SQUID loop during zero field cooling.

The two modes independent of the external magnetic field correspond to the resonators that do not contain a dc SQUID. On the chip, there are three reference resonators for the purpose of characterizing the MoRe film. One of the reference resonators is the lumped element linear resonator. The mode slightly below 5.5 GHz is the mode of the lumped element reference linear resonator. The other two reference resonators have a CPW quarter wavelength geometry. The mode around 5.85 GHz corresponds to the resonance frequency of one of the two CPW resonators. The colour scale indicates the depth of the transmission spectrum. As the response gets darker, the depth of the response gets bigger. The x-axis is the bias current applied to the superconducting solenoid.

Fig. 6.3 (b) shows the flux dependence of the frequency of the lowest mode in Fig. 6.3 (a). The Josephson junction participation ratio to the total inductance was calculated from the curvature of the frequency shift due to the flux through the SQUID loop [15], which is shown in the blue line of Fig. 6.3 (b). Using Eq. 6.9, the Josephson inductance participation ratio was determined to be 11%. In order to determine the Josephson inductance from the participation ratio, we performed simulations in Sonnet to determine the effective geometric inductance seen at the position of the junction. First, we adjusted the property of the metal in the simulation: we changed the value of the sheet inductance so that the resonance frequency in the simulation would match with the reference mode found in the measurement. To find the Josephson inductance at integer flux quantum, we introduced an ideal lumped element inductive element into the circuit in the simulation. This ideal inductive element takes the role of a Josephson inductance in a real circuit and we can adjust it to match the peak value by adjusting this ideal inductance to match with the peak value of the resonance frequency at integer flux quantum in the measurement. We found a total inductance of 2.9 nH and a Josephson inductance of the SQUID at integer flux quantum of 0.35 nH. The participation ratio, including the geometric inductance and capacitance, can be

further identified by looking at the frequency shift of the resonance upon increasing the ideal inductance. The shift can be thought as a shift due to flux tuning, which is adjusting the inductance participation ratio. The critical current can be estimated from the room temperature resistance over the SQUID and superconducting gap of the aluminium, which is discussed in the appendix 1: we find agreement of these estimates based on R_n to unity about 50%.

Fig. 6.3 (c) shows the transmission spectrum of the resonant mode shown in Fig. 6.2 (b) at zero flux quantum with an input power of -133.77 dBm at the device. The response is not symmetric Lorentzian. Its asymmetry arises from a Fano resonance, the origin of which is most likely to be from an impedance mismatch of the transmission line including coaxial cables both outside and inside the fridge, and wire-bonds. We chose to normalize the response to the first point of the sweep. The right half of the sweep, which goes above one, does not indicate a larger signal coming out of the cavity at that frequency but is instead an artifact due to the Fano resonance interference effects and our choice of normalization. The response is fitted to the skewed Lorentzian function with loaded and unloaded quality factors of 1670.4 and 24022.2.

Fig. 6.3 (d) shows the internal quality factor determined from the fits as a function of the flux through the SQUID loop. The y-axis is the internal quality factor and the x-axis is the flux applied through the SQUID loop. A reduction in internal Q when approaching half-integer flux quantum is also observed in [15] and [16]. The origin of this loss at half integer flux quantum has been discussed in the literature but it is not totally understood. However, [15] proposed that these losses could come from thermal fluctuations inside the cavity. The number of intracavity thermal photon of microwave cavity can be expressed as $n_{th} = 1/[exp(\hbar\omega_0/k_B T) - 1]$. For a resonance of 4~5 GHz, the thermal occupation should be well below 1 if the field is thermalized to the base temperature of the fridge, 20 mK, and therefore the thermal occupation should not be a leading cause of degradation in the vicinity of half-integer flux quantum. However, thermalization of superconducting circuits to the base temperature of the fridge can also be difficult as the effective temperature could be higher, but probably not higher than 100 mK [17].

Sandberg et al.[16] suggested that this loss is generated from subgap resistance. When there is a voltage bias of a Josephson junction based resonant system, the subgap resistance is a parameter to determine the quality of the cavity. However, the subgap resistance is not expected to depend on the flux. In addition, if the subgap resistance is the leading term of the loss in the cavity, the power dependence at an arbitrary flux point away from integer-flux quantum may show a different trend at integer-flux quantum, something which we do not observe.

Another source of the larger linewidth is flux noise. The flux sensitivity of a SQUID is enhanced when approaching a half-integer flux quantum; the susceptibility to noise going through the SQUID loop is also increased, which leads to the reduction of quality as flux noise. The source of flux noise could be either extrinsic or intrinsic, e.g. small fluctuations of the magnetic field on background which might exist constantly

in the lab, and the quality decreases as the flux sensitivity is enhanced approaching half integer flux quantum, while the global magnetic field noise contributes to the loss. Flux noise might also arise from origins intrinsic to the sample. The model proposed for this phenomenon is a process of unpaired electrons occupancy defects and neighboring voids that causes fluctuations of the electron spin residing in a defect on the surface of the substrate or superconducting metal[18].

In Fig. 6.4, we study the flux dependence of the internal decay rates in more detail. We assume the leading term of the microwave loss away from integer flux quantum to be flux noise, and that the flux noise is constant as a function of the flux. At that point, all the fluctuation noise of the flux contributes to microwawve loss via the SQUID. This gives the relation

$$\kappa_{int} = \sqrt{\kappa_{min}^2 + \frac{d\omega}{d\Phi}\sigma_\Phi} \tag{6.11}$$

where $\kappa_{min} = f(\Phi)/Q_{int}(\Phi)$ at integer flux quantum, and σ_Φ is the flux noise. The cyan points in the figure are the experimental data which is defined by $f(\Phi)/Q_{int}(\Phi)$. The red solid line is the plot with Eq. 6.11 with 1 mΦ_0 of flux noise. The purple solid line is the plot with 2.6 mΦ_0 of flux noise. The flux noise was initially calculated from the change in the frequency under flux and the change in the internal quality factor. A flux noise of 1 mΦ_0 is the estimated value at -0.3 Φ_0 of flux bias.

Looking at the figure, we can see that neither of the estimated plots lies on top of the experimental data (cyan). The red line agrees near integer flux quantum and the purple plot matches around 0.4 Φ_0. From this we can conclude: (1) The noise cannot be explained by the flux noise itself with the assumption of confstant flux noise over a period of one flux quantum. (2) The noise required to cause an increase in the linewidth at 0.3 Φ_0 is in the range of 1 mΦ_0 of the flux fluctuation. This appears quite large for flux noise, although we cannot draw any conclusions, since the deviation from the prediction of the flux dependence also points to another unknown origin.

6.4. POWER DEPENDENCE

Fig. 6.5 shows the power dependence of the internal quality factor of two devices. Here, we have fixed the external flux such that the resonant mode is the maximum point, where $\pi\Phi/\Phi_0 = 0$. The measured transmission spectrum is a function of the power, and the unloaded quality factor is determined at different powers. The resonators are driven in the linear regime and fitted to a Lorentzian function as a function of power. The input power to the device has been varied from ~ -142.86 dBm to ~ -112.86 dBm, which is estimated by adding up the total attenuation of the input line (see Appendix 2). Fig. 6.5 shows a comparison of two flux-tunable resonators. The yellow points indicate the internal quality factors of one device at zero flux quantum fabricated with the hybrid process. The x-axis is the intracavity photon number, which is converted from total attenuation from the VNA to the sample. The blue points are the internal quality factors of a sample fabricated with the single lift off pro-

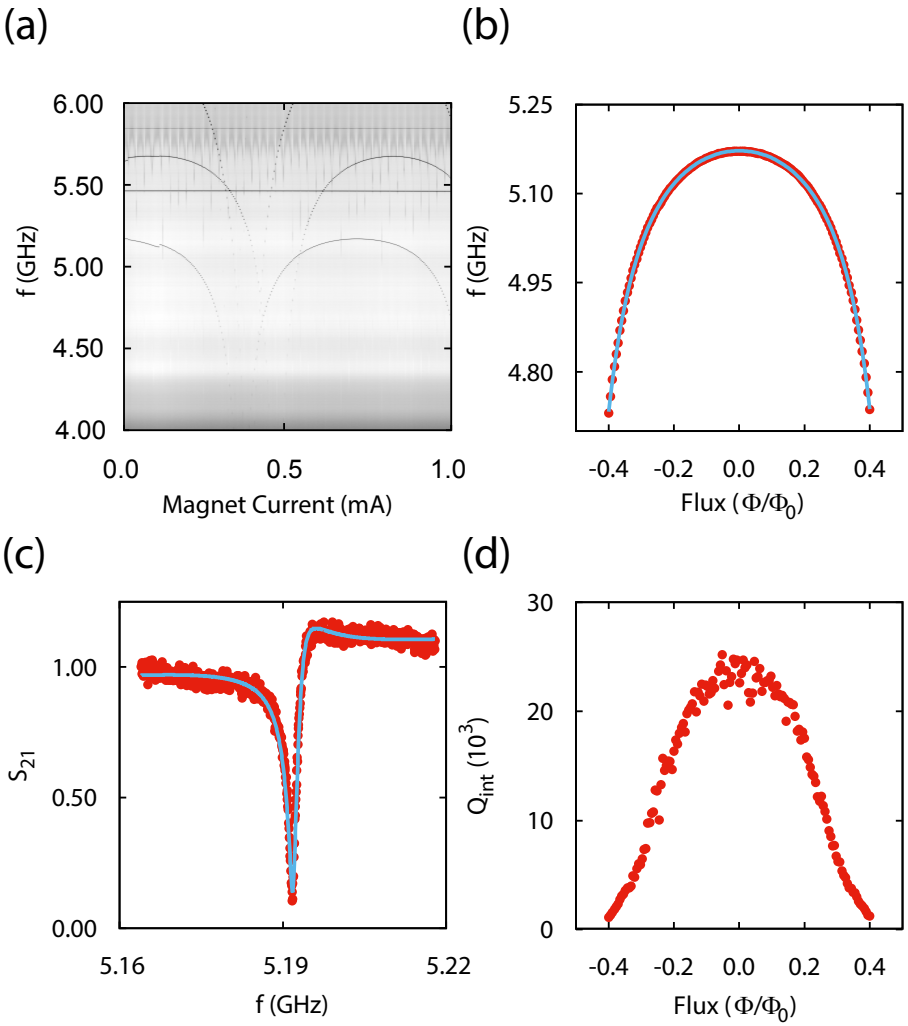

Figure 6.3: Basic characterization of flux-tunable Josephson junction resonator, device **HY 1**. (a) Multiple resonances of different devices are measured simultaneously while applying external flux through the SQUID loops. Colour scale in the figure indicates depth in $|S_{21}|$. The x-axis represents current applied through the superconducting solenoid for approximately one and one-half full flux quantum. The y-axis is the driving frequency f with a VNA. (b) Critical current of dc SQUID is estimated from the fitting to be 940 nA. The y-axis of the figure represents the drive frequency f, and the red points indicate the resonance frequency, f_0, of one of the lowest modes in Figure 6.3 a. (c) Spectrum measurement of the resonator response, S_{21}. The trace is taken at integer flux quantum, with an unloaded quality factor Q_{int} of 24022.2. (d) Unloaded quality factor of the resonator as a function of flux through the SQUID loop.

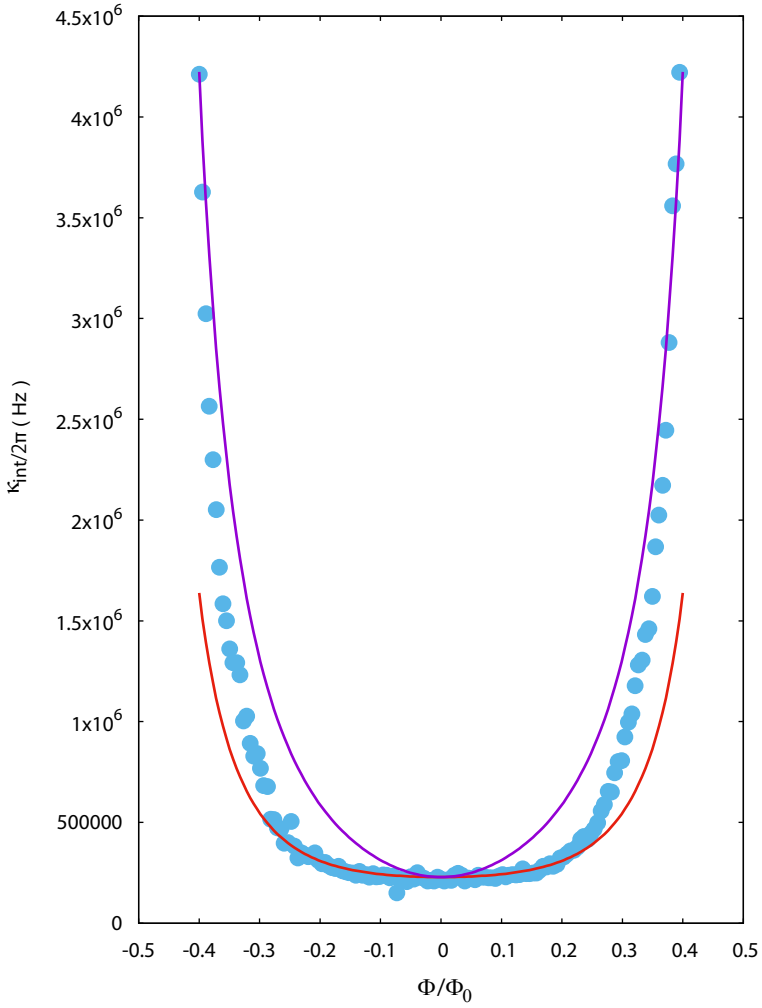

Figure 6.4: **Linewidth vs flux of device HY 1.** Cyan points are linewidths of unloaded resonator mode at different fluxes, ω_0/Q_{int}. Purple and red solid lines are numerical simulations of κ, assuming the flux dependent loss is determined by constant flux noise. The red line corresponds to the case when the flux noise is 1 mΦ_0. The purple line corresponds to 2.6 mΦ_0 of flux noise.

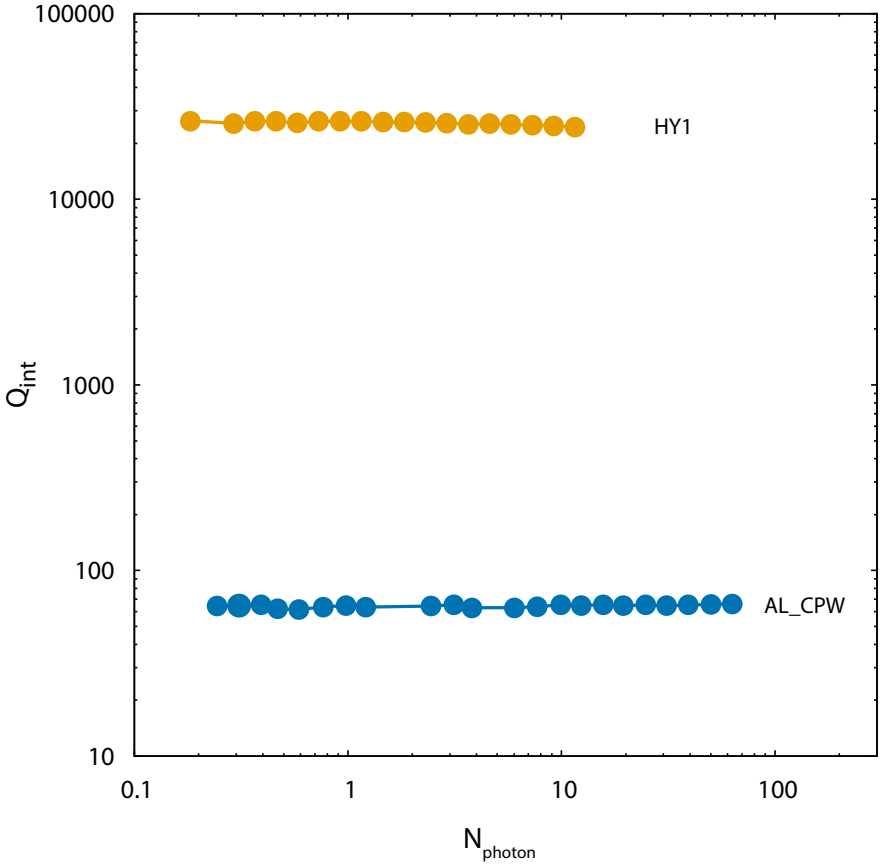

Figure 6.5: Comparison of internal quality factors as functions of power. Yellow dots represents Hybrid flux tunable resonator (**HY 1**). Blue dots represent single step Al lift-off process (**AL_CPW**).

cess in the CPW geometry. This data is also taken at zero flux quantum. The data is shown only for fits that show a good fit to the Lorentzian response, discarding higher powers where the response becomes non-linear. The figure is cropped so that all the responses at the different powers fit well with a Lorentzian function. For the hybrid device, the dynamic range is limited around 10. From the figure, the internal quality factor of the hybrid device is much higher than the device made with the single lift off technique.

Table 6.1: Comparison of quality factors of the hybrid devices, the Al SQUID devices, and the MoRe reference resonators

Device	Type	$Q_{int}(10^3)$	$Q_{ext}(10^3)$	f_0	Metal
HY 1	hybrid	25	2.3	5.172 GHz	MoRe+Al/AlOx/Al
HY 2	hybrid	12	1.1	5.710 GHz	MoRe+Al/AlOx/Al
AL_LE 1	Al SQUID lumped element	0.167	1.27	5.4786 GHz	Al/AlOx/Al
AL_LE 2	Al SQUID lumped element	0.152	2.12	5.1054 GHz	Al/AlOx/Al
AL_CPW	Al SQUID CPW	0.039	0.044	6.084 GHz	Al/AlOx/Al
REF_LE 1	lumped element reference	11	1.73	5.44 GHz	MoRe
REF_LE 2	lumped element reference	18	1.60	5.46 GHz	MoRe
REF_-CPW 1	CPW reference	17	4.4	6.37 GHz	MoRe
REF_-CPW 2	CPW reference	15	7.72	5.83 GHz	MoRe
REF_-CPW 3	CPW reference	10	7.4	5.845 GHz	MoRe

6.5. QUALITY FACTORS AT INTEGER FLUX QUANTUM

Table 6.1 shows a list of different resonator tests with quality factors. The first thing to note is the internal quality factors of reference resonators. Two types of reference resonator, CPW and lumped element, are comparable to the values of hybrid1 and hybrid2. This indicates that the internal quality factors of hybrid devices are not limited by dielectric loss from an interface between MoRe/AlO_x or AlO_x insulating layer of the junction. However, the internal quality factors of the reference resonators are not as high as the ones reported previously for MoRe. For CPW resonators made on top of a sapphire substrate, the internal quality factor can reach 0.7 million at high power [19]. On a substrate of intrinsic silicon, the internal quality factor can be as high as 0.1 million[20]. Our device was fabricated on top of an intrinsic silicon substrate, and the MoRe was deposited with the same machine as for the devices in the references above. One possible reason for the degradation is insufficient surface preparation. For the fabrication of the device, the substrate was cleaned to remove organic material that could possibly be on top of the surface from dicing with RCA1 and piranha. And subsequently native oxide was removed with buffered hydrofluoric oxide (BHF) prior to the sputtering of the MoRe film. Although this surface preparation seems thorough, there could be small details of the fabrication that could have degraded the interface quality.

6.6. DISCUSSION

In Fig. 6.5, the device fabricated with the hybrid process shows higher coherence than the CPW device fabricated with the single lift-off process. Also, the lumped element resonators fabricated with the single lift-off process show low internal quality factors compared with the hybrid devices, which can be seen in Table 6.1. Flux tunable resonators fabricated for a Josephson parametric amplifier[21] in a similar fashion also do not show very high quality: their internal quality factor is limited to several thousand. One possible cause of the loss in the single lift-off process is insufficient surface treatment. For devices patterned with lift-off, there is the risk of creating a contamination carbon layer due to insufficient surface preparation, as well as ~ 2 nm AlO_x on top of the carbon layer, which is probably a product of a reaction of unpassivated Al with resist contamination or solvent from the development, or has resulted from heating the substrate[14]. One problem is that after development, a rigorous cleaning to remove resist residue is very difficult. In [14] it is shown that the estimated loss tangent of 2 nm of the resist residue left due to insufficient de-scumming could leads to $\delta_{\mathrm{TLS}} = 3 \times 10^{-3}$. This has reasonable agreement with what we observed in the single step lift off devices.

On the other hand, in the process employed to fabricate the hybrid devices, the substrate–metal interface should have much less resist residue since the RCA1 and piranha cleaning were done before the deposition of the MoRe. In addition the dielectric loss from carbon contamination is minimized due to the limited exposure areas for lift off. Especially, contamination with the electron-beam resist in MMA is hard to remove. Previous work performing AFM measurements on silicon substrates after removing EB resist from the silicon substrates for 30 min in hot acetone has been tried, where the substrates are cleaned without baking. It turns out that the resist residue of MMA gives the highest roughness, $\sim$ 2 nm, which is pretty large compared with the roughness of bare silicon substrate, $\sim$ 0.2 nm [22]. The dielectric loss due to the electron beam resist may not be limited to the metal–substrate interface, but also any metal–resist contact might degrade the microwave quality as a result of collapsing the side wall of the resist stack on top of the Al electrodes (see Appendix 6). A smaller dielectric loss might be achieved by changing the bottom layer MMA into another resist layer, such as PMGI. We believe that the low coherence observed in the single step lift off devices could have suffered from carbon contamination. This suggests two things: (1) The coherence can be improved by optimizing the oxygen ashing parameters even for the lift off devices. (2) BHF cleaning before lift-off may not be as effective as oxygen plasma with optimized parameters.

Another cause could be that the dielectric losses in the AlO_x layer between the two aluminium layers from the shadow evaporation may play a role. This insulating layer inside the SQUID cavity could form a self capacitance where energy is stored, and degrade the coherence of the mode. This dielectric loss is not a leading cause of microwave energy loss in 3D realizations of a superconducting qubit [5][23][24]. This could be due to the geometry of their 3D devices: the dielectric loss resides in the

substrate–metal, substrate–air, or metal–air interfaces, and possibly even in the AlO_x layer there is a reduction of this loss to the cavity field by increasing the mode volume of the cavity where there is no dielectric loss in vacuum.

6.7. CONCLUSION

In conclusion, we fabricated microwave flux-tunable resonators with a new recipe, in which the superconducting contacts are made between MoRe and AlOx. We measured the coherence of these flux-tunable resonators and compared this with devices of the same design and a dc SQUID terminated CPW resonator (fabricated with the single step lift-off procedure). The hybrid systems show high internal quality factors (~ 20000 at zero flux quantum) two orders of magnitude larger than those of the devices made with the single step lift-off procedure. The internal quality factors of hybrid devices are not limited by fabricating a Josephson junction inside the resonators.

We believe the observed low coherence in SQUID cavities of single lift-off devices is due to the combination of two factors: (1) Carbon contaminations on the S–M interface, as well as possible flip down of a resist wall after lift-off to metal electrodes. (2) A high participation ratio of the dielectric layers silicon–aluminium, aluminium–aluminium, and aluminium–air. Further investigations might be beneficial, such as optimization of the oxygen plasma de-scumming, comparison of the internal quality factors of the single evaporation of Al with those from shadow evaporated Al with the diffusive oxide layer in the middle.

6.8. APPENDIX 1: ESTIMATION OF CRITICAL CURRENT FROM NORMAL STATE RESISTANCE

The measured samples contain reference Josephson junctions to estimate the critical current (we refer to them as witness junctions). Measuring the resistance of the witness junctions provides information about the evaporation, whether the junctions are shorted, open, or successful. Inspection with a scanning electron microscope is helpful and tells us that the junction works well as long as two Al electrodes make good overlap, like the one shown in Fig. 6.6.

A witness junction typically consists of two large contacting pads and a Josephson junction with metal electrodes that connect the two pads. Fig. 6.6 shows witness junctions made for the device. For each witness junction, the contacting pads are made of MoRe and the junctions and electrodes which connect the two pads are made of Al, separated by $\sim 70\ \mu$m. Since Al is a good electric conductor at room temperature compared with MoRe, the residual resistance of the connecting electrodes minimizes its contribution to the measured resistance. The sample contains 5 identical witness junctions for each device: by comparing the resitance value of the 5 identical junction, one can estimate the junction yield of the batch. Fig. 6.6 (b) is a zoomed image of a witness junction, which contains two Josephson junctions in a loop instead of a single junction. The resistance of the junctions is measured using a probe station with a resistance box. The critical current of a witness junction is estimated from the room temperature resistance R_n and the superconducting gap of the Al. In the low-temperature regime, where $T << T_c$, the Ambegaokar and Baratoff relation says

$$I_0 = \frac{\pi\Delta}{2eR_n} \tag{6.12}$$

where Δ, e, and R_n are the superconducting gap of the Al, the electric charge, and the room temperature resistance over the junction. The measured resistance of the witness junctions which contain two junctions in parallel is in the range between $500 \sim 1$ KΩ using a 'beeper box'. On average, the room temperature resistance of witness junction is around 700 Ω on one SQUID, whose critical current is estimated to be ~ 490 nA using the equation above. The corresponding Josephson inductance would then be around 0.8 nH (Eq. 6.8). The value of the Josephson inductance found from the fit of the frequency dependence to the flux, is estimated to be around 0.35 nH. The room temperature resistance measured with the beeper box gives a ballpark estimate of L_J and I_c to within a factor of two.

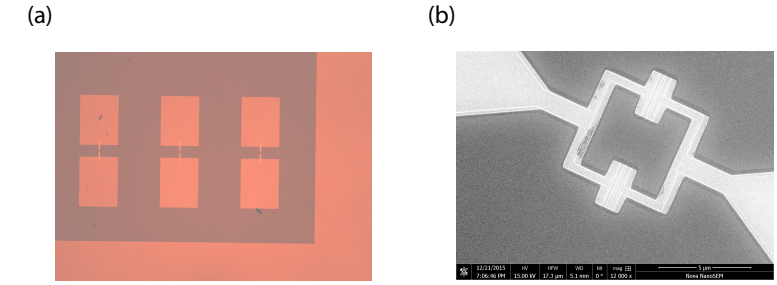

Figure 6.6: (a) **Optical image of witness junctions.** There are 5 witness junctions on one chip. The contacting pads are made with MoRe, which is the same material as the other circuit elements. Aluminium electrodes from evaporation of AlO_x are connected galvanically to each MoRe contacting pads. (b) **SEM image of a witness junction.** Each pair has a dc SQUID, the same as the measurement devices.

6.9. APPENDIX 2: ESTIMATION OF INPUT POWER AT THE DEVICE

We calculated the total attenuation at the sample stage in three different ways: (1) The input power is estimated by calculating the attenuation on the input line. (2) The input power is estimated from the background noise of the VNA and the gain of the amplifiers and the attenuation on the output line. (3) The input power is estimated from the signal to noise ratio on the VNA.

First, we estimated the input power by calculating the total attenuation on the input line. The microwave signal sent from a VNA is attenuated to reduce the thermal noise fluctuation. The measurement setup is shown in Fig. 6.9. The microwave signal sent from the output of the VNA goes into the input line of the fridge, which passes through multiple attenuators at each temperature stage. For the input line, there are attenuators placed at each stage of the fridge, which add up to 47 dB. In addition, the microwave loss in the coaxial cables on the input line is estimated. From the top flange to the 4 K stage, $SC-219/50-SCN-CN$ is used. The outer conductor is cupronickel with a diameter of 2.2 mm and a silver-plated cupronickel centre conductor. The distance from top flange to the 50 K stage is 176 mm, and the distance from the 50 K stage to the 4 K stage is 270 mm. We estimated the attenuation between the top flange to the 4 K stage through the cupronickel coaxial cables to be 0.826 dB. Below the 4 K stage, SC-086/50-SCN-CN is used. The cable has a diameter of 0.86 mm, and is made of cupronickel with a silver-plated cupronickel inner conductor. The attenuation in this cable is 3.2 dB/m at 4 K. The distance between the 4 K stage to the still flange is 240 mm, and from the still flange to the MC plate is 228 mm. The attenuation below the 4 K stage was estimated to be 1.498 dB. The total attenuation through the coaxial cable in the input line excluding the attenuators was estimated to be 2.32 dB. At the output port of the VNA, extra attenuators to the amount of 60 dB were added. The coaxial cable between the output of the VNA and

the top of the fridge has been estimated to be 3.54 dB at resonance frequency. The starting output power of the VNA was set to -30 dBm. Therefore, the total power at the sample is around -142.86 dBm.

Second, the total attenuation was calculated from the attenuation and the gain in the output line. The second way we tried is from the attenuation and the gain in the input line to the VNA, and the output power of the VNA. The noise level of the VNA indicates the attenuation and gain, and the attenuation level at the device can be inversely calculated by subtracting the gain and adding the attenuation in the amplifier line. In one of the measurements, the measured noise level was -91.5 dBm. At room temperature, two Meteq amplifiers were used for better visibility. Each amplifier has a gain of 28 dB. The gain of the HEMT amplifier is 37 dB around 4 to 8 GHz. From the cold temperature amplifier to the top of the fridge, we estimate the attenuation to be 1.8 dB, including the 1 dB attenuator. From the HEMT to the 10 mK stage, we ignored cable losses because NbTi is superconducting at 3 K or below. We considered each isolator's contribution to be a 0.2 dB loss. By starting at -30 dBm on VNA output power, the power at the device is -182 dBm.

The third technique is to estimate the power at the device from the S/N of the measurement. The two techniques mentioned previously lead to a discrepancy in the estimated values. We believe this discrepancy is due to cable losses somewhere inside both the input line and the output lines. The signal comes out of the amplifier line and goes into the input port of a VNA passing through two room temperature amplifiers. The fluctuating noise in the measurement is dominated by the Johnson noise of the HEMT amplifier. The thermal noise power that goes into the HEMT amplifier is determined as follows.

$$P_{dBm} = 10\log 10(K_B T \times 1000) + 10\log 10(\Delta f) \tag{6.13}$$

where K_B is Boltzmann's constant, T is the noise temperature of the HEMT, and Δf is the IF bandwidth of the VNA. A factor of 1000 is used for conversion to dBm. The noise temperature of the HEMT is 5.5 K(`LNF_LNC1_12A`), and the noise power with an IFBW of 10 Hz gives -181.20 dBm, which corresponds to 0.195 nV in RMS voltage. The noise power is proportional to the attenuation between the HEMT and the input/output port of the device, the fluctuation of the measurement in the noise level, and some proportionality constant.

$$\sigma_{V_{in}^{amp}} = \alpha A \sigma_M. \tag{6.14}$$

The left-hand side of the equation is the power which goes into the HEMT amplifier. On the right-hand side, α is the attenuation between the HEMT amplifier and the output of the device, and σ_M is the noise determined by taking the standard deviation of the measured voltage on the VNA. The total attenuation from the HEMT amplifier to the input/output port of the device was determined to be 1 dB, considering each isolator to have an insertion loss of 0.2 dB. Here, A is a proportionality constant so

Table 6.2: Important parameters of the devices

#	Estimation Technique	$P_{in,min}$ (dBm)	$N_{ph,min}$	$P_{in,max}$ (dBm)	$N_{ph,max}$
1	PNA output power + input line attenuation estimation	-142.86	0.18	-112.86	183.29
2	PNA input power + amplifier chain gain estimate	-182	0.00	-152	0.02
3	PNA SNR + HEMT input noise estimate +attenuation loss between sample and HEMT estimate	-155.75	0.01	-125.75	9.41

that

$$|V_{out}| = A \times M \tag{6.15}$$

where M is the measured transmission spectrum, in this case $|S_{21}|$. The voltage of the signal that goes into the HEMT is easily found by multiplying the attenuation factor by the input voltage to the HEMT. The output voltage can be converted into power in dBm and photon number. With this procedure, the estimated attenuation from the output of the VNA to the device is -155.77 dBm. We believe the discrepancy in power at the device calculated from the first two procedures comes from estimating the attenuation or amplification gain with the wrong numbers, which most likely comes from a bad connector/cable on the input and output line of the transmission line.

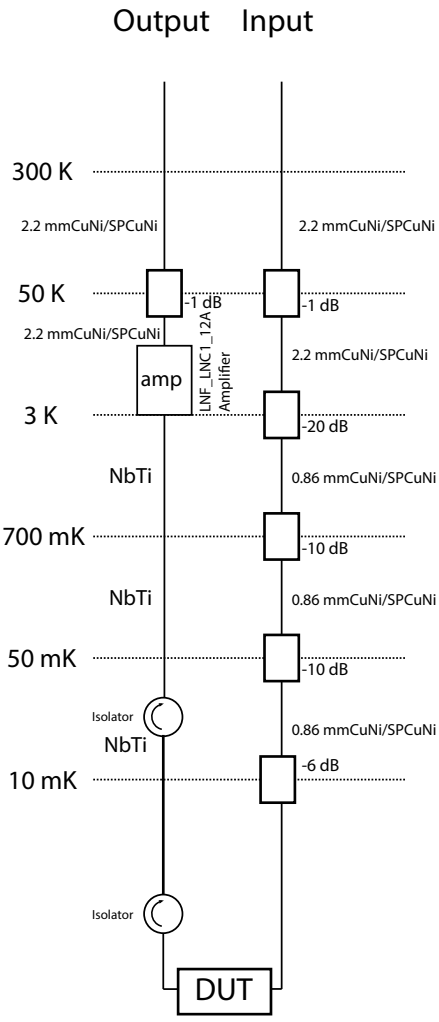

Figure 6.7: **Measurement setup of one of the devices.**

6.10. APPENDIX 3: ESTIMATION OF GEOMETRIC CAPACITANCE AND INDUCTANCE OF THE DEVICE

We determined the geometric inductance and capacitance of the device from a simulation. In the experiments, we measured a lumped element resonator and a hybrid SQUID cavity, in which both the resonators, made of MoRe, have the same geometry with only one difference: the hybrid SQUID cavity has a dc SQUID in the middle of the inductive element. We first estimated the contribution of the kinetic inductance in the MoRe film. Fig. 6.9 (b) is an optical image of a reference resonator which was made in the same batch as the hybrid device shown in Fig. 6.9 (a). A Sonnet simulation of the same design as shown in Fig. 6.9 (c) found that the resonance frequency of the reference resonator should be around 7.05 GHz. The observed resonance frequency of the mode is around 5.425 GHz. The discrepancy between the resonance frequencies of the reference resonator in the measurement and in the Sonnet simulation is due to the kinetic inductance of the 60 nm thick MoRe film. In order to find the contribution of the kinetic inductance in terms of sheet resistance, we added sheet inductance until the resonance of S_{21} response in Sonnet went down to 5.425 GHz. We found the corresponding sheet inductance to be 1.575 pH/sq.

Now the Josephson inductance of the SQUID can be found by comparing the resonance frequency of the reference resonator with the maximum frequency of the hybrid SQUID cavity. The difference in the frequencies is due to the Josephson inductance, which can be calculated in the simulation by introducing an ideal inductive element in the circuit until the frequency of the response matches the maximum frequency of the hybrid SQUID cavity. From the simulation, the estimated Josephson inductance is 0.35 nH.

Two unknown parameters which are still to be calculated are the geometric inductance and the geometric capacitance. The assumption we made here is that the geometric inductance and capacitance are constant with respect to the power or field strength, which is a reasonable assumption for the dynamic range of a dc SQUID. Then we further increased the ideal inductive element, which corresponds to a frequency shift of the SQUID cavity either by Kerr non-linearity or tuning the flux through the SQUID loop. The frequency shift in terms of the Josephson junction can be expressed as

$$\omega_0 = \frac{1}{2\pi\sqrt{(L_g + L_j)C_g}}. \tag{6.16}$$

From the equation above, both unknown parameters can be determined simultaneously. Fig. 6.8 shows the fit using Eq. 6.13. The blue points are simulated points whose y-values are the square of the resonance frequency and whose x-values are the values of the ideal inductor. The black line is the fit to the points. The fit works nicely with geometric inductance, L_g=2.93nH and geometric capacitance, C_g=288 fF. Josephson inductance participation ratio 0.11, which is in a good agreement with the value estimated from the curve of frequency under flux which is shown in Fig. 6.3 (b).

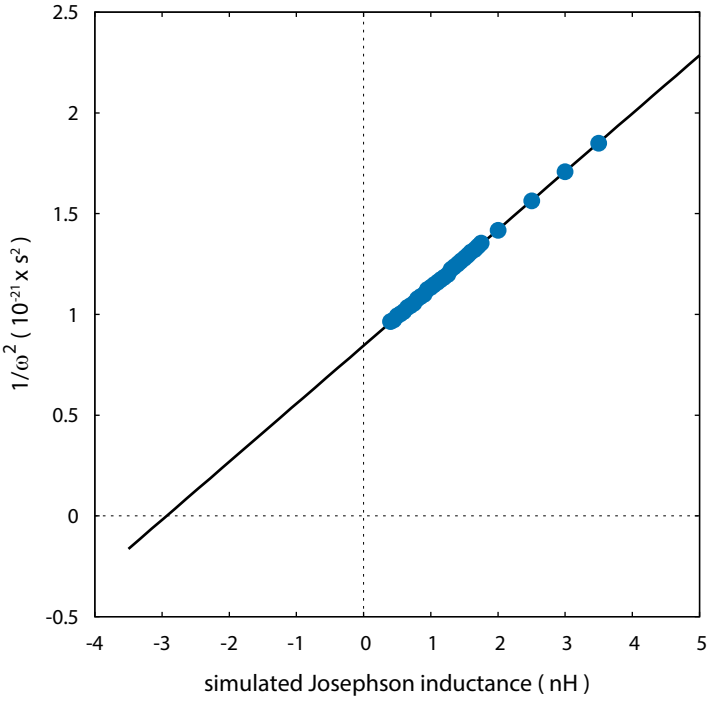

Figure 6.8: Fit to $1/\omega^2(L_J)$ as a function of ideal inductance. Blue points are numerical values from a simulation where the ideal inductance was varied point by point. The black line is a fit with Eq. 6.16. The lowest point of the inductance is 0.35 nH, which is the estimated Josephson inductance at integer flux quantum. The slope crosses of the x-axis on $\sim -2.9\ nH$, which corresponds to the geometric inductance of the resonator with a negative sign.

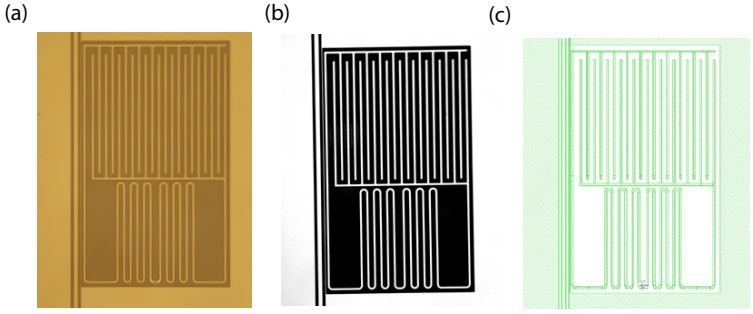

Figure 6.9: (a) Optical microscope image of a hybrid resonator. (b) Optical microscope image of a reference lumped element resonator having the same geometry as the hybrid device shown left. (c) Screen shot image of the design used for estimating resonance frequency of the device.

6.11. APPENDIX 4: ASYMMETRIC RESPONSE FITTING

When we measure the quality factor of a microwave resonator, we get two quality factors, the internal and the external quality factor. In measurements of superconducting resonators, small signal reflections or non-negligible impedances could give rise to an asymmetric Lorentzian response. The transmission spectrum of a side coupled resonator, also called the notch type geometry, is given by[25].

$$S_{21} = ae^{i\alpha}e^{-2\pi i f\tau}[1 - \frac{Q_{loaded}/|Q_{ext}|e^{i\theta}}{1+2iQ_{loaded}(f/f_r - 1)}]. \tag{6.17}$$

The prefactor describes non-ideal events in the measurement line, such as attenuation, impedance mismatch, and cable delay. Inside the brackets is the response of an ideal side coupled cavity. The term is a complex Lorentzian function which is subtracted from unity. The resonance response has the relation such that $1/Q_{loaded} = 1/Re\,[Q_{ext}] + 1/Q_{int}$, where the external quality factor, Q_{ext}, is a complex value such that $Q_{ext} = Q_{ext}e^{-i\theta}$. The ideal resonance response term can be rewritten in terms of the cavity decay rates:

$$S_{21} = 1 - \frac{\kappa_{ext}e^{i\theta}}{\kappa_{loaded} + 2i\delta\omega} \tag{6.18}$$

where κ_{ext}, κ_{loaded}, and $\delta\omega$ are the external decay rate, total decay rate, and detuning of the drive tone from the resonance frequency. Here θ plays a role to compensate for the asymmetry in the resonance due to any impedance mismatch in the measurement line. The formula below was used to plot the cavity response, including environmental effects.

$$S_{21} = Ae^{i(a' + b'\omega)}[1 - \frac{\kappa_{ext}e^{i\theta}}{\kappa_{loaded} + 2i\delta\omega}] \tag{6.19}$$

The prefactor of Eq. 6.19 is equivalent to that of Eq. 6.17, except we assume a small fluctuation of the background which depends on the frequency, $A = a + b\omega + c\omega^2$, where a, b, and c are fitting parameters of background of zeroth, first, and second order, respectively. a' and b' play the roles of phase shift and electrical length of the meter-long coaxial cable. Any impedance mismatch of the measurement line causes a rotation of the complex-resonance circle in the $I-Q$ plane, and θ takes into account the accumulated rotation due to an impedance mismatch. Here, the fitting is done with the amplitude of S_{21}. Fig. 6.3 (c) is fitted with Eq. 6.18. The transmission spectrum goes above unity on the right side of the plot, which is an artifact resulting from the accumulated phase θ from any impedance mismatch inside the connecting cables or connectors or wirebonds. Fig. 6.10 shows a Lorentzian response of one of the linear reference CPW resonators. The response is fitted with the function above with the parameters below.

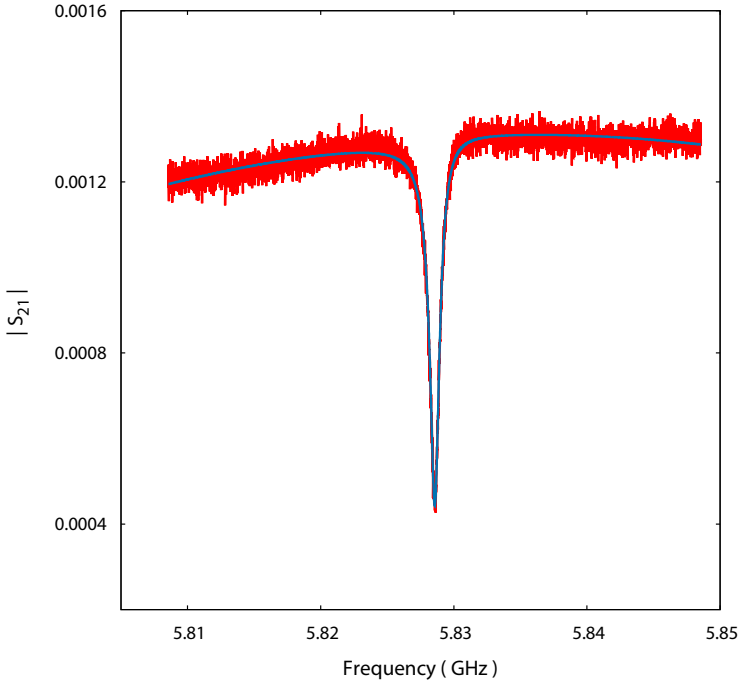

Figure 6.10: One of the measured responses of a linear CPW resonator(**REF_CPW2**) and fit. For this fit, the fitting parameters were f_0=5.83 GHz, Q_{int}= 15.08×10^3, Q_{ext}=7.72×10^3, a= -4.86, b=1.67e-09, c=-1.43e-19, a'=2.21e+03, b'=-3.80e-07, and θ=-0.09°.

6.12. APPENDIX 5: RESONANCE FREQUENCIES OF THE CIRCUIT

The resonance frequencies of a SQUID cavity was simulated in the Quite Universal Circuit Simulator (QUCS). Fig. 6.11 (a) is a circuit representation of one of our devices, where L_g and C_g are the geometric inductance and capacitance, respectively. In the device, a meander strip forms a geometric inductance, L_g. The interdigitated capacitor in Fig. 6.9 is equivalent to C_g in Fig. 6.11 (a). L_J, C_J, and $L_{g-squid}$ are the Josephson inductance of the junction, the parallel plate capacitance of the junction, and the geometric inductance of the SQUID loop. In this circuit, there are three resonances, represented in three different colours in Fig. 6.11 (a). The red arrow represents a mode consisting of the interdigitated capacitor, a meander inductor, and a SQUID inductance. We use this mode for the measurements in the main text. The green arrow represents a mode of two coupled Josephson junctions via a small SQUID loop inductance. From the design of our Josephson junction and the size of the SQUID loop, this mode should have a much higher frequency than the one represented by the red arrow. The blue arrow indicates a mode between the geometric inductance of the SQUID loop and the parallel plate capacitance from two Josephson junctions. Compared with the mode represented by the green arrow, this mode should have a much higher frequency, since $L_J >> L_{g-squid}$.

Fig. 6.11 (b) shows a simulation of the voltage response of the circuit represented in Fig. 6.11 (a) with parameters close to the experimental values. Three resonances are observed. The lowest mode corresponds to the red arrow in Fig. 6.11 (a). The middle mode corresponds to the green arrow in the figure above. The highest mode corresponds to the blue arrow. In the measurement, the two higher modes cannot be observed in the measurements because the measurement bandwidth is limited to 4~8 GHz. The mode which is associated with the circulating current of the SQUID (oscillating ϕ) is the highest mode, whose resonance frequency lies around 400 GHz. The time derivative of the circulating current mode becomes approximately flat over many oscillations during the time scale corresponding to a frequency of the 6 GHz resonance frequency.

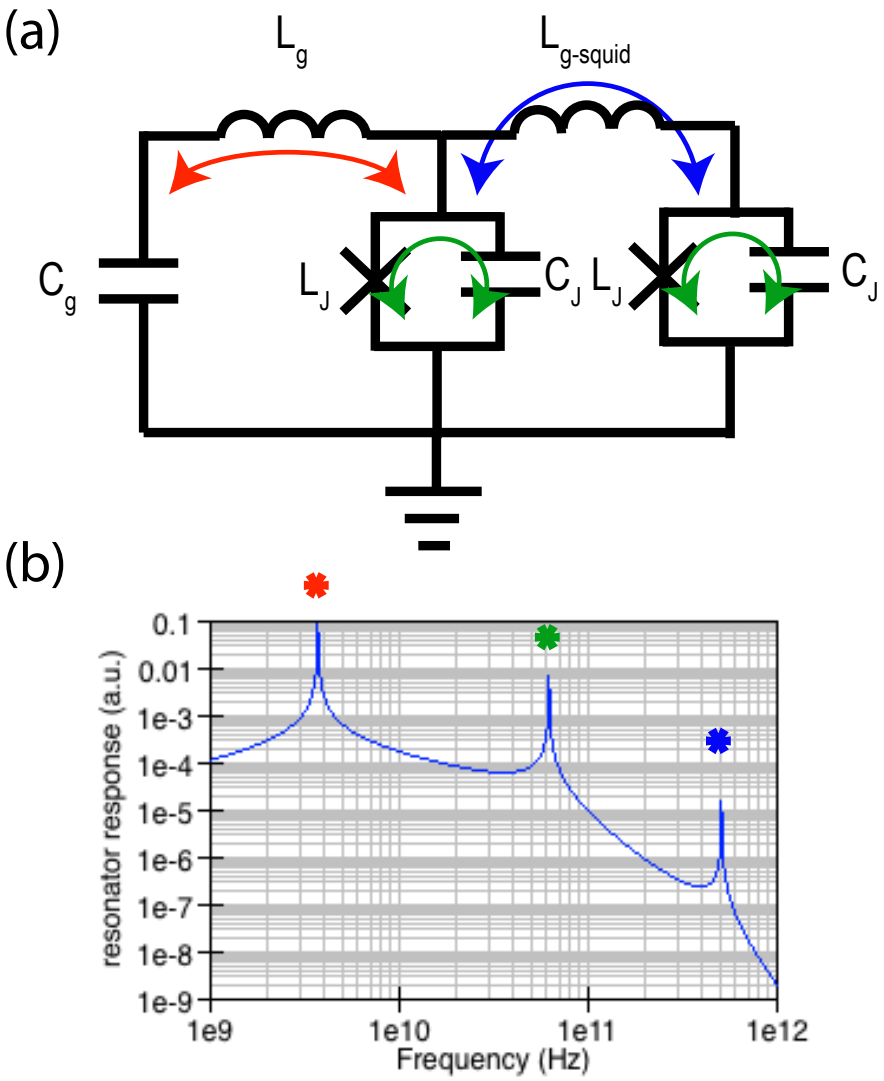

Figure 6.11: **QUCS simulation of possible resonances in the circuit.** (a) Circuit representation of our hybrid device. There are three possible resonances: (1) Resonance frequency of SQUID cavity is indicated by red arrow. (2) Plasma frequency of two Josephson junction is represented by green arrows. (3) Circulating current mode is indicated by blue arrow. This circulating current mode satisfies the condition that $L_J >> L_{g-squid}$. The resonance mode is created by the geometric inductance of the SQUID and the capacitance of the Josephson junctions. (b) QUCS simulation of an equivalent circuit to our device. Here we estimate resonance frequencies with parameters close to the device values, where L_J= 350 pH, C_J=20fF, $L_{g\text{-squid}}$=20 pH, L_g=2.9 nH, and C_g=0.6 pF. Three resonances are observed. The lowest resonance corresponds to the SQUID cavity and is indicated by a red asterisk. The second highest mode is around 60 GHz. This mode is the mode of the plasma freuency of two Josephson junctions coupled via the small SQUID loop inductance, $L_{g\text{-squid}}$. The highest one is the circulating mode, whose resonance lies around 400 GHz. The circulating current mode has a phase dependence on time, but this is neglected since the dynamics of the highest mode moves fast compared with the lowest mode, which is our interest.

6.13. APPENDIX 6: FALLING OVER OF RESIST SIDEWALL DURING LIFT OFF PROCESS

Fig. 6.12 (a) shows a SEM image of a dc SQUID after lift off. There are several parts which appear darker on the SQUID loop. These parts are known as the black veil of death [26], which is a resist residue sidewalls of possibly the resist stack flipping over on top of the device during the lift off of the Josephson junctions. This could be a result of a chemical reaction of the electron beam resist during the evaporation, and these contaminations falling over on top of the device as shown in Fig. 6.12 (b).

For the hybrid devices of our measurements, the internal quality factors are not limited by dielectric loss due to the carbon contamination of resist residue in the Josephson junctions because their coherences are comparable to those of the reference devices. However, for the devices made with the single step lift off, the resist residue might not be negligible, and post oxygen ashing with oxygen plasma should be considered to reduce the dielectric loss.

Post cleaning with oxygen plasma is known to remove the black veil of death. This is also helpful to minimize the aging of the junctions, which becomes crucial for flux qubits, where a large proportion of the circuit consists of Josephson inductance, which gives rise to a large frequency shift due to aging. More stable junctions are beneficial for any kind of circuit, and it is always better to do de-scum after lift off.

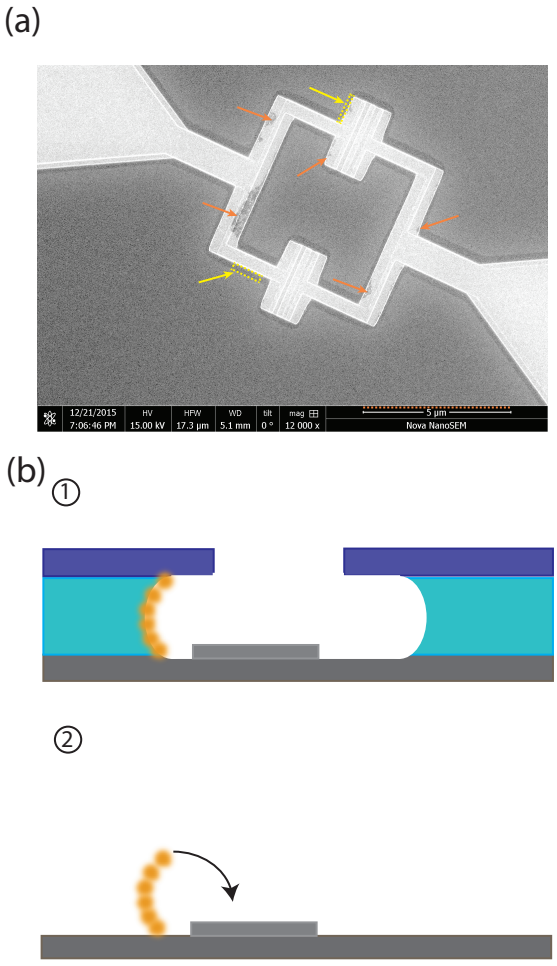

Figure 6.12: (a) SEM image of a dc SQUID. The yellow arrows indicate a darker colour compared with the area away from the dc SQUID. These darker regions have seemingly less resist residue in those regions, and indicate the size of the bottom layer undercut. During oxygen plasma or BHF etching or a combination of both, resist residue is removed and produces this different colour away from the SQUID. There are dark spots on top of the SQUID, which are indicated with orange arrows. They are probably the residue of the electron beam resist. This resist residue is known as the black veil of death [26]. (b) Possible formation of black veil of death: ①. The chemical reaction of this sidewall occurs during evaporation. ② Free standing sidewall falls over during lift off.

REFERENCES

[1] G. Hammer, S. Wuensch, K. Ilin, and M. Siegel, *Ultra high quality factor resonators for kinetic inductance detectors,* Journal of Physics: Conference Series **97**, 012044 (2008).

[2] H. G. Leduc, B. Bumble, P. K. Day, A. D. Turner, B. H. Eom, S. Golwala, D. C. Moore, O. Noroozian, J. Zmuidzinas, J. Gao, B. A. Mazin, S. McHugh, and A. Merrill, *Titanium Nitride Films for Ultrasensitive Microresonator Detectors,* Applied Physics Letters **97**, 102509 (2010), arXiv: 1003.5584.

[3] P. Szypryt, B. A. Mazin, G. Ulbricht, B. Bumble, S. R. Meeker, C. Bockstiegel, and A. B. Walter, *High Quality Factor Platinum Silicide Microwave Kinetic Inductance Detectors,* Applied Physics Letters **109**, 151102 (2016), arXiv: 1610.00725.

[4] J. Bylander, S. Gustavsson, F. Yan, F. Yoshihara, K. Harrabi, G. Fitch, D. G. Cory, Y. Nakamura, J.-S. Tsai, and W. D. Oliver, *Dynamical decoupling and noise spectroscopy with a superconducting flux qubit,* Nature Physics **7**, 565 (2011), arXiv: 1101.4707.

[5] H. Paik, D. I. Schuster, L. S. Bishop, G. Kirchmair, G. Catelani, A. P. Sears, B. R. Johnson, M. J. Reagor, L. Frunzio, L. Glazman, S. M. Girvin, M. H. Devoret, and R. J. Schoelkopf, *Observation of high coherence in Josephson junction qubits measured in a three-dimensional circuit QED architecture,* Physical Review Letters **107** (2011), 10.1103/PhysRevLett.107.240501, arXiv: 1105.4652.

[6] N. Bergeal, F. Schackert, M. Metcalfe, R. Vijay, V. E. Manucharyan, L. Frunzio, D. E. Prober, R. J. Schoelkopf, S. M. Girvin, and M. H. Devoret, *Phase-preserving amplification near the quantum limit with a Josephson ring modulator,* Nature **465**, 64 (2010).

[7] J. Mutus, T. White, E. Jeffrey, D. Sank, R. Barends, J. Bochmann, Y. Chen, Z. Chen, B. Chiaro, A. Dunsworth, J. Kelly, A. Megrant, C. Neill, P. O'Malley, P. Roushan, A. Vainsencher, J. Wenner, I. Siddiqi, R. Vijayaraghavan, A. Cleland, and J. Martinis, *Design and characterization of a lumped element single-ended superconducting microwave parametric amplifier with on-chip flux bias line,* Applied Physics Letters **103**, 122602 (2013), arXiv: 1308.1376.

[8] L. Zhong, E. P. Menzel, R. Di Candia, P. Eder, M. Ihmig, A. Baust, M. Haeberlein, E. Hoffmann, K. Inomata, T. Yamamoto, Y. Nakamura, E. Solano, F. Deppe, A. Marx, and R. Gross, *Squeezing with a flux-driven Josephson parametric amplifier,* New Journal of Physics **15**, 125013 (2013), arXiv: 1307.7285.

[9] Y. Tabuchi, S. Ishino, T. Ishikawa, R. Yamazaki, K. Usami, and Y. Nakamura, *Hybridizing ferromagnetic magnons and microwave photons in the quantum limit,* Physical Review Letters **113** (2014), 10.1103/PhysRevLett.113.083603, arXiv: 1405.1913.

[10] M. Yuan, V. Singh, Y. M. Blanter, and G. A. Steele, *Large cooperativity and microkelvin cooling with a three-dimensional optomechanical cavity,* Nature Communications **6**, 8491 (2015), arXiv: 1507.08898.

[11] Y. Kubo, F. R. Ong, P. Bertet, D. Vion, V. Jacques, D. Zheng, A. Dréau, J.-F. Roch, A. Auffeves, F. Jelezko, J. Wrachtrup, M. F. Barthe, P. Bergonzo, and D. Esteve, *Strong Coupling of a Spin Ensemble to a Superconducting Resonator,* Physical Review Letters **105** (2010), 10.1103/PhysRevLett.105.140502, arXiv: 1006.0251.

[12] A. Bruno, G. de Lange, S. Asaad, K. L. van der Enden, N. K. Langford, and L. DiCarlo, *Reducing intrinsic loss in superconducting resonators by surface treatment and deep etching of silicon substrates,* Applied Physics Letters **106**, 182601 (2015), arXiv: 1502.04082.

[13] A. Palacios-Laloy, *Superconducting qubit in a resonator: test of the Leggett-Garg inequality and single-shot readout,* Ph.D. thesis, Université Pierre et Marie Curie - Paris VI (2010).

[14] C. M. Quintana, A. Megrant, Z. Chen, A. Dunsworth, B. Chiaro, R. Barends, B. Campbell, Y. Chen, I.-C. Hoi, E. Jeffrey, J. Kelly, J. Y. Mutus, P. J. J. O'Malley, C. Neill, P. Roushan, D. Sank, A. Vainsencher, J. Wenner, T. C. White, A. N. Cleland, and J. M. Martinis, *Characterization and reduction of microfabrication-induced decoherence in superconducting quantum circuits,* Applied Physics Letters **105**, 062601 (2014), arXiv: 1407.4769.

[15] A. Palacios-Laloy, F. Nguyen, F. Mallet, P. Bertet, D. Vion, and D. Esteve, *Tunable resonators for quantum circuits,* Journal of Low Temperature Physics **151**, 1034 (2008), arXiv: 0712.0221.

[16] M. Sandberg, C. M. Wilson, F. Persson, T. Bauch, G. Johansson, V. Shumeiko, T. Duty, and P. Delsing, *Tuning the field in a microwave resonator faster than the photon lifetime,* Applied Physics Letters **92**, 203501 (2008).

[17] D. Ristè, C. C. Bultink, M. J. Tiggelman, R. N. Schouten, K. W. Lehnert, and L. DiCarlo, *Millisecond charge-parity fluctuations and induced decoherence in a superconducting qubit,* Nature Communications **4**, 1913 (2013), arXiv: 1212.5459.

[18] R. H. Koch, D. P. DiVincenzo, and J. Clarke, *Model for l/f Flux Noise in SQUIDs and Qubits,* Physical Review Letters **98** (2007), 10.1103/PhysRevLett.98.267003, arXiv: cond-mat/0702025.

[19] V. Singh, B. H. Schneider, S. J. Bosman, E. P. J. Merkx, and G. A. Steele, *Molybdenum-Rhenium alloy based high-Q superconducting microwave resonators,* Applied Physics Letters **105**, 222601 (2014), arXiv: 1411.4815.

[20] V. Singh, S. J. Bosman, B. H. Schneider, Y. M. Blanter, A. Castellanos-Gomez, and G. A. Steele, *Optomechanical coupling between a multilayer graphene mechanical resonator and a superconducting microwave cavity,* Nature Nanotechnology **9**, 820 (2014), arXiv: 1403.5165.

[21] M. A. Castellanos-Beltran, K. D. Irwin, G. C. Hilton, L. R. Vale, and K. W. Lehnert, *Amplification and squeezing of quantum noise with a tunable Josephson metamaterial,* Nature Physics **4**, 929 (2008), arXiv: 0806.0659.

[22] J. van den Berg, *Surface residue: eliminating a source of disorder in carbon nanotube devices,* (2007).

[23] Y. Chu, C. Axline, C. Wang, T. Brecht, Y. Y. Gao, L. Frunzio, and R. J. Schoelkopf, *Suspending superconducting qubits by silicon micromachining,* Applied Physics Letters **109**, 112601 (2016), arXiv: 1606.02822.

[24] C. Rigetti, S. Poletto, J. M. Gambetta, B. L. T. Plourde, J. M. Chow, A. D. Corcoles, J. A. Smolin, S. T. Merkel, J. R. Rozen, G. A. Keefe, M. B. Rothwell, M. B. Ketchen, and M. Steffen, *Superconducting qubit in waveguide cavity with coherence time approaching 0.1ms,* Physical Review B **86** (2012), 10.1103/PhysRevB.86.100506, arXiv: 1202.5533.

[25] S. Probst, F. B. Song, P. A. Bushev, A. V. Ustinov, and M. Weides, *Efficient and robust analysis of complex scattering data under noise in microwave resonators,* Review of Scientific Instruments **86**, 024706 (2015), arXiv: 1410.3365.

[26] D. H. Slichter, *Quantum Jumps and Measurement Backaction in a Superconducting Qubit,* Ph.D. thesis, University of California, Berkeley (2011).

7

A NON-LINEAR ANALYSIS OF THE RESPONSE OF A SQUID CAVITY

In Chapter 7, we studied the response of a SQUID Josephson cavity at very low excitation powers. At these low powers, the Josephson cavity can be treated as a simple harmonic oscillator. Intrinsically, however, Josephson junctions contain marked non-linearities in their response. One type of non-linearity comes directly from the Josephson relations: the Josephson inductance results in a non-linear restoring force on the harmonic oscillator, similar to that studied in the non-linear Duffing equations. In addition, Josephson junctions could contain non-linear damping terms in their response: for example, terms analogous to an $x^2\dot{x}$ force on a harmonic oscillator. In a Josephson junction, an additional power-dependent damping could, for example, arise from the generation of non- equilibrium quasiparticle excitations in a superconductor driven by oscillating currents in the junction. To determine the possible presence of these non-linear phenomena from the observations in our experiments, one needs to be able to model the microwave reflectance of a non-linear inductor with non-linear dissipation embedded in a resonator circuit that is coupled to a transmission line, which is not currently available in the literature.

7.1. INTRODUCTION

Josephson resonators are used ubiquitously in the field of superconducting circuits. The Kerr non-linearity of Josephson junctions is indispensable for circuit QED experiments with superconducting qubits[1, 2], high fidelity superconducting qubits[3], Josephson parametric amplifiers[4], non-linear readout for superconducting qubits[5], etc. The decoherence of a microwave linear resonant circuit has been extensively studied, and great efforts are being made to minimize its loss by using better superconducting metal, clean substrate/metal layer, etc. Microwave decoherence due to a higher order non-linear decay channel in a non-linear resonant circuit has been reported[6]. This could be due to the generation of non-equilibrium quasiparticles, coupled non-linearly to different resonant modes (TLSs), etc. However, it is still not clearly known what is the origin of these losses.

Here, we present a model for a Josephson resonator circuit that incorporates both non-linear restoring forces and non-linear damping. We use this model to analyse the reflectance measurements of a Josephson resonator and determine from the observations the strengths of the conservative and the non-conservative non-linearities in the circuit. Simulating the response of the device using electromagnetic finite-element modelling, and calibrating the design using the measurements of a reference design that is identical except that the junctions are replaced by short circuits, we are also able to use the analysis of the non-linear response to perform an independent calibration of the photon number of the device, providing an alternative route to photon number calibrations to those based on absolute noise power measurements. We can study the non-linear loss occuring in Josephson junction resonators by simulating a non-linear cavity response, S_{21}, from the Duffing equation with a non-linear damping term $\gamma_{nl} x^2 \dot{x}$. Then we can compare this with the measured cavity responses at higher powers.

7.2. DEVICE AND MEASUREMENT SETUP

The device of our interest in this experiment is a superconducting microwave resonator whose inductive element consists of geometric and Josephson inductors. Our device comprises lumped element resonators with a dc SQUID embedded inside lumped element inductors. A circuit representation of the device is shown in the inset of Figure 7.1, and an SEM image of dc SQUID is shown in the inset of Figure 7.1. The devices were fabricated on top of a high resistivity ($\rho \sim 10000\Omega$ cm) silicon substrate. The device was fabricated in two different steps: The lumped element inductor and capacitor were fabricated with molybdenum rhenium (MoRe) 60:40 with a thickness of 60 nm whose transition temperature is T_c = 8.6 K. The film was sputtered using an RF sputter with a flow of Ar. Then the lumped element capacitor and inductor were patterned using electron beam lithography with a tri-layer resist stack of S1813/Tungsten/PMMA 950. The MoRe film was etched with SF_6/He. Subsequently, the Al/AlOx/Al was evaporated using the Dolan bridge technique with MMA(copolym-

er)/PMMA 950. One linear lumped element resonator with the same geometry as the Josephson resonator device, except having no dc SQUID, was made on the same chip as the reference resonator. All the resonators were side coupled to a transmission line whose impedance of 71 Ω, including the contribution of the kinetic inductance of the 60 nm MoRe film. The resonator of these measurements has a characteristic impedance $Z_r = 104.9\ \Omega$ including the kinetic inductance contribution of the Josephson junction at integer flux quantum, as well as the kinetic inductance of the film.

The sample was tightly shielded inside a microwave copper sample box which was thermally anchored to the mixing chamber plate of a dilution refrigerator whose temperature was below 20 mK. The microwave input line was heavily attenuated in order to suppress the Nyquist noise of the signal at room temperature. The signal that passed through the device was first amplified by an HEMT amplifier, $LNF-LNC1\_12A$, whose gain was 40 dB with a noise temperature of 5.5 K. The signal was further amplified at room temperature with room temperature amplifiers, $AFS3-04000800-18-10P-4$, where each amplifier gain was 28 dB before the signal was sent to the input port of the VNA. Details of the fabrication and setup were discussed in Chapter 6.

7.3. THE LINEAR RESPONSE OF THE JOSEPHSON RESONATOR

The transmission spectrum, S_{21}, was measured using a VNA of the Josephson junction resonators. The resonance frequency of the mode of interest was tuned to the maximum frequency with external flux through the SQUID loop using a superconducting solenoid to minimize the thermal noise fluctuation mentioned in [7]. At small excitation powers, the cavity has a linear response and Lorentzian shape, as represented with the black line in Figure 7.1 b. The mode has a resonance frequency of 5.17203 GHz. The internal (Q_{int}) and external (Q_{ext}) quality factors were determined from the fit: the quality factors were found to be 26255.45 and 2145.05, respectively, using Eq. 6.18. The excitation power of the device was estimated to be around -148 dBm, where the average photon number is well below the single photon level.

7.4. DUFFING NON-LINEAR RESPONSE

Next, the output power of the VNA was gradually increased (by increments of 1 dBm) until the linear cavity response showed non-linear behaviour and came near the bifurcation point. Figure 7.2 shows the power dependence of the mode. Each response is plotted for the different excitation powers, on top of each other. The uppermost response corresponds to an excitation power of -133 dBm. The output power increases by increments of 3 dBm from top to bottom. The cavity responses look like the typical Duffing oscillator responses for higher sweeping powers. The resonance frequency of the mode is pulled lower as a function of the power, and has an asymmetric response shape, which is common for all Josephson junction resonators having a negative Duffing coefficient. The Duffing responses of the cavity mode are modelled based on the

equation below.

$$\ddot{x} + 2\gamma\dot{x} + x + 2\beta x^3 = \phi\cos(\Omega t) \tag{7.1}$$

Here γ,β, and ϕ are the cavity decay ratio, the Duffing coefficient, and the normalized force. Ω in the equation is the driving frequency with a small detuning of ϵ where $\Omega = \omega_0 + \epsilon$ and $\epsilon << \omega_0$.

The black points in Figure 7.3 b are the minimum point in each sweep corresponding to the resonance frequency of the mode as a function of power. It can be seen that at lower power, the resonance frequency shifts linearly in power. This linear dependence on the power can be used to calibrate the input power/intra cavity photon number if the Duffing coefficient β is known with no free variables. The Duffing coefficient β is defined as given below,

$$\beta = -\frac{1}{6}\left(\frac{L_J}{L_J + L_g}\right)^3\left(\frac{2\pi}{\Phi_0}\right)^2 \tag{7.2}$$

Here, L_J, L_g, and Φ_0 are the Josephson inductance, the geometric inductance and the magnetic flux quantum, respectively. The Josephson inductance as well as the geometric inductance are found to be 0.35 nH and 2.9 nH, respectively, using the frequency shift vs flux through the SQUID loop.

The linear dependence of the resonance frequency on the power deviates at higher power in Figure 7.2 b. This is mostly due to the non-linear damping, which will be discussed next.

7.5. NON-LINEAR DAMPING IN A JOSEPHSON CIRCUIT

Already in the power dependence of the frequency, we saw that it deviated from the predicted straight line. This behaviour, unusual for a normal Duffing response, becomes more pronounced in the black points of Figure 7.3 c. The black points of the figure show the minimum points at each power sweep on the VNA. We observed that the depth of each response becomes less deep with an increase in power. If there were only Duffing non-linearity, the normalized responsivity as well as the dip of S_{21} would be flat as the power increases. However, the dip of S_{21} clearly goes up for higher powers. This can also be seen in Figure 7.2. We believe the deviation of the resonance frequency from the linear trend and the depth reduction of S_{21} as a function of power are due to a high order non-linear damping term.

To investigate the effects of non-linear damping, we numerically modelled our cavity response in transmission geometry including a quadratic non-linear damping term $x^2\dot{x}$ in the Duffing equation, Equation 7.1[8–10] .

$$\ddot{x} + 2(\gamma + \gamma_{nl}x^2)\dot{x} + x + 2\beta x^3 = \phi\cos(\Omega t) \tag{7.3}$$

The non-linear damping term has the form of $x^2\dot{x}$, where the effect of this becomes stronger with a higher driving force. There could possibly exist another type of

non-linear damping term other than $x^2\dot{x}$, such as $x^2, \dot{x}^2, x\dot{x}$ for quadratically proportional terms and $\dot{x}^3$, and $\dot{x}x^2$ in experiments. The addition of these terms to Equation 7.3 would still yield the same form of a secular equation of the coefficient of the solution, but gives an effective Duffing coefficient β_{eff} and non-linear dumming coefficient γ_{eff}[8].

Figure 7.3 a shows a non-linear cavity response at an excitation power of -122 dBm. The black line represents the experimental data of the device. The response is already starting to become asymmetric, and a frequency shift towards lower frequencies. The red line represents a simulation of the cavity response derived from equations of motion including a non-linear damping term γ_{nl}. The solutions of the Duffing equation above have either one real solution or two real and one imaginary solution. The solutions of Equation 7.3 are converted into the input impedance Z_{in} and the transmission spectrum can be calculated.

In Figure 7.3 b, the red line represents the simulated resonance frequency of a Josephson Duffing resonator as a function of the power, which is taken from the frequency of the minimum point in S21 in Figure 7.3 a for all the different powers. Figure 7.3 c shows the depth of the simulated S_{21} responses as a function of power. Both figures capture the correct qualitative trend by including the quadratic damping term, where the red line in Figure 7.3 b shows that the shift is suppressed at higher powers and the red line in Figure 7.3 c shows a reduction of the depth in the S_{21} response at higher powers. This reduction of coherence as a function of power was also observed in T1 in a circuit QED experiment with detuning on the cavity [11], which could be related to the observation presented here. However, deviations of the simulated responses at higher power, especially in Figure 7.3 c, become more pronounced, and fail to capture all the details quantitatively. This suggests that perhaps there is a different underlying non-linear dissipation term.

7.6. CONCLUSIONS

We studied the microwave dissipation of non-linear Josephson resonators. By developing a model for the microwave response of a resonator that includes both non-linear restoring forces and non-linear damping, we showed that the qualitative behaviour of the measured response of the SQUID cavity can be captured by including non-linear dissipation. Using the observed frequency shift as a function of the power at powers before the non-linear damping plays a role, we also have provided a method for an independent calibration of the intracavity photon number and the input power of the device. The observation of a response that suggests the effect of a non-linear damping on the response of the Josephson junctions provides new insight into the behaviour of these devices at higher power. From our measurements, it is not possible to determine the microscopic origin of such a non-linear damping. As aluminium is well known for its long quasiparticle recombination times[12], non-equilibrium quasiparticle heating of the Al superconductor could be playing a role. Resonant two-level defects can be neglected as these would lead to an opposite de-

pendence on the power. It is also unlikely that the heating of the microwave photons plays a role at the photon numbers considered here for the classical circuit. One limitation of our analysis is that we have treated the circuit entirely classically: it would be interesting to consider the possible effects of quantum mechanics on the response of the circuit, and whether they could play a role in the observations of the apparent non-linear cavity damping presented here.

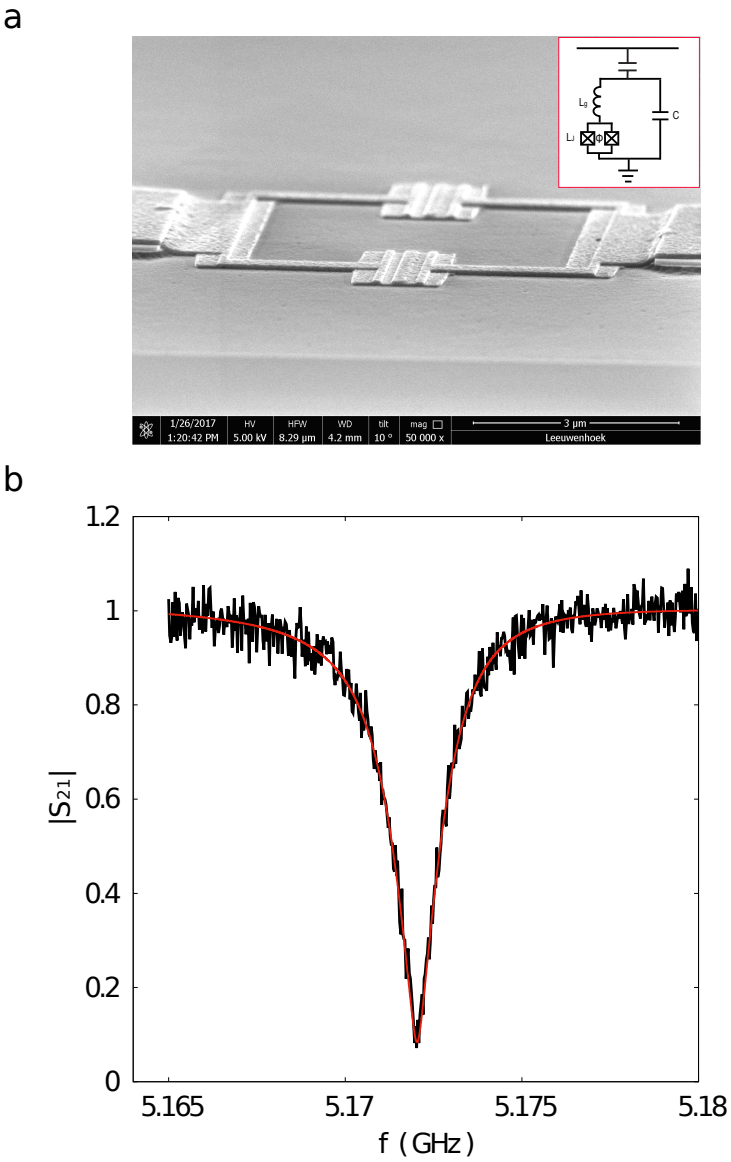

Figure 7.1: **Microwave resonance of a SQUID cavity**. (a) High angle SEM image of device zoomed on the SQUID. The sample was fabricated on top of a high resistivity silicon substrate. The device consists of a lumped element microwave cavity made of rf sputtered MoRe and Al/AlOx/Al dc SQUID evaporated by the conventional Dolan bridge technique. The image captures the superconducting contacts between the sputtered MoRe and evaporated aluminium junctions. The inset shows a schematic diagram of the device. The resonator was side coupled to a transmission line, and the transmision spectrum S21 was measured. The resonance frequency of the device can be tuned periodically with flux applied through the SQUID loop. (b) Microwave response of the device (**HY 1**) whose resonance frequency was chosen to be maximum with external magnetic field. S_{21} was normalized such that fitted the off-resonant $S_{21} = 1$ (red line). The response is fitted with a skewed Lorentzian function (solid cyan line). The mode has fundamental frequency at 5.17203 GHz, and external and internal quality factors of 2335.89 and 26255.45, respectively.

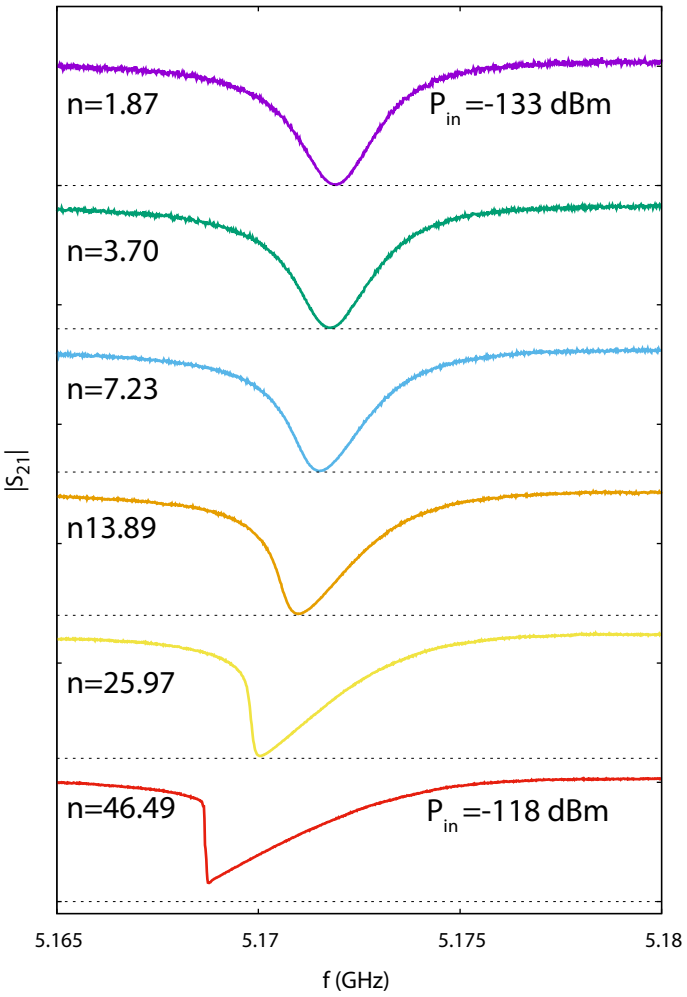

Figure 7.2: **Observation of the non-linear response of the SQUID cavity (HY 1).** The transmission spectrum S_{21} as a function of input power P_{in}. The excitation power was varied at the output power of a VNA. Vertical axis: S_{21} normalized such that off resonant $S_{21} = 1$. Curves are offset for clarity, dashed lines below each curve indicate $S_{21} = 0$ for each curve. The lowest excitation power corresponds to -133 dBm at the device. Corresponding averaged photon number is <n>=1.87 for the uppermost response. Note that due to the non-linearity in both the stiffness and damping, it is non-trivial to calculate the photon number accurately without using a full theory of the S21 of the coupled non-linear cavity (see Fig. 7.3). Photon numbers are estimated from energy stored inside the capacitor, $n_d = \frac{CV_r^2}{2\hbar\omega_0}$, where V_r^2 is the maximum amplitude of the Duffing response considering the non-linear damping term. The highest power of excitation was -118 dBm at the device. Average photon occupation with the highest excitation power corresponds to <n>=46.49. Between the lowest and highest excitation powers in the figure, the excitation powers increase with increments of 3 dBm. At the higher powers, the response is asymmetric, indicating the device is entering the non-linear response regime.

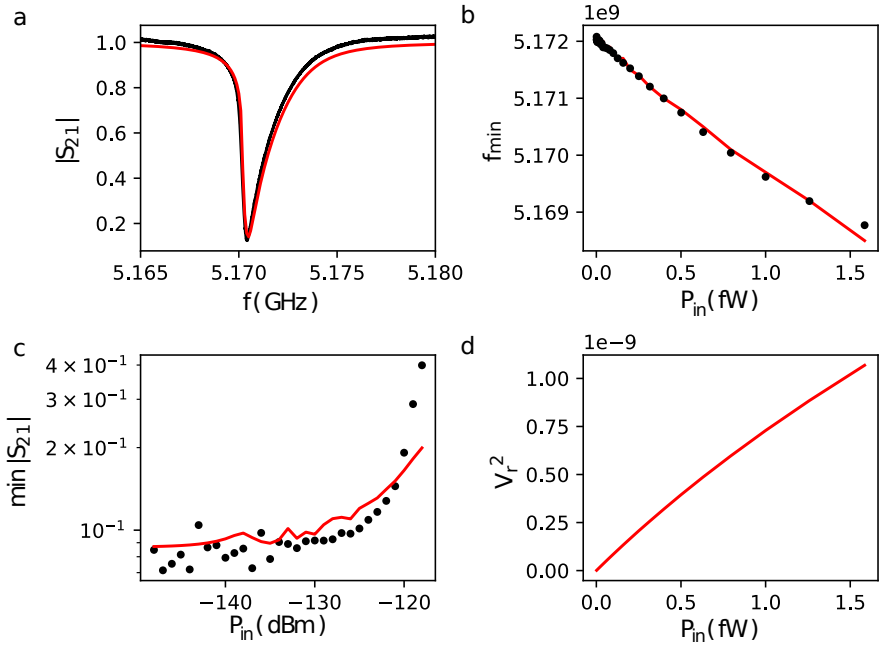

Figure 7.3: **Analysis of the SQUID cavity (HY 1) non-linear response and the observation of non-linear damping** (a) Measured cavity response in the non-linear regime, together with a full model of the S_{21} of a microwave cavity that includes both Duffing non-linearity and non-linear damping. (b) Positions of $f_{S_{21,\min}}$, the frequency minimum of the S_{21} response observed from the data and predicted by the model. Due to the non-linear restoring force of the SQUID junctions, $f_{S21_{\min}}$ decreases for larger amplitdues. The x-axis represents the input power P_{in} (fW), where 1 fW= −120 dBm. (c) Observed and predicted minima of the S_{21} curve as a function of input power. Without non-linear damping, $S_{21,\min}$, the minimum of S_{21}, is independent of power (dashed line). With non-linear damping in the model, $S_{21,\min}$ increases due to the increased dissipation at higher powers. One can also think of this as an decreasing effective internal quality factor, which in an S_{21} measurement results in a shallower resonance dip. At the highest powers, the observed $S_{21,\min}$ deviates from the model, indicating that the approximation by a quadratic non-linear damping $x^2\dot{x}$ no longer holds for the SQUID cavity device.

7.7. APPENDIX 1: CALCULATION OF THE INPUT IMPEDANCE OF A NON-RESONANT CIRCUIT WITH NON-LINEAR DAMPING

For a linear RLC circuit, the system can be expressed by a differential equation,

$$C\ddot{V} = \frac{\dot{V}}{R} + \frac{V}{L} = \dot{I}. \tag{7.4}$$

Here, V is the voltage across the circuit and I is the current through the circuit. By dividing by C, the equation becomes

$$\ddot{V} + 2\gamma\dot{V} + \omega_0^2 V = \frac{\dot{I}}{C} \tag{7.5}$$

where $2\gamma = 1/CR$ and $\omega_0 = 1/\sqrt{LC}$. Next we introduce a Duffing term which is proportional to the third power of the voltage, βV^3, and a non-linear damping term $2\gamma_{nl}V^2$. For harmonic excitation, we have $I(t) = I_0 e^{i\omega t}$. We substitute the derivative $\dot{I} = i\omega I_0 e^{i\omega t}$.

$$\ddot{V} + 2(\gamma + \gamma_{nl})\dot{V} + \omega_0^2 V + \beta V^3 = \frac{i\omega I_0}{C}\cos(\omega t + \phi) \tag{7.6}$$

For a driven system with dissipation, the response has a phase shift of ϕ. We find the first order solution making the assumption that a zeroth order solution has the form $V_0 = V_r \cos(\omega t)$.

$$\ddot{V}_1 = -2(\gamma + \gamma_{nl}V_0^2)\dot{V}_0 - \omega_0^2 V_0 - \beta V_0^3 + \frac{\omega I_1}{C}\cos\omega t - \frac{\omega I_2}{C}\sin\omega t \tag{7.7}$$

We substitute the zeroth order solution into the equation above, and integrate twice. This gives

$$V_1 = A_1\cos\omega t + B_1\sin\omega t + \frac{1}{36}\frac{\beta}{\omega^2}V_r^3\cos 3\omega t - \frac{1}{18}\frac{\gamma_{nl}}{\omega}V_r^3\sin 3\omega t \tag{7.8}$$

where

$$A_1 = \frac{1}{\omega_0^2}[\omega_0^2 V_r + \frac{3}{4}\beta V_r^3 - \frac{\omega I_1}{C}] \tag{7.9}$$

$$B_1 = \frac{1}{\omega^2}[\omega_0^2 I_r + 2\gamma\omega V_r - \frac{1}{2}\gamma_{nl}V_r^3] \tag{7.10}$$

For the zeroth order solution, our guesses for the coefficients are $A_1 = V_r$ and $B_1 = 0$. This gives a set of equations

$$\frac{\omega I_1}{C} = (\omega_0^2 - \omega^2)V_r + \frac{3}{4}\beta V_r^3 \tag{7.11}$$

$$\frac{\omega I_2}{C} = 2\gamma_r + \frac{1}{2}\gamma_{nl}\omega V_r^3. \tag{7.12}$$

By using Equations 7.11 and 7.12, the input impedance $Z_{in} = V/I$ can be found.

$$\frac{1}{Z_{in}} = \frac{I_1 + iI_2}{V_r} = -i\frac{C}{\omega}[\omega_0^2 - \omega^2 + \frac{3}{4}\beta V_r^2] + \frac{C}{\omega}[2\gamma\omega + \frac{1}{2}\gamma_{nl}\omega V_r^2] \tag{7.13}$$

Here i is introduced into the equation because the time derivative of $I_0 e^{i\omega t+\phi}$ is given by $i\omega I_0 e^{i\omega t+\phi}$.

Here we have the new variables

$$\Gamma_{nl} = \frac{1}{4}\frac{\gamma_{nl}}{\gamma}V_r^2 \tag{7.14}$$

$$\gamma_{nl} = \frac{3}{8}\frac{\beta}{\omega}V_r^2 \tag{7.15}$$

and the input impedance can be expressed as follows.

$$Z_{in} = \frac{Z_r Q_i}{1 + \Gamma_{nl} + 2iQ_i\frac{\Delta - \delta_{nl}}{\omega_0}} \tag{7.16}$$

7.8. APPENDIX 2: S_{21} SIMULATION

The calculation of S_{21} is made for a capacitively coupled Josephson junction resonator whose Josephson inductance is diluted with a geometric linear inductor. The resonator considered here is coupled to a transmission line which has a characteristic impedance, and we assign the characteristic impedance of the input port and the output port to be Z_1 and Z_2, respectively. By applying Thevenin's theorem, the output voltage gives an out voltage of 2 V. The voltage applied from the signal generator is calculated to be

$$Z_r = V_{out}\frac{Z_c}{Z_{in} + Z_c} \tag{7.17}$$

where $Z_c = 1/i\omega c$ is the impedance of the coupling capacitor. The output voltage after the device can be found to be

$$V_{out} = 2V_0\frac{Z_2(Z_{in} + Z_c)}{(1+z)(Z_{in} + Z_c) + Z_1 Z_2} \tag{7.18}$$

By substituting the above equation into its predecessor,

$$V_r = 2V_0\frac{Z_{in}}{(1+z)(Z_{in} + Z_c) + Z_1} \tag{7.19}$$

where $z = Z_1/Z_2$. The voltage out of the signal generator with the input power is $\sqrt{2Z_1 P_{in}}e^{i\phi}$. Here a phase factor $e^{i\phi}$ is introduced to make V_r always take real values. This can be expressed as

$$V_r = \sqrt{8Z_1 P_{in}}\frac{Z_r Q_i}{1 + \Gamma_{nl} + 2iQ_i\frac{\Delta - \delta_{nl}}{\omega_0}} \tag{7.20}$$

where $\Gamma_{nl} = \frac{1}{4}\frac{\gamma_{nl}}{\gamma}V_r^2$ and $\delta_{nl} = \frac{3}{8}\frac{\beta}{\omega}V_r^2$. By squaring both sides of the equation, one has

$$\frac{V_r^2}{8Z_1P_{in}} = \left|\frac{Z_{in}}{(1+z)(Z_{in}+Z_c)+Z_1}\right|^2 \tag{7.21}$$

This reduces to a bicubic equation of V_r^2

$$a_1V_r^6 + a_2V_r^4 + a_3V_r^2 + a_4 \tag{7.22}$$

where

$$a_1 = (\tfrac{1}{4}\tfrac{\gamma_{nl}}{\gamma})^2 + (\tfrac{3\beta}{8\gamma\omega})^2[Z_1 + \tfrac{(1+z)^2}{\omega^2C_c^2}]$$
$$a_2 = [\tfrac{1}{2}\tfrac{\gamma_{nl}}{\gamma} - \tfrac{3\Delta\beta}{4\gamma^2\omega}][Z_1^2 + \tfrac{(1+z)^2}{\omega^2C_c^2}] + \tfrac{1}{2}(1+z)Z_1R\tfrac{\gamma_{nl}}{\gamma} - (1+z)^2\tfrac{3R\beta}{4\omega^2C_c}$$
$$a_3 = (1+z)^2[R^2 + \tfrac{2R\Delta}{\gamma\omega C_c}] + 2(1+z)Z_1R + [Z_1^2 + \tfrac{(1+z)^2}{\omega^2C_c^2}][1 + \tfrac{\Delta^2}{\gamma^2}]$$
$$a_4 = -8Z_1R^2P_{in}$$

By substituting $2\gamma = \omega_0/Q_i$, $R = Z_rQ_i$, and $Z_1 = Z_2 = Z_0$, the coefficients of the polynomial can be rewritten as $a_1 = \frac{Q_i}{\omega_0^2}[\frac{\gamma_{nl}}{4} + (\frac{3\beta}{4\omega})][Z_0^2 + \frac{4}{\omega^2C_c}]$

$$a_2 = \frac{Q_i}{\omega_0[\gamma_{nl} - 3\frac{\Delta\beta Q_i}{\omega\omega_0}]}[Z_0^2 + \tfrac{4}{\omega^2C_c^2}] + 2Z_r\tfrac{Q_i}{\omega_0}[Z_0\gamma_{nl} - \tfrac{3\beta}{\omega^2C_c}]$$
$$a_3 = 4Z_rQ_i[Z_0 + Z_rQ_i + 4\tfrac{Q_i\Delta}{\omega_c}] + [Z_0^2 + \tfrac{4}{\omega^2C_c^2}][1 + 4Q_i^2\tfrac{\Delta^2}{\omega_0^2}]$$
$$a_4 = -8Z_0Z_r^2Q_i^2P_{in}$$

Equation 7.9 with the coefficients above can be solved numerically. The solutions are substituted into the equation below.

$$Z_{in} = \frac{Z_rQ_i}{1 + \Gamma_{nl} + 2iQ_i\frac{\Delta - \delta_{nl}}{\omega_0}} \tag{7.23}$$

Now the power dependant response can be calculated as

$$S_{21}(P_{in}) = \frac{2(Z_{in}+Z_c)}{2(Z_{in}+Z_c)+Z_0}. \tag{7.24}$$

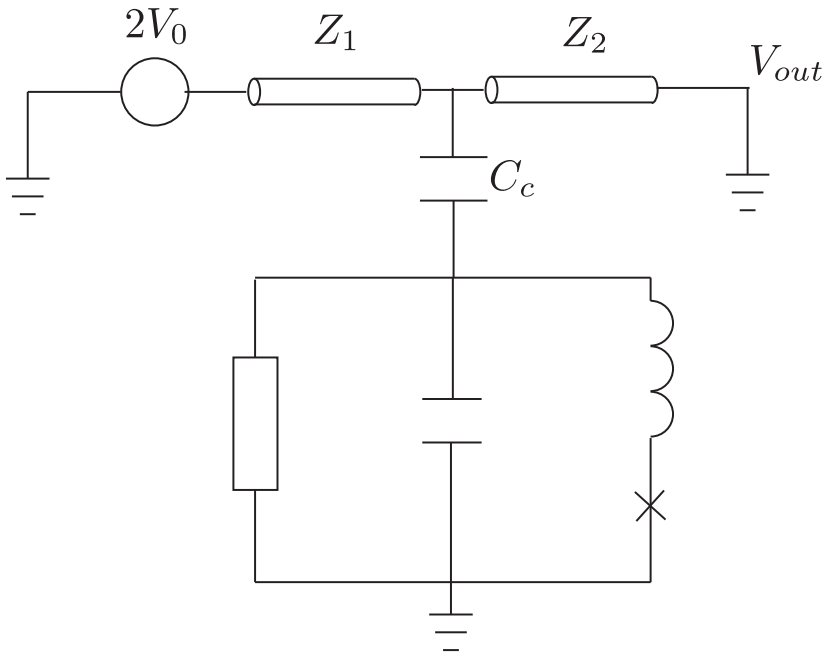

Figure 7.4: **Effective circuit diagram of the system. The equivalent non-linear circuit model consists of a Josephson junction, a linear geometric inductance, a linear resistance, a non-linear resistance, and a capacitance.** The resonant circuit is capacitively coupled to the transmission line with a coupling capacitor, C_c. The microwave source is replaced by its equivalent voltage source that has 2 V_0. The impedance of the input line of the system is denoted by Z_1. The impedance of the output line is denoted by Z_2. The transmission spectrum S_{21} is defined by the ratio of the output voltage V_{out} to the input voltage V_0.

Table 7.1: Important parameters of the devices

#	Estimation Technique	$P_{in,min}$ (dBm)	$N_{ph,min}$	$P_{in,max}$ (dBm)	$N_{ph,max}$
1	PNA output power + input line attenuation estimation	-142.86	0.18	-112.86	183.29
2	PNA input power + amplifier chain gain estimate	-182	0.00	-152	0.02
3	PNA SNR + HEMT input noise estimate +attenuation loss between sample and HEMT estimate	-155.75	0.01	-125.75	9.41
4	Power-dependent frequency shift + formula for β	-148	0.06	-118	56.04
5	Power estimation based on amplitudes of non-linear Duffing response, V_r^2	NA	0.06	NA	46.49

7.9. APPENDIX 3: INPUT POWER/NUMBER OF PHOTONS

The equation below is used to estimate the intracavity photon numbers.

$$n_d = \frac{2P_{in}\kappa_{ext}}{\hbar\omega_{cav}(\kappa_{loaded}^2 + 4\delta^2)} \tag{7.25}$$

Here, P_{in}, κ_{ext}, κ_{loaded}, ω_{cav}, and δ are the input power at the device, the external cavity decay rate, the loaded cavity decay rate, the resonance frequency of the cavity, and the detuning from the resonance frequency. Both the external and loaded cavity decay rates and the resonance frequency are determined from a linear Lorentzian fitting. The input power at the device can be estimated in several ways. A detailed discussion of the input power estimation can be found in the Appendix 2 of Chapter 6, and a table is given in Table 7.1.

The technique used to estimate the attenuation at the sample (fourth row) is the use of the known Duffing coefficient with monitoring the simulated cavity response S_{21} as a function of power while adjusting the non-linear damping coefficient γ_{nl}. The minimum excitation power has a value in agreement with the value estimated by adding up the total attenuation on the input line.

The last row shows the estimated input power as well as the correspxonding photon numbers based on the amplitudes of the non-linear Duffing response, V_r^2. The energy stored inside the capacitor of the device can be expressed as $CV_r^2/2$. The number of photons inside the resonator is then $n_d = \frac{1CV_r^2}{2\hbar\omega_0}$.

REFERENCES

[1] A. Blais, R.-S. Huang, A. Wallraff, S. M. Girvin, and R. J. Schoelkopf, *Cavity quantum electrodynamics for superconducting electrical circuits: an architecture for quantum computation,* Physical Review A **69** (2004), 10.1103/PhysRevA.69.062320, arXiv: cond-mat/0402216.

[2] A. Wallraff, D. I. Schuster, A. Blais, L. Frunzio, R.-S. Huang, J. Majer, S. Kumar, S. M. Girvin, and R. J. Schoelkopf, *Strong coupling of a single photon to a superconducting qubit using circuit quantum electrodynamics,* Nature **431**, 162 (2004).

[3] M. D. Reed, L. DiCarlo, B. R. Johnson, L. Sun, D. I. Schuster, L. Frunzio, and R. J. Schoelkopf, *High-Fidelity Readout in Circuit Quantum Electrodynamics Using the Jaynes-Cummings Nonlinearity,* Physical Review Letters **105** (2010), 10.1103/PhysRevLett.105.173601, arXiv: 1004.4323.

[4] M. Hatridge, R. Vijay, D. H. Slichter, J. Clarke, and I. Siddiqi, *Dispersive magnetometry with a quantum limited SQUID parametric amplifier,* Physical Review B **83**, 134501 (2011).

[5] P. Bertet, F. R. Ong, M. Boissonneault, A. Bolduc, F. Mallet, A. C. Doherty, A. Blais, D. Vion, and D. Esteve, *Circuit quantum electrodynamics with a nonlinear resonator,* arXiv:1111.0501 [quant-ph] (2011), arXiv: 1111.0501.

[6] C. Beltran, *Development of a Josephson Parametric Amplifier for the Preparation and Detection of Nonclassical States of Microwave Fields*, Ph.D. thesis, University of Colorado (2010).

[7] A. Palacios-Laloy, F. Nguyen, F. Mallet, P. Bertet, D. Vion, and D. Esteve, *Tunable resonators for quantum circuits,* Journal of Low Temperature Physics **151**, 1034 (2008), arXiv: 0712.0221.

[8] Lifshitz Ron and Cross M. C., *Nonlinear Dynamics of Nanomechanical and Micromechanical Resonators,* Reviews of Nonlinear Dynamics and Complexity Wiley Online Books (2009), 10.1002/9783527626359.ch1.

[9] A. Eichler, J. Moser, J. Chaste, M. Zdrojek, I. Wilson-Rae, and A. Bachtold, *Nonlinear damping in mechanical resonators based on graphene and carbon nanotubes,* Nature Nanotechnology **6**, 339 (2011), arXiv: 1103.1788.

[10] S. Zaitsev, R. Almog, O. Shtempluck, and E. Buks, *Nonlinear damping in nanomechanical beam oscillator,* arXiv:cond-mat/0503130 (2005), arXiv: cond-mat/0503130.

[11] I. Pietikäinen, S. Danilin, K. S. Kumar, A. Vepsäläinen, D. S. Golubev, J. Tuorila, and G. S. Paraoanu, *Observation of the Bloch-Siegert shift in a driven quantum-to-classical transition,* Physical Review B **96** (2017), 10.1103/PhysRevB.96.020501, arXiv: 1610.09153.

[12] P. J. de Visser, J. J. A. Baselmans, P. Diener, S. J. C. Yates, A. Endo, and T. M. Klapwijk, *Generation-Recombination Noise: The Fundamental Sensitivity Limit for Kinetic Inductance Detectors,* Journal of Low Temperature Physics **167**, 335 (2012).

8

CONCLUSION

This chapter includes conclusions from the experimental chapters, as well as perspectives for cavity readout of quantum systems and coherence in microwave resonant systems. Cavity readout of quantum systems provides great platforms for accessing quantum systems where our interest for probing was mechanical oscillators. The study of microwave coherence allows understanding how a microwave resonator mode interacts with dissipation channels, and this becomes a great testbed for coherence in superconducting qubits. Moreover, advances in nanotechnology have overcome the difficulties encountered in the project, and may lead to a new regime of physics, for instance single photon strong coupling.

Throughout the project, microwave cavities have been essential components of the experiments, such as microwave CPW, lumped element cavities, microstrips, and flux tunable cavities. In the field of low temperature microwave systems, the importance of superconducting linear and non-linear resonant circuits cannot be emphasized enough, to name a few, cavity readout of hybrid systems[1, 2], microwave kinetic inductance detectors (MKID) [3, 4], Josephson parametric amplifier/ frequency converters [5, 6], and superconducting qubits[7].

In this thesis, microwave cavities made of molybdenum rhenium (MoRe) have been used for the detection of mechanical motion in cavity optomechanical systems. In Chapter 4, the use of high impedance microstrip resonators to detect the motion of MoRe mechanical drums was described. The modulation of the cavity frequency due to mechanical motion up-converts a mechanical signal to a microwave signal. A mechanical drum is electrostatically actuated, and a microwave cavity is used for detection. The temperature dependence and power dependence give suggestive evidence of non-resonant TLSs in our MoRe metal drums. In Chapter 5, the system is similar to the device in Chapter 4. Instead, the system consists of a mechanical nanowire which is a silicon nitride (SiN) nanowire covered with MoRe and a CPW cavity. The mechanical element is dissipatively coupled to the CPW. The mechanical motion is detected using homodyne detection in the same way as in Chapter 4. Away from zero dc bias voltage, with an ac voltage signal at twice the mechanical resonance frequency, parametric excitation of the mechanical response is enabled. By introducing an extra strong tone near the cavity frequency, the amplified mechanical signal is up-converted to microwave frequency.

In Chapter 6, the decoherence of microwave flux tunable cavities was investigated. The aim is to use these cavities for coupling to nanowires. A comparison was made between two different fabrication processes: hybrid devices (MoRe lumped element and Al/AlOx/Al dc SQUID) and a single lift off process with Al/AlOx/Al. There was a difference in their coherence. The hybrid devices had a coherence two orders of magnitude larger than the single lift off devices, which is due to insufficient surface treatment in the single lift off devices. For the single lift off devices, further improvement may be achieved by optimizing the parameters of the oxygen de-scumming. For the hybrid devices, the optimization of the fabrication conditions may be necessary considering the previously reported [8] achievment of internal quality factors of up to 100,000 with a CPW fabricated on top of silicon. Further, recent reports show improvements in internal quality factors by over a million at the single photon level by carefully controlling the fabrication parameters[9], which give us options to employ for higher Q from the use of better material.

In Chapter 7, non-linear dissipation in the microwave in Josephson resonators was investigated. We modelled the cavity response that included a non-linear dissipation term $\gamma x^2 \dot{x}$ in the Duffing equation. The existence of this decoherence is known, and used for high fidelity measurement of transmon qubits in the dispersive regime[10]. The origin of the non-linear loss has been much studied, but further in-

vestigation may be beneficial.

The biggest challenge in this particular project has been to combine microwave and mechanical resonators without sacrificing their coherences. The technique presented in this thesis requires three different materials for three different purposes: Al/AlOx/Al for the Josephson junctions, MoRe for the high Q cavity, and SiN for a high Q mechanical oscillator. If one of the materials could accomodate one more function, fabrication would become relatively easy. Perhaps new ideas and progress in nanotechnology will lead to advances in this field which may lead the way to single photon strong coupling. This would be a wonderful milestone in the field of cavity optomechanics, and provide novel experiements unreachable with current state of the art devices.

REFERENCES

[1] J.-M. Pirkkalainen, E. Damskägg, M. Brandt, F. Massel, and M. A. Sillanpää, *Squeezing of quantum noise of motion in a micromechanical resonator,* Physical Review Letters **115** (2015), 10.1103/PhysRevLett.115.243601, arXiv: 1507.04209.

[2] J. M. Fink, M. Kalaee, A. Pitanti, R. Norte, L. Heinzle, M. Davanco, K. Srinivasan, and O. Painter, *Quantum Electromechanics on Silicon Nitride Nanomembranes,* Nature Communications **7**, 12396 (2016), arXiv: 1512.04660.

[3] M. Faverzani, P. K. Day, E. Ferri, A. Giachero, B. Margesin, R. Mezzena, A. Nucciotti, and A. Puiu, *Electron-phonon coupling in Ti/TiN MKIDs multilayer microresonator,* (2017).

[4] J. Gao, M. R. Visser, M. O. Sandberg, F. C. S. da Silva, S. W. Nam, D. P. Pappas, K. D. Irwin, D. S. Wisbey, E. Langman, S. R. Meeker, B. A. Mazin, H. G. Leduc, and J. Zmuidzinas, *A titanium-nitride near-infrared kinetic inductance photon-counting detector and its anomalous electrodynamics,* Applied Physics Letters **101**, 142602 (2012), arXiv: 1208.0871.

[5] N. Bergeal, F. Schackert, M. Metcalfe, R. Vijay, V. E. Manucharyan, L. Frunzio, D. E. Prober, R. J. Schoelkopf, S. M. Girvin, and M. H. Devoret, *Phase preserving amplification near the quantum limit with a Josephson Ring Modulator,* Nature **465**, 64 (2010), arXiv: 0912.3407.

[6] C. Eichler and A. Wallraff, *Controlling the dynamic range of a Josephson parametric amplifier,* EPJ Quantum Technology **1** (2014), 10.1140/epjqt2, arXiv: 1305.6583.

[7] A. Wallraff, D. I. Schuster, A. Blais, L. Frunzio, R.-S. Huang, J. Majer, S. Kumar, S. M. Girvin, and R. J. Schoelkopf, *Strong coupling of a single photon to a superconducting qubit using circuit quantum electrodynamics,* Nature **431**, 162 (2004).

[8] V. Singh, S. J. Bosman, B. H. Schneider, Y. M. Blanter, A. Castellanos-Gomez, and G. A. Steele, *Optomechanical coupling between a multilayer graphene mechanical resonator and a superconducting microwave cavity,* Nature Nanotechnology **9**, 820 (2014), arXiv: 1403.5165.

[9] S. Ohya, B. Chiaro, A. Megrant, C. Neill, R. Barends, Y. Chen, J. Kelly, D. Low, J. Mutus, P. O'Malley, P. Roushan, D. Sank, A. Vainsencher, J. Wenner, T. C. White, Y. Yin, B. D. Schultz, C. J. Palmstrøm, B. A. Mazin, A. N. Cleland, and J. M. Martinis, *Sputtered TiN films for superconducting coplanar waveguide resonators,* arXiv:1306.2966 [cond-mat] (2013), arXiv: 1306.2966.

[10] M. D. Reed, L. DiCarlo, B. R. Johnson, L. Sun, D. I. Schuster, L. Frunzio, and R. J. Schoelkopf, *High-Fidelity Readout in Circuit Quantum Electrodynamics*

Using the Jaynes-Cummings Nonlinearity, Physical Review Letters **105** (2010), 10.1103/PhysRevLett.105.173601, arXiv: 1004.4323.

SUMMARY

In this thesis, the microwave detection of mechanically compliant objects is investigated. This starts with a system of a suspended metal drum capacitively coupled to a high impedance microstrip resonator. The mechanical non-linear dissipation of the drums is studied. Next, a suspended nanowire coupled to a CPW resonator is studied. With an electrostatic drive at twice the mechanical resonance frequency, there occurs a parametric excitation of either the mechanical signal or the coupled microwave resonance frequency of the cavity. Then the microwave loss in flux-tunable resonators is investigated for future experiments. One of the goals of this project was to couple a suspended nanowire with a SQUID loop of a flux tunable cavity. Here, the dielectric loss in flux tunable resonators is studied in order to optimize the design of future devices.

In **Chapter 2**, the theoretical background is discussed. The chapter consists of four sections, covering cavity optomechanics, electrostatic driving, SQUID cavities, and non-linear dissipation. First, cavity optomechanics is briefly discussed with a basic introduction, linearization, the strong coupling regime, cooperativity, and quadratic coupling. The section on the electrostatic driving starts with the derivation of an actuating force applicable for our measurement setups discussed in Chapter 4. Then parametric resonance is discussed. The equation of motion of an object whose motion is modulated at twice its natural frequency is considered. Then parametric amplification and squeezing are discussed, talking about the differences between two different kinds of parametric amplification processes: three-wave mixing and four-wave mixing, using examples of Josephson parametric amplifiers. In the section on the SQUID cavity, first there is covered the standard SIS Josephson junction. Then we treat a Josephson junction as a non-linear inductance, which is of the essence of SQUID cavities. It also covers the Duffing response of a SQUID cavity in terms of the excitation voltage and shows that a small signal input along with a strong pump near the cavity resonance leads to four-wave mixing amplification. Applications to devices similar to a SQUID cavity are discussed.

Chapter 3 describes the fabrication of the devices. This section is based mostly on things done in the cleanroom for making a device of a suspended nanowire coupled to a SQUID cavity. First, the fabrication of MoRe superconducting resonators is discussed. Then the fabrication of Josephson junctions is covered. For the fabrication of Josephson junctions, the Dolan bridge technique is used. This subsection contains information about shadow evaporation and lift off, as well as some problems involved with the fabrication of Josephson junctions. In the section on the fabrication of SQUID cavities, basically two different techniques for fabricating SQUID

cavities are discussed. One is a combination of RIE etching and lift off of Josephson junctions. This fabrication step first patterns a lumped element resonator with sputtering, EBL, and RIE etching. Subsequently, a dc SQUID is shadow evaporated using a bilayer resist stack, and lifted off, which creates superconducting contacts between the MoRe and Al. The other process is single step lift off of all the circuit elements with Al/AlO_x/Al. It also includes a discussion of the difficulties encountered during fabrication. In addition, it presents a simulation of the circuit element, L_J, L_g, and C_g in Sonnet. Next, the fabrication of the nanowire device is described. The idea is to use the high mechanical quality of stoichiometric LPCVD silicon nitride as a foundation which is covered by MoRe to form a SQUID loop, and a nanowire is latter released by RIE etching. Lastly, the measurement setup, such as the microwave lines and sample boxes, as well as the dilution refrigerator is discussed.

In **Chapter 4**, the non-linear mechanical loss of the MoRe superconducting metal drum is discussed. The metal drum is dissipatively coupled to a microwave superconducting resonator via a capacitance, which enables actuating the mechanical drum electrostatically and using a microwave cavity for readout. As a function of the actuation force, the mechanical quality factor increases in both the linear and non-linear regime. Further, the drum is tested for temperature dependence and frequency shift as well as an increase of the quality factor, which is observed when approaching the base temperature. These observations can be explained by non-resonantly coupled TLS.

In **Chapter 5**, a MoRe/SiN mechanical nanowire is used for amplification of microwave resonant mode. The mechanical resonator is capacitively coupled to a microwave CPW cavities in dissipative coupling configuration. The motion of the nanowire modulates the cavity linewidth as well as resonance frequency of the cavity. Having the mechanical oscillator in between the transmission line and the cavity, it enables to electrostatically actuate the nanowire with dc and ac voltages, and cavity is used to read out mechanical motion with a drive tone near resonance frequency of the cavity. By properly choosing detuning of the strong drive from the cavity resonance along with parametric excitation, microwave amplification at the cavity frequency can be achieved. In this chapter, parametric amplification of microwave cavity frequency with electrostatical driving at twice of the mechanical resonance frequency.

In **Chapter 6**, the microwave loss in flux tunable SQUID cavities fabricated using two different techniques is investigated. The first one is the hybrid SQUID cavity. A lumped element resonator is patterned from 60 nm of sputtered MoRe film, and subsequently a dc SQUID is lifted-off with shadow evaporation. The second technique is single step lift-off process of SQUID cavities. In this fabrication technique, the design of the SQUID cavity is kept the same as for the first technique. Also a CPW resonator terminated by a dc SQUID fabricated with the latter technique is tested. From a comparison of the quality factors, the first technique achieves a coherence greater by two orders of magnitudes at integer flux quantum. The origins within the latter process of the microwave losses sterm from two different dielectric losses: (1) Carbon contam-

ination of electron beam resist residue for lift off gives rise to a large dielectric loss compare with intrinsic silicon. (2) A large participation ratio of the AlO_x layer from shadow evaporation to the field volume seems to be the other source of microwave loss.

In **Chapter 7**, the non-linear loss of Josephson junction resonators is investigated. This non-linear damping term leads to the suppression of the amplitude and an increase of the critical power to reach bifurcation. We numerically simulated the Duffing response, as well as the Duffing cavity response as a function of the driving force. Using this simulation, we simultaneously estimate the non-linear damping term and the input power at the device using the parameters that give the best fits to the measurements.

SAMENVATTING

In dit proefschrift wordt de microgolfdetectie van mechanisch flexibele objecten onderzocht. Dit begint met een systeem van een hangende metalen trommel die capacitief is gekoppeld aan een microstripresonator met hoge impedantie. We bestuderen de mechanische niet-lineaire dissipatie van de trommels, en vervolgens een hangende nanodraad gekoppeld aan een CPW-resonator. Bij een elektrostatische aandrijving met tweemaal de mechanische resonantiefrequentie treedt er een parametrische excitatie op van ofwel het mechanische signaal ofwel de gekoppelde microgolfresonantiefrequentie van de holte. Vervolgens onderzoeken we de microgolfdemping in resonatoren met regelbare flux voor toekomstige experimenten. Een van de doelen van dit project was om een hangende nanodraad te koppelen aan een SQUID-lus van een holte met regelbare flux. Hier bestuderen we het diktrisch verlies in resonatoren met regelbare flux om het ontwerp van toekomstige apparaten te optimaliseren.

In hoofdstuk 2 wordt de theoretische achtergrond besproken. Het hoofdstuk bestaat uit vier secties: over optomechanica van holtes, elektrostatische aandrijving, SQUID-holtes en niet-lineaire dissipatie. Eerst bespreken we kort de optomechanica van holtes met een basisintroductie, linearisering, het sterke koppelingsregime, cooperativiteit en kwadratische koppeling. De sectie over elektrostatische aandrijving begint met het afleiden van een aandrijfkracht die van toepassing is op onze meetopstellingen zoals besproken in hoofdstuk 4. Vervolgens bespreken we de parametrische resonantie. We beschouwen de bewegingsvergelijking van een object waarvan de beweging wordt gemoduleerd met tweemaal de eigenfrequentie. Vervolgens bespreken we parametrische versterking en samendrukking, met aandacht voor de verschillen tussen twee verschillende soorten parametrische versterkingsprocessen, namelijk driegolvenmenging en viergolvenmenging, waarbij voorbeelden van Josephson-parametrische versterkers worden gebruikt. In de sectie over SQUID-holtes bespreken we eerst de standaard SIS Josephson-junctie. Vervolgens behandelen we een Josephson-junctie als niet-lineaire zelfinductie, een verschijnsel dat karakteristiek is voor SQUID-holtes. In deze sectie bespreken we ook de Duffingrespons van een SQUID-holte in termen van excitatiespanning, en laten we zien dat een kleine signaalinvoer samen met een sterke pomp dichtbij de holteresonantie leidt tot versterking van de viergolvenvermenging. We kijken naar toepassing op apparaten die vergelijkbaar zijn met een SQUID-holte.

In hoofdstuk 3 beschrijven we de fabricage van de apparaten. Deze sectie betreft grotendeels de dingen die in de cleanroom worden gedaan voor het maken van een apparaat van een opgehangen nanodraad gekoppeld aan een SQUID-holte. Eerst

wordt de fabricage van MoRe-supergeleidende resonatoren besproken. Vervolgens kijken we naar de fabricage van Josephson-juncties, waarvoor de Dolan-brugtechniek wordt gebruikt. Deze subsectie bevat informatie over schaduwverdamping en het optilproces, evenals enkele problemen bij de fabricage van Josephson-juncties. In de sectie over de fabricage van SQUID-holtes worden hiervoor twee verschillende technieken besproken. De ene is een combinatie van RIE-etsen en ?optillen? van Josephson-juncties. In deze fabricagestap wordt eerst een patroon maakt van een lumped element-resonator met sputteren, EBL en RIE-etsen. Vervolgens wordt op een dc SQUID schaduwverdamping toegepast met behulp van een tweelaagse resist stack en wordt de dc SQUID eraf getild, zodat er supergeleidende contacten ontstaan tussen MoRe en Al. Bij de andere techniek worden alle circuitelementen met Al/AlOx/Al in stap eraf getild. We bespreken ook de problemen bij de fabricage, en we presenteren een simulatie van de circuitelementen LJ, Lg en Cg in Sonnet. Vervolgens beschrijven we de fabricage van het nanodraadapparaat. Het idee is om de hoge mechanische kwaliteit van stoichiometrische LPCVD-siliciumnitride te gebruiken als een basislaag die wordt bedekt door MoRe om een SQUID-lus te vormen, en een nanodraad wordt later losgemaakt door middel van RIE-etsen. Ten slotte bespreken we de meetopstelling met de microgolflijnen en de monsterkastjes, en het dilutiekoelapparaat.

In hoofdstuk 4 bespreken we het niet-lineaire mechanische verlies van de MoRe-supergeleidende metalen trommel. De metalen trommel wordt via capaciteit dissipatief gekoppeld aan een microgolf-supergeleidende resonator. Hierdoor kan de mechanische trommel elektrostatisch worden aangedreven en kan een microgolfholte worden gebruikt voor het aflezen. Als een functie van de aandrijfkracht neemt de factor mechanische kwaliteit toe in zowel het lineaire als het niet-lineaire regime. Verder wordt de trommel getest op temperatuurafhankelijkheid en frequentieverschuiving en is er een toename van de kwaliteitsfactor, die blijkt op te treden bij het naderen van de basistemperatuur. Deze waarnemingen kunnen worden verklaard door niet-resonant gekoppelde TLS?en.

In hoofdstuk 5 wordt een mechanische nanodraad van MoRe/SiN gebruikt voor versterking van de microgolfresonantiemodus. De mechanische resonator wordt capacitief gekoppeld aan microgolf-CPW-holtes in een dissipatieve koppelingsconfiguratie. De beweging van de nanodraad moduleert de lijnbreedte en de resonantiefrequentie van de holte. Doordat de mechanische oscillator zich tussen de transmissielijn en de holte bevindt, kan de nanodraad elektrostatisch worden geactiveerd met gelijkstroom- en wisselstroomspanningen. De holte wordt gebruikt om mechanische beweging uit te lezen met een ?aandrijftoon? die dichtbij de resonantiefrequentie van de holte ligt. Door de verstemming van de sterke aandrijving vanaf de holteresonantie juist te kiezen, samen met parametrische excitatie, kan microgolfversterking op de holtefrequentie worden bereikt. Parametrische versterking van de microgolfholtefrequentie wordt bereikt door elektrostatische aandrijving op tweemaal de mechanische resonantiefrequentie.

In hoofdstuk 6 onderzoeken we microgolfdemping in SQUID-holtes met regelbare flux, die vervaardigd zijn met behulp van twee verschillende technieken. De eerste is de hybride SQUID-holte. Er wordt een patroon gemaakt van een lumped element-resonator van 60 nm gesputterde MoRe-film, en vervolgens wordt er een dc SQUID met schaduwverdamping afgetild. Bij de andere techniek worden SQUID-holtes in stap eraf getild. Bij deze fabricagetechniek is het ontwerp van de SQUID-holte hetzelfde als bij de eerste techniek. Ook testen we een CPW-resonator die wordt afgesloten door een dc SQUID, gefabriceerd met de tweede techniek. Wanneer we de kwaliteitsfactoren vergelijken, wordt bij de eerste techniek een coherentie bereikt die twee ordes van grootte groter is bij een geheeltallig fluxkwantum. De oorsprong binnen het laatste proces van de microgolfdemping komt voort uit twee vormen van diktrische verliezen: (1) koolstofverontreiniging met het resist-residu van de elektronenbundel voor het optillen zorgt voor een groot diktrisch verlies in vergelijking met intrinsiek silicium; (2) een grote participatieratio van de AlOx-laag van schaduwverdamping tot het veldvolume lijkt de andere oorzaak van microgolfdemping.

In hoofdstuk 7 onderzoeken we de niet-lineaire demping van Josephson-junctieresonatoren. Deze niet-lineaire dempingterm leidt tot onderdrukking van de amplitude en vergroting van de kritieke kracht voor het bereiken van bifurcatie. We hebben numeriek de Duffing-respons gesimuleerd, en ook de Duffing-holterespons als functie van de aandrijfkracht. Met behulp van deze simulatie schatten we tegelijkertijd de niet-lineaire dempingterm en het invoervermogen op het apparaat, met de parameters die het beste passen bij de metingen.

ACKNOWLEDGEMENTS

I would like to thank anyone contributed for finishing my dissertation directory or indirectly. Experience that I had in Delft was quite valuable and there were many wonderful moments.

First, I would like to thank Gary Steele for all advises and encouragements for scientific improvements. Your deep understanding in physics, explaining physical events in precise language, excitement in physics, and excellent interpersonal skills are qualities that I admire.

I would like to thank Yaroslav for being my promotor at the end of my PhD.

To people in the Steele group, thank you for being patient and supportive for doing experiments or fabrication or analysis with me. I could not have finished my thesis without your help. Special thanks to Vibhor, who was always nice to talk to whether inside or outside the university. I found it fortunate that you were a post-doc during my first a few years in Delft.

To people in QN, I am very grateful to get to know you, and interaction with you guys made my days in Delft better, discussion on a hallway, MED outing, beer in the city center on Friday afternoon, dinner we had, and so much more. Thank you!!

To people in Kavli nanolab , thank you so much for maintaining the cleanroom always accessible. Through the years in Delft, I had the luxury of accessing to the cleanroom without concerning the cost of use. This provided opportunities to test, and learn from the outcomes. And I deeply appreciate for support outside of the cleanroom, as well.

Also, I would like to thank my family for all the support they provided.

A

APPENDIX

A.1. PYTHON CODE FOR DUFFING RESPONSE

Simulation used in Figure 2.5 and Figure 2.6 solve equation 2.50 numerically for r^2. The script below finds roots of the equation for excitation power, and solutions are plotted against frequency, f. Internal and external quality factors are loaded into this code where the only internal and external quality factors are used to calculate decay ratio.

```
import numpy as np
import matplotlib.pyplot as plt
from numpy.polynomial import Polynomial as P
from numpy import arange,array,ones,linalg
import Gnuplot
data=np.loadtxt('MoRe_Qint_v2.txt')
data2=np.loadtxt('freqvspower.txt')
ind=np.linspace(0,30,31)
Qint=data[1,:]
Qext=data[2,:]
Ql=1/(1/Qint+1/Qext)
gamma_nl=0.0
omega_0=5.172e9
omega_start=5.155e9
omega_stop=5.185e9
omega_points=(600)
m=1.0e-30
```

A

```
alfa=-1.0e-2
force_start=1.00e-17
force_stop=1.0e-14
force_points=20


n=36
a=((force_start)/(force_stop))**(-1.0/(n-1))
resonance=data2[0,:]
power=data2[1,:]


zeta=1/(2*(Ql[0]))0.5*1.0e-4
Max_lin=[]
freq_max=[]
alfa_list=[]
comp=[]
IND=[]
omega=np.linspace(omega_start,omega_stop,omega_points)
force_list=[]
RFREQ=[]
RAMP=[]
F=1.0e-16


for ii in range(0,n):
    F=force_start*(a**(ii))
    force_list.append(F)
    NewCoeff1=[]
    NewCoeff2=[]
    NewCoeff3=[]
    NewCoeff=[]
    OMG=[]
    newcoeff1=[]
    newcoeff2=[]
    newcoeff3=[]
    for i in range(0,600):
        OMG=omega[i]/omega_0
        rho=1-OMG*OMG
        delta=2*zeta*OMG
        Phi=F/m/omega_0/omega_0
        coeff=[9*alfa*alfa+gamma_nl*OMG*OMG,
        (24*alfa*rho+16*OMG*OMG*zeta*gamma_nl),16*(rho*rho+delta*delta),-16*Phi*Phi]
        comp.append(coeff)
        newcoeff=np.roots(coeff)
```

```
        NewCoeff1.append(np.array(newcoeff[0]).tolist())
        NewCoeff2.append(np.array(newcoeff[1]).tolist())
        NewCoeff3.append(np.array(newcoeff[2]).tolist())
        NewCoeff.append([omega[i],newcoeff[0],newcoeff[1],newcoeff[2]])

    NewCoeff=np.array(NewCoeff)
    for iii in range(0,600):
        if np.abs(NewCoeff[iii,1].imag)<=0.00000000000000001:
            NewCoeff1=[NewCoeff[iii,0].real,NewCoeff[iii,1].real]
            newcoeff1.append(NewCoeff1)
        if np.abs(NewCoeff[iii,2].imag)<=0.00000000000000001:
            NewCoeff2=[NewCoeff[iii,0].real,NewCoeff[iii,2].real]
            newcoeff2.append(NewCoeff2)
        if np.abs(NewCoeff[iii,3].imag)<=0.0000000000000001:
            NewCoeff3=[NewCoeff[iii,0].real,NewCoeff[iii,3].real]
            newcoeff3.append(NewCoeff3)
    newcoeff1=np.array(newcoeff1)
    newcoeff2=np.array(newcoeff2)
    newcoeff3=np.array(newcoeff3)

    if len(newcoeff1)==0 and len(newcoeff2)==0:
        NEWCOEFF=newcoeff3

    if len(newcoeff1)==0 and len(newcoeff3)==0:
        NEWCOEFF=newcoeff2
    if len(newcoeff2)==0 and len(newcoeff3)==0:
        NEWCOEFF=newcoeff1
    if len(newcoeff1)!=0 and len(newcoeff2)!=0 and len(newcoeff3)!=0:
        NEWCOEFF=np.concatenate([newcoeff1,newcoeff2,newcoeff3])
    if len(newcoeff1)!=0 and len(newcoeff2)!=0 and len(newcoeff3)==0:
        NEWCOEFF=np.concatenate([newcoeff1,newcoeff2])
    if len(newcoeff1)!=0 and len(newcoeff3)!=0 and len(newcoeff2)==0:
        NEWCOEFF=np.concatenate([newcoeff1,newcoeff3])
    if len(newcoeff2)!=0 and len(newcoeff3)!=0 and len(newcoeff1)==0:
        NEWCOEFF=np.concatenate([newcoeff2,newcoeff3])

    NEWCOEFF=np.transpose(NEWCOEFF)
    NEWCOEFF=np.array([NEWCOEFF[0],NEWCOEFF[1]])
    freq=np.array(NEWCOEFF[0])
    amp=np.array(NEWCOEFF[1])
    sorter=np.lexsort((amp,freq))
    nc=[]
```

A

```
for duf in zip(freq[sorter],amp[sorter]):
    nc.append(duf)
nc=np.array(nc)
nc1=list(nc[:,0])
Uni=[]
Uni_lor = []
R1 = []
R2 = []
R3 = []

unique, counts =np.unique(nc1,return_counts=True)
for iii in range(0,len(counts)):#counting frequency.
if counts[iii]>2:#if count is larger than zero, it appended to Uni
        Uni.append([unique[iii],counts[iii]])#theoretically only three solution roots
        region is appended.

Uni=np.transpose(Uni)

Uni=np.array(Uni)
Uni_lor=np.array(Uni_lor)

if len((Uni))==0:
    Maxlin=max(np.transpose(nc[:,1]))
    nRfreq=np.transpose(nc[:,0])
    nRamp=np.transpose(nc[:,1])
    RFREQ.append(nRfreq)
    RAMP.append(nRamp)
    plt.plot(nRfreq,nRamp,'-')
    IND.append(np.argmax(nc[:,1]))

    Max_lin.append(Maxlin)
    freq_max.append([max(nRamp),nRfreq[np.argmax(nRamp)],(F)])

if len(Uni)>0:
    Uni=list(Uni)
    Uni=np.array(Uni)
    for iv in range(0,len(nc[:,0])):
        if (min(Uni[0]))<=(nc[iv,0]) and (nc[iv,0])<=max(Uni[0]):
            R2.append([nc[iv,0],nc[iv,1]])
        if nc[iv,0]<min(Uni[0]):
            R1.append([nc[iv,0],nc[iv,1]])
        if nc[iv,0]>max(Uni[0]):
```

```
                R3.append([nc[iv,0],nc[iv,1]])

        R1=np.array(R1)
        R2=np.array(R2)
        R3=np.array(R3)
        R2first=R2[::3,1]
        R2second=R2[1::3,1]
        R2third=R2[2::3,1]
        R2freq1=R2[::3,0]
        R2freq2=R2[1::3,0]
        R2freq3=R2[2::3,0
        Rfreq=np.concatenate([R1[:,0],R2freq1,R2freq2,R2freq3,R3[:,0]])
        Ramp=np.concatenate([R1[:,1],R2first,R2second,R2third,R3[:,1]])

        freq_max.append([max(Ramp),Rfreq[np.argmax(Ramp)],(F)])
        Max_lin.append(max(Ramp))
        cfreq=Rfreq[np.argmax(Ramp)]
        IND.append(min(range(len(omega)),key=lambda vivi: abs(omega[vivi]-cfreq)))

        RFREQ.append(np.array(Rfreq))
        RAMP.append(np.array(Ramp))
        plt.plot(Rfreq,Ramp,'.')

plt.show()
plt.ylabel('Amplitude_(A*A)')
plt.xlabel('frequency')
plt.savefig('Lorentizan_nonlindiss.pdf')
freq_max=np.array(freq_max)
plt.clf()
forcesq=freq_max[:,2]*freq_max[:,2]
plt.plot(forcesq,freq_max[:,0],'.')
plt.xlabel('F*F')
plt.ylabel('max AA')
plt.xscale('log')
plt.yscale('log')
plt.grid()
plt.savefig('nonlin-diss1e-4.pdf')
plt.clf()
plt.plot(force_list,(freq_max[:,1]-freq_max[0,1])/(freq_max[0,1]),'.',label='simulation')
plt.xlabel('Force')
plt.ylabel('(freq_max-freq_max[0])/(freq_max[0])')
plt.legend(loc='bottom left')
```

```
plt.savefig('freqshift_nonlin-diss_test.pdf')
np.savetxt('ddata1.txt',[forcesq,freq_max[:,0]],delimiter=' ')
np.savetxt('ddata2.txt',[forcesq,(freq_max[:,1]-freq_max[0,1])/(freq_max[0,1])]
,delimiter=' ')
```

A.2. PYTHON CODE FOR S21 SIMULATION USED FOR FIGURE 7.3

Cavity responses, *S*21, are simulated with equation above using Python script.

```
 import numpy as np


import matplotlib.pyplot as plt
from numpy.polynomial import Polynomial as P
data=np.loadtxt('Shun_2016_10_10_14.57.10_fieldsweep_1.txt')
with open('params2read.txt','r') as myfile:
    p2r=myfile.read().replace('','')
p2r=p2r.split(',')
p2r=np.array(p2r)
newp2r=np.array([p2r[0],p2r[1],p2r[2]])
newp2r=newp2r.astype(np.float)
beta=newp2r[0]
Pdbm_start=newp2r[1]
gamma_nl=newp2r[2]
x_quad=data[:,1]
y_quad=data[:,2]
freq=data[:,0]
x_quad=np.reshape(x_quad,(31,5001))
y_quad=np.reshape(y_quad,(31,5001))
freq=np.reshape(freq,(31,5001))
z=(x_quad[:,:]+1j*y_quad[:,:])
Z0=72
Z1=72
Z2=Z1
Cc=10.05e-15
Qi=26255.45

omega0=2*np.pi*5.26145e9
omega_start=2*np.pi*5.15e9
omega_stop=2*np.pi*5.2e9
omega_points=501

Pdbm_stop=Pdbm_start+30
Pdbm_step=31
Pdbm_list=np.linspace(Pdbm_start,Pdbm_stop,Pdbm_step)
Pin=10**((Pdbm_list-30)/10)
omega=np.linspace(omega_start,omega_stop, omega_points)
```

A

```
Zr=104.9
Zc=1/(1j*omega*Cc)
gamma=omega0/(2*Qi)
plt.clf()

Newcoeff=[]
for i in range(0,31):
    for w in omega:
        Delta=(w**2-omega0**2)/2/w
        a1=Qi**2/(omega0**2)*(gamma_nl**2/4+(3*beta/(4*w))**2)*(Z0**2+4/(w**2*Cc**2))
        a2=Qi/omega0*(gamma_nl-3*Delta*beta*Qi/(w*omega0))*(Z0**2+4/(w**2*Cc**2))
        +2*Zr*Qi**2/omega0*(Z0*gamma_nl-3*beta/(w*Cc*w))
        a3=4*Zr*Qi*(Z0+Zr*Qi+4*Qi*Delta/(omega0*w*Cc))
        +(Z0**2+4/(w**2*Cc**2))*(1+4*Qi**2*Delta**2/omega0**2)
        a4=-8*Z0*Zr**2*Qi**2*Pin[i]
        coeff=[a1,a2,a3,a4]
        newcoeff=np.roots(coeff)
        newcoeff = np.real(newcoeff[np.isreal(newcoeff)])
        if len(newcoeff) == 1:
            newcoeff = np.ones(3)*newcoeff[0]
        elif len(coeff) == 2:
            newcoeff = np.append(newcoeff,newcoeff[-1])
        elif len(coeff) == 3:
            pass
        Newcoeff.append(newcoeff)

Newcoeff=np.asarray(Newcoeff).T
Newcoeff=np.reshape(Newcoeff,(3,31,501))
vrsq=[]
S21_data=[]
Freq=[]
znorm=[]
s21min=[]
fmin_model=[]

    for VrsSQ0 in Newcoeff:
    Gamma_nl = 1.0/4.0*gamma_nl/gamma*VrsSQ0
    delta_nl_0 = 3.0/8*beta*VrsSQ0/omega
    DELTA=(omega**2-omega0**2)/2/omega
    Zin_0 = Zr*Qi/(1 + Gamma_nl + 2*1j*Qi*(DELTA-delta_nl_0)/omega0)
    S21_0 = 2*(Zin_0+Zc)/(2*(Zin_0+Zc)+Z0)
```

```
    vrsq.append(VrsSQ0)
    for ii in range(0,31):
        plt.plot(freq[30,:],np.abs(z[0,:])/(np.abs(z[ii,5000])),'r.')
        plt.plot(omega/2/np.pi,np.abs(S21_0[0]),'-b')
        znorm.append(np.abs(z[ii,:])/(np.abs(z[ii,500])))
        S21_data.append(np.abs(S21_0[ii]))
        Freq.append(omega/2/np.pi)
        fmin_model.append(omega[np.argmin(S21_0[ii])]/(2*np.pi))
        s21min.append(min(np.abs(S21_0[ii])))

vrsq=vrsq[0]
np.savetxt('fitdata_s21.txt',S21_data,fmt='%s')
np.savetxt('fitdata_freq.txt',Freq,fmt='%s')
np.savetxt('fitdata_pow.txt',Pdbm_list,fmt='%s')
np.savetxt('fitdata_vrsq.txt',vrsq,fmt='%s')
np.savetxt('fitdata_znorm.txt',znorm,fmt='%s')
np.savetxt('fitdata_datafreq.txt',freq[30,:],fmt='%s')
np.savetxt('low_model.dat',S21_data[0],fmt='%s')
np.savetxt('high_model.dat',S21_data[26],fmt='%s')
np.savetxt('S21min_model.dat',s21min,fmt='%s')
np.savetxt('fmin_model.dat',fmin_model,fmt='%s')
```

A

Once solutions are found, all the parameters for the plotting are plotted in a different script shown below.

```
import numpy as np
import matplotlib.pyplot as plt
import matplotlib.patches as mpatches
params2read=np.loadtxt('params2read.txt')
low_model=np.loadtxt('low_model.dat')
high_model=np.loadtxt('high_model.dat')
S21min_model=np.loadtxt('S21min_model.dat')
fmin_model=np.loadtxt('fmin_model.dat')

freq=np.loadtxt('fitdata_freq.txt')
znorm=np.loadtxt('fitdata_znorm.txt')
znorm=znorm[0:31,:]
vsqr=np.loadtxt('fitdata_vrsq.txt')
datafreq=np.loadtxt('fitdata_datafreq.txt')
pdbm=np.loadtxt('fitdata_pow.txt')
plin=10**((pdbm-30)/10)

plt.clf()
mins21=[]
maxvsqr=[]
freqshift=[]
minznorm=[]
freqshiftdata=[]
inds21min=[]

for i in range(0,31):
    Minznorm=znorm[i,np.argmin(znorm[i])-2:np.argmin(znorm[i])+2]
    minznorm.append(np.mean(Minznorm))
    maxvsqr.append(max(vsqr[i,:]))
    freqshiftdata.append(datafreq[np.argmin(znorm[i,:])])
    inds21min.append(np.argmin(znorm[i,:]))
plt.plot(pdbm,maxvsqr/plin,'.')
plt.xlabel('power(dBm)')
plt.ylabel('Vsqrd')
plt.clf()

plt.subplot(221)
plt.plot(datafreq*1.0e-9,znorm[26,:],'-k')
```

```
plt.plot(freq[0,:]*1.0e-9,high_model,'r')
plt.text(3,12,'aaa',fontsize=20)
plt.xlabel('f ( GHz )')
plt.ylabel('S21')
one=mpatches.Patch(color='k', label=str(params2read[0]))
two=mpatches.Patch(color='k', label=str(params2read[1]))
three=mpatches.Patch(color='k',label=str(params2read[2]))
plt.xlim((5.165,5.18))
plin=plin*1.0e15

plt.subplot(222)
newfmin_model=fmin_model[0:31]
nfmin_model=np.array(newfmin_model)
nfmin_model=nfmin_model.T

plt.plot(plin,nfmin_model,'-r')
plt.plot(plin,(freqshiftdata),'.k')
plt.ylabel(' f_min')
plt.xlabel('Pin ( fW )')

plt.subplot(223)
plt.plot(pdbm,minznorm,'.k')
plt.plot(pdbm,S21min_model[0:31],'-r')
plt.ylabel('min |S21|')
plt.yscale('log')
plt.xlabel('Pin ( fW )')

plt.subplot(224)
plt.plot(plin,maxvsqr,'-r')
plt.xlabel('Pin ( fW )')
plt.ylabel('V_r')

plt.tight_layout()
plt.savefig('figure'+str(params2read[1])+str(params2read[2])+'.pdf')
plt.show()
```

CURRICULUM VITÆ

Shun YANAI

06-04-1983	Born in Fujimi, Japan.

EDUCATION

1999-2002	Maebashi Ikuei high school, Japan
2009 Summer	Bachelor of Science in Physics Northern Michigan University, USA
2011–2013	Master of Science in Frontier Science, Graduate school of Pure and Applied Sciences, University of Tsukuba, Japan supervisor:Tsai Jaw Shen
2013–2018	Ph.D. Applied Science Delft University of Technology, The Netherlands
Thesis:	Coherence and nonlinearity in mechanical and Josephson superconducting devices
Promotor:	Prof. dr. G. A. Steele

LIST OF PUBLICATIONS

4. **S. Yanai, et al**. *Nonlinear analysis of SQUID cavity response,* in preperation.

3. **S. Yanai, et al**. *Hybrid SQUID cavities for improved coherence compared to all-aluminium, single step devices,* in preperation.

2. **D. Bothner, S. Yanai, et al**. *A microwave optomechanical circuit with parametric mechanical driving,* in preperation.

1. **S. Yanai, V. Singh, M. Yuan, F. Gely, S. J. Bosman, and G. A. Steele** . *Mechanical dissipation in MoRe superconducting metal drums.* Applied Physics Letters 110, 083103 (2017).